UNIVERSITY OF SOUTHAMPTON

FACULTY OF NATURAL AND ENVIRONMENTAL SCIENCES

Chemistry

Volume 1 of 1

Analysis of internal diesel injector deposit formation by separation science and mass spectrometry

by

Krina Patel

Thesis for the degree of Doctor of Philosophy

September_2016

UNIVERSITY OF SOUTHAMPTON

ABSTRACT

FACULTY OF NATURAL AND ENVIRONMENTAL SCIENCES

Chemistry

Thesis for the degree of Doctor of Philosophy

ANALYSIS OF INTERNAL DIESEL INJECTOR DEPOSIT FORMATION BY SEPARATION SCIENCE AND MASS SPECTROMETRY

By Krina Patel

Abstract: Modern high pressure fuel injection equipment (FIE) has been developed to comply with stricter emission regulations and control of fossil fuel consumption in the petrochemical industry. This incorporates smaller diameter injection holes to promote atomisation and operation at higher pressures and temperatures. These new systems are more susceptible to internal diesel injector deposits (IDID) formation which can deteriorate engine performance causing a range of operational problems such as injector failure and filter blocking, leading to increased fuel usage and emission issues.

The objectives of the project are to investigate the causes of IDID and develop analytical methods for possible deposit precursor species. A number of approaches where undertaken to investigate deposit formation.

The solvency of fuel was investigated to determine if the fuels ability to dissolve particulates has an effect on deposit formation. A 10 peak data reduction model was developed to allow for quick and easy qualitative analysis of data and determination of aliphatic and aromatic components present in fuel. It was seen that injector and filter deposit samples showed greater amounts of high mass aliphatic content.

A UHPSFC-MS screening method was also developed to identify steryl glucosides, the presence of SGs in biodiesel has been implicated in deposit formation as they show limited solubility. Tandem MS experiments were also explored to identify fragmentation patterns and aid in structure elucidation.

Surface analysis was investigated to analyse the metal injector surfaces to characterise components that may be present in deposits. DART-MS and SEM-EDX were both explored for this. From the SEM-EDX data, three distinct regions were seen and a vast difference in topology was observed in the non-deposited region, a transitional region and deposited region. These different approaches worked well to give an overall understanding of the deposit formation issue and the complexity of the problem.

Table of Contents

List of Tables

List of Figures

DECLARATION OF AUTHORSHIP

I, Krina Patel

declare that this thesis and the work presented in it are my own and has been generated by me as the result of my own original research.

Analysis of internal diesel injector deposit formation by separation science and mass spectrometry

I confirm that:

1. This work was done wholly or mainly while in candidature for a research degree at this University;
2. Where any part of this thesis has previously been submitted for a degree or any other qualification at this University or any other institution, this has been clearly stated;
3. Where I have consulted the published work of others, this is always clearly attributed;
4. Where I have quoted from the work of others, the source is always given. With the exception of such quotations, this thesis is entirely my own work;
5. I have acknowledged all main sources of help;
6. Where the thesis is based on work done by myself jointly with others, I have made clear exactly what was done by others and what I have contributed myself;
7. None of this work has been published before submission

Signed:.....

Date:.....

Acknowledgements

First of all I would like to thank my supervisor Dr John Langley, for giving me this great opportunity. His constant support and guidance has helped me throughout my PhD and he has always been there when needed.

This project was sponsored by Innospec Inc. and I would like to give special thanks to my industrial supervisors Jim Barker and Jacqueline Reid for their constant help and advice throughout. Thanks also to Cristian Lapthorn at the University of Greenwich and Alex Clarke (University of Southampton) for their help with DART-MS and SEM-EDX respectively.

Thanks to the Langley group members past and present: Chrissie, Jo, Waraporn, Stathis, Ammar, Ed, Steph, Ana and Maria. For making the office a happier environment to work with, and the endless amounts of cakes and sweets. Thanks also for Julie for always being there when you need her.

Finally, I would like to thank my parents, my sister and Aasem. For your faith in me, your continuous support and never giving up on me.

Definitions and Abbreviations

AC	Alternating current
APCI	Atmospheric pressure chemical ionisation
API	Atmospheric pressure ionisation
APPI	Atmospheric pressure photo ionisation
ASAP	Atmospheric solids analysis probe
ASTM	American society for testing and materials
AU	Absorbance unit
BPI/BPC	Base peak ion/ base peak chromatogram
CE	Collision energy
CID	Collision induced dissociation
CG	Campersteryl glucoside
CO	Carbon monoxide
CO_2	Carbon dioxide
CRM	Charged residue model
Da	Daltons
DART	Direct analysis in real time
DART-MS	Direct analysis in real- mass spectrometry
DEA	Dietyl adipate
DESI	Desorption electrospray ionisation
DC	Direct current
DCA	Deposit control additive
DDSA	Dodecenyl succinic acid
DOA	Dioctyl adipate
EI	Electron ionisation
ESI	Electrospray ionisation

eV	Electron volts
FAME	Fatty acid methyl ester
FIA ESI-MS	Flow injection analysis electrospray ionisation- mass spectrometry
FIE	Fuel injection equipment
FT-ICR MS	Fourier transform- ion cyclotron resonance mass spectrometry
FWHM	Full width at half maximum
GC-FID	Gas chromatography- flame ionisation detector
GC-MS	Gas chromatography- mass spectrometry
HC	Hydrocarbons
HPLC-MS	High performance liquid chromatography- mass spectrometry
HPCR	High performance common rail
HR-MS	High resolution- mass spectrometry
i.d.	Internal diameter
IDID	Internal diesel injector deposits
IEM	Ion evaporation model
IR	Infrared
IRMS	Isotope-ratio mass spectrometry
JFTOT	Jet fuel thermal oxidation tester
kV	Kilovolts
LOD	Limit of detection
LOQ	Limit of quantitation
MALDI	Matrix-assisted laser desorption/ionisation
MDa	Milli daltons
min	Minute

mg/kg	microgram/ kilogram
mL	millilitre
mm	millimetre
mPa	Millipascals
MRM	Multiple reaction monitorin
MS	Mass spectrometry
MS/MS	Mass spectrometry/mass spectrometry (tandem MS)
MW	Molecular weight
m/z	Mass/charge (mass-to-charge)
Na	Sodium
NIST	National institute of standards and technology
NMR	Nuclear magnetic resonance
NO_X	Nitrogen oxides
PAH	Polycyclic aromatic hydrocarbon
PM	Particulate matter
PEG	Polyethylene glycol
PDMS	Polydimethyl siloxane
PIBSI	Polyisobutylene succinimide
Ppm	Parts per million
Q-TOF-MS	Quadrupole time of flight mass spectrometry
RI	Retention index
RICC	Reconstructed ion current chromatogram
rf	Radiofrequency
RP-LC	Reversed phased-liquid chromatography
Rs	Resolution
SAE	Society of automative engineers

$ScCO_2$	Supercritical carbon dioxide
SI	Similarity index
SiG	Sitosteryl glucoside
SEM-EDX	Scanning electron microscopy- energy dispersive x-ray spectroscopy
SFC	Supercritical fluid chromatography
SGs	Steryl glucosides
SO_x	Sulphur oxides
SPE	Solid phase extraction
SRM	Single reaction monitoring
StG	Stigmasterol glucoside
s/n	Signal/noise (signal-to-noise)
TICC	Total ion current chromatogram
THC	Total hydrocarbons
TOF	Time of flight
TOF-SIMS	Time of flight- secondary ion mass spectrometry
TPO	Temperature programmed oxidation
TQD	Triple quadruple detector
uHPLC	Ultra-high performance liquid chromatography
UHPSFC-MS	Ultra-high performance supercritical fluid chromatography-mass spectromtry
ULSD	Ultra low sulphur diesel
UPC^2	Ultra performance convergence chromatography
UV	Ultraviolet
V	Volts
v/v	volume/volume
µA	Microamp

µg	Microgram
µL	Microlitre
µm	Micrometer
° C	Degrees celcius

Chapter 1: Introduction

1.1 Energy

There are expected to be oil reserves that are sufficient to meet the world's need for energy for around 80 years. One major area of concern is that the consumption of energy is increasing at a rapid rate compared to the discovery and production of fossil fuels.

Energy can be defined as primary energy or secondary energy, dependent on the usage and source of energy. Primary energy sources include fossil energy such as oil, coal and natural gas, nuclear energy and renewable energy such as wind, solar and hydropower. Fossil fuel energy sources are non-renewable and formed by natural processes of anaerobic decomposition of buried dead organisms.

Crude oil is a fossil fuel, originating from the remains of organic matter such as dead organisms accumulating in aquatic deposits over a period of millions of years. Petroleum-saturated rock was formed from deposited layers of mud and organic debris under high pressures and temperatures forming oil and gas. Crude oil is composed of hydrocarbons including paraffins, naphthenes and aromatics, with minor amounts of olefins. Crude oil exhibits a chemical fingerprint dependent on the location, geological conditions and ages under which it was formed generating light, medium or heavy crude oils.

1.2 Fuels

Fuels serve as an important role of our energy requirement in everyday life. Fuels are any materials that store potential energy in forms that, can be released by combustion and can be converted to heat or power.

The world consumption of fuel in 2011 according to the European Commission is shown in Figure 1-1, with the largest share of consumption of fuels being derived from petroleum and products, which include crude oils, natural gas liquids and petrol/diesel fuel at 41 %, followed by gas at 16 % world consumption.

Solid fuels include solid fossil fuels such as coal and make up the world consumption at 10 %. Renewable energy accounts for 13 % of the world consumption of fuel and includes hydropower (2%), geothermal energy (0.5%), solar/wind (0.5%) and biofuels and waste (10%). [1]

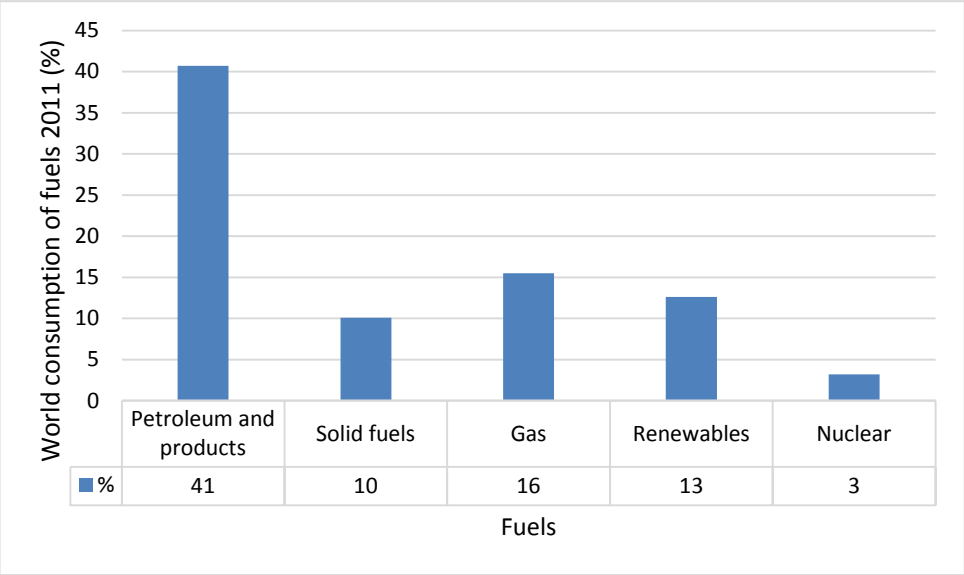

Figure 1-1. World consumption of fuel such as petroleum and gas in 2011. Reference adapted from European Commission, EU energy in figures: statistical pocketbook 2014. [1]

At present, around 80 % of the world's demand for transportation fuels, which include fuel for road, rail, air and sea are met by derivatives of crude oil. The other 20% is made from electric cars including full battery electric vehicles and plug-in hybrid vehicles.

1.2.1 Hydrocarbons

Hydrocarbons are organic compounds consisting entirely of carbon and hydrogen atoms. There are three major classes of hydrocarbons as shown in Figure 1-2, alkanes (referred to as paraffins in the petrochemical industry), cycloalkanes and aromatics.

Alkanes are long chain, saturated hydrocarbons (containing single bonds) containing carbon and hydrogen. Alkanes have a general formula C_nH_{2n+2}, where n refers to the number of carbon atoms. Alkanes can be either straight chained or branched (referred to as isomers or iso-alkane). Hydrocarbons with values of 'n' between 5 and 8, pentane (C5),

hexane (C6), heptane (C7) and octane (C8) are all refined into petrol fuel. In diesel fuel, the hydrocarbons typically used are C16-C20, referring to hexadecane (C16), heptadecane (C17), octadecane (C18), nonadecane (C19) and eicosane (C20). The boiling point of alkanes are roughly around 170 °C for carbon chain lengths of C1-C10 and increase to 350 °C for C10-C20.

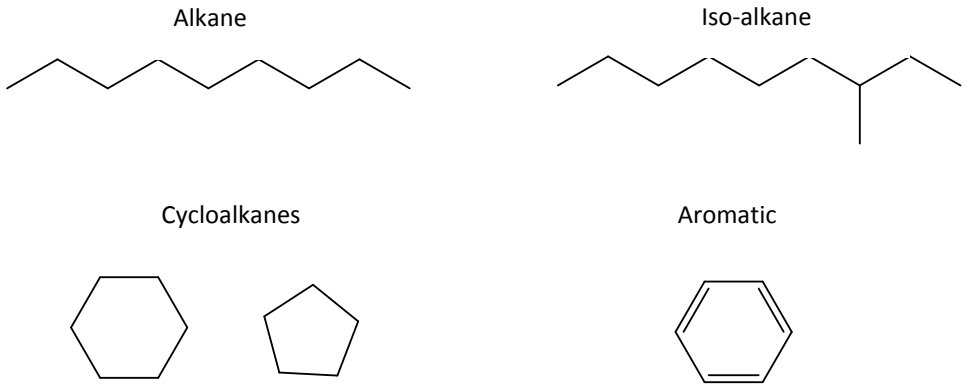

Figure 1-2. Three major classes of HC found in fuels, alkanes and branched isoalkanes, cycloalkanes and aromatic compounds.

Cycloalkanes also known as naphthenes, are saturated hydrocarbons having one or more carbon rings with a general structure of C_nH_{2n}. Cycloalkanes have similar properties to alkanes however with higher boiling points. Diesel fuels typically contain 1-ring to 3-ring cycloalkanes such as decalin (bicyclic ring structure).

Aromatic hydrocarbons are unsaturated hydrocarbons (containing double bonds) with a general formula of C_nH_n, and contain at least one six-carbon ring. Examples of aromatic compounds include benzene C_6H_6 and naphthalene $C_{10}H_8$ which is a fused double-ring aromatic hydrocarbons. More complex aromatics include three or more fused aromatic rings known as polycyclic aromatic hydrocarbons (PAH) such as anthracene and phenanthrene.

1.2.2 Refinery process

In the refining process, crude oil is converted into a range of refined products such as petrol, diesel and jet fuel. Modern refining processes can be classified into three basic processes: separation, conversion and purification.

1.2.2.1 Separation process

The first step in the refinery process is to separate the crude oil into its naturally occurring components. This is accomplished by applying heat through a process called distillation which takes place in a distillation tower. Distillation is the process that separates the compounds in the column based on the boiling points of the components. [2]

Figure 1-3 shows a schematic diagram of crude oil distillation and the crude oil fractions that can make the refined products such as petrol, kerosene and diesel fuel. [2]

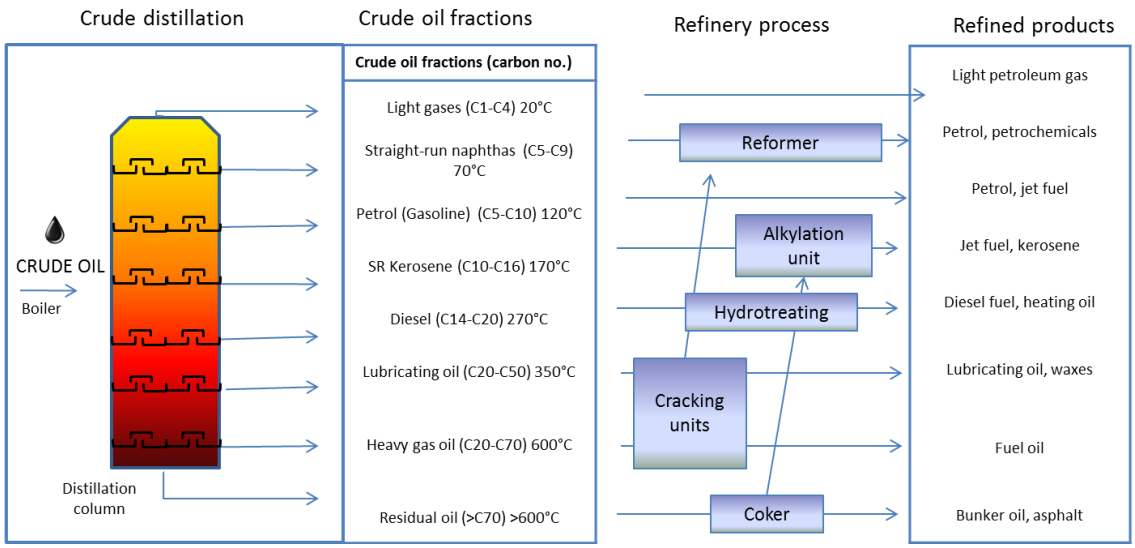

Figure 1-3. Schematic diagram of crude oil distillation showing the crude oil fractions obtained and the refinery processes involved to produce the refined products. Reference adapted from Babich, I et al., Science and technology of novel processes for deep desulfurization of oil refinery streams. [2]

In this process, the crude feedstock is heated to around 400 °C and then feed into the distillation column in the form of vapour. The distillation column contains a series of collecting plates with valves that allow vapour to bubble through the liquid in the plate. As the vapour moves up the column, each fraction cools and condenses at a different temperature and it collected on the plates.

The lightest fractions, including light gases such as liquid petroleum gas, straight run naphthas and petrol (gasoline) vaporise and rise to the top of the tower, where they condense back to liquids and are collected. Medium-weight liquids including kerosene and diesel stay in the middle of the tower, where they are collected. The heavier fractions such as residual oils that are tar-like fractions have the highest boiling points and settle at

the bottom of the tower. The fractions are then piped to the next station where they undergo conversion processes to become high-value products. [3]

1.2.2.2 Conversion process

The conversion step involves fracturing or "cracking" large, high-boiling point HC molecules (with lower value) into smaller, lighter molecules more suitable for blending to petrol, jet and diesel fuel (higher value). The most common conversion processes are fluid catalytic cracking and hydrocracking, which both involve breaking larger molecules into smaller ones through the use of catalysts and/or high pressures. [4]

Fluid catalytic cracking (FCC), the most widely used conversion process, uses a hot, fluid catalyst (zeolite, aluminium hydrosilicate) and low pressures to convert heavy gas oil into diesel oils and petrol fuel. FCC also produces a large volume of lighter gases (C1-C4) which can be used as feedstocks in the upgrading process. [5]

Hydrocracking is another major conversion process, similar to catalytic cracking which involves a catalyst but reactions take place under a high pressure of hydrogen gas. During hydrocracking, large molecules are cracked into smaller molecules by cleaving carbon-carbon bonds. The process takes heavy oils and cracks them into petrol fuel and kerosene (jet fuel). Hydrocracking also acts to remove heteroatoms especially sulfur from the streams, which is advantageous in fuels. [3]

1.2.2.3 Upgrading/ Purification process

Upgrading processes are undertaken to combine and rearrange molecular structures of compounds to improve their properties such as octane rating and produce high-value streams, examples of this process include catalytic reforming and alkylation.

Alkylation is generally used for petrol components and combines some of the lighter gaseous by-products of cracking to form higher value octane petrol blend stocks (also known as alkylates). Alkylation units use a strong liquid acid catalyst (typically hydrofluoric acid and sulfuric acid) and are essentially the cracking process in reverse.

Catalytic reforming also occurs in the refinery process, this process converts low-value components such as naphtha into reformate which has a higher octane number and can be used for petrol/diesel fuel blending. [6]

The final step in the refinery process is the purification step, this acts to remove trace components that may be present in the fuel that give it undesired qualities. The most common process in purification is hydrotreating, which involves removing heteroatoms (*e.g*. sulfur, nitrogen and heavy metals) from fuel compounds with hydrogen in the presence of a catalyst. The hydrogen combines with the heteroatoms to form non-hydrocarbon molecules that are easily separated from refinery streams. This process can form ultra-low sulfur diesel (ULSD) and remove benzene in petrol fuel to comply with government standards and will be explained in more detail further on. [7]

1.2.3 Properties of diesel fuel

Diesel fuel is produced by blending fractions of crude oil distillates particularly straight-run middle distillates with varying proportions of gas oils and thermally and catalytically-cracked distillates. Diesel fuel is a highly complex mixture of a range of compounds; including paraffins (C_nH_{2n+2}), iso-paraffins (C_nH_{2n+2}, n>3), naphthenes (C_nH_{2n}), and aromatic compounds.

Diesel fuel comes in several different grades depending upon its use and the refinery processes used. By controlling specifications and properties, it is possible to satisfy the ever-increasing requirements of diesel fuel and its quality. The most commonly used guidelines for diesel fuel quality in USA are established by the American Society for Testing and Materials (ASTM) international. The current ASTM standard for diesel fuels is 'ASTM D 975- standard specification for diesel fuel oils'. [8] In Europe, the European committee for standardization establishes the fuel quality. The guidelines are named 'EN 590- automative fuels- diesel requirements and test methods'. [9]

The most important parameters for the standards of diesel fuel are shown below and include cetane quality, viscosity and lubricity and Table 1-1 shows a comparison of ASTM D975 and EN590 specifications for each parameter.

1.2.3.1 Cetane quality

One of the most important characteristics of diesel fuel is its ability to auto ignite, which refers to the minimum temperature required to spontaneously ignite a substance in normal atmospheric conditions in the absence of an external source of ignition. This is quantified by the cetane number of the fuel, where the higher the cetane number the quicker the fuel ignites. The cetane number provides a measure of the ignition characteristics of diesel fuel, which relates to the ignition delay - the period that occurs between the start of fuel injection and the start of combustion. The higher the cetane number equates to the shorter the ignition delay and the better the quality of combustion. [10-11]

Increasing the cetane number of the fuel improves fuel combustion, reduces white smoke on start-up and tends to reduce nitrogen oxides (NO_X) and particulate matter (PM) emissions. A minimum cetane number is set to 40 (ASTM D975) or 51 (EN490) dependent on specification, below these values could result in poor ignition quality, long ignition delay, abnormal and inefficient combustion and engine knock.

1.2.3.2 Volatility

The ideal fuel volatility requirements are dependent on engine size and design, speed and atmospheric conditions. For engines involving fluctuating loads and speeds such as trucks, fuels that are more volatile are preferred for better performance. However, for best fuel economy, heavier types of fuel contain greater heat content.

1.2.3.3 Viscosity

Viscosity is an important property of diesel fuel and is a measure of the resistance of the fuel to flow (or fluid motion). The greater the viscosity, the higher the resistance to flow. If the viscosity of the fuel is too low, it could result in leakage losses in the fuel-injection system at low engine speed and therefore lead to power deficiencies. If the viscosity is too high however, it can impair the pump function and result in poor fuel atomisation. In general, fuels with low viscosity tend to have poorer lubrication properties. Viscosity should be roughly 1.3 - 5 mm^2/s dependant on the fuel specification.

1.2.3.4 Flash point

Flash point refers to the temperature at which a combustible liquid gives off just enough vapour to the air that it can ignite when exposed to a flame or spark. The flash point is controlled to meet safety requirements for fuel handling and storage. Typically, a flash point of 38-52 °C (ASTM D975) and above 55 °C (EN590) is required for diesel fuel.

1.2.3.5 Lubricity

Lubricity is another important characteristic of diesel fuel and is a measure of the reduction in friction of a material. The lubricity of the fuel is an indication of the amount of wear that occurs between two metal parts covered with fuel; high lubricity fuel can provide reduced wear and lengthen component life. Diesel fuel injection equipment heavily relies on fuel as a lubricant to coat the internal parts of the engine. [2]
Previously, naturally occurring lubricity agents present in diesel fuel provided adequate protection. However, due to the new requirements of diesel fuel naturally occurring sulfur and aromatic compounds have been removed from the fuel, reducing its lubricity requiring the addition of lubricity additives.

1.2.3.6 Density

The diesel fuels calorific value can depend on its density, which refers to the mass per unit volume of diesel fuel at a given temperature and is a useful indication of the fuel's composition and performance - related characteristic. Changes in fuel density affect the energy content of the fuel; reducing fuel density tends to reduce NO_X emissions in older engines, however emission from modern engines are not influenced by the density of the fuel. A limit is needed to the maximum density of the fuel to avoid smoke formation, typically around 800 kg/m^3.

1.2.3.7 Low temperature operability

At low temperatures, wax crystals can begin to precipitate from the diesel fuel especially by the paraffinic compounds present in diesel fuel. These wax crystals can result in operational issues such as clogging of fuel filter and malfunctioning of the engine. The low temperature properties are defined by wax-related tests that measure the cloud point and pour point of the fuel.

The cloud point of diesel fuel refers to the temperature at which the amount of precipitated wax crystals becomes large enough to make the fuel appear cloudy. Cloud point depends on the boiling range and paraffin content of the fuel and for diesel fuels is normally in the range of 10°C and -20°C depending upon the location and season.

Pour point refers to the lowest temperature at which the fuel will flow and is used to predict the lowest temperature at which the fuel can be pumped without gelling. The pour point for diesel fuel is generally 5 - 10°C below the cloud point.

Cold filter plugging point (CFPP) is defined as the lowest temperature at which a given volume of fuel passes through a filter in a limited time interval.

1.2.3.8 Sulfur content

Sulfur limits are now set by the US and European Environmental Protection Agency. In the ASTM D975 guidelines the limit of sulfur is a maximum of 500 ppm for low sulfur diesel and 15 ppm for ultra-low sulfur diesel. The presence of sulfur in diesel fuel is an environmental concern because on combustion, the sulfur is converted to SO_X, which can poison the catalytic converter used for exhaust emission treatment and contributes to acid rain.

1.2.3.9 Thermal stability/oxidative stability

Stability is also an important characteristic of fuel; fuels with poor oxidation stability can contain insoluble particles that can plug fuel filters in vehicles. [12] Fuel stability refers to the fuel being resistant to change which can be from high or low temperatures (thermal stability) and storage conditions (storage stability). Degradation of fuel can result in development of particulate matter and deposits, change in physical properties or fuel

composition that can have a great impact on the combustion efficiency. Oxidative stability is a particular concern to biodiesel fuel; this is a result of its chemical structure being influenced by the nature of the fatty acid groups and number of double bonds. [13-15] Table 1-1 shows a comparison of the ASTM D975 and EN 590 specifications for the diesel fuel properties.

Table 1-1. Properties of diesel fuel with comparisons to ASTM D975 and EN 590 specifications. Reference adapted from ASTM and EN specifications [8, 9]

Properties	ASTM D975 specifications	EN 590 specifications
Cetane number - Cetane index	(minimum) 40	(minimum) 51 (minimum) 46
Volatility (T_{90})	280 - 340 °C	
Viscosity at 40 °C	1.3 - 4.1 mm^2/s	2.0 - 4.5 mm^2/s
Flash point	38 - 52 °C	(minimum) Above 55 °C
Lubricity (high pressure reciprocating rig at 60 °C)	520 µm	460 µm
Density at 15 °C	800 - 860 kg/m^3	820 - 845 kg/m^3
Cloud point Pour point CFPP	-20 to 10 °C -35 to -15 °C	
Sulfur content	15 mg/kg (ppm)	10 mg/kg (ppm)
Oxidative stability		(minimum) 20 hrs.

1.2.4 Diesel engine

The development of the compression-ignition engine began in the late 18th century. By 1892 a patent was taken out by Dr Rudolf Diesel on a engine in which the fuel was ignited by compression. [16-17] After many years, the first diesel engine was produced in 1897, achieving 20 horsepower at 175 rpm. The aim of this design was to achieve higher thermal efficiency and improved fuel consumption by using higher compression ratios. One of the biggest challenges of this engine was the fuel supply system; the compressor required was very bulky and the combustion system was not capable of operating at higher engine speeds. In the 1920s, Robert Bosch began development of a fuel-injection

system and the Bosch fuel injection pumps produced were the breakthrough in achieving higher running speeds in diesel engines. [18-20]

The diesel engine is a compression-ignition engine in which the fuel and air are mixed inside the engine. The air is highly compressed inside the combustion chamber which generates high temperatures sufficient for the diesel fuel to auto-ignite when injected into the cylinder. The diesel engine uses heat to release the chemical energy contained within the diesel fuel and convert it into mechanical force for power.

Diesel engines may operate either as two-stroke or four-stroke engines; with the latter being most commonly used. A stroke refers to the movement of a piston through the cylinder that causes the crankshaft to rotate driving the combustion of the air and fuel mixture.

The two stroke engine has been defined by the Society of Automative Engineers (SAE), in which the four 'cycles' of internal combustion engine theory referring to intake, compression, ignition and exhaust occur in one revolution (360 mechanical degrees) whereas the four stroke engine occurs in two complete revolutions (720 mechanical degrees).

The four-stroke engine works in four distinct cycles or strokes referred to as the induction stroke, compression stroke, ignition stroke and exhaust stroke. The inlet valve controls the intake of air into the combustion chamber and the exhaust valve removes the burnt gases after combustion. Figure 1-4 shows a schematic diagram of the four-stroke process in diesel engines.

1. The induction stroke involves the introduction of air into the combustion chamber. The piston is forced down, increasing the capacity of the cylinder, and at the same time the inlet valve is opened which allows air to enter the cylinder.
2. In the compression stroke, the piston moves back up which acts to compress the air trapped inside the cylinder. In the process, the air heats up to around 900 °C. When the compression stroke is almost complete, the fuel injection system injects fuel at high pressure (around 2000 bar) into the compressed air.
3. The ignition (or combustion) stroke then occurs, when the finely atomised diesel fuel enters the combustion chamber it spontaneously auto ignites and burns due to the heat of the compressed air. The amount of energy released by combustion

is dependent on the mass of the fuel injected. The chemical energy released by combustion is then converted into kinetic energy, which is translated by the crankshaft into turning force or torque. In a petrol engine, the compressed air-fuel mixture is ignited by a spark plug.

4. The exhaust stroke occurs when the exhaust valve is opened to allow the hot, pressurised gases flow out of the cylinder. As the piston moves upwards again, it forces the remaining exhaust gases out. On completion of the exhaust stroke, the cycle restarts back to the induction stroke. [21]

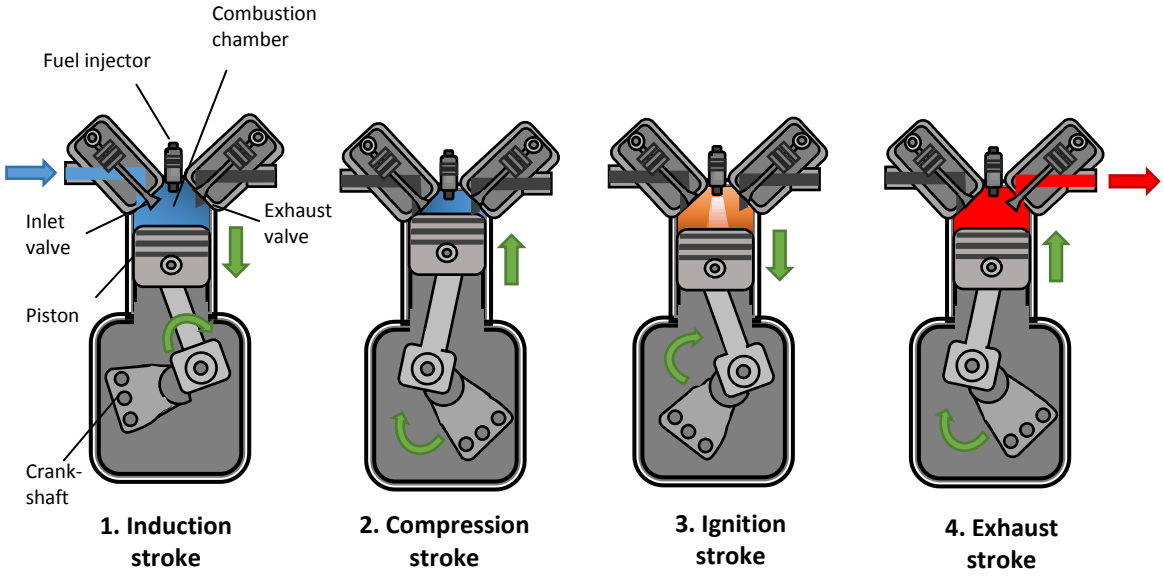

Figure 1-4. Four-stroke process of the diesel engine; induction, compression, ignition and exhaust stroke. Reference adapted from dieselnet.com.

1.2.5 Diesel fuel additives

Additives are chemicals that are introduced to the fuel in very low concentrations to improve its performance, enhance certain properties or reduce undesirable ones. Diesel fuel additives are used for a wide range of purposes; four principal areas they are used in include engine and fuel delivery system performance, fuel handling, fuel stability and contamination control. Some examples of these additives are shown in Figure 1-5

including cetane number improver, deposit control additive, lubricity improver and corrosion inhibitor.

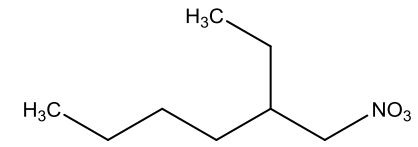

2-ethylhexyl nitrate (2-EHN), cetane number improver

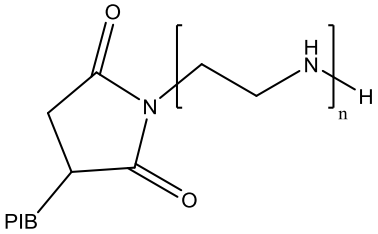

Polyisobutylene succinimide (PIBSI), deposit control additive

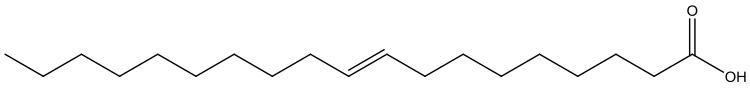

Oleic acid, lubricity improver

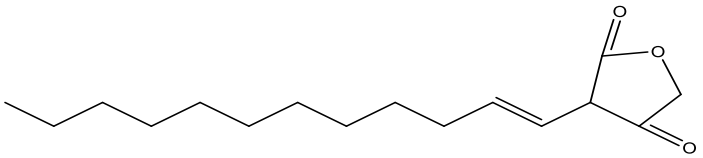

Dodecenyl succinic acid, corrosion inhibitor

Figure 1-5. Additives commonly used in diesel fuel, including cetane number improvers, deposit control additives, lubricity improver and corrosion inhibitor.

Engine and fuel delivery system performance additives can improve the injection system and engine performance. An example of these types of additives are cetane number improvers, which act to reduce combustion noise and smoke and can improve the cold-starting properties of the fuel. 2-Ethylhexyl nitrate (EHN) is the most widely used cetane number improver. EHN is thermally unstable and decomposes in the combustion chamber, the products of this decomposition help initiate fuel combustion and shorten the ignition delay period of the engine. [22]

Detergent additives are used to keep the injector clean and free from deposits, the additives are composed of a polar group which bonds to deposits and deposit precursors, and a non-polar group that readily dissolves in the fuel. This acts to redissolve the deposit and transport it out of the fuel system.

Lubricity additives are used to counteract the hydrotreating process which significantly lowers the lubricity of the fuel. They contain a polar group which is attracted to metal surfaces causing the additive to form a thick surface film which acts as a boundary lubricant when two metal surfaces come into contact. Three additive chemistries are mainly used for lubricity additives and contain mono-acids, amides and esters.

Fuel handling additives include antifoam additives, de-icing additives and low-temperature operability additives. Low-temperature operability additives can lower a fuel's pour point, cloud point or improve its cold flow properties which has advantages for use at low temperatures. Many of the additives are polymers that interact with the wax crystals formed when the fuel is cooled, the polymers moderate the effect of wax crystals by modifying their size, shape and degree of agglomeration.

Another type of diesel fuel additive is fuel stability additives which work by blocking one-step in a multi-step reaction pathway of fuel stability. One type of fuel instability is related to oxidation, which takes place when oxygen from the dissolved air attacks reactive compounds in the fuel. This initial reaction sets off complex chain reactions involving initiation, propagation and termination. Antioxidants work by interrupting the chain reactions and therefore prevent auto-oxidation reactions from occurring. Hindered phenols and amines such as phenylenediamine, are the most commonly used antioxidants in diesel fuel.

Contaminant control additives are used to deal with contaminants present in the fuel and storage systems, and include biocides used to stop biological growth when microorganisms reach problematic levels. Corrosion inhibitors are also used to stop the formation of rust in pipelines and tanks. Corrosion inhibitors act by attaching to the metal surface and forming a protective layer that prevents attack by corrosive agents.

Additives may be added to the fuel at the refinery, during distribution or after the fuel has left the terminal. Fuel manufacturers and marketers all have a legal requirement to produce a product that meets all the specific requirements, which can be achieved from the use of additives. [22]

1.3 Developments of diesel engines and fuel

1.3.1 Introduction of government regulations

The transport sector is one of the fastest growing sectors and, apart from energy generation and industrial processing, contributes greatly to emissions of the major air pollutants. Air pollution is a significant risk factor for a number of health conditions including respiratory infections and conditions including asthma, heart disease, lung cancer and in some cases has led to premature death. This has caused the area to become a major priority of action with many of the world's governments enforcing emission regulations. Many countries have adopted US and European emission regulation levels as a starting point and developed their national regulations dependent on local conditions.

The emission legislations define the acceptable limits for exhaust emissions particularly for nitrogen oxides (NO_X) [23], total hydrocarbons (THC) [24], volatile organic compounds (VOC) [25], non-methane hydrocarbons [26], carbon monoxide (CO) [26], sulfur (S) [27], lead (Pb) [28] and other particulate matter (PM) [29]. Each of these, along with secondary by-products such as ozone, can cause severe health effects and damage to the environment. [30-32]

The control of pollutants has been regulated since the 1960s in both the US and European Union. In the US, the first emission regulations were established by California in 1966. This forced the control of total hydrocarbons (THC) and carbon monoxide (CO) for passenger vehicles in the US. In Europe, individual countries such as France and Germany set individual emission regulations, however these were opposed by other members of the European Union and any EU emission regulations were delayed until the 1990s as a result.

The US clean air act was first introduced in the 1970s and has been the driving force for these changes; it required a 75 % reduction in THC and CO emissions from motor vehicles and introduced the control of nitrogen oxide (NO_x) emissions with a 70 % reduction.

In the early 1990s, the European emission standards were set to define acceptable limits of emissions and were set as a series of targets staging the progressive introduction of more stringent emission standards. The stages start from Euro I (introduced in July 1992),

Euro 2 (January 1996), Euro 3 (January 2000), Euro 4 (January 2005), Euro 5a (September 2009), Euro 5b (September 2011) and finally to Euro 6 (September 2014).

Figure 1-6 shows the progression in emissions standards from Euro 1-6 for CO, NO_X, HC + NO_X and PM. The biggest reductions are seen in particulate matter (PM) emissions at a 93 % reduction, nitrogen oxides (NO_x) emissions at 72 % reduction, hydrocarbon (HC) emissions 70 % reduction and carbon dioxide (CO) emissions at 69 % reduction. [33-34]

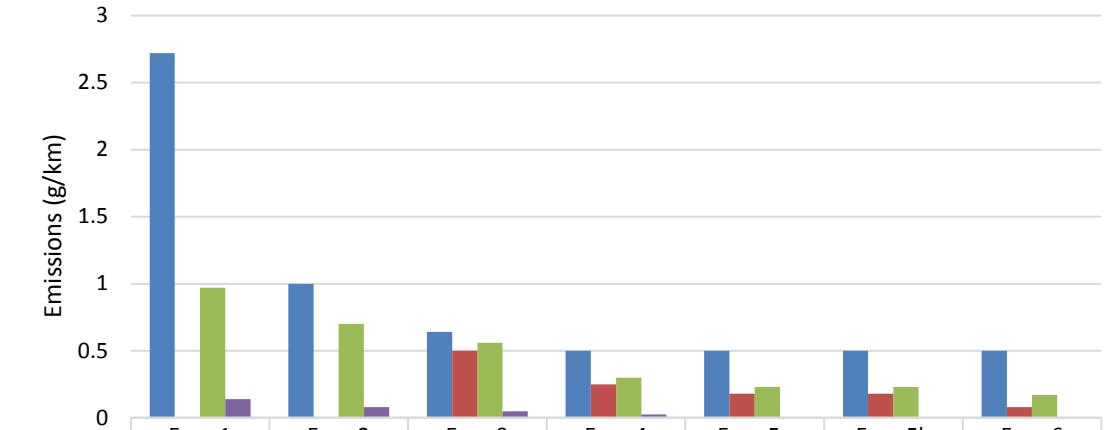

	Euro 1	Euro 2	Euro 3	Euro 4	Euro 5a	Euro 5b	Euro 6
CO	2.72	1	0.64	0.5	0.5	0.5	0.5
Nox	0	0	0.5	0.25	0.18	0.18	0.08
HC + NOx	0.97	0.7	0.56	0.3	0.23	0.23	0.17
PM	0.14	0.08	0.05	0.025	0.005	0.005	0.005

Figure 1-6. European emission standards for passenger cars from Euro 1-6. Reference adapted from the International council on clean transportation (ICCT).

To comply with these regulations a number of engine modifications were required, which can be seen in **Figure 1-7**. In Euro 1 and 2, indirect fuel injection (IDI) was introduced to comply with the emission regulations and the injection pressure was low at 700-800 bar.

Euro 3 regulations started the shift from mechanical injection to electromechanical injection and direct injection (DI). Electronic fuel timing became the dominant technology, with the introduction of common rail systems and high pressure fuel injection systems operating at around 1300 bar.

In Euro 4, the main focus was on direct injection improvements with electronic control and increasing injection pressures operating at around 1300-1600 bar.

Euro 5, saw improvements in the combination of in-cylinder measures and modifications of the diesel oxidation catalyst (DOC) and diesel particulate filter (DPF). Higher injection pressures of around 1600-1900 bar were also introduced.

Euro 6, typically involved operating at higher pressures of around 1800-2100 bar and involved improvements to DOC/DPF systems to control PM emissions.

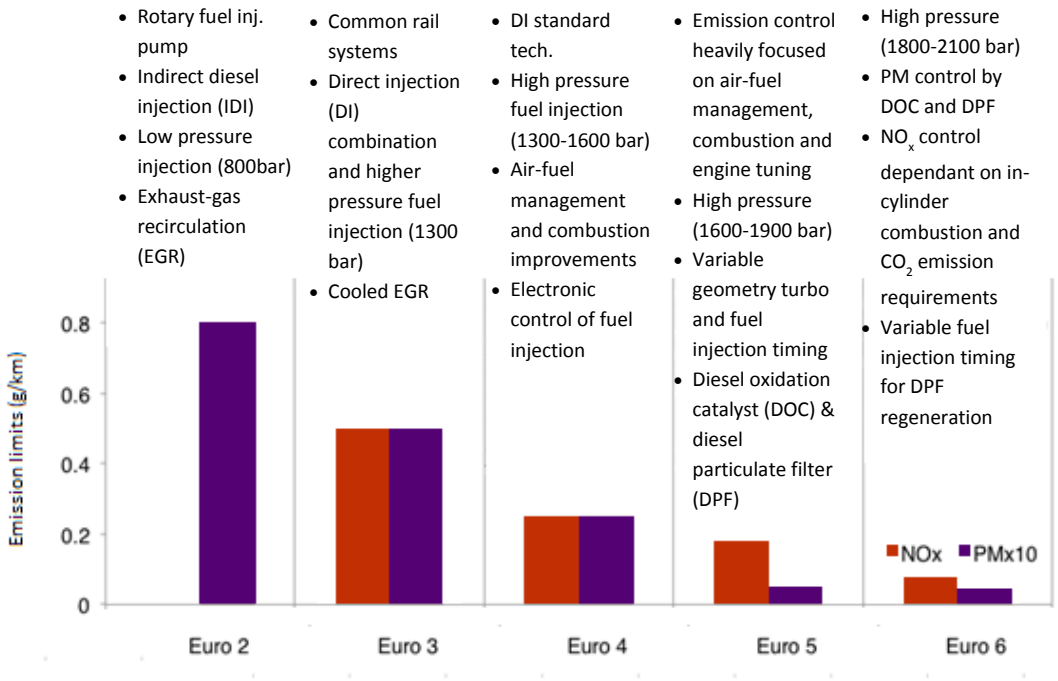

Figure 1-7. Technologies developed in the diesel engine required to comply with the European emission standards. Reference adapted from www.dieselnet.com.

1.3.2 High pressure common rail system

The recent regulations in emissions and need for reduction in fossil fuel usage, has caused an increased demand on the fuel injection equipment (FIE). This has led to the development of modern common rail fuel injection systems which incorporate smaller diameter injection holes to promote atomisation of fuel and reduce particulate emissions as well as being able to operate at elevated temperatures (above 200 °C) and pressures of around 300 MPa (or 3000 bar). [35]

The fuel injection system has to deliver the precise amount of fuel to suit the operating conditions at any given moment. The electronic diesel control (EDC) system allows the quantity of the injected fuel to be adjusted individually for each cylinder to achieve smooth engine running.

High pressure common rail (HPCR) systems deliver a more controlled quantity of atomised fuel, which leads to better fuel economy, a reduction in exhaust emissions and a significant decrease in engine noise during operation. The functions of pressure generation and fuel injection systems are separated. In common rail systems as shown in Figure 1-8, a high pressure pump stores a reservoir of fuel at high pressure up to 2000 bars (200 MPa), the fuel injectors are supplied by a common rail where the fuel is stored at high pressure and supplies multiple fuel injectors. The fuel injectors are electronically controlled, allowing parameters such as pressure in the common rail and duration of injection to be maintained. [36-37]

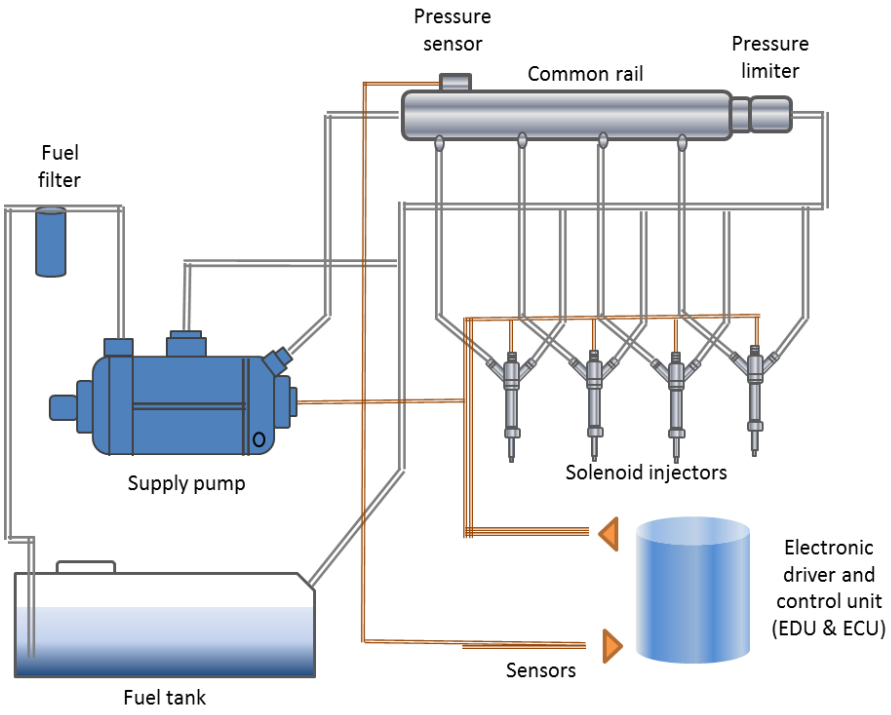

Figure 1-8. Schematic diagram of the diesel engine containing the high pressure common rail system delivering fuel to the solenoid injectors. Reference adapted from www.dieselnet.com.

1.3.3 Ultra-low sulfur diesel

Sulfur is a natural component present in crude oil and the products refined from it, however the air pollutant sulfur dioxide (SO_2) is produced on combustion. Sulfur dioxide is not only a major air pollutant and a precursor to acid rain but also has significant impact on the environment in terms of human health and animal life.

Sulfur dioxide can be oxidised gradually to form sulfur trioxide (SO_3) (Equation 1-1), which then goes on to react with water to form sulfuric acid (H_2SO_4) (Equation 1-2). Sulfuric acid is a strong acid and ionises completely to form hydrogen ions (Equation 1-3) which gives rain water a pH below 5 making it acidic, causing a vast number of ecological effects. Some of these include damage to buildings and statues and also affect aquatic environments.

$$2SO_{2\,(g)} + O_{2\,(g)} \rightarrow 2SO_{3\,(g)} \qquad \textbf{Equation 1-1}$$

$$SO_{3\,(g)} + H_2O_{(l)} \rightarrow H_2SO_{4\,(aq)} \qquad \textbf{Equation 1-2}$$

$$H_2SO_{4\,(aq)} \rightarrow 2H^+ + SO_4{}^{2-} \qquad \textbf{Equation 1-3}$$

Ultra-Low Sulfur Diesel (ULSD) was recently introduced as a means to reduce the concentration of sulfur in the fuel and comply with government regulations by reducing the environmental impact on emissions. ULSD contains less than 15 parts per million (ppm) sulfur content and is a much cleaner fuel than traditional diesel fuels, aiming to significantly reduce sulfur emissions. The move to lower sulfur content has resulted in a reduction of smoke emissions of up to 60 %, sulfur dioxide emissions by 90 % and a 20 % reduction in particulate matter. The sulfur reduction in diesel fuel is necessary to preserve the proper function of the advanced emissions control systems on new diesel engines. [38]

The process to remove sulfur is known as hydrotreating or hydrodesulfurisation and involves reacting the fuel containing a sulfur compound (RSH) with hydrogen (H_2) under heat and high pressures (35 -170 bar) in the presence of a catalyst (cobalt-molybdenum or nickel-molybdenum catalyst), producing hydrogen sulphide (H_2S) and the desulfurised fuel product. [39] The general reaction is represented below in Equation 1-4.

$$RSH + H_2 \rightarrow RH + H_2S \qquad \textbf{Equation 1-4}$$

This process of hydrotreating however has severe effects on the properties of the fuel. Diesel fuel naturally contains sulfur compounds that provide good lubricity, therefore, diesel fuels with low sulfur content have lower lubricity and require the addition of lubricity improving additives to prevent excessive engine wear. Since the introduction of ULSD fuel, the number of reported issues with diesel engines has risen, these include premature fuel filter plugging and injector fouling. Injector fouling occurs when deposits form in the FIE and fuel filter plugging can result from insoluble sediments or contaminants that could be present in the fuel clogging up the fuel filter. [40-41]

The process of hydro treating also has a significant impact of the final fuel composition; it reduces the amount of aromatics/olefin compounds, polar compounds, natural stabilisers, and natural biocides and reduces the density of the fuel but also increases the amount of saturated hydrocarbons, reducing the solvency of the fuel. This is in turn can lead to poor in-vehicle stability, low temperature issues, corrosion and increased microbial growth. [42]

1.3.4 Incorporation of biodiesel fuels

Growing concerns over fossil fuel depletion and a requirement to meet the "Renewable Fuels Transport Fuel Obligations Order (2007)" [34] which requires renewable fuels to make up 5 % of road fuel, have caused the fuel industry to replace conventional hydrocarbon fuel with equivalents obtained from renewable resources.
At present, the most common renewable fuel used is biodiesel, which is formed from the inclusion of esterified seed oils, collectively known as fatty acid esters. In Europe these are fatty acid methyl esters (FAME**).** The term biodiesel refers to the use of monoalkyl esters of long chain fatty acids derived from plant or animal matter which meet the relevant regulations. [43]

The engine manufacturers association (EMA) and a consortium of original engine manufacturers (OEMs) recommend the use of biodiesel fuel that contain no more than five percent by volume biodiesel (B5). Higher concentrations such as B20 (containing 20 % biodiesel, 80 % diesel fuel) are not universally accepted but some OEMs have produced engines that can run on B20 fuels. The concern with higher than B5 fuels (containing 5 % biodiesel, 95 % diesel fuel) is the lack of evidence around the improvements of biodiesel

fuel on engine performance. Testing has been found that supports the claims of lower emissions of HC, CO and PM through the use of biodiesel fuel.

The CO emission is lowered by around 30-50 % depending on the percentage of biodiesel used in the blend. In addition, the use of biodiesel fuel offers a number of distinct advantages including that it is biodegradable, non-toxic and an environmentally friendly source of fuel compared to fossil fuels, which are a finite source of fuel.Some main area of concerns are that biodiesel fuel has poor pour point properties limiting its use in cold weather, biodiesel is also known to degrade more rapidly and is more susceptible to oxidative degradation than conventional diesel fuel. Oxidative degradation is caused by contact with ambient air (auto-oxidation) during long-term storage, which can compromise the quality of the fuel. These properties have been associated with operational issues such as corrosion, engine deposits, injector coking and filter plugging. [43]

1.3.4.1 Biodiesel

In 1985, Dr Rudolf Diesel first demonstrated the use of vegetable oil (peanut oil) as a fuel in the diesel engine. Since that time, however, the diesel engine has been run using fossil-based diesel fuel due to its availability and cheaper price. However, Diesel's ambitions for the engine were for the fuel to be renewable and run on biodiesel.

Biodiesel fuel is produced by a process known as transesterification, in which various oils (triglycerides) are converted into esters through a chemical reaction involving methanol in the presence of a catalyst, such as sodium or potassium hydroxide. Biodiesel blend stocks are methyl or ethyl esters derived from a variety of renewable sources such as vegetable oil, animal fat and recycled cooking oil (see Figure 1-9).

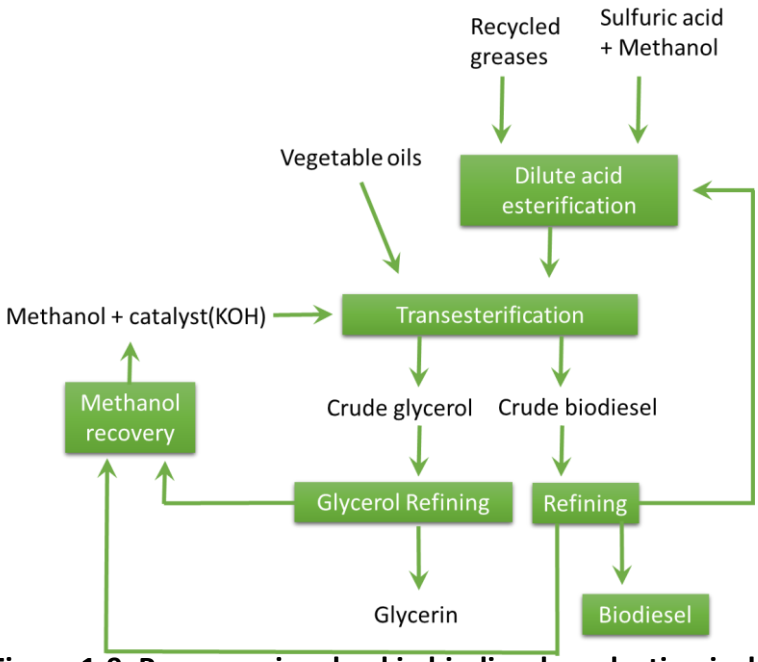

Figure 1-9. Processes involved in biodiesel production including the transesterification processes. Reference adapted from www.afdc.energy.gov.

By-products of this process include glycerols and water (see **Figure 1-10**). The process produces fatty acid methyl esters (FAME) and the physical and chemical properties of biodiesel depend on the fatty acid compositions of the feedstocks used in the production. In the process a triglyceride is transformed to diglyceride, monoglyceride and finally to glycerol. Where R_1, R_2 and R_3 are represented as a mixture of various fatty acid chains. [44-45]

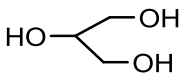

Figure 1-10. Transesterification reaction of triglyceride with methanol to produce biodiesel, R_1, R_2, R_3 are represented as a mixture of various fatty acid chains. Reference adapted from www.kfch.upce.cz.

First generation biofuels are produced from food crops such as palm, rapeseed, soy, beets and cereals. Second and third generation biofuels include feedstocks that do not compete directly with food crops such as waste and agricultural residues. These also include biofuels produced from lignocellulosic biomass (any non-food part of plants that humans cannot digest).

The selection criteria of feedstocks used to produce biodiesel are dependent on the geographical location, availability and cost. The most common sources of oil for biodiesel in the United States are soybean oil and recycled cooking oil and in Europe the most common source is rapeseed oil; however other vegetable oils such as palm oil and coconut oil are also being used.

1.3.4.1.1 Oxidation of FAME

Fuel stability is a major area of concern with regards to diesel fuel and biodiesel. The stability of biodiesel is lower than that of conventional diesel fuel and is susceptible to auto-oxidation. Stability takes into account interactions of olefins, dienes, nitrogen, sulfur and oxygen-containing compounds that can potentially lead to deposit formation. Properties of fuel can change over long-term storage including oxidation or autoxidation from contact with ambient air, thermal or thermal-oxidative degradation from excess

heat, hydrolysis from contact with water or moisture or microbiological contamination. [46-48]

Auto-oxidation processes occur when biodiesel is exposed to and reacts with ambient oxygen, this process is accelerated at high temperatures. Oxidative degradation can occur when the fuel is kept in long-term storage, or as a result of circulation through the engine system with exposure to high temperatures and pressure. Degradation due to auto-oxidation can impact on the fuels properties significantly, including altering the flash point, ester content, the amount of insoluble contaminants and cetane number. Degraded biodiesel has been observed to result in injector deposit formation, due to the increase in viscosity caused by the formation of polymeric species in the fuel. [49-51]

The degree of saturation of fatty acid methyl ester (FAME) feedstock is also a factor in oxidative stability. Biodiesel contains a mixture of fatty acid mono-alkyl esters with high concentrations of long-chain monounsaturated and polyunsaturated compounds, the level of unsaturation depends on the parent feedstock used in biodiesel production. Unsaturated organic compounds (containing carbon double bonds C=C) are more susceptible to oxidation compared to saturated compounds, and polyunsaturated fatty acid chains are much more reactive than monounsaturated chains. [52-53]

Many of the unsaturated fatty acids derived from vegetable oils, such as rapeseed oil and soybean oil, have a methylene-interrupted pattern. Whilst fatty acids with low levels of natural oils, have a conjugated array which tends to be more stable due to the delocalisation of the π electrons, whereas the methylene-interrupted motif is less stable. Figure 1-11 shows chemical structures of methylene-interrupted and conjugated chemical configuration.

A. 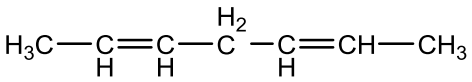

B. 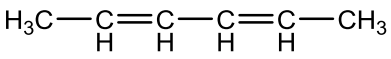

Figure 1-11. Chemical structures of A. methylene-interrupted configuration and B. conjugated configuration.

Biodiesels containing an increased number of double bonds are also more vulnerable to auto-oxidation, due to the increase in π (pi) bonds which have increased chemical reactivity compared to σ (sigma) bonds. These unsaturated bonds can undergo free radical reactions and result in hydroperoxide formation. Hydroperoxides form and decompose to form problematic secondary products as explained earlier.

Temperature has significant effect on the oxidative stability of biodiesel. At high temperatures, highly stable conjugated structures are formed by isomerisation of methylene-interrupted polyunsaturated olefin units. At temperatures of around 180 °C, thermal dimerisation of FAME occurs *via* the Diels Alder reaction to form the dimer as shown in Figure 1-12.

At these high tempertures, the methylene- interrupted polyunsaturated olefin structure begin to isomerise to the more stable conjugated formation. Once this isomerisation has started, a conjugated diene group from one fatty acid can then react with a single olefin group of another fatty acid chain to form a cyclohexene ring. This reaction is called the Diels Alder reaction, where the products formed are dimers.

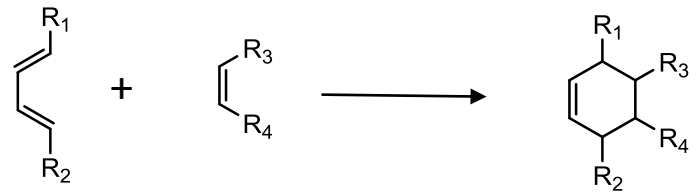

Figure 1-12. Diels Alder reaction to show thermal polymerisation.

1.4 Diesel fuel injection

The fuel injector is an electronically controlled valve that is supplied with pressurised fuel by the fuel pump and when energised, atomises the fuel into a fine mist so that it can burn easily. Injectors are critical to the delivery of the right amount of fuel at the right time in the combustion cycle and they must produce a fine mist or spray which will vaporise rapidly to ensure fast mixing of the fuel vapour and air.

1.4.1 Internal diesel injector deposits (IDID)

Historically, manufacturers have been concerned with coking deposits which form on the injector nozzle and within the fuel spray hole, the effects were of limited concern in the absence of emissions regulations and increased visible smoke emissions. However, modern compression ignition engines have now been designed to meet stringent emission regulations (see Chapter 1.3), and where the engine operates at much higher pressures and temperatures. Therefore, the problem of deposit formation is now of particular concern and needs to be investigated further. [36]

Older injector needles were bulkier and their mass and the mechanical force used to move them enabled them to deliver fuel with little reduction in the performance of the engine in spite of the presence of deposits. However, new engine technology relies on smaller, lighter and more intricate parts, with much tighter tolerances between the moving parts. The new injector needles (roughly 1-2 inches long) have much lower inertia and are more prone to stick in the presence of deposits. The complex injection sequences utilised in common rail engines can involve six or more discrete injections during a single combustion cycle, and a delay or reduction in fuel volume during any one of these injections can have serious performance repercussions. [36]

Fuel-related deposits can form on critical diesel engine components, resulting in a reduction in the engine performance and an increase in harmful exhaust emissions. Unlike conventional coking deposits that form on the tips of fuel injectors, internal diesel injector deposits (IDID) form within the injector body itself. IDID formation within the FIE has grown to be a major area of concern for the industry and the two known issues that commonly affect diesel engines using ultra-low sulfur diesel (ULSD) fuel are premature fuel filter plugging and injector fouling. Figure 1-13 below shows the possible locations of IDID formation within the injector. [54]

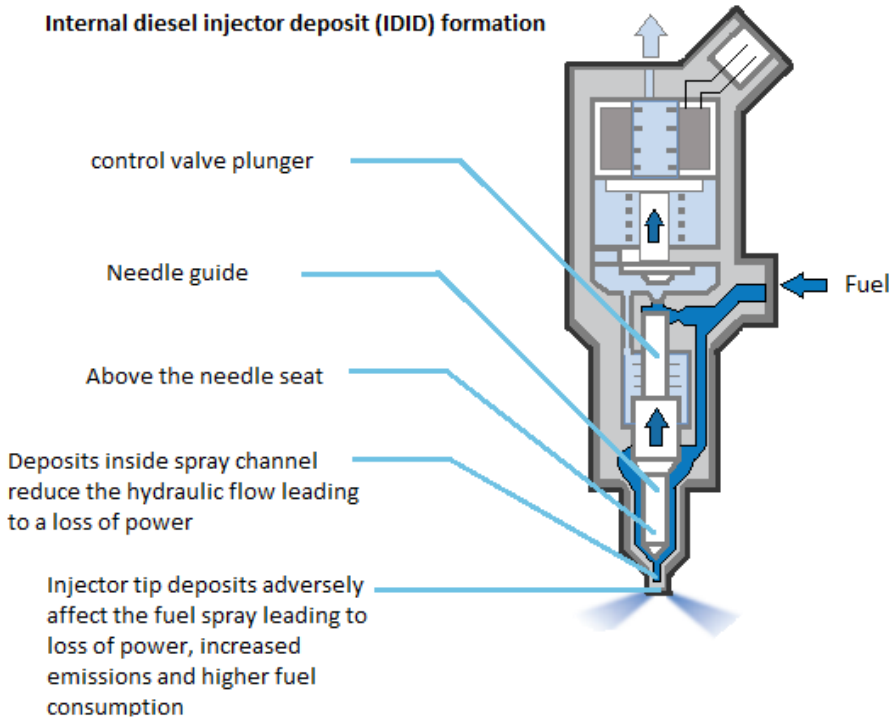

Figure 1-13. Locations of internal diesel injector deposit (IDID) formation within the fuel injection equipment of a diesel engine. Reference adapted from www.cumminsforum.com.

Since the first incidence of IDID formation there have been no shortage of theories around the causes of it. Possible causes have included mechanical issues, due to the higher pressures and temperatures in common rail systems and tighter tolerances resulting in narrower injection channels and less clearance in the needle guide. Other causes could be attributed to the fuel itself, such as the hydrotreatment process to produce ULSD which reduces the lubricity of the fuel, biodiesel inclusion and possible impurities such as inorganic salts carryover in the fuel. Additives such as corrosion and lubricity additives as well as cetane and cold flow improvers have also been implicated as potential causes of IDID formation. [43, 55-61]

These deposits can slow down the response of the fuel injector, and cause sticking of the internal moving parts of the injector, resulting in a significant loss of control of injection event timings and the quantity of fuel delivered per injection. These deposits can also restrict fuel flow and modify the fuel spray pattern; leading to insufficient mixing of fuel

and air, distortion of the optimum spray pattern as well as inefficient combustion. Consequently, this can result in significant loss of power to the engine; increase in unwanted emissions and reduced fuel economy and, in extreme cases can lead to engine failure. [59]

The problem of IDID formation is widespread; within the United States (USA) it is primarily an issue with heavy-duty off-road diesel vehicles. The high-duty cycle of heavy-duty diesel engines may contribute to the prevalence of IDID in off-road equipment. Within Europe, the problem appears mostly in diesel passenger cars, reflecting the higher concentration of diesel-powered vehicles in the market.

1.4.2 Deposit precursors

Injector deposits can take several forms such as sodium carboxylate type deposits known as “sodium soaps”, polymeric organic materials or “amide lacquers” and fuel oxidation products. Table 1-2 shows the possible causes of IDID from the fuel components such as trace contaminants and additives, as well as the possible root causes and appearance of the deposits. [62]

Table 1-2. Relationship between deposit type and fuel chemistry and IDID identifying the possible root causes of deposits as well as identification of the deposits. Reference adapted from Lacey *et al.* [46]

Deposit type	Root cause	Fuel component	Typical appearance	Identification
Metal carboxylate salt	Sodium > 0.1 mg/kg Acidic material, possibly alkenyl succinic acids	Trace contaminants		Soapy deposit and soluble in water
Polymeric amide	Degradation of PIBSI DCA or residual components from PIBSI manufacture	Additives		Very hard and impervious to solvents
Aged fuel	Poor stability, inappropriate storage, high/low temperature conditions	Hydrocarbon or FAME (steryl glucosides)	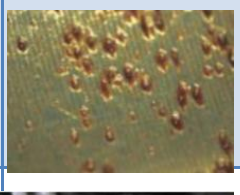	Soft, sticky deposits. Soluble in light hydrocarbons
Pyrolised fuel	Poor hydrocarbon stability, high temperatures, formation of cavities	Hydrocarbon base		Fine black particulates which can form coatings and cause filter plugging

1.4.2.1 Metal carboxylate salt deposits

Metal carboxylate salt deposits are the product of an acid/base reaction, involving carboxylic acid and an alkali metal (sodium) hydroxide producing the metal carboxylate, as seen in Equation 1-5.

$$RCOOH + NaOH_{(aq)} \rightarrow RCOONa + H_2O \qquad \textbf{Equation 1-5}$$

The presence of sodium ions is thought to arise from the base fuel/biodiesel water ingression especially on barge traffic or from additives such as sodium nitrite corrosion inhibitors which were used to protect the fuel pipeline from corrosion.

The sodium ions and carboxylic acid, present in the fuel as contaminants can react to form a metal carboxylate micelle (Figure 1-14), and a theory has been put forward either

the transport or destruction of the micelle can result in deposit formation. Though no evidence of micelle formation has been offered it is thought that the sodium hydroxide, an aggressive caustic (base) chemical, can degrade lubricity improvers, biodiesel and polyisobutylene succinimide (PIBSI) detergent additives to form other carboxylate salts. [57-58]

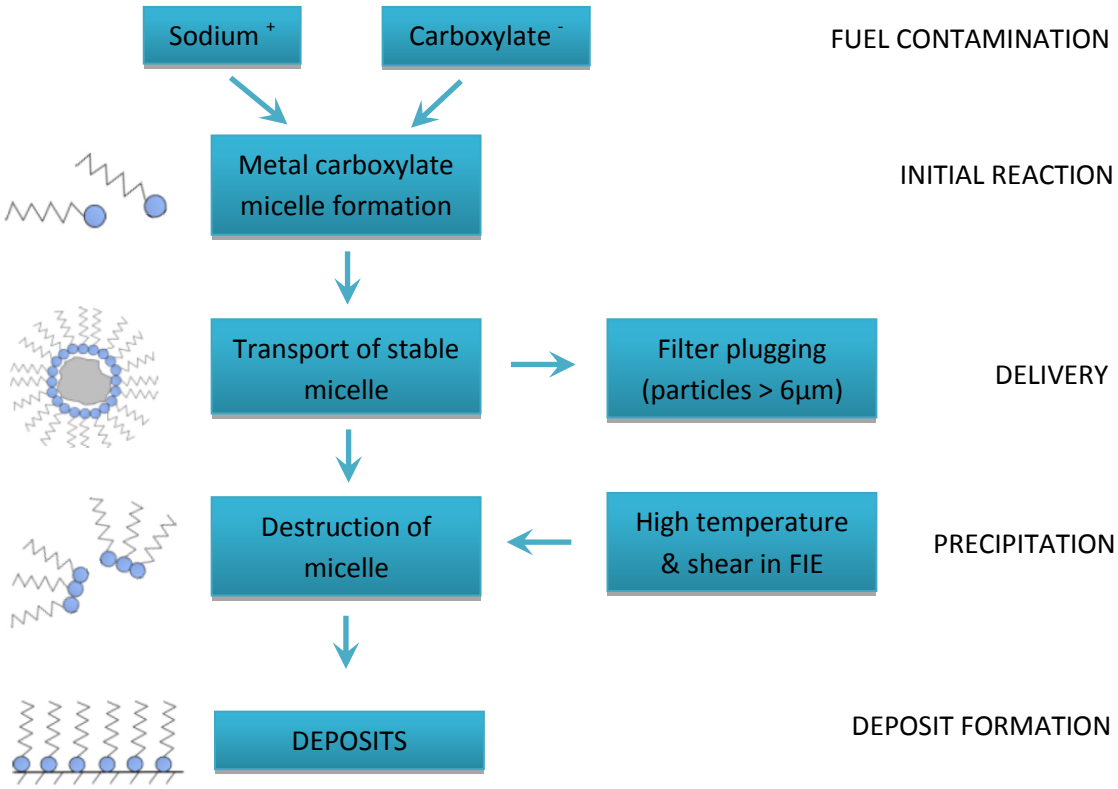

Figure 1-14. Schematic diagram showing likely mechanism of metal carboxylate salt deposit formation. Reference adapted from Lacey *et al.* [46]

A study by Quigley *et al.* [63] analysed a range of failed fuel injectors from engines in North American. SEM-EDX analysis of the fuel injector showed the elemental composition of the deposit to consist predominately of carbon and oxygen, as well as showing large amounts of calcium and sodium. The deposit was also extracted into dichloromethane and the resulting ESI mass spectrum showed the presence of dodecyl succinic acid (DDSA) or hexadecenyl succinic acid and alkylbenzene sulphonate. [63]

Ullmann *et al*. [64] also identified metal based deposits, particularly those containing sodium by FT-IR with the FT-IR spectrum correlating to the sodium C18 fatty acid soap, with SEM and microanalysis results also showing the presence of sodium. Zinc based fatty acid soaps have also been associated with the formation of nozzle tip and spray hole

deposits. The presence of a reactive sodium source in the fuel system is typically thought to be from sodium hydroxide from “fuel polishing” water ingress during barge trafficking water bottom in storage tanks.

The presence of sodium in the fuel system is typically thought to be from corrosion inhibitor additives in pipelines and also sodium salts such as sodium chloride used as drying agents. The use of FAME can also contribute to this phenomenon, due to acid impurities from FAME production or the cleavage of fatty esters by metal ions which will increase the presence of metal soaps. [64]

1.4.2.2 Polymeric organic deposits

Polymeric organic deposits also known as ‘amide lacquers’ have a relatively unknown source compared to sodium carboxylate deposits, and the reaction mechanism has proved to be far more complex. They are believed to arise from a reaction polyisobutylene succinimide (PIBSI) a detergent and the amides may also be originally from biodiesel. [55]

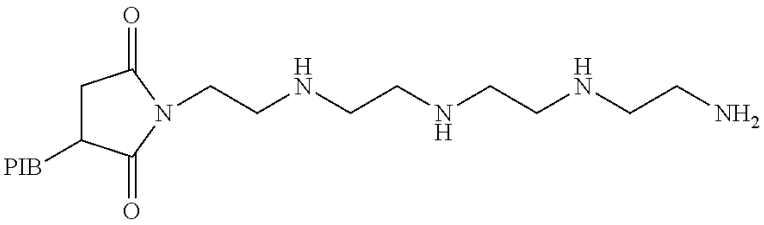

Figure 1-15. Structure of PIBSI

PIBSI is used for its dispersant qualities in fuel and oil, it is an ashless used in diesel fuel. PIBSI is made of a long, non-polar polymer backbone which has polar amine sites attached. Due to the polar amine sites which are attracted to polar particles, the foreign matter in the fuel will become surrounded by the detergent molecule with their active sites commonly oriented inwards.

Three additive chemistries commonly used are mono acids, amides and esters; an example is polyisobutylene succinimide (PIBSI). Polymeric organic deposits are thought to arise from a reaction between PIBSI additives and other acidic components present in fuel, and possible degradation of PIBSI or residual components from the manufacture of it are thought to cause polymeric amide deposits.[55]

Ullmann *et al*. [64] also characterised organic polymeric internal deposits using FTIR, which provided a fingerprint including peaks showing the presence of isobutylene groups, amide bonds and amino groups, which could be due to PIBSI. [64]

Barker *et al.* [65] identified low molecular weight (MW) PIBSI to be present in the inner layer of a deposit as shown by infra-red spectroscopy. Hydropyrolysis results show the presence of aromatic deposit precursors and injector needle showed material of higher MW alkanes. The low MW PIBSI was found to be sparingly soluble in fuel and could precipitate compared to higher molecular weight PIBSI which is fully soluble in fuel. [65]

1.4.2.3 Pyrolised fuel

Deposits have also been observed as a result of the hydrocarbon base fuel itself; as lower stability petroleum based fuels have the potential to degrade easily causing precipitates and resulting in filter plugging. Due to the high temperatures and pressure, the base oil degrades and becomes pyrolised in the form of fine black particulates coating the injector surface and leads to the formation of deposits. [66]

Kouame and Liu [67] investigated fully and partially additised lubricant deposits by temperature programmed oxidation (TPO) they identified carbonaceous deposits which that, evolved at oxidation temperatures less than 450° C. [67]

Pyrolysis GC-MS has also been investigated by Venkataraman and Eser [68] on high pressure diesel injectors. The deposits consisted of polyaromatic compounds (PAH) with oxygen moieties. When excursion deposits are removed, carbon based deposits will remain as they are the result of fuel decomposition within the fuel injection system.

1.4.2.4 Biodiesel

The impact of biodiesel in this area is relatively unknown; however it has been suggested that the instability of fatty acid methyl esters (FAME) plays an important role in deposit formation. The quality of FAME is influenced by the source of the fatty acid as well as the esterification process; this can cause significant variations between biodiesel fuels. It may contain un-reacted fatty acid groups and un-reacted methanol, water, glycerides and metals. The unsaturated bonds in the FAME can deteriorate easily through high

temperatures and pressures resulting in a build-up of acids as well as causing the formation of polymers and precipitates- this will be explained further in Chapter 3. [69]

1.4.2.4.1 Steryl glucosides

Steryl glucosides (SGs) are a minor contaminant in biodiesel and have been implicated in deposit formation and the formation of precipitates in biodiesel. In plant tissues and vegetable oil, sterols occur naturally in the form of free sterols, steryl esters, steryl glucosides and acylated steryl glucosides. [70-71]

Steryl glucosides are initially present in vegetable oils in an acylated form with a long chain fatty acid, however during the transesterification process to produce biodiesel; the fatty acid chain is removed leaving the sterol glucoside which reduces the solubility of the compound. SGs show limited solubility in FAME, causing them to precipitate out depending on their concentration and the temperature of the sample.

Cold temperatures can accelerate the formation of precipitates, as well as increasing the likelihood of SGs acting as seed crystals for the development of larger agglomerates. These agglomerates or clusters can then settle on the fuel filters and cause filter blocking. [72-74]

A study was carried out by Dunn [71] investigating the effect of minor constituents on properties of biodiesel fuel, including cold-flow and performance. He identified trace contaminants of unconverted acylglycerols and steryl glucosides which aggregate and grow into solid residues, which then settle on fuel filters.

Bondioli *et al.* [75] identified a white insoluble powder as being a mixture of SGs consisting of campesteryl, stigmasterol and sitosteryl (at approximately 25, 10 and 65 % respectively) in palm oil biodiesel. Soybean oil biodiesel contained the same SGs but in different ratios (20, 20 and 60 % respectively). An analytical test was developed to separate polar fractions of SG, free sterols and sugars from SGs. A pre-treatment step before the transesterification reaction seemed to be critical for the final SG content in biodiesel.

1.5 Current approaches to the analysis of fuels

A wide array of analytical techniques have been employed in the analysis of fuels including infrared (IR) [63, 76-77] and ultraviolet (UV) spectroscopy [78], gas chromatography-mass spectrometry (GC-MS) [79-82-83] and GC coupled to flame ionisation detector (GC-FID) [84-85] , high-performance liquid chromatography (HPLC) [86-88] and supercritical fluid chromatography (SFC) [89-91]. Other techniques that have been used in the analysis of fuels include nuclear magnetic resonance spectroscopy (NMR) [92], isotope ratio mass spectrometry (IRMS) [79] and inductively coupled plasma mass spectrometry (ICP-MS) [93].

Cook and Richards have studied the oxidation of fuel components to produce deposit precursors using GC-MS and shown that some materials accelerate fuel ageing such as hydro peroxides [94]. Barker *et al.* studied internal injector deposits by a novel hydropyrolysis technique, the data showed that the deposits contained small structures of small ring size heavily alkyl substituted aromatics. Steranes and sterenes were also found in hydropyrolysis products that could derive from steryl glycosides present in biodiesel as impurities [95].

Multidimensional GC (or 2D GC) has also been used for the analysis of petroleum products, the technique was able to determine members of homologous series and PIONA quantification. [96]

Further studies carried out by Barker *et al.* [97] used Temperature Programmed Oxidation (TPO) and showed a degree of crystallinity in the carbon of the internal injector deposits not found in the external deposits. This is indicative of rapid degradation of the fuel by the high temperatures and pressures within the fuel system. The deposits formed on the injector tip were found to be more amorphous in nature than deposits formed on the injector needles which were more structured, the more amorphous in structure is thought to be more reactive and can therefore oxidise at a lower temperature. [97]

Studies carried out by Barker and Langley [13] showed that a fuel's propensity to foul cannot be correlated with the presence of calcium, sodium or zinc as shown by elemental analysis using ICP-MS. This shows that the presence of metals does not seem to be indicative of deposits. [13]

Schwab *et al.* [98] and Arters *et al.* [99] reported analyses of internal injector deposits taken from failing injectors and showed the presence of sodium salts of low molecular weight hexadecenyl and dodecenyl succinic acids which are commonly used as corrosion inhibitors in diesel fuel. Test fuel was treated with dodecenyl succinic acid and solutions of aqueous sodium chloride or hydroxide to generate sodium salts; it was found that this fuel resulted in injector sticking and the formation of injector deposits and analysis using Fourier Transform IR (FT-IR) showed they contained the alkenyl succinic acid sodium salt. However, when this testing was repeated with fuel treated with mono-acidic type lubricity improver and aqueous sodium hydroxide no injector sticking or deposits were observed.

Time of flight secondary ion mass spectrometry (TOF-SIMS) was also carried out by Barker, Snape and Scurr [35, 62] and showed the complexity and layering formation of the deposits, which may be a result of the residual fuel either evaporating and leaving a residue or being unable to keep an insoluble residue in solution during the injection process. Results showed these deposits are built up of multiple layers both containing a nitrogen species layer and an iron based compound dispersed as particles throughout the CH - layer. [35, 62]

Scanning electron microscopy- electron dispersive X-ray (SEM-EDX) was also used to investigate injector deposits by Barker *et al.* showing clear images of a layer of light brown lacquer deposit around a needle tip associated with the presence of metals. [65]

1.6 Use of chromatography for the analysis of fuel

Chromatography is a widely used technique that allows for the separation, identification and determination of the chemical components in complex mixtures. Chromatography was originally founded by Russian scientist Mikhail Tswett, who demonstrated the separation of plant pigments using column chromatography. [100]

Chromatography has the ability to separate molecules using their partitioning characteristics. The major components of chromatographic separation are the mobile phase which can be a gas (gas chromatography (GC), liquid (high performance liquid chromatography (HPLC)) or a supercritical fluid (supercritical fluid chromatography (SFC))

and acts by flowing through the column carrying the analyte compound. The column consists of a stationary phase, which interacts with the analyte and is needed for separation of the analytes.

The separation is based on differences in the extent to which solutes are distributed between the mobile and stationary phases. Equation 1-6 shows the distribution constant or partition coefficient (K_c) equation, where C_s refers to the concentration of analyte in the stationary phase and C_m is the concentration of analyte in the mobile phase. The partition coefficient measures the tendency of an analyte to be attracted to the stationary phase. [101]

Partition coefficient equation (K_c):

$$K_c = \frac{[C_s]}{[C_m]} \qquad \textbf{Equation 1-6}$$

There are a range of key parameters involved in separation in chromatography. These include the retention or capacity factor (k) used to describe the migration rate of an analyte and measures the peak retention of a compound. Equation 1-7 shows the capacity factor equation; where; t_R = retention time of a component and t_0 = dead time or retention of an unretained component.

Capacity factor equation (k):

$$k = \frac{(t_R - t_0)}{t_0} \qquad \textbf{Equation 1-7}$$

The selectivity factor (α) for analytes within a column provides a measure of how well two components will separate on a column. Equation 1-8 shows the selectivity equation where; k_1 and k_2 refer to retention time of compound 1 and 2, respectively.

Selectivity equation (α)

$$\alpha = \frac{k_2}{K k_1} \qquad \textbf{Equation 1-8}$$

Efficiency is also a very important parameter; it is a measure of the dispersion of the analyte band as it travels through the stationary phase. The plate number (N) is a measure of the peak dispersion in chromatography, and reflects the column performance.

Each ('theoretical') plate refers to the distance over which the sample components achieve one equilibration step between the stationary and mobile phase in the column. Therefore the greater the number of theoretical plates the more equilibrations possible and the better the quality of separation. The length of the column and particle size of the stationary phase can influence column efficiency. [101]

Equation 1-9 shows how efficiency (N) is related to the length of the column (L) and height equivalent to a theoretical plate (H). Equation 1-10 shows how N is related to the retention time of a component (t_R) and peak width at half height ($W_{1/2}$).

Efficiency equations (N):

$$N = \frac{L}{H} \qquad \textbf{Equation 1-9}$$

$$N = 5.54 \left(\frac{t_R}{W_{1/2}}\right)^2 \qquad \textbf{Equation 1-10}$$

One of the most important parameters in chromatography is resolution which is calculated using the separation of two peaks in terms of their average peak width. Resolution (Rs) refers to the degree of separation between two adjacent peaks. To obtain high resolution, three terms must be maximised: an increase in efficiency (by reducing the particle size of stationary phase);and controlling the capacity factor and the selectivity factor (by changing mobile phase composition and column temperature). The resolution equation is shown below (Equation 1-11) and takes into account the variables of efficiency (N), capacity (k) and selectivity (α).

Resolution equation (R_S):

$$R_S = \sqrt[1/4]{N} \times \frac{\alpha - 1}{\alpha} \times \frac{k}{1 + k} \qquad \textbf{Equation 1-11}$$

Column efficiency is affected by the degree of band broadening that occurs. Band broadening refers to the spreading of a chromatographic band as it travels through the column. There are two theories that describe this effect: the theoretical plate model, and

the rate theory of chromatography. The theoretical plate model describes the chromatographic column as being divided into equilibrium plates, which are allotted a length called theoretical plate height in which the components spend a finite time sufficient to achieve equilibrium between both phases. Although the plate theory is a useful concept, it does not take into account all of the mechanisms that determine these factors. [102]

The rate theory of chromatography however is based on such parameters such as rate of mass transfer between stationary and mobile phases and diffusion rates of solute and was derived from an equation developed by Van Deemter *et al.* in 1956 as shown in Equation 1-12, where A refers to eddy diffusion, B is the random molecular diffusion and C refers to mass transfer within particle caused by the mobile phase.

$$HETP = A + \frac{B}{u} + Cu \qquad \textbf{Equation 1-12}$$

The first factor Eddy diffusion or the A term, is used to describe the variations in mobile phase flow or analyte flow path within the column. It refers to the analyte molecule taking a number of paths through the column, which can occur due to the lack of homogeneity of the column packing. This multiple path effect tends to cause band broadening and reflects the quality of the column packing. Another flow variation commonly seen in column chromatography is the laminar flow profile of liquids flowing under pressure through tubes. The profile is termed laminar due to the linear velocity near the walls of the tube being lower than at the centre of the column. This effect can also lead to broadening of the chromatographic analyte band. The A term can be reduced by selecting well-packed columns and using smaller stationary phase particles. [102]

Longitudinal diffusion or the B term occurs when the analyte band diffuses out in every direction due to the concentration gradient at the outer edges of the band. This occurs when the chromatography system contains internal volumes larger than necessary such as when the tubing length is too long, wide or using the wrong column fittings. This effect is much greater at low mobile phase velocity, therefore the use of higher mobile phase flow with narrow columns and keeping system tubing short and as narrow as possible with the use of the correct fittings can reduce this effect.

Mass transfer or the C term occurs when the stationary phase is porous and the mobile phase within the pores becomes stationary. As the analyte moves through the stationary

phase to react with the surface of the packing material, it does so by diffusion. Analytes react with the stationary phase differently, some enter the pore and quickly exit, some do not enter the pore or some that penetrate deeply into the pore will be confined for longer causing band broadening. These effects can be minimised by using smaller diameter stationary phase particles, using lower mobile phase flow rates and heating the column. [102]

Figure 1-16 shows the effect of all three terms on a Van Deemter plot.

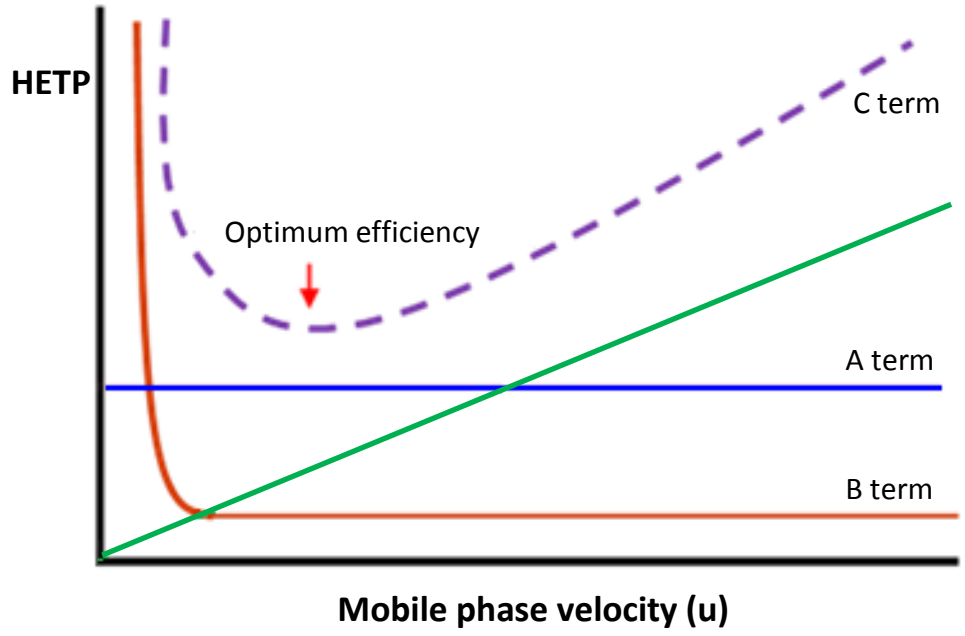

Figure 1-16. Van Deemter plot showing the effect of the three terms, A term= eddy diffusion, B term= longitudinal diffusion and the C term= mass transfer effects. Figure adapted from www.restek.com.

1.6.1 Gas chromatography

Gas chromatography was initially developed in 1941 by A.J.P. Martin and R.L.M. Synge [103] in the field of liquid-solid chromatography and advanced by A.T. James and A.J.P. Martin who demonstrated the first gas chromatographic separations. [104]

Gas chromatography (GC) uses a carrier gas as a mobile phase to transport sample components through either packed columns or hollow capillary columns containing the stationary phase. [105]

Figure 1-17 shows a schematic diagram of a GC-MS instrument, the sample is injected into the heated sample inlet port where it is volatilised and carried by a carrier gas into a oven containing the column. The oven can operate typically from 0 - 450 °C and can be programmed to operate isothermally or with a temperature gradient. Carrier gases used in GC include hydrogen, nitrogen and helium, with helium being the most commonly used gas when GC is coupled ot a mass spectrometer. Separation of the components is achieved by interactions with the analyte and stationary phase in the column. After this separation, the components are then passed into a detector such as a mass spectrometer (GC-MS) as shown in Figure 1-17.

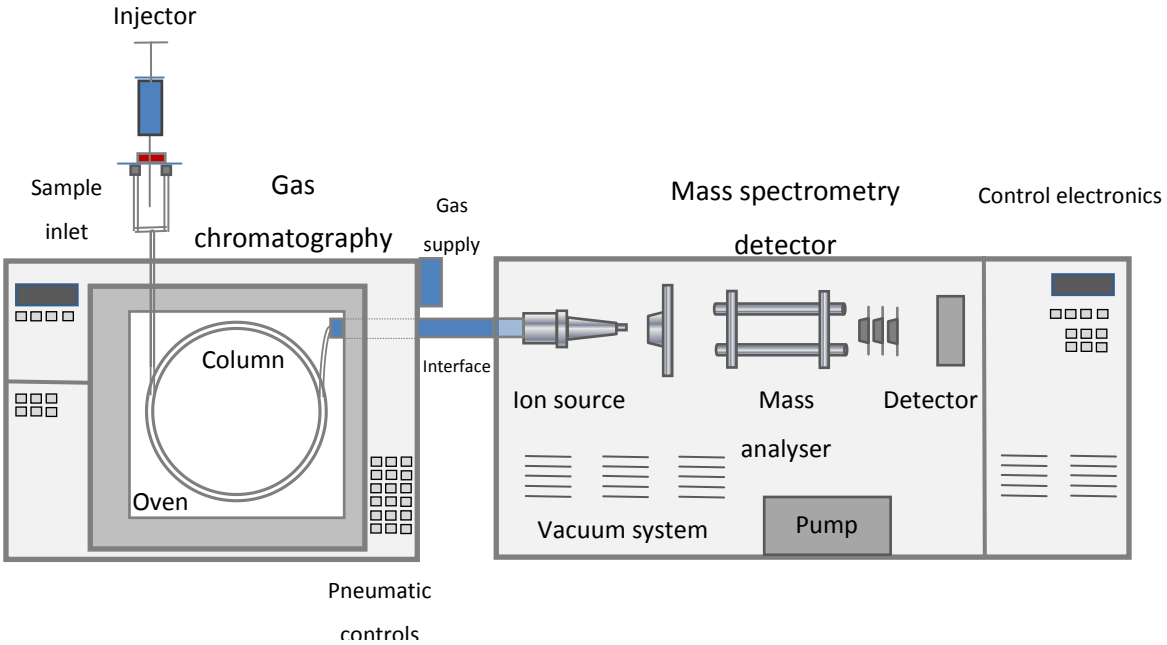

Figure 1-17. Schematic diagram of a GC-MS. Reference adapted from http://www.chromacademy.com/mass-spec-training.html.

There are two general types of columns used in GC, packed and capillary columns. Packed columns contain a finely divided, inert, solid support material coated with a liquid stationary phase. Capillary columns can either be support-coated open tubular (SCOT) or wall-coated open tubular (WCOT) columns, with WCOT columns being more popular. The latter are made of capillary tubes with a thin layer of stationary phase coated along the column walls, with a film thickness of around 0.1 to 0.5 µm and column diameter of 0.25 - 0.5 mm. In SCOT columns, the column walls are first coated with a thin layer of solid adsorbant such as diatomaceous earth that is then treated with a liquid stationary phase.

There are a wide range of stationary phases that can be used in GC, and can include non-polar and polar stationary phases. The main principle in GC is “like dissolves like” meaning that a polar stationary phase column such as polyethyleneglycol (PEG) is used to separate polar analytes and a non-polar stationary phase column such as polydimethyl siloxane (PDMS) is used for non-polar analytes (Figure 1-18). Separations using non-polar stationary phases are separated by boiling points, whilst polar stationary phase analytes are separated by polar interactions with the stationary phase.

A. 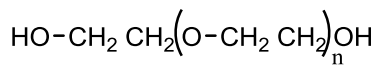

B. 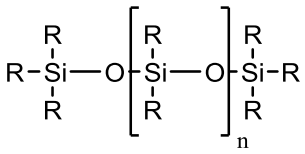

Figure 1-18. Stationary phases commonly used in GC-MS where A. polyethylene glycol (polar stationary phase) and B. polydimethyl siloxane (non-polar stationary phase).

Gas chromatography (GC) has been to date the most widely used technique for the analysis of fuels; GC can be coupled with a range of detectors. Commonly used detectors in fuel analysis include a mass spectrometer (GC-MS) and flame ionisation detector (GC-FID). Both techniques are well-established, robust and relatively cheap. GC-MS is able to identify and fingerprint hydrocarbons including aliphatic and aromatic hydrocarbons present in fuel, however GC-FID is a non-selective detector and therefore not able to target individual components without non-target compounds interfering with the analysis. [105]

GC separations are highly efficient and can separate highly complex mixtures by modifying a range of parameters such as the temperature and the stationary phase. For samples to be analysed successfully by GC, the sample must be volatile or have a significant vapour pressure below 250 °C and most GC analytes to be analysed are preferably below 500 *m/z*. [106]

1.6.2 High performance-liquid chromatography (HPLC)/ ultra-high performance liquid chromatography (UHPLC)

Liquid chromatography was initially developed in the early 1900s, in the form of column chromatography. This involved a glass cylinder packed with finely divided powder such as chalk, and the sample is introduced from the top of the column. A solvent is poured down the column and the components present in the sample are separated down the column according to their differing interactions with the stationary phase. [107-108]

In the 1940s, paper chromatography was then introduced which was later modified to thin layer paper chromatography (TLC). TLC involves a thin layer of powdered silica packed onto a glass plate on which the sample is spotted at the bottom and placed in a solvent which runs up the plate, separating the analytes.

High performance liquid chromatography (HPLC) was developed at the end of the 1960s, it involves the use of a high pressure pump which delivers the mobile phase around the system and transports the analyte through a column packed with a stationary phase. HPLC is driven by the selectivity of the analyte with the mobile phase and stationary phase. Some compounds will have a greater preference for the stationary phase than the mobile phase and will be retained longer, whilst other compounds will have a stronger preference for the mobile phase and elute quicker depending on their polarity. [107]

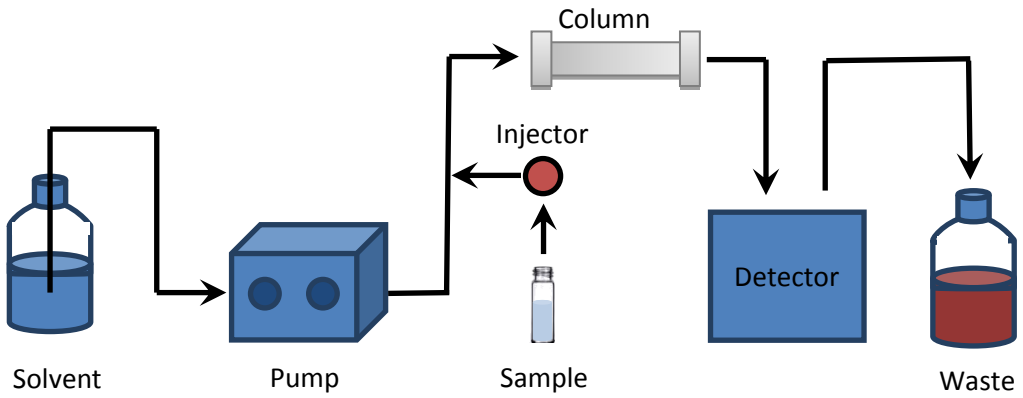

Figure 1-19. Schematic diagram of HPLC, consisting of solvent reservoir, pump, sample introduction, column and then to detector. Reference adapted from chromacademy.

Figure 1-19 shows the HPLC system, which consists of a mobile phase reservoir and high pressure pump, used to generate the flow of the mobile phase and high pressures. The

sample manager is used to inject the sample into the system, and carried by the mobile phase into the HPLC column. The HPLC column is located in a column oven where the required temperature is maintained. In the column, a range of stationary phases chemistries can be used with the most common being Octadecylsilane also known as C18), see **Figure 1-20** for other commonly used stationary phases.

Normal phase HPLC uses a polar stationary phase and a non-polar mobile phase whereas in reversed phase HPLC the stationary phase is non-polar (such as C18) and the mobile phase is polar.

The principle of reversed phase HPLC (RP-LC) is based on the partitioning of analytes between the mobile phase and stationary phase. RP-LC uses a mobile phase which is more polar than the stationary phase, therefore a less polar molecule will have a greater interaction with the non-polar stationary phase than a more polar molecule and will be retained longer on the column. A more polar molecule will have a higher affinity for the polar mobile phase and will therefore be carried through the system faster and elute with a shorter retention time. [107]

A range of intra- and intermolecular interactions occur between the analyte molecule and mobile/stationary phases, these include covalent bonds, ionic interactions, hydrogen bonding and van der Waals interactions. Typical reversed phase stationary phases are hydrophobic and chemically bonded to the surface of a silica support particle, the most commonly used stationary phases include C18, C18, C4, Cyano and Amino (in order of increasing polarity) as shown in Figure 1-20.

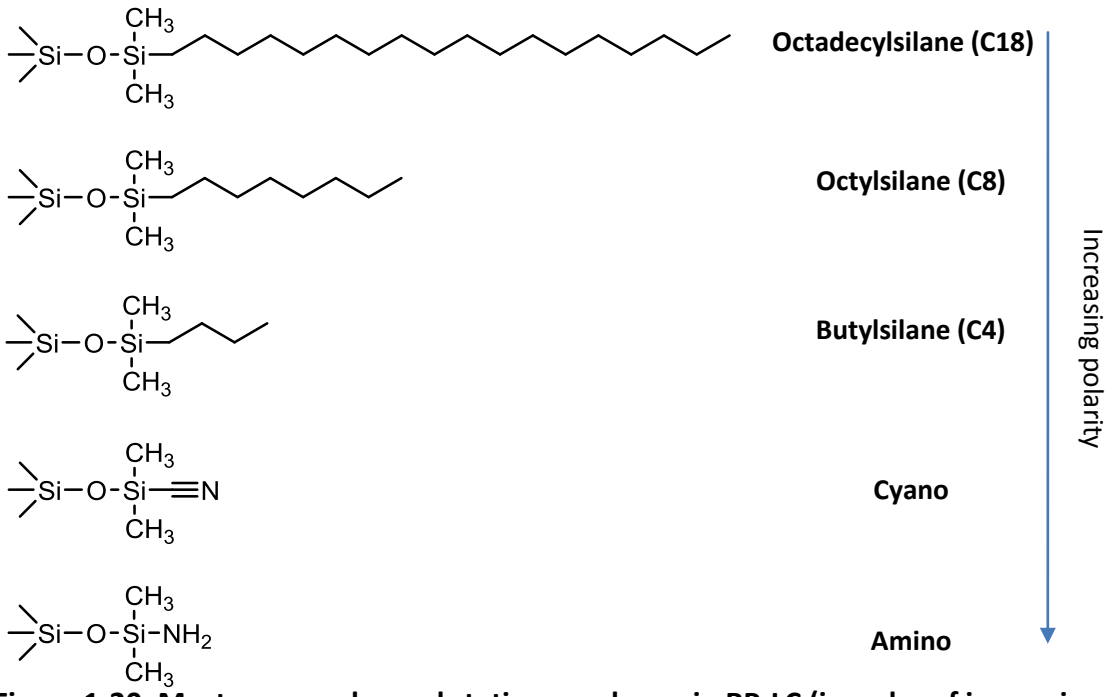

Figure 1-20. Most commonly used stationary phases in RP-LC (in order of increasing polarity).

HPLC-MS is commonly used because it can analyse samples over a wide polarity range, as well as analysing both volatile and non-volatile compounds. It also has no real upper molecular weight limit therefore large molecules can be easily analysed. It also has a relatively fast analysis time compared to GC-MS.

Recent developments in technology have led to the use of smaller stationary phase particles. This has led to the use of higher solvent flow rates and pressures compared to conventional HPLC separations. This results in improvements in column performance and higher separation efficiencies that can be explained by the Van Deemter equation.

Ultra-high performance liquid chromatography (UHPLC) uses sub-2 µm stationary phase particles and can operate at higher pressures of up to 1050 bar. These improvements can lead to a significant improvement in the analysis time without sacrificing separation efficiency. Figure 1-21 shows a Van Deemter plot of the development of stationary phase particle sizes, UHPLC systems can operate at much higher linear velocities and lower HETP, the coloured section shows the optimal area for separation which is only achieved by UHPLC systems.

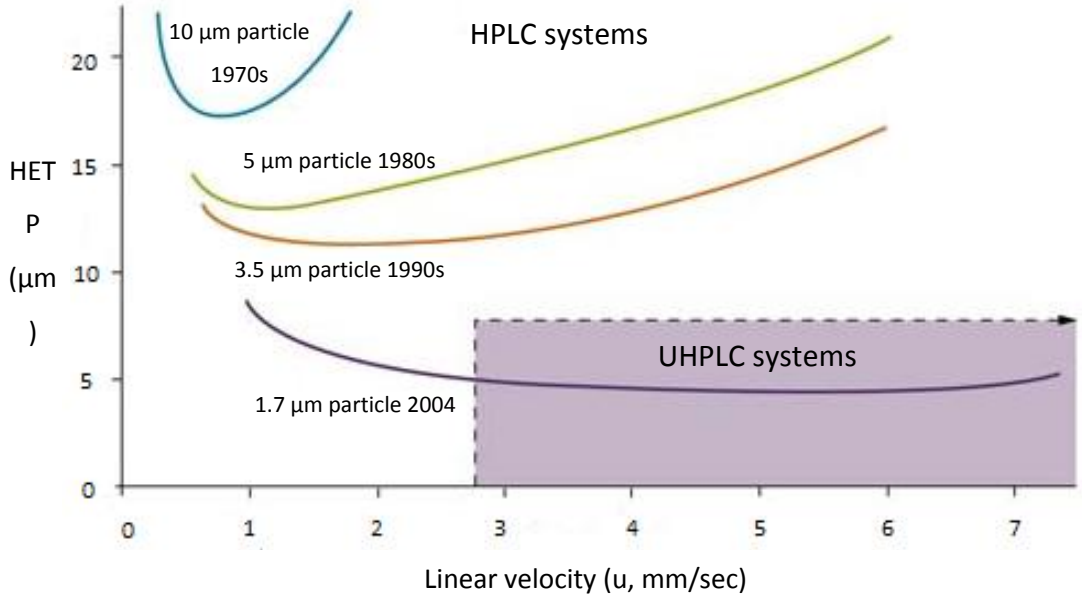

Figure 1-21. Van Deemter plot showing the development of stationary phase particles in stationary phases. Reference adapted from [www.restek.com.](http://www.restek.com)

1.6.3 Supercritical fluid chromatography

A supercritical fluid is any substance at a temperature and pressure above its critical point, where distinct liquid and gas phases do not exist. Critical pressure is the highest pressure at which a liquid can be converted to a gas by increasing its temperature and critical temperature refers to the highest temperature at which a gas can be converted to a liquid by increasing its pressure. Supercritical fluids are neither gases nor liquids, they are compressible fluids with the dissolving properties of liquids but the diffusivity of gases. [109-111]

Figure 1-22 shows the phase diagram for CO_2, for pure CO_2 the triple point conditions of temperature and pressure are T_{tr}= -56.6 °C and P_{tr}=5.17 bar. The critical point for pure CO_2 is T_c=31.1°C and P_c= 73.9 bar.

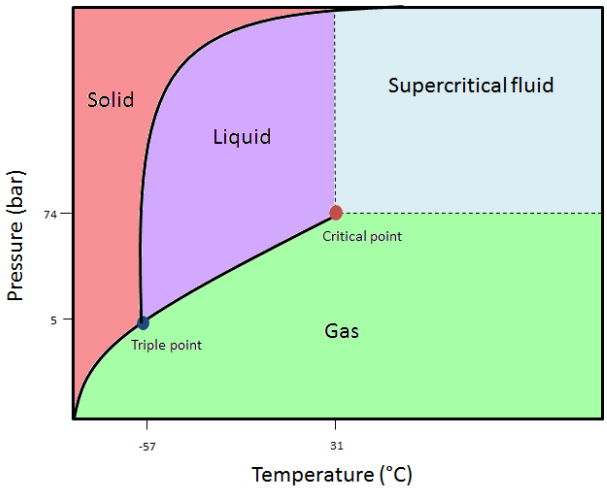

Figure 1-22. Phase diagram for carbon dioxide (CO_2), the blue dot represents the triple point at which the temperature and pressure of the three phases (gas, liquid and solid) of the substance coexists in thermodynamic equilibrium The critical point (red dot) specifies the temperature and pressure at which a phase boundary ceases to exist.

Table 1-3 shows the properties of supercritical fluids compared to gases and liquids. The advantages of using supercritical fluids are that they have low viscosities and high diffusivities (gas-like properties) resulting in a lower pressure drop across the column and higher efficiency through the use of smaller particle size stationary phases. Supercritical fluids also have high densities (liquid-like) ensuring good solvent properties. [112-113]

Table 1-3. Properties of supercritical fluids compared to gases and liquids.

	Diffusivity (cm^2/s)	**Viscosity (g/cm x s)**
Gas	10^{-1}	10^{-4}
Supercritical fluid	10^{-4} - 10^{-3}	10^{-4} - 10^{-3}
Liquid	$<10^{-5}$	10^{-2}

Figure 1-23 shows a schematic diagram of SFC instrument, the mobile phase (CO_2) is initially pumped as a liquid and is brought into the supercritical region by heating above its supercritical temperature before it enters the column. Modifier solvents (or co-solvents), such as methanol or acetonitrile, are added to modify the mobile phase

polarity. The sample is introduced through the injection port *via* an autosampler or manual injection, where it is introduced into the mobile phase stream and onto the analytical column. The back-pressure regulator (BPR) work as a relief valve and regulates the higher inlet pressure by opening up only as much as necessary to hold back the desired pressure at the inlet. The sample flow is then diverted through a splitter to detectors such as a mass spectrometer and a PDA detector.

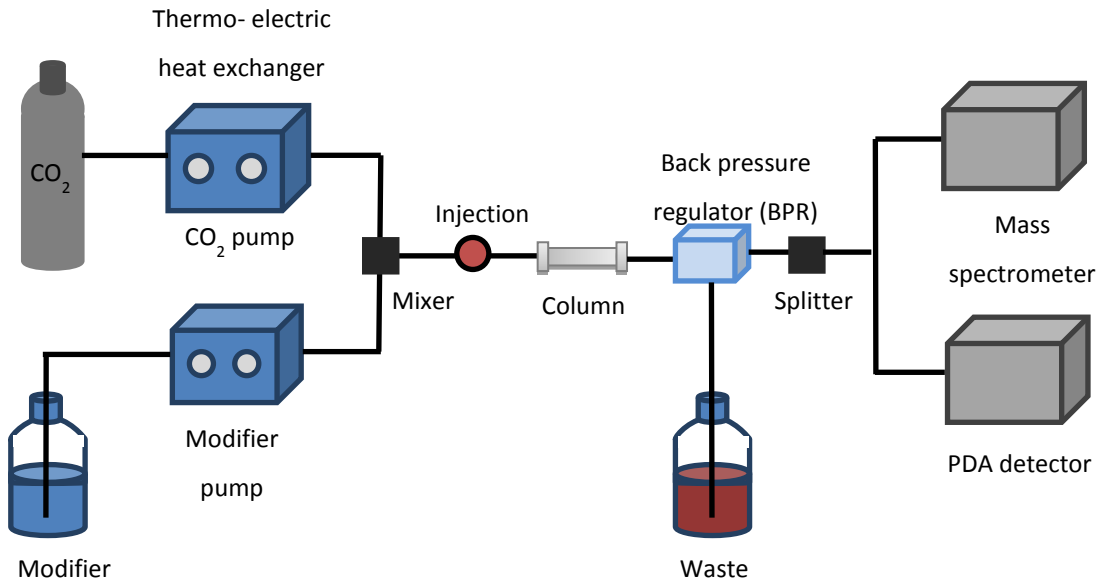

Figure 1-23. SFC schematic diagram consisting of a CO_2 and modifier supply and pump, chromatography column, with back-pressure regulator (BPR) and detector. (Figure adapted from www.waters.com)

There are a number of possible fluids that can be used as supercritical fluids, carbon dioxide being the most commonly used mobile phase. This is due to its non-flammable, non-toxic and eco-friendly properties as well as its low critical temperature of 31°C and moderate critical pressure of 74 bar. It is also miscible with a wide range of organic solvents, and has high diffusivity properties.

Using water as a supercritical fluid is also of particular interest in SFC; however it is less popular than CO_2 because it reaches its supercritical state at much higher extremes than CO_2 with a critical temperature of 373 °C and critical pressure is 220 bar. [114-116]

The solubilizing power of a supercritical fluid, which is directly related to its density is much greater than that of a gas in GC, which makes the technique useful for analysis of a broader range of analytes including higher molecular weight compounds whilst also not

being restricted to volatile analytes. In addition to this, due to the diffusion coefficients of many analytes being greater in a supercritical fluid than in liquid form, and because the resistance to mass transfer term in SFC is lower than that in HPLC, the separation speed in SFC is reduced greatly. [73]

1.6.3.1 UltraPerformance Convergence Chromatography (UPC^2)

In 2012, a new generation of SFC instrumentation was developed by Waters named UltraPerformance Convergence Chromatography™ (UPC^2). Designed to enable the use of sub-2 µm particle size stationary phases with a wide range of column chemistries. UPC^2 delivers high efficiency, shorter separation times and reduced solvent consumption. [117]

Convergence chromatography can exhibit the strengths of normal phase liquid chromatography (NPLC) which is orthogonal to reversed phase liquid chromatography (RPLC) for compounds with a large range of hydrophobicities and chemical properties, further expanding beyond the chiral and normal-phase application space.
This versatility allows it to address challenging analyses from a range of application areas, whilst also allowing for high throughput analysis as sample preparation and analysis times can be significantly reduced.

1.7 Detectors- Mass spectrometry

Mass spectrometry is an analytical technique that allows for the determination of the mass of a molecule by measuring the mass-to-charge (*m/z*) ratio of an ion. There are considered to be five founding fathers of the development of mass spectrometry in the late 19th century and 20th century these include Francis Aston, Sir Joseph John Thompson, Eugene Goldstein, Josef Mattauch and Arthur Dempster. [118]

A mass spectrometer can be considered to comprise of five main components, these include a method of sample introduction, ion production in the ion source, ion separation in a mass analyser, ion detection and data output, see Figure 1-24.

Sample introduction is dependent upon the sample and can include chromatographic techniques such as GC and HPLC or direct injection. Ions are then generated in the ion

source; there are a number of ionisation methods including electron ionisation and electrospray ionisation that are explained in chapter 1.7.1. Most ionisation techniques either excite the analyte molecule which then ejects or add an electron to form a radical ion or involve ion molecule reactions to product adduct ions.

Once ions are generated they are then accelerated into the mass analyser by an electric field which separates the ions according to their *m/z*. Examples of mass analysers include quadrupole mass analysers and time-of-flight mass analysers which will be explained further on in more detail.

The detector then records either the charge induced or the current produced when an ion passes by or hits a surface. Electron multipliers, microchannel plate detectors and photomultipliers are commonly used detectors in modern commercial instruments.

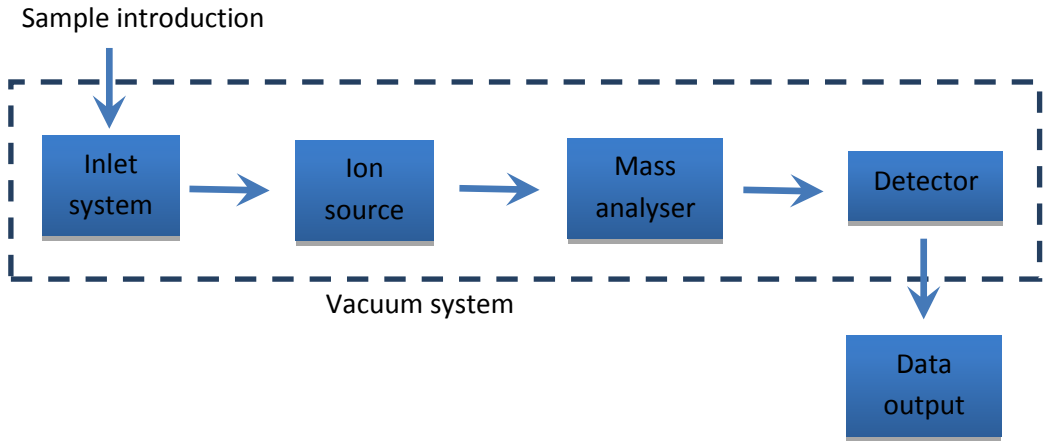

Figure 1-24. Schematic representation of a MS instrument consisting of sample introduction, ion production, ion separation and ion detection.

1.7.1 Ionisation sources

1.7.1.1 Electron ionisation

Electron ionisation (EI) is an ionisation technique that is used in GC-MS and works well for many gases and volatile organic molecules. The ion source consists of a heated filament (typically tungsten or rhenium) which emits electrons, these are accelerated across the source using a suitable potential to achieve the required electron energy. The sample is introduced into the ion source perpendicular to the electron beam, which results in a

number of interactions between the analyte and electron beam. These include electron ejection from the analyte to create a radical ion, or energy transfer from the electron beam to the analyte to cause fragmentation. The radical cations are then directed towards the mass analyser by a repeller electrode and are subsequently separated and detected. Figure 1-25 shows a schematic of an electron ionisation source. [119]

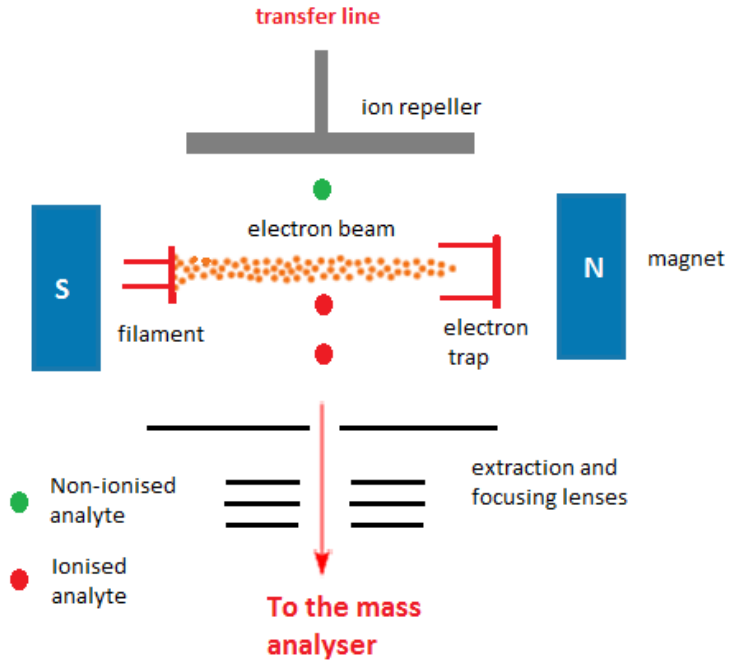

Figure 1-25. Schematic diagram of an electron ionisation source used in GC-MS.

Equation 1-13 shows the formation of radical ions, from the interaction of the molecule (M) with the electron beam (e^-) and subsequent formation of the radical cation ($M^{+\bullet}$). Removal of a valence electron from a molecule can occur at a lone electron pair, π-bonded pair and at σ-bonded pair (in order of ease with which electrons are lost under EI conditions).

$$\mathbf{M + e^- \rightarrow M^{+\bullet} + 2e} \qquad \textbf{Equation 1-13}$$

In EI, spectra are generally acquired at 70 eV this is because at low energies known as the threshold region (10-15 eV) less fragmentation is produced as well as a reduction in signal intensity is also seen. At around 15-20 eV the production of fragment ions becomes important. The plateau of the curve occurs at 70 eV, at this energy reproducibility of fragmentation patterns is achieved and it is the universal energy at which mass spectral

databases are obtained. At energies higher than this, the wavelength becomes too small and molecules become transparent to the electron.

In electron ionisation, reactions are generally unimolecular this is due to the low sample pressure in the EI source so that ion-molecule reactions rarely occur. The radical cation ($M^{+\bullet}$ or $ABC^{+\bullet}$ in the example below) typically undergoes a series of fragmentation steps or intermolecular re-arrangement reactions, as shown in Figure 1-26. The degree of fragmentation or re-arrangement is dependent on the analyte molecule and the energy of ionisation. Each of the fragmentation products shown below may undergo further fragmentation. Isomerisation is also possible and involves intermolecular rearrangement and results in the formation of an odd electron species ($AC^{+\bullet}$).

$\mathbf{ABC^{+\bullet}} \longrightarrow \mathbf{AB^{+}} + \mathbf{C^{\bullet}}$ (cation and radical formed *via* homolytic fission)

$\mathbf{AB^{\bullet}} + \mathbf{C^{+}}$ (cation and radical formed *via* homolytic fission)

$\mathbf{A^{\bullet}} + \mathbf{BC^{+}}$ (cation and radical formed *via* homolytic fission)

$\mathbf{A^{+}} + \mathbf{BC^{\bullet}}$ (cation and radical formed *via* homolytic fission)

$\mathbf{AC^{+\bullet}} + \mathbf{B}$ (intermolecular rearrangement leads to loss of a neutral and the formation of a new radical cation)

Figure 1-26. Series of possible fragmentation reactions that can occur in electron ionisation.

These fragmentation reactions can be homolytic cleavage (one electron at a time) where the products are even-electron cation and a free radical, heterolytic (two electrons at time) and secondary fragmentations of even-electron cations. Rearrangement reactions such as the McLafferty rearrangement can also take place, which involves the rearrangement of γ-Hydrogen to an unsaturated group with β-cleavage. See Figure 1-27 for an example of a McLafferty rearrangement.

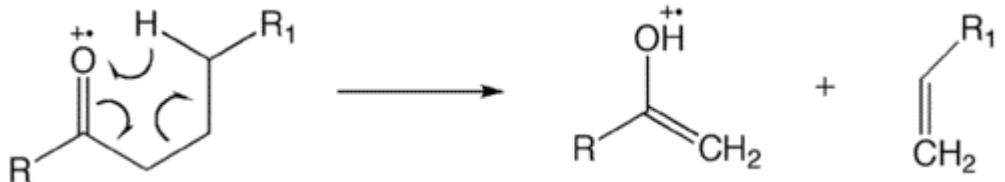

Figure 1-27: Schematic diagram to show an example of a McLafferty rearrangement equation

In this rearrangement an unpaired electron can be donated to another molecule to form a new bond to an adjacent atom. The second electron of this pair is supplied from the transfer of another bond to this atom, this results in β-cleavage. McLafferty rearrangement is common for compounds containing an unsaturated functionality such as a carbonyl group, the γ-hydrogen atom is transferred by a more favourable six-membered ring.

1.7.1.2 Electrospray ionisation

Electrospray ionisation (ESI) is an atmospheric pressure ionisation (API) technique, widely used for small polar molecules and also large molecules. Dole *et al.* [120] initially developed the idea of electrospray and Fenn *et al.* [121] were the first to couple the ESI source to a mass spectrometer and demonstrated the analytical potential of the technique.

Electrospray ionisation (ESI) involves three primary processes; the production of charged droplets at the capillary tip, the subsequent shrinkage/desolvation of the charged droplets leading to coulombic fission events and finally the production of gas phase ions from small, highly charged droplets. [120, 122-123]

The analyte is first introduced into the desolvation chamber in solution either from a syringe pump (known as flow injection analysis (FIA)) or as eluent flow from a HPLC. The analyte solution then passes through the electrospray needle which has a high potential difference (with respect to the counter electrode) applied to it (typically 2.5 – 4 kV). A strong electric field causes the dispersion of the sample into an aerosol of highly charged electrospray droplets as shown in Figure 1-28. Depending on the nature of the analyte of interest, positive or negative ions can be selected. [124-125]

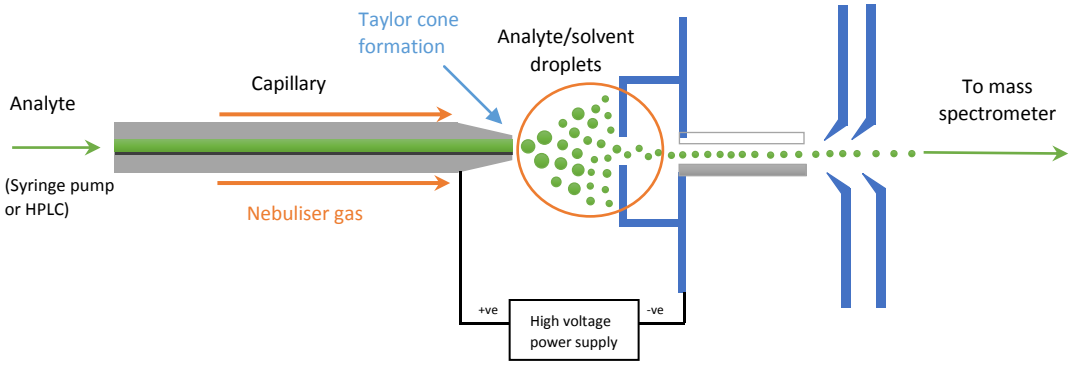

Figure 1-28. Schematic of ESI showing the interface of a syringe pump or HPLC going to the MS analyser. Reference adapted from [www.bris.ac.uk.](www.bris.ac.uk)

In the case of positive ion electrospray, the capillary acts as the positive electrode and the sampling cone acts as the negative electrode. The positive ions within the eluent are repelled from the inner walls of the sprayer needle and move into the droplet formed at the capillary tip by electrophoresis; as shown in Figure 1-28. The reverse situation occurs for negative ion electrospray, causing negative ions to predominate the sprayed droplet. Figure 1-29 shows an expanded region of the desolvation zone which is circled in Figure 1-28.

The charged analyte ions are expelled from the capillary tip and form a conventional meniscus, containing relatively few ions and a low charge density. However, when the charge density at the liquid meniscus is raised due to the repulsion of cations the coulombic repulsion forces are also increased. When the number of ions of the same charge is increased, coulombic repulsions overcome the Rayleigh instability limit (the point at which the surface charge repulsion matches the surface tension of the eluent). This causes the shape of the meniscus to form a cone shape known as a Taylor cone as shown in Figure 1-29. Upon formation of the cone, a stream of droplets or fine spray containing an excess of either cations or anions is produced from the tip of the Taylor cone. [126]

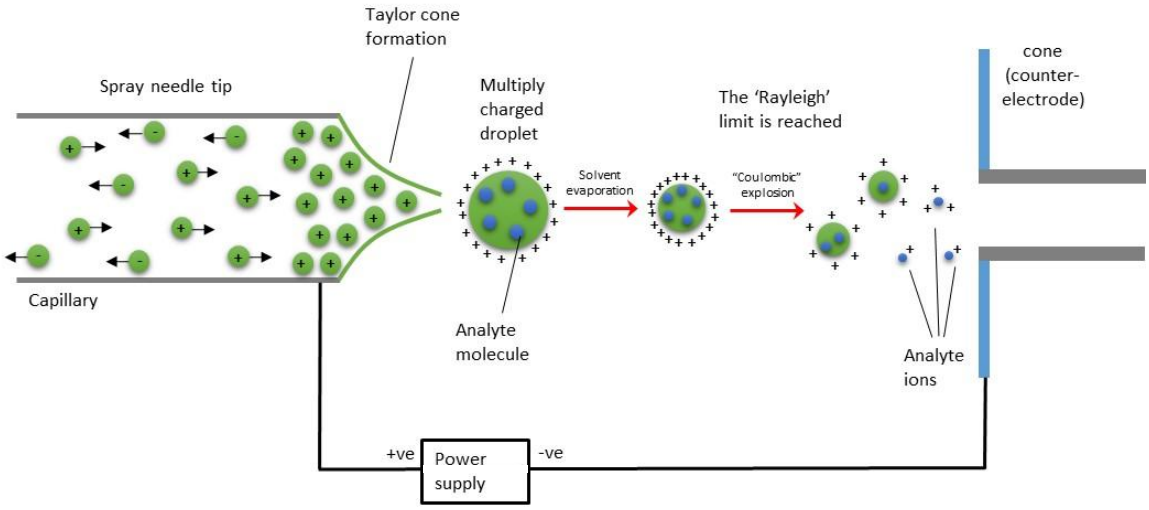

Figure 1-29. Expanded section of the desolvation zone, with Taylor cone and droplet formation. Reference adapted from [www.bris.ac.uk.](http://www.bris.ac.uk)

The charged droplets then travel towards the counter-electrode leading to the mass analyser, whilst they travel solvent evaporation causes the droplets to shrink in size which forces the charges closer together, increasing the charge density. Coulombic fission events then occur when the electrostatic repulsion causes the droplet to become unstable and the electrostatic forces overcome the surface tension which produces a number of smaller, highly charged droplets. [127]

Two principal mechanisms have been proposed to account for the formation of gas phase ions from small highly charged electrospray droplets; the charge residue model (CRM) by Dole *et al.* [120] and the ion evaporation (IEM) model proposed by Iribarne and Thomson [128]. Figure 1-30 shows a schematic diagram of both theories of gas phase formation.

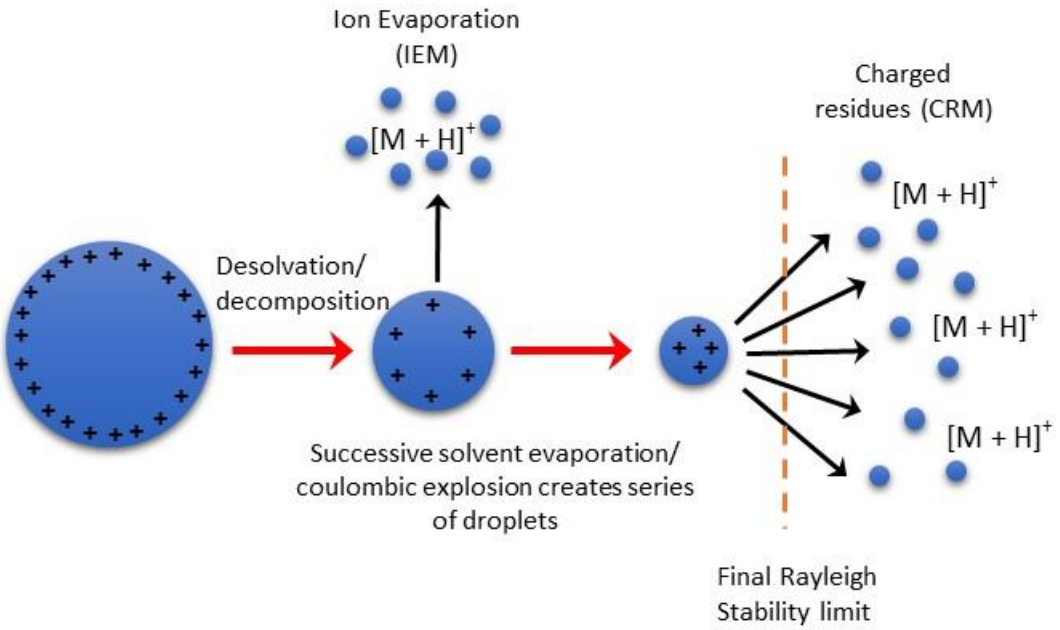

Figure 1-30. Schematic diagram showing the two possibilities for gas phase ion production and their likely relative positions within the desolvation zone in the electrospray interface. Reference adapted from www.bris.ac.uk.

In the charged residue model, a number of solvent evaporation and coulombic fission events result in small solvent droplets containing single ions. Solvent evaporation from these droplets will lead to the formation of gas-phase ions. [120, 129]

The second theory of gas phase ion formation is the ion evaporation model, which proposes that small droplets with a radius below 10 nm are able to evaporate from within the droplet. It has been suggested that the formation of small ions in the gas phase can be accounted for by the ion evaporation model and larger ions such as biomolecules form by the charged residue model. [128]

These subsequent gas phase ions are then directed to the counter electrode and skimmer cone where they are accelerated to the mass analyser for separation and detection. ESI is a soft ionisation technique as very little residual energy is retained by the analyte during ionisation, which is why the technique is important for biological studies. However, this can also be a disadvantage of the technique as little or no fragmentation. In general, ESI will produce protonated ions in positive ion ESI-MS $[M + nH]^{n+}$ or deprotonated ions in negative ion ESI-MS $[M - nH]^{n-}$. For small molecules (n=1) ESI typically generates singly

charged ions, while for larger molecules ESI can produce a series of multiply charged ions. Some molecules may produce abundant adduct ions such as $[M + Na]^+$ or $[M + NH_4]^+$ depending on other ions present in solution. [130-131]

ESI works well for charged, polar or basic compounds however, it is not as sensitive for non-basic and low-polarity compounds. Due to the technique being able to produce multiple charge states the resulting spectra can often be highly complex and require additional software to simplify them, the technique is also very sensitive to contaminants such as alkali metals and solvent clusters, which can dominate the spectra.

1.7.1.3 DART-MS

Direct analysis in real time- mass spectrometry (DART-MS) is a atmospheric pressure ion source that can ionise gases, liquids and solids in open air under ambient conditions, where the initial ionisation step involves Penning ionisation. DART grew out of discussions between Laramèe and Cody at JEOL USA, Inc., regarding the development of an atmospheric pressure thermal electron source which could replace the radioactive sources commonly used in detectors for chemical weapons agents and explosives. [132-133]

The source typically consists of two chambers through which the DART gas flows, as shown in Figure 1-31. In the first chamber, a corona discharge between a needle electrode and perforated disk electrode produces ions, electrons and excited state atoms known as metastable atoms or molecules. The cold plasma then passes through the second chamber where an electrode is used to remove cations from the gas stream, which is then passed over a gas heater and onto a final grid electrode which removes oppositely charged species, leaving only neutral gas molecules and metastable species. [134]

The ability to heat the gas allows for control of both the thermal desorption and pyrolysis of samples in the sample gap. Finally, as the gas exits the insulator cap it is directed towards the sampling orifice of an API interface or may hit the sample surface at an angle suitable for its reflection into the entrance of the mass spectrometer. The insulator cap ensures that no exposure to high voltages occurs outside of the plasma chamber. [132, 135-136]

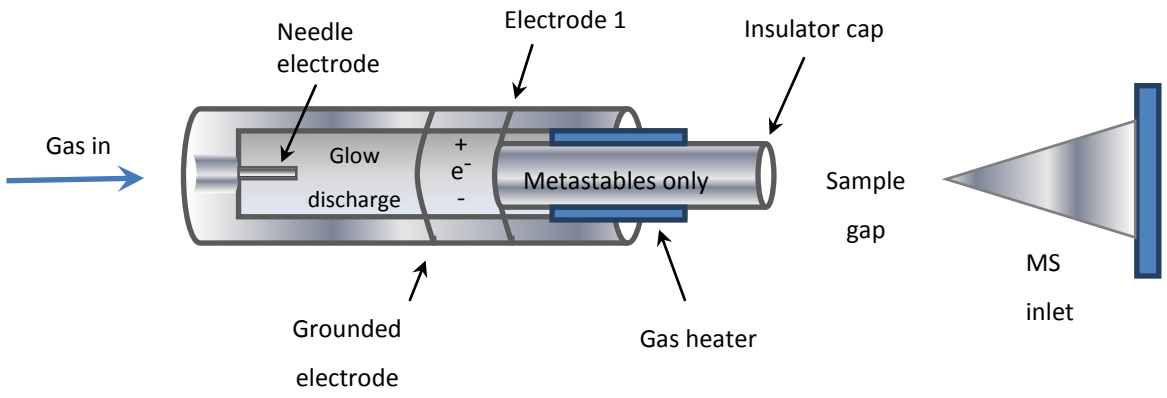

Figure 1-31. Schematic diagram to show the DART ion source and MS inlet. Reference adapted from JEOL USA, Inc.

Ion formation in DART typically involves gas-phase ionisation processes, and DART-ionisation may generate positive or negative ions which are predominately even-electron species. Several ionisation mechanisms are possible in DART depending on the polarity and the reagent gas used, the proton affinity and ionisation potential of the analyte as well as the presence of dopants or additives. [132] Ion formation in DART-MS will be explained further in Chapter 5.

The benefits of DART-MS include the speed and simplicity of the technique, with spectra being obtained in a few seconds with no or limited sample preparation needed which is very useful for trace analysis. DART-MS does not produce multiply charged states or adduct ions, instead it only produces $[M + H]^+$ species. The technique is also unaffected by choice of solvents and chromatographic separation is unnecessary and it can be used to analyse samples which are not amenable to ESI-MS or APCI-MS.

Due to the nature of the technique, analysis can be done by in open air under ambient conditions, including the ionisation of gases, liquids and solids and ionisation can take place directly on the sample surface.

1.7.2 Mass analysers

1.7.2.1 Quadrupole mass analyser

A quadrupole mass analyser consists of an array of four parallel rod electrodes that have fixed or direct current (DC) voltages or alternating current (AC) voltages that vary at a radiofrequency (rf) applied to them. Depending on the magnitude of these voltages, it can be arranged that ions of certain masses are allowed through the centre of the rods with a stable trajectory through the quadrupole rods and all other ions undergo unstable trajectories causing them to collide with the rods, see Figure 1-32. [137]

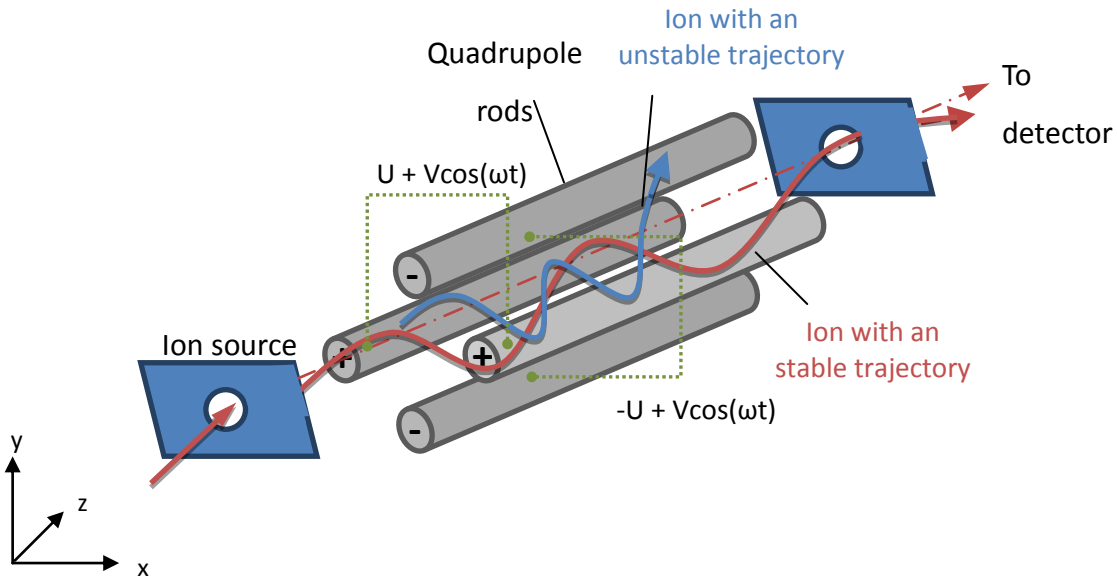

Figure 1-32. Schematic diagram of a quadrupole mass analyser showing ions with a stable and unstable trajectory and their path through the quadrupole rods. Reference adapted from www.bris.ac.uk.

Each rod is paired with its diametric opposite and has a potential of +(U+Vcos(ωt)) or -(U+Vcos(ωt); where U is the DC voltage (either positive or negative) and Vcos is the voltage which oscillates with a radio frequency (ω) in the time domain (t). Each rod is successively positive or negative, which allows ions to be attracted to or repelled away from the rods. Whether an ion has a stable or collisional trajectory is governed by Equation 1-14;

$$\theta = [U + Vcos(\omega t)]\frac{x^2 - y^2}{{r_o}^2} \quad \textbf{Equation 1-14}$$

Where x and y are the distances along the given coordinate axis and r_0 is the distance from the centre, z-axis (radius). Mathieu provided a solution to the equation that is based on Newton's second law of motion; he deduced that two factors were critical to regions of stable ion trajectory as shown in Equation 1-15. [138-139]

$$a_u = \frac{8eU}{m{r_o}^2\omega^2} \text{ and } q_u = \frac{4eV}{m{r_o}^2\omega^2} \quad \textbf{Equation 1-15}$$

where $_u$ is the position along the coordinate x and y-axis, e is the charge on an electron and m is the mass of the ion. This is simplified as shown in Equation 1-16;

$$\frac{a_u}{q_u} = \frac{2U}{V} \quad \textbf{Equation 1-16}$$

When a_u is plotted against q_u it can deduce the stability regions in the x and y-axis also known as the Mathieu stability diagrams as shown in Figure 1-33. Region A refers to the first region which represents the operating region for any particular ion where it is stable. [138-140]

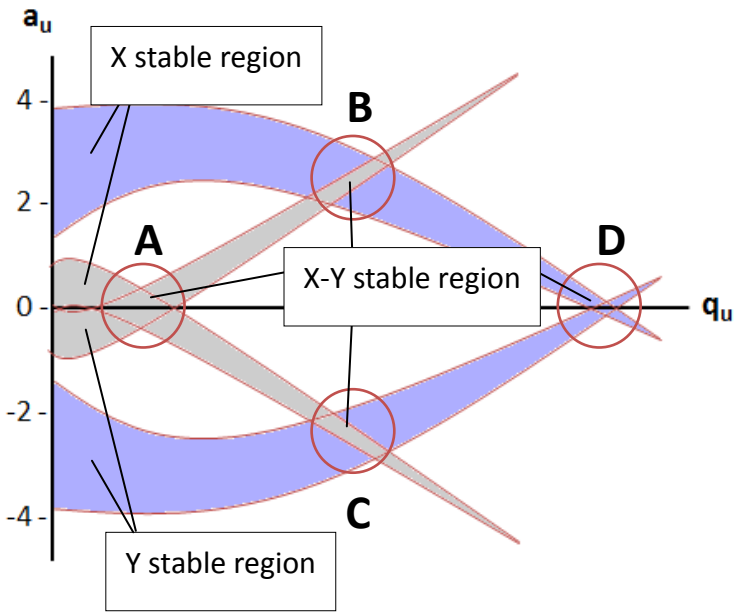

Figure 1-33. Mathieu stability diagrams for quadrupole mass analyser showing the stable regions A, B, C and D. Reference adapted from chromacademy.

Most commercial mass spectrometers operate in region A of the Mathieu diagram, which is stable in both x and y- axis. The expanded view of the first stability region (A) is shown in Figure 1-34, which shows the stability diagrams for three ions of mass m_1, m_2 and m_3 with substitutions for the Mathieu parameters *a* and *q* to convert as a function of U and V values. The DC voltage (U) and RF voltage (V) are altered as a function of a linear relationship known as the 'scan line or scan function'.

The slope of the scan line (the rate of U against V) is referred to as quadrupole gain. The intersection of the scan line with the U axis or the magnitude of the initial DC voltage is referred to as the quadrupole offset. To transmit ions of higher mass, the voltages U and V are increased whilst the ratio of U/V is fixed.

Increasing the mass gain (the slope of the scan line) will lead to increased spectral resolution however with reduced sensitivity. If a quadrupole is operated with a constant ratio U/V the resolution will be constant across a mass range.

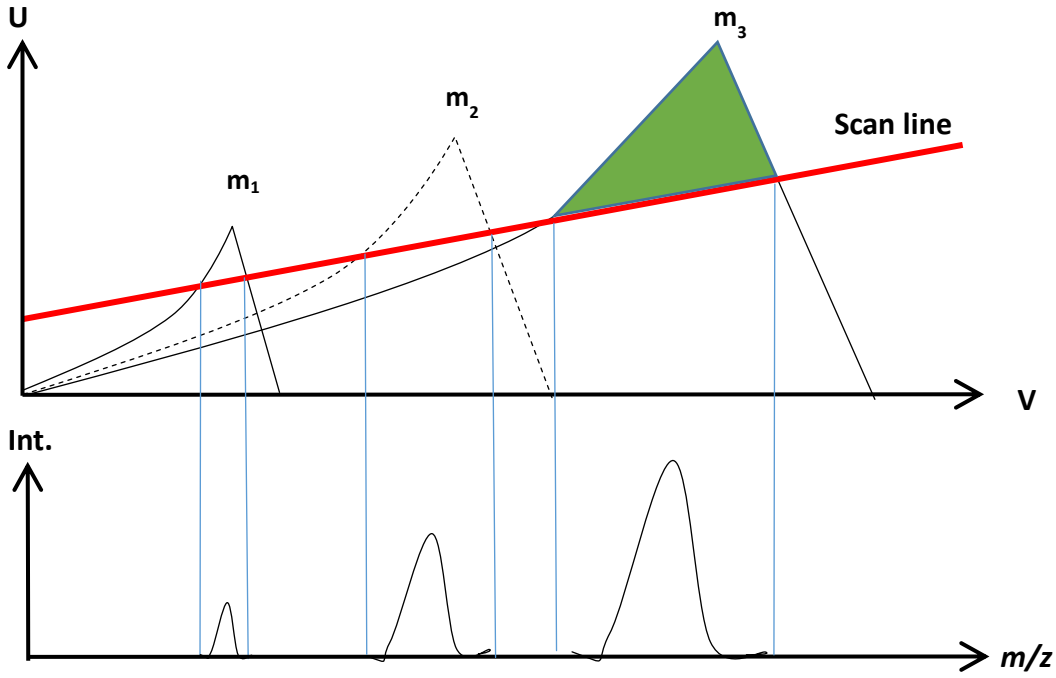

Figure 1-34. Stability diagram as a function of U and V for ions with different masses ($m_1<m_2<m_3$) (upper part), the area under the curve is equivalent to spectral peak area. Reference adapted from chromacademy.

Quadrupole mass analysers are now widely used in LC-MS and GC-MS instruments. The quadrupole mass analyser is compact in size, has a fast scan rate, high transmission efficiency and inexpensive compared to other instruments. However, most quadrupole instruments are limited to unit mass resolution and have a low mass range in the order of up to *m/z* 4000.

1.7.2.2 Time-of-flight mass analyser

Time-of-flight MS (TOF-MS) is based on a simple mass separation principle in which the mass-to-charge (*m/z*) ratio of an ion is determined by the time-of-flight of the ion. Ions are expelled from the ion source in bundles which are either produced by an intermittent process (Figure 1-35) such as matrix-assisted laser/desorption (MALDI) or through orthogonal acceleration in which a continuous ion source such as ESI is interfaced to the TOF mass analyser by orthogonal extraction. Orthogonal extraction refers to ions being accelerated along the axis which is perpendicular to their initial direction of motion.

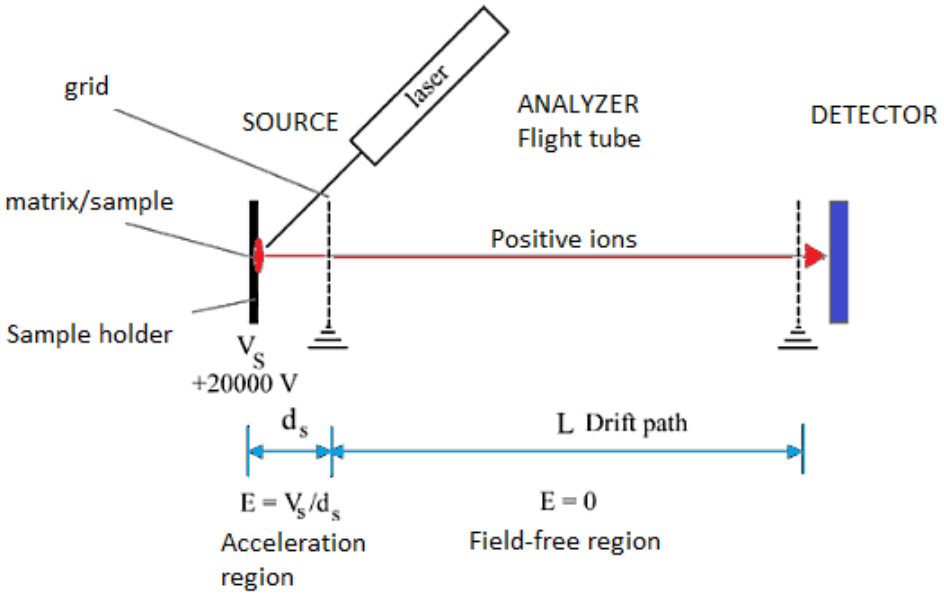

Figure 1-35. Principle of a time-of-flight instrument after ionisation by matrix assisted laser desorption ionisation (MALDI).

Ions are then accelerated towards the flight tube (acceleration region) by a difference in potential applied between the electrode and the extraction grid. As all ions acquire the same kinetic energy, ions characterised by a distribution of their masses present a distribution of their velocities. When leaving the acceleration region, they enter into a field-free region where they are separated according to their velocities, before reaching the detector.

Equation 1-17 shows how the velocity of an ion is related to *m/z*.

$$E_k = \frac{mv^2}{2} \qquad \textbf{Equation 1-17}$$

where E_K refers to the kinetic energy of the ion, m is the mass of the ion and v refers to its velocity. Kinetic energy can also be expressed in terms of potential energy applied, Vs, and total charge of the ion, ze, where z is the charge state and e refers to the absolute charge of a proton or electron (Equation 1-18).

$$E_k = zeVs \qquad \textbf{Equation 1-18}$$

Both equations can be combined and rearranged to give Equation 1-19;

$$V = \left(\frac{2zeVs}{m}\right)^{1/2} \qquad \textbf{Equation 1-19}$$

The time taken, t, for an ion to leave the accelerating region and travel through the drift tube to the detector is calculated from dividing the length of the flight tube (L) with the velocity (Vs). Rearranging this equation gives Equation 1-20.

$$t = L\sqrt{\frac{m}{2zeVs}} \qquad \textbf{Equation 1-20}$$

Mass-to-charge *(m/z)* ratios are determined by measuring the time that ions take to move through the field-free region. Theoretically, TOF mass analysers have no upper mass limit and are particularly suited for high molecular weight analytes such as biomolecules.

1.7.2.2.1 Hybrid instruments

Mass spectrometers that use a combination of two or more mass separation devices in the first and second stages of mass analysis can often be referred to as "hybrid" mass spectrometers. The general goal of hybrid instruments is to combine advantageous performance characteristics offered by various types of analysers, such as high mass resolving power and speed of analysis. An example of a hybrid instrument is a quadrupole-time of flight mass spectrometry known as Q-TOF-MS, this instrument is a tandem-in-space instrument employing a transmission quadrupole with a collision cell as MS1 and a reflectron TOF as MS2 (which acts to replace the third quadrupole in a triple quadrupole instrument) as seen in Figure 1-36. [105, 141]

Q-TOF-MS has the advantages of high mass accuracy around 5 - 10 ppm and high resolution of around 10,000 – 40,000 full width at half maximum (FWHM). The success of this instrument is due to the simplicity of the quadrupole and high performance of the TOF mass analyser. The TOF analyser can be advantageous as the second stage of the instrument because its capability to transmit all ions simultaneously leading to an increase in sensitivity in the attomole range and a mass range in the order of *m/z* 20,000. [142]

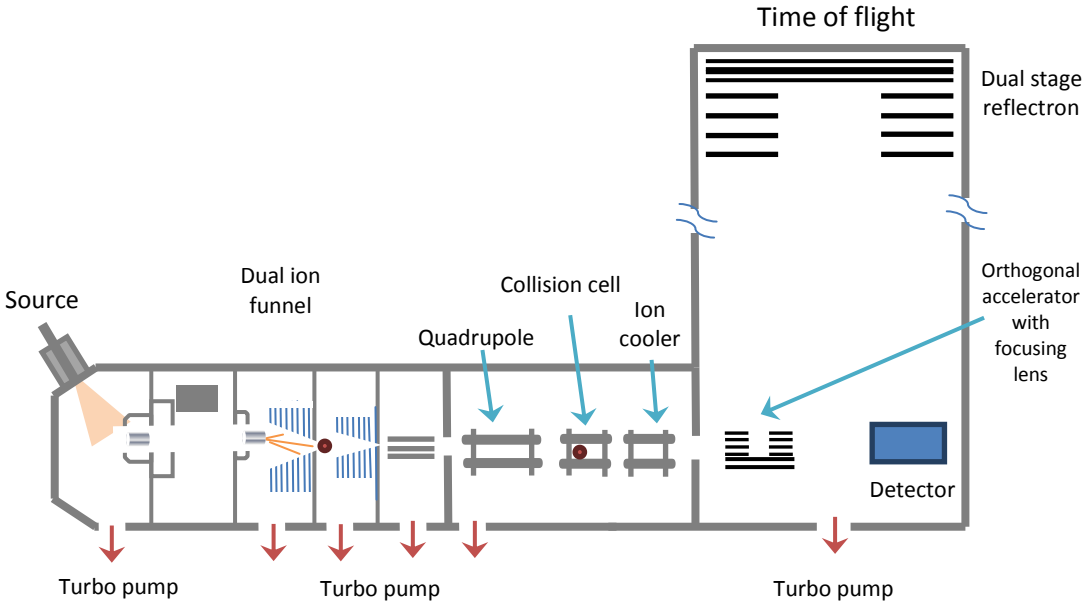

Figure 1-36. Schematic of a Quadrupole- Time of flight (Q-TOF) mass spectrometry. Reference adapted from Bruker.

1.7.2.3 Fourier transform-ion cyclotron resonance mass spectrometry

E. O. Lawrence initially developed ion cyclotron resonance (ICR) in 1932 and later this principle was applied to construct Fourier transform-ion cyclotron resonance mass spectrometry (FT-ICR MS) by Comisarow and Marshall.

FT-ICR mass analysers consist of four main components, these include a magnet, ultra-high vacuum system, analyser cell and a data acquiring system. The magnet can be either a permanent magnet, an electromagnet or a superconducting magnet, with the latter being the most common. Superconducting magnets typically have field strengths from 3 to 9.4 Tesla (T). The performance of the instrument improves greatly as the magnetic field strength increases. The ultra-high vacuum system is needed in FT-ICR MS to achieve high resolution. The higher the vacuum, the longer the mean free path of the ion and reduction in the possibility of collisions of gas molecules with the ion of interest. For ultra-high vacuum systems, pressures of $10^{-9} - 10^{-11}$ mbar are required.

The analyser cell, is another important component of the FT-ICR and is composed of three sets of plates for trapping, excitation and detection of ions as shown in Figure 1-37, these

cells can come in several different configurations including cubic (Figure 1-37) and cylindrical (Figure 1-38). The cubic cell was the first type of analysed developed and is composed of six plates arranged in the shape of a cube. Another commonly used cell is the cylindrical cell also consisting of six plates however, the shape and dimension of this cell make it easier to fit into the bore of a superconducting magnet.

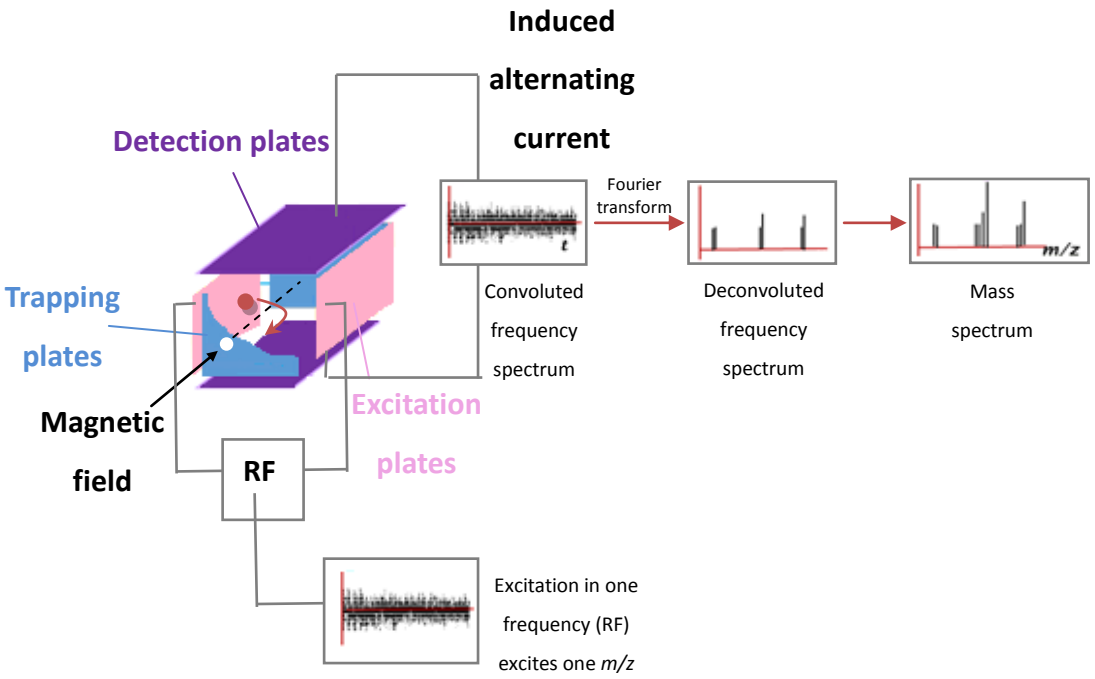

Figure 1-37. Schematic diagram of a cubic FT-ICR cell with subsequent production of a mass spectrum. Figure adapted from jlab.chem.yale.edu.

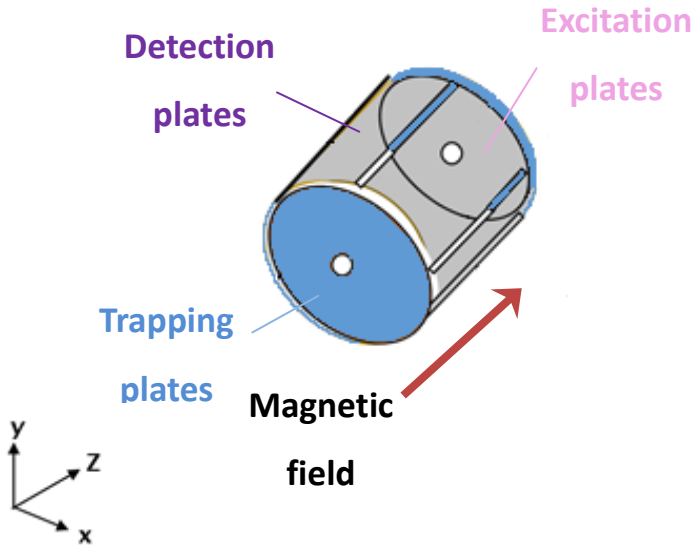

Figure 1-38. Schematic diagram of a cylindrical analyser cell, composed of three sets of plates for trapping, detection and excitation of ions. Figure adapted from jlab.chem.yale.edu.

The basis of ion cyclotron motion is derived from the interaction of an ion with a magnetic field, as they enter the magnetic field they experience a force named the Lorentz force (F). This causes the ions to have a circular trajectory, this is shown in Equation 1-21, where F refers to the Lorentz force, q = the total charge of the ion, v = the velocity and B is the magnetic field.

$$F = qv \times B \qquad \textbf{Equation 1-21}$$

The ICR frequency of an ion is dependent on its mass-to-charge which is given in the equation for ion cyclotron motion (Equation 1-22), where ω_c refers to the cyclotron frequency, z= number of charges and m= mass of the ion.

$$\omega_c = \frac{zB}{m} \qquad \textbf{Equation 1-22}$$

Within the ICR cell, the ions undergo three types of motion including cyclotron motion due to the magnetic field, trapping motion due to the electric field produced by the trapping plates and magnetron motion which is a combination of both magnetic and electric fields acting upon the trapped ions.

Cyclotron motion has a specific angular frequency. This frequency is the experimentally measured value that allows for the calculation of the mass of an ion. The cyclotron

motion involves the interaction of an ion with the magnetic field, which acts on the ion's velocity that is perpendicular to the magnetic field axis. The cyclotron frequency is determined by three physical parameters, the strength of the magnetic field, the charge present on the ion and the mass of the ion.

Magnetron motion is a form of radial motion derived from the Lorentz equation involving the combination of magnetic and electric fields, which results in a superimposed circular motion on the cyclotron trajectory creating a 3D ion trap. This motion is typically many orders of magnitude lower in frequency than cyclotron frequency. In general, the magnetron frequency is mass independent, and the cyclotron motion is inversely proportional to mass. The motion allows for ions to be stored in the ICR analyser cell for a period of time.

Trapping within the analyser cell is achieved through a combination of magnetic and electric fields. Ions enter the cell and experience a strong magnetic field, which traps them in the radial direction and induces cyclotron motion. A small electric potential is applied to two trapping plates to prevent the ions from moving in axial direction out of the cell.

The measurement of the ion cyclotron frequency of the ions is carried out by first exciting the trapped ions, followed by detection of the motion of the excited ions. Excitation of the ions is carried out by the application of an RF signal to the excitation plates in the analyser cell. When the frequency of the RF signal is on-resonance with the cyclotron frequency of a given *m/z*, the ions are excited to a larger ICR radius. Ions with the same *m/z* are excited together as a coherent package.

Detection of the ions is completed using the detection plates, an image current is induced when the ions pass the detector plate and the resulting ion frequency signals are detected. The signal is amplified and stored in the computer as a time domain response function, referred to as a transient, or a free induction decay (FID). The FID can be mathematically transformed using a Fourier transform (FT), which converts the time-dependent function into a frequency dependent function, which can be converted into a mass spectrum. The attractive features of FT-ICR MS involve high resolving power, high sensitivity and its non-destructive capabilities.

1.7.3 Tandem MS

Tandem MS can also be performed on a tandem-in space instrument, where the separation elements are physically separated. An example of this is a triple quadrupole mass analyser, where there are two transmission quadrupole *m/z* analysers known as quadrupole 1 (Q1) and quadrupole 3 (Q3), which are separated by a collision cell which is operated in RF-only mode known as quadrupole 2 (Q2).

Tandem MS (also known as MS/MS) involves multiple stages of mass separation and fragmentation. Tandem MS can be used as an aid in structural elucidation studies and as final confirmation of elemental analysis. An ion formed in the ion source, the precursor ion, is mass-selected in the first stage of analysis and then caused to fragment in a collision cell by a range of different types of dissociation such as collision-induced dissociation (CID). CID occurs when the selected ion is directed into a collision cell, where it collides with neutral molecules of a collision gas, *e.g.* argon. In the collision cell, some of the kinetic energy transferred from the collision gas to the analyte ion is converted into internal energy which results in bond breakage and fragmentation of the precursor ion into smaller fragments.

The fragment ions are then detected in the final stage of analysis. This can be referred to as a product ion scan or daughter scan where the selected precursor ion is chosen and the resulting product ions are analysed. However there are a range of other scan experiments that can be performed using tandem MS instruments such as precursor ion scans, neutral loss scans and selected reaction monitoring, these will be explained further in chapter 1.7.3.1. [105]

Tandem MS can be accomplished using more than one mass analyser known as tandem mass spectrometry in space (such as Q-TOF-MS or triple quadrupole instruments) or in ion trap instruments known as tandem mass spectrometry in time. Triple quadrupole instruments are one of the most widely used MS/MS instruments and consist of three sets of quadrupole rods, in which the first and third quadrupole are mass-selective and the second quadrupole is operated in RF only and used as a collision cell. The precursor ion is transmitted to the collision cell (RF-only quadrupole) and the third quadrupole provides a means of analysing all of the products from the collision cell.

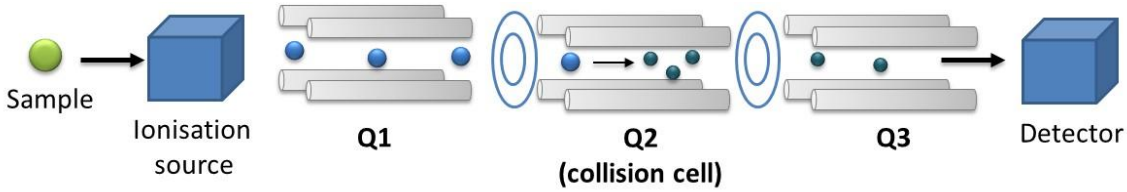

Figure 1-39. Schematic of a triple quadrupole mass spectrometer.

The quadrupole ion-trap (QIT) known as the ion-trap, is a three-dimensional quadrupole instrument, which confines ions in a small area between a ring electrode and two end-cap electrodes. When an RF voltage is applied to the ring electrode, ions of a particular *m/z* then become unstable and are directed towards the detector. The individual processes (ion accumulation, ion selection, dissociation and *m/z* analysis) for MS/MS are performed in the same coordinates of space, but in sequential periods of time. The selection and dissociation or fragmentation processes can be repeated a number of times; this can be referred to as MS^n.

In an ion trap, tandem MS is achieved by the use of an additional sequence of operations in the scan functions. The scan function begins with ionisation, followed by selection of a parent ion in a step which involves ejecting all the other ions from the trap. The parent ion is then excited by applying a RF voltage to the end caps. The product ions resulting from CID of these excited ions with the collision gas are then recorded by scanning the RF voltage to perform another mass scan.

The capability to perform MS^n is a unique feature of the ion trap mass analyser, the selectivity of MS^n means that a compound can be fragmented, and the resulting fragments further isolated and analysed to yield structural information on molecules. However, one weakness of the ion trap is the poor dynamic range which is due to space charge effects. Space charge effects can be eliminated by removing matrix ions. The ability to selectively store ions is expected to provide a substantial improvement in limits of detection. [105, 118]

1.7.3.1 Tandem MS scan modes

There are four main scan modes available in tandem MS. The examples below are for triple quadrupole mass analysers;

1. Product ion scan which consists of selecting a precursor ion (in Q1) of a chosen *m/z* and determining all of the product ions (in Q3) resulting from collision induced dissociation in the collision cell (Q2).

2. Precursor ion scan consists of choosing a product ion in Q3 and determining the precursor ions. All of the precursor ions that produce ions at the selected *m/z* are detected.

3. Neutral loss scan involves scanning both Q1 and Q3 but with a constant mass offset between the two, by selecting a neutral fragment such as H_2O and detecting all of the fragmentation leading to that neutral loss. This type of scan can aid in identification of closely related molecules.

4. Selected reaction monitoring (SRM) or multiple reaction monitoring (MRM) involves selecting a fragmentation reaction. For this type of scan, Q1 and Q3 are set to a selected mass, allowing only a distinct fragment ion from a certain precursor ion to be detected. The absence of scanning allows the focus on one precursor ion and product ion which therefore increases sensitivity in this scan. If Q1 and/or Q3 are set to more than a single mass, this is known as multiple reaction monitoring.

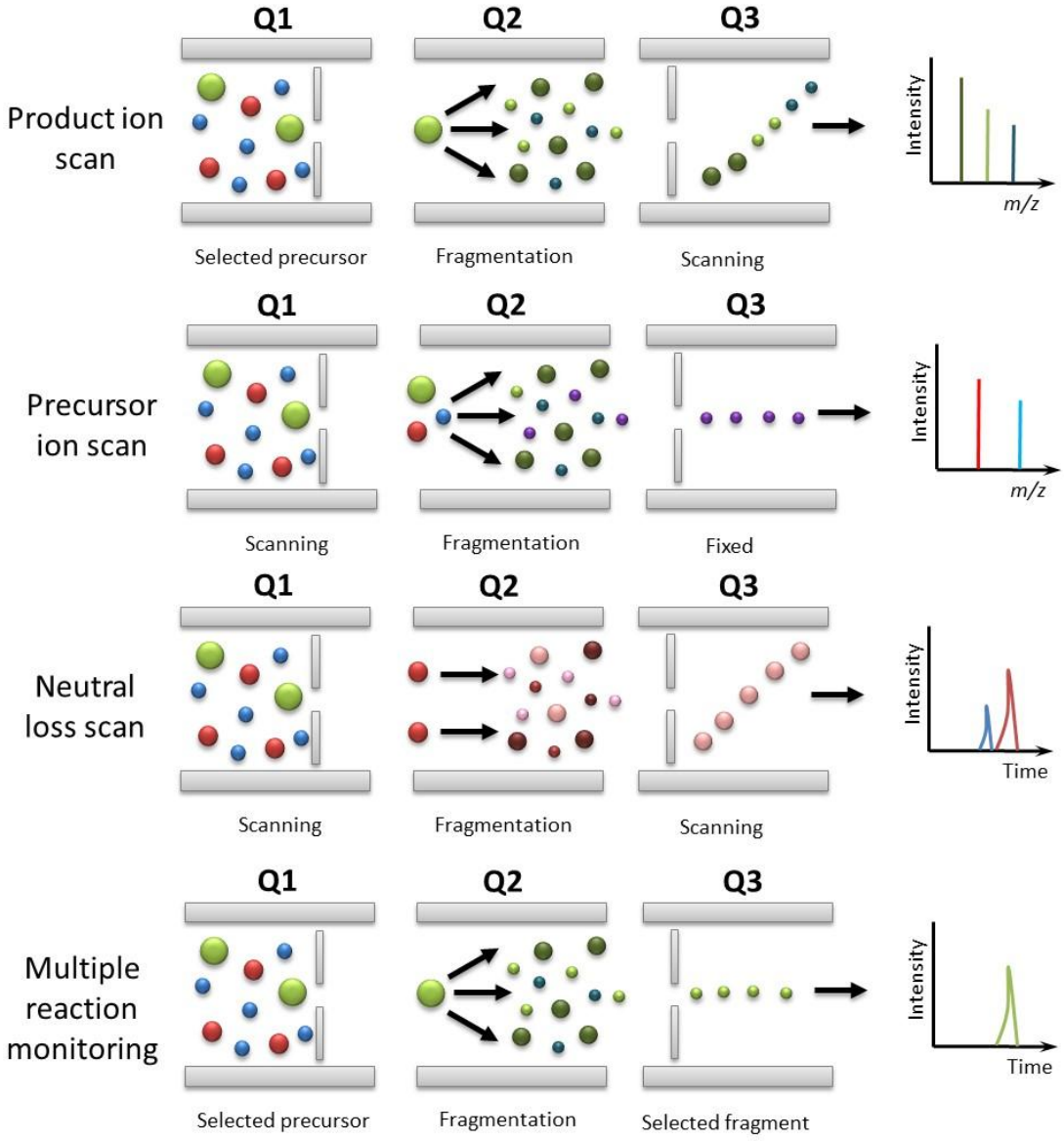

Figure 1-40. Schematic diagram of the scan modes used in tandem MS.

1.8 Other techniques

1.8.1 Scanning electron microscopy- energy dispersive X-ray analysis (SEM-EDX)

SEM utilises a high-energy focused electron beam which scans across the surface of the sample, producing a large number of signals. These electron signals are later converted to a visual signal displaced on a cathode ray tube.

The signals produced from the interactions between the electron beam and samples result in image formation. These interactions are divided into two categories; elastic interactions and inelastic interactions. [143]

Elastic scattering refers to the deflection of the incident electron by the sample's outer shell electrons. Backscattered electrons refer to incident electrons that are elastically scattered through an angle of more than 90°.[143]

Inelastic scattering occurs through a range of interactions between the incident electrons and electrons and atoms of the sample, and results from the incident beam transferring substantial energy causing excitation of sample electrons leading to the formation of secondary electrons. Figure 1-41 shows the types of signals created in SEM.[144]

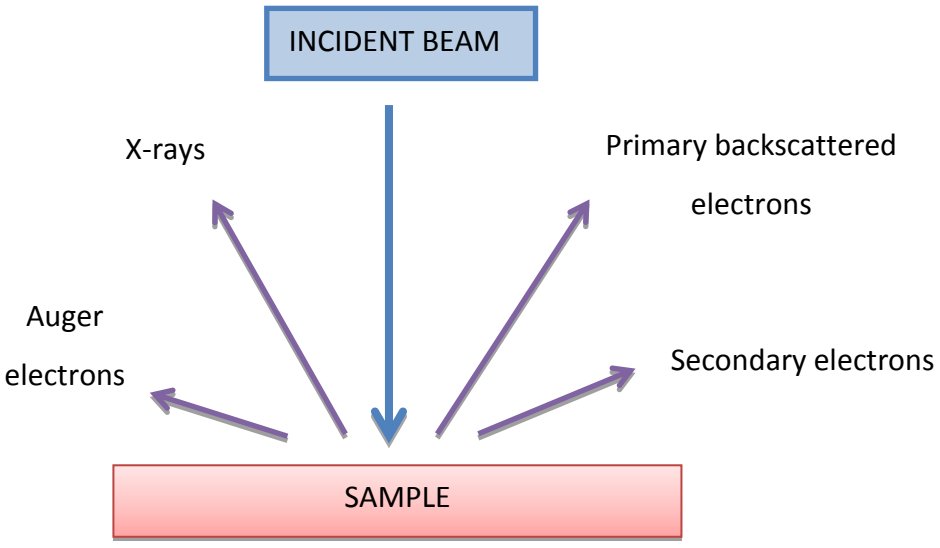

Figure 1-41. Illustration of several signals created by the electron beam- sample interaction in the scanning electron microscope. Figure adapted from hit.ac.il.

Secondary electrons are the most widely used signal in SEM, produced by the interaction between the primary electron beam with the sample. When the primary electron beam strikes the surface of the sample causing ionisation of sample atoms, a number of loosely bound electrons may be emitted known as secondary electrons. Secondary electrons can give topographic information of the surface with good resolution due to their low energy.

Backscattered electrons can give compositional and topographical information in SEM. X-rays are produced by the interaction of the primary electron beam with the sample, and can provide chemical information about the sample. When an inner shell electron is displaced by a collision with a primary electron, an outer shell electron may fall into the inner shell to re-establish the charge balance. By the emission of an X-ray photon, the ionised atom returns to ground state.

Auger electrons are produced following the ionisation of an atom by the incident electron beam and the falling back of an outer shell electron to fill an inner shell vacancy. The excess energy released may be carried away by the Auger electron.

Energy dispersive X-ray spectroscopy (EDX) is typically utilised in conjunction with SEM (known as SEM-EDX) and allows for semi-quantitative characterisation of the sample's chemical composition. The technique is non-destructive, and relies on the interaction between X-ray excitation and the sample, see Figure 1-42. The impact of the electron beam on the sample may excite an electron in an inner shell, ejecting it from the shell. An electron from an outer, higher energy shell then fills in the vacancy and the difference in energy between the higher-energy shell and lower-energy shell may be released in the form of X-ray emission. The number and energy of the X-rays emitted from the specimen can be measured by the EDX spectrometer. X-rays emitted from the sample atom are characteristic in energy and wavelength to the element. [145]

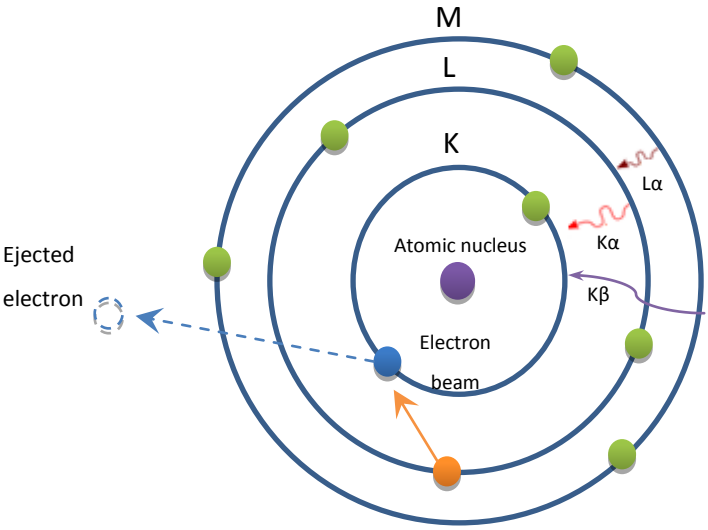

Figure 1-42. EDX scheme showing energy shells (M, L and K) and the impact of the electron beam with subsequent ejection of electrons. Figure adapted from hit.ac.il.

1.9 Aims of the project

The aims and objectives of this project are to investigate the phenomenon of internal diesel injector deposits by initially studying the variations in diesel fuels and understanding the issues of injector failure in particular filter and injector deposits.

In addition to this, the effects of fuel solvency will be investigated, by exploring the ratio of aromatic and aliphatic components present in a range of fuels Including ULSD fuel and G-Diesel fuel. The solvency of fuel is seen to affect the formation of deposits, therefore a range of fuels exhibiting deposit formation will be investigated.

A range of deposit precursors will be investigated and the most applicable analytical technique will be used for its analysis including optimisation of the operating parameters. Steryl glucoside was observed to be a deposit precursor found in biodiesel fuel, an assay will be developed for this and structure elucidation techniques will be explored.

The surface of the deposit will also be analysed by surface analysis techniques including SEM-EDX and DART-MS, to identify components present which could be deposit precursors.

Chapter 2: Experimental

This chapter describes the experimental conditions for Chapters 3, 4 and 5, including instrumentation conditions, sample and the chemicals used. Any deviations to these conditions or any other parameters used and will be explained in the subsequent chapters.

2.1 Chemicals

2.1.1 Reagents

Methanol (MeOH, LC-MS grade), acetonitrile (ACN, LC-MS grade), water (LC-MS grade), formic acid (HCOONa) and dichloromethane (DCM) were purchased from ThermoFisher Scientific (Loughborough, UK). Sodium formate (HCOONa) was purchased from Sigma-Aldrich (Gillingham, UK) and food grade carbon dioxide was purchased from BOC special gases (Manchester, UK).

2.1.2 Calibrant standards

The external calibration solution (soton mix) was prepared using a standard solution of diphenhydramine (monoisotopic mass 255.1623 Da), oxybutynin (monoisotopic mass 357.2304 Da), terfenadine (monoisotopic mass 471.3137 Da), reserpine (monoisotopic mass 608.2734 Da), erythromycin (monoisotopic mass 733.4612 Da) and gramicidin_S (monoisotopic mass 1140.7059 Da) mixed at a concentration of 1 µg/mL per compound. The chemical structures are shown in Figure 2-1.

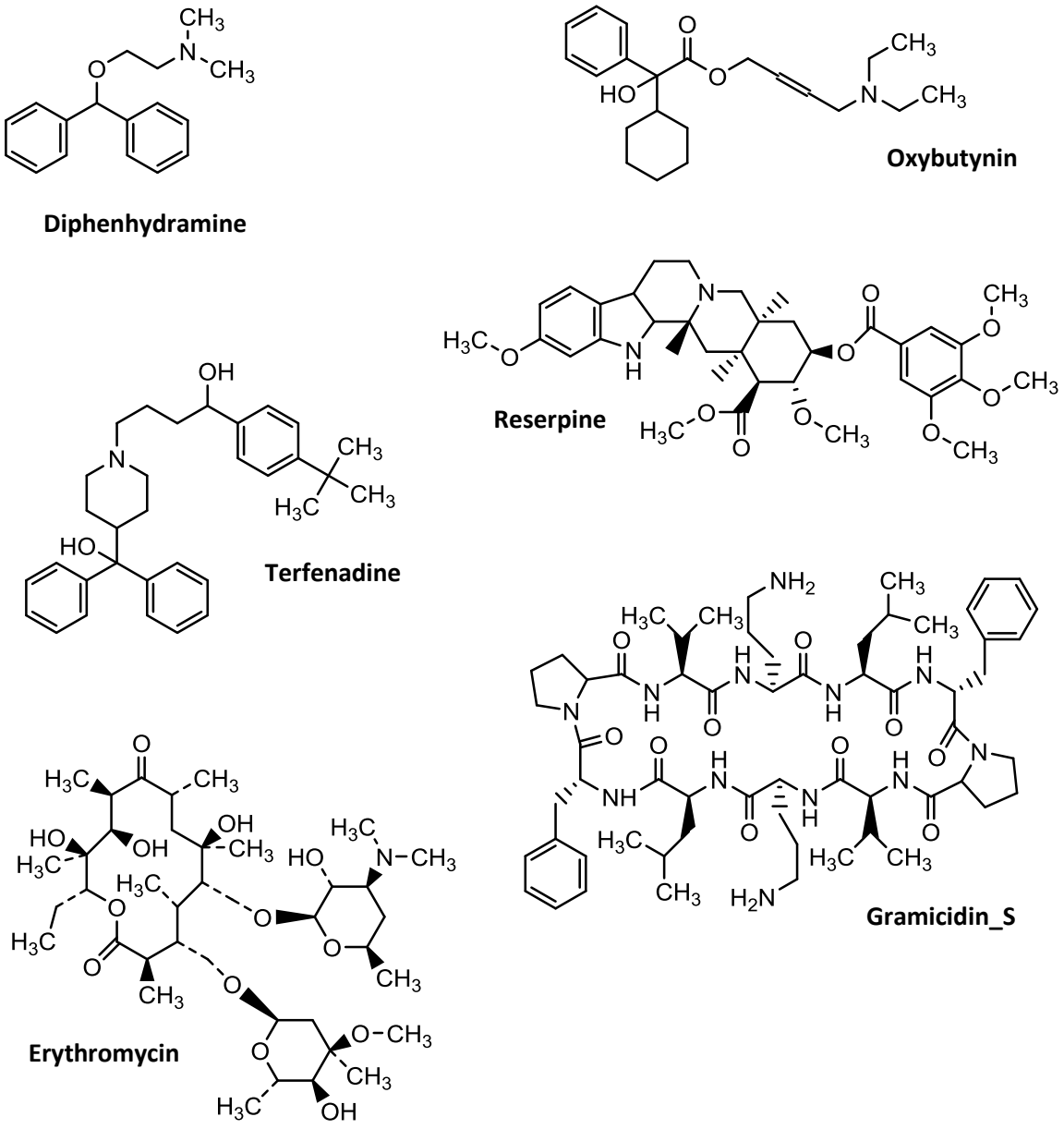

Figure 2-1. Chemical structures of the calibration compounds.

2.1.3 Steryl glucoside standards- Chapter 4

Steryl glucoside standards were obtained from Matreya LLC. (Universal Biologicals Ltd., Cambridge, UK): see Table 2-1 for the relevant structures and masses. Samples were prepared at 100 mg/kg initially, for optimisation of the analytical conditions.

Table 2-1. Steryl glucoside standards including chemical structures, of Campesteryl, stigmasterol and sitosteryl glucoside with masses.

Structure	Name	Ions observed
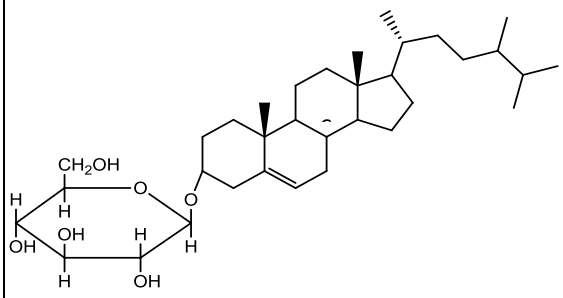	Campesteryl glucoside	$[M + Na]^+$ = *m/z* 585.4 $[M + H – sugar]^+$ = *m/z* 383.2
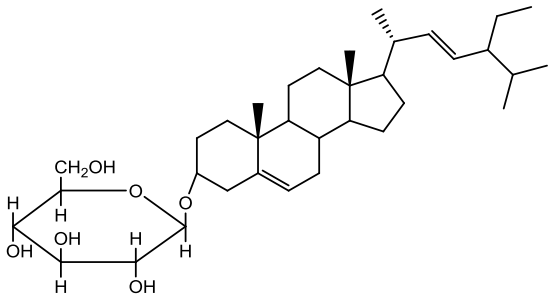	Stigmasterol glucoside	$[M + Na]^+$ = *m/z* 597.7 $[M + H – sugar]^+$ = *m/z* 395.7
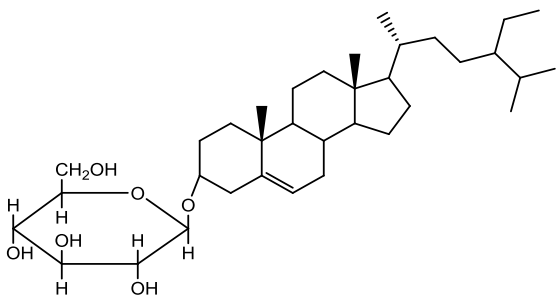	β-Sitosteryl glucoside	$[M + Na]^+$ *m/z* 599.4 $[M + H – sugar]^+$ = *m/z* 397.5

2.1.4 Samples

Fuel samples and JF-TOT rods (full details in Chapter 5) were obtained from Innospec Inc. (Ellesmere Port, UK).

2.2 Instrumentation

A general introduction will be described here however full details will be given in the relevant chapters. All sample analysis were performed in triplicates (3 replicates) for precision.

2.2.1 Gas chromatography- mass spectrometry (GC-MS) conditions

All analyses were performed using a Trace GC 2000 series coupled to a mass spectrometer (Thermo Finnigan, Manchester, UK). The GC column used for separation was an Innowax capillary column (J&W Scientific, Berkshire, UK) 60 m x 0.25 mm; 0.5 µm i.d., 0.50 µm film thickness. The stationary phase used was 100 % polyethylene glycol (PEG). Helium (He) was used as the carrier gas and the flow rate was set to 1.0 mL/min, and the sample injection volume was 1 µL introduced into a split-splitless inlet system operating in the splitless mode. The temperature programme was set initially at 40 °C, held for 4 minutes and then increased at a 5 °C/minute to 240 °C and held at this temperature for 16 minutes.

70 eV electron ionisation (EI) mass spectra were acquired with a trap current of 150 µA and a detector voltage of 350 V. Data were acquired over *m/z* 20- 510 at a scan rate of 2 scans per second. Data were collected and processed using Xcalibur™ software (Version 2.0) and individual components analysed using a NIST Mass Spectral Library (NIST 14, Version 2.2) for comparisons using similarity index (SI). After the initial splitless injection, samples were re-analysed using split injection with a split ratio of 50:1.

2.2.2 Supercritical fluid chromatography-mass spectrometry (SFC-MS) conditions

All analyses were performed using an Acquity UPC^2 coupled to a Waters Xevo triple quadrupole detector (TQD) mass spectrometer (Waters, Manchester, UK). CO_2 was used as the supercritical fluid and methanol was used as the organic modifier, see Table 2-2 for the gradient conditions.

The column used was a High Strength Silica C18 for Bases (HSS C18 SB, 100 mm x 3.0 mm column dimension with 1.8 µm particle size) and the column temperature was set to 40 °C. The back-pressure was regulated to 150 bar using the back-pressure regulator to maintain supercritical fluid conditions.

Table 2-2. SFC gradient conditions with % of mobile phase A and B.

Time (minutes)	Flow rate (mL/min)	Mobile phase A % (CO_2)	Mobile phase B % (Organic)
Initial	1.5	98	2
2	1.5	60	40
3	1.5	60	40
30	0	98	2

The sample temperature used was 10 °C and the sample injection volume was 2 µL. The PDA detector was set to 220-400 nm wavelength. Make-up solvent was used at a flow rate of 0.45 mL/min using methanol in 0.1% formic acid.

Mass spectra were acquired using a Waters Xevo TQD (Waters, Manchester, UK) triple quadrupole mass spectrometer. Positive ion electrospray ionisation (+ve ESI) was used for the analysis of steryl glucosides. The operating conditions were as follows: capillary voltage 3.5 kV, cone voltage 20 V, source temperature 150 ^{o}C, desolvation temperature 500 ^{o}C. Nitrogen was used as the desolvation gas at a flow rate of 650 L/h.

The collision energies for tandem-MS experiments were 10, 20, 40 and 60 V for optimisation of fragmentation. Product ion scans were acquired for the free steroid at *m/z* 383, 395 and 397 for campesteryl, stigmasterol and sitosteryl.

2.2.3 Fourier transform- ion cyclotron resonance mass spectrometry (FT-ICR MS) conditions

Experiments were conducted using a 4.7 Tesla (T) Solarix mass spectrometer (Bruker Daltonics, Coventry, UK). The samples were introduced using an ESI source and experiments were undertaken by direct infusion using a 100 µL Hamilton syringe (Coventry, UK) and syringe pump with the sample solution in methanol at a concentration

of 0.1 mg/mL. The instrument was calibrated using 1 µg/mL per component soton mix calibration solution in methanol as explained in section 2.1.2.

The ESI source parameters for positive ion ESI were as follows: capillary voltage - 4000 V, end plate offset 500 V, drying gas flow rate 4.0 L/min, drying gas temperature 180 °C with a nebuliser pressure of 1.2 bar. Instrument control and data acquisition were performed using Compass Solarix control (Bruker Daltonics) and data was processed using Compass Data Analysis. Positive ion ESI-MS were acquired between *m/z* 150-1500.

2.2.4 Scanning electron microscope- electron dispersive X-ray (SEM-EDX) conditions

All analyses were performed using the FEI XL30ESEM. The X-ray analysis system was a Thermo Scientific Noran System Seven, with an Ultradry energy dispersive X-ray spectrometer (EDX).

Accelerating voltage used was 10 kV; spot size used was 5 mm, with a scan rate of 40 ms per line over 484 lines. The magnification used for imaging was 100 or 1000x.
The JF-TOT rod metal surface and injector needle were both analysed and different regions analysed by SEM-EDX.

2.2.5 Direct analysis in real time- mass spectrometry (DART-MS) conditions

Positive ion mass spectra was acquired using a DART-SVP™ ion source (Ionsense, Saugus, MA, USA) interfaced to an LCQ ion trap-MS (Finnigan MAT, USA). The JF-TOT fuel samples were dipped onto the closed end of the Dipit- capillary tubes™ (Ionsense) and positioned on a rack between the DART ion source and detector inlet, see Figure 2-2.

The rack is placed on a linear rail system which provides automated delivery of the sample to the correct sampling position; the rack is perpendicular to the ionising gas stream and allows reproducibility, automation and optimal positioning of the sample. The rack is transported along the rail system at 0.2 mm per second while acquiring the data. An external standard of caffeine was used and placed on a Dipit- tube to check the calibration of the instrument.

Figure 2-2. DART-MS instrument setup for the fuel samples.

The JF-TOT rods had to be sampled directly from the metal surface of the rod, and the angle of the DART gun had to be positioned and optimised for effective ionisation of the sample surface of the rod shown in Figure 2-3. The rod was secured into place onto a metal holder, typically used to hold capsules. The external calibration standard (caffeine) was placed on either side of the JF-TOT rod in areas free from deposits. The metal holder is placed on the linear rail system and transported along the system at 0.2 mm per second. Data analysis was performed by Xcalibur software (Version 2.0).

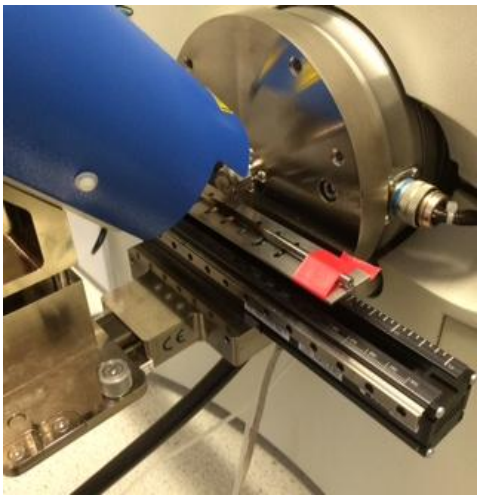

Figure 2-3. DART-MS instrument setup for the JF-TOT rods.

2.2.5.1 DART-MS interfaced to Synapt G2-MS

DART-MS was also interfaced to the Synapt G2-MS (Waters, Manchester, UK) for accurate mass measurements, see Figure 2-4. DART-MS experimental details are shown above. Synapt G2-MS conditions were as follows, mass spectra were obtained over a range of 50-800 *m/z.* Background spectra of siloxanes was used as a calibration file with their accurate masses calculated. For tandem-MS experiments, collision energy was evaluated in the range of 0-20 V. Data analysis was performed using Masslynx software (Version 4.1).

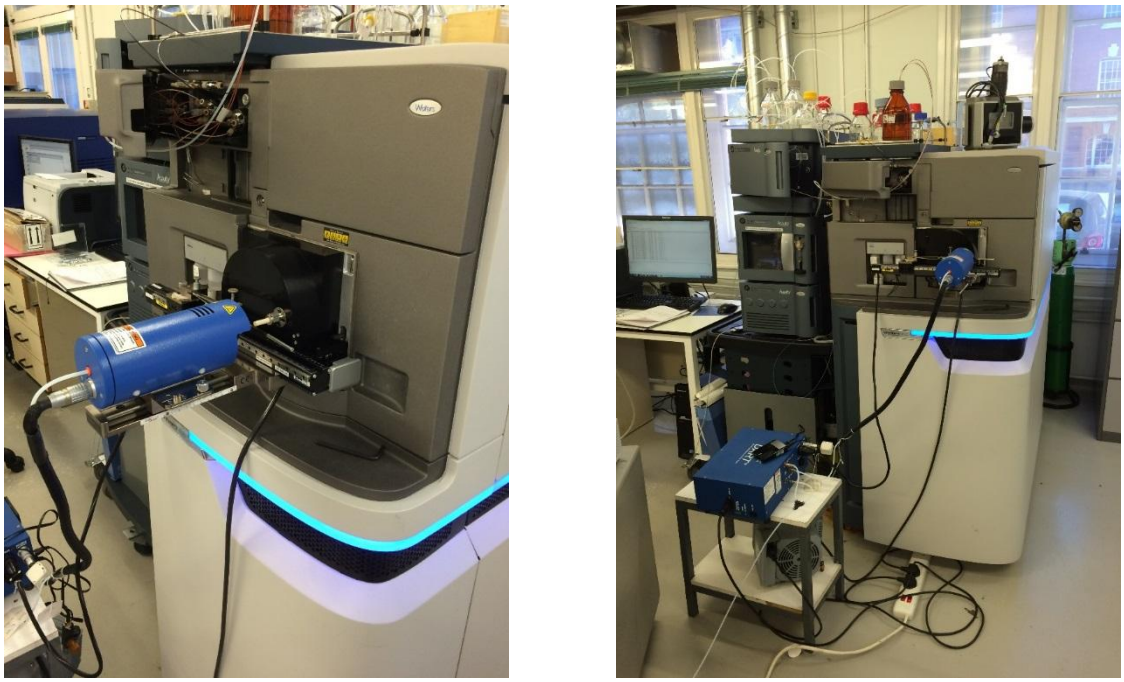

Figure 2-4. DART-MS instrument setup interfaced to the Synapt G2-MS.

Chapter 3: Fuel solvency

3.1 Introduction

The focus of this chapter involves the effects of fuel solvency on deposit formation. A data reduction model will be investigated which allows for qualitative analysis of large sample sets, and can identify aliphatic and aromatic content.

3.1.1 Fuel solvency effects

Fuel solvency refers to the ability of the fuel to dissolve particles or larger molecular weight compounds that may be present in the fuel. The term 'solvency' indicates that the substance can dissolve a solute that is chemically different to the substance and results in a solution.

Internal diesel injector deposits (IDID) have been a major concern for diesel engines recently, due to government regulations on emissions and the development of new fuel injection equipment, with more intricate injector parts being susceptible to deposit formation. Solubility can play an important factor in deposit formation, because deposits can often appear to be formed from a number of particulates, which agglomerate to form a deposit. Hence the ability of the fuel to solubilise these deposits is crucial and fuels with higher solvency properties could aid in dissolving particulates in the fuel. [146-148]

Solvency can be tested using the ASTM Standard Test Method for Kauri-Butanol (KB) Value of Hydrocarbon Solvents (D-1133) [149], where a higher KB value indicates increased solvency. The KB value refers to the maximum amount of the solvent that can be added to a solution of Kauri resin (fossilized resin derived from Kauri pine tree sap) in butyl alcohol without causing cloudiness (referred to as the cloud point). Aromatic compounds have the highest KB values of around 100 (best solvency) of the four hydrocarbon classes including cyclo-paraffins, iso-paraffins and paraffins which have the lowest KB values of around 30. [150]

Therefore, the higher the content of aromatic hydrocarbons present in the fuel, the increased fuel solvency, whereas straight-chain and branched chain aliphatic

hydrocarbons (paraffins and iso-paraffins) tend to exhibit lower solvency properties. [151-152]

Biodiesel also has a greater solvency effect than that of conventional diesel fuel, this is due to the presence of methyl esters, which are the primary components in biodiesel fuel and act as low volatility cleaning agents. [153]

However, the high solvency power of biodiesel can also be detrimental for the fuel injection system and engines as it can also degrade rubber tubing or other susceptible parts of the engine system resulting in subsequent leakages and increased amount of particulates. For this reason, FAME is often blended with diesel at low percentages typically less than 20% (known as B20, *i.e.* 20% biodiesel and 80% diesel fuel). [154]

3.1.2 G-Diesel fuel

Recently, a ULSD fuel alternative was introduced into the US, which was claimed as a breakthrough in diesel fuel. The fuel named G-Diesel, after its creator Dr. Rudolf Gunnerman (Advanced Refining Concepts, LLC) has high claims of increased combustion characteristics including a cleaner burn with a reduction in emissions compared to conventional diesel fuel. Other claimed benefits include improved engine power, better performance, reduced maintenance costs and improved car mileage. [155]

G-diesel is produced by combining conventional diesel fuel with natural gas, in a blend ratio of 2:1 blended using proprietary catalysts. Standard ULSD is pressurised in a steel tank and heated to around 120 °C; natural gas is then piped into the diesel tank. The resulting mixture is blended and passed through a wheel-shaped filter wrapped with four different metal catalysts (cobalt *etc.*). The catalysts are claimed to cause the gas molecules to chemically bind with the liquid, facilitating the attachment of hydrogen in natural gas to the carbon chain in diesel molecules. The results have claimed to have an increase in low mass carbon chains and vast improvements in combustion characteristics, fuel economy and a reduction in emissions. [155-156]

3.1.3 Data reduction model

Due to the large amount of information gained from a single chromatogram of diesel fuel by GC-MS and high complexity of diesel fuel itself, the development and use of a data reduction model was explored. Diesel fuel contains approximately 75% saturated hydrocarbons including paraffins and cycloparaffins and around 25% aromatic hydrocarbons including naphthalenes. Diesel fuel is a highly complex mixture of a range of compounds including carbon chains C9-C26 compared to those of petrol fuel C4-C12.

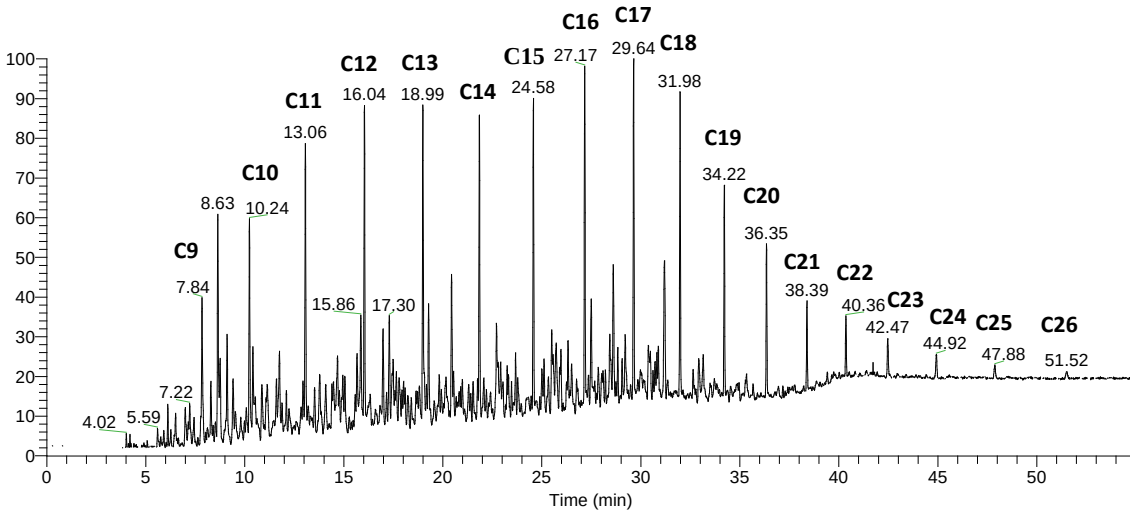

Figure 3-1. Chromatogram obtained of diesel fuel, showing some of the typical components present by GC-MS.

Figure 3-1 shows the chromatogram obtained for diesel fuel and displays the complexity of data and the vast number of components typically present in diesel fuel. To examine components present in this chromatogram and identify each peak is difficult and time-consuming due to the large amount of data present.

A data reduction model is needed to simplify this process. A method has been presented in this chapter, which involves selecting a range of the most intense aliphatic and aromatic peaks and work out the total peak area ratios from this. The resulting data should act as a fair representation of the whole sample set, without the need for full identification thereby reducing the time needed.

The development of this data reduction model is presented, including the number of data points needed for successful and accurate analysis of the whole dataset. Then a range of samples were investigated including a comparison of G-diesel fuel samples with ultra-low

sulfur diesel (ULSD) fuel and fuel samples with a range of filter and injector deposits in order to investigate the aliphatic to aromatic content which can impact on the solvency of the fuel.

3.2 Experimental

Fuel solvency effects were investigated for G-Diesel fuel and ULSD fuel samples, of which some exhibited injector and filter deposit formation tendencies by GC-MS (as explained in Chapter 2- Experimental).

Component groups such as alkanes and aromatics were identified from the GC-MS dataset and the GC-MS data was obtained by taking the area under individual peaks as a percentage of the total area.

3.2.1 Data reduction model development

Data reduction models were developed to investigate the components present in the fuels and account for differences between different fuel samples. Different models were explored by using the 5, 10 or 20 most intense peaks (named 5 peaks data reduction model, 10 peaks data reduction model and 20 peaks data reduction model).

For the different models, the total ion current (TICC) peak area ratios of 5, 10 or 20 aliphatic and aromatic peaks were obtained and tabulated in Microsoft Excel™. The data reduction model will be employed to investigate the aliphatic and aromatic content of the fuels and probe for any differences within them, as this should give an indication of the solvency of the fuel.

The G-Diesel fuel sample set will then be compared with conventional ULSD fuel sample set. Initially, the fuel samples were examined for their aliphatic to aromatic content ratios; this was calculated using the TICC obtained from GC-MS. Fragment ions at *m/z* 29 $(C_2H_5)^+$, 43 $(C_3H_7)^+$ and 57 $(C_4H_9)^+$ were chosen for aliphatic compounds and base peak ions at m/z 77 $(C_6H_5)^+$ and 91 $(C_7H_7)^+$ were chosen for aromatic compounds, as these are the most common fragments for the two different compounds. Low mass aliphatic ions were identified as *m/z* 29, 43 and 57 and high mass aliphatic ions were identified as *m/z* 71, 85 and 99.

Qualitative analysis was then undertaken using the Xcalibur™ software (Version 2.0.5), the GC-MS data points were normalised and the area under the individual peaks was calculated as a percentage of the total area (as shown as Equation 3-1, Area A and B %)

and subsequently the peak area ratio % (PAR) was calculated (as shown as Equation 3-1, peak area ratio %).

$$Area\ A\ \% = \frac{Area\ A}{Total\ Area}$$

$$Area\ B\ \% = \frac{Area\ B}{Total\ Area}$$

$$Peak\ area\ ratio\ \% = \frac{Area\ A\ \%}{Area\ B\ \%}$$

Equation 3-1. Area A and B % equations and Peak area ratio % equation.

3.2.2 Samples

The following fuel samples of G-Diesel and ULSD samples were investigated using the data reduction model and for comprehensive analysis.

3.2.2.1 G-Diesel fuel

The following G-Diesel fuel samples were investigated, with the sample name given below.

Table 3-1. List of G-Diesel fuel samples.

Fuel sample	Sample name
Sample # 52	G-Diesel feedstock 1 # 1
Sample # 53	G-Diesel feedstock 1 # 1
Sample # 54	G-Diesel feedstock 1 # 2
Sample # 55	G-Diesel ULSD # 2 of 2
Sample # 56	G-Diesel ULSD # 2 of 1
Sample # 57	G-Diesel feedstock # 2 #2
Sample # 58	G-Diesel 1 of 2 ULSD
Sample # 59	G-Diesel 2 of 1 ULSD

3.2.2.2 ULSD fuel samples

The following ULSD fuel samples were investigated, the sample name and deposit formation tendency of the sample is shown including filter and injector deposits. These deposits are determined by in-vehicle field testin and engine tests.

Table 3-2. List of ULSD fuel samples, where cert= certified, CARB= California Air Resources Board.

Fuel sample	Sample name	Deposit formation tendencies
ULSD # 1	ULSD standard blend US	None
ULSD # 2	ULSD Cert. blend US	Filter deposit
ULSD # 3	B20/ULSD blend US	Filter deposit
ULSD # 4	East Coast ULSD US	Filter deposit
ULSD # 5	ULSD CARB Calif US	None
ULSD # 6	ULSD CARB Calif US	None
ULSD # 10	ULSD US	Injector deposit
ULSD # 20	Off road ULSD US	Injector deposit
ULSD # 21	ULSD US	Injector deposit
ULSD # 22	ULSD ref fuel Europe	None
ULSD # 23	Off road High S US	None
ULSD # 24	B20 ULSD same as # 25 US	None
ULSD # 25	#24 truck blackened US	Both injector and filter deposits
ULSD # 26	Engine stand diesel	Injector deposit
ULSD # 27	Rail diesel UK exstock tank	Filter deposit
ULSD # 28	European diesel ex injector	Injector deposit
ULSD # 29	European diesel ex injector	Injector deposit
ULSD # 30	Engine stand diesel US	None
ULSD # 31	Engine stand diesel US	Injector deposit
ULSD # 32	Supermarket diesel France	Filter deposit
ULSD # 33	Supermarket diesel France	None
ULSD # 34	Diesel Germany	Filter deposit
ULSD # 35	Off road M diesel US	Both injector and filter deposits
ULSD # 36	Off road M diesel US	None
ULSD # 37	Off road M diesel US	None

3.3 Results and Discussion

3.3.1 Comparison of 5/10/20 peak data reduction model

Three different data reduction models were investigated namely the 5, 10 and 20 peak data reduction model, which take into account 5, 10 or 20 of the most intense aliphatic and aromatic peaks respectively.

Figure 3-2 shows a bar chart to compare the three different data reduction models using the 5, 10 and 20 peak model for aliphatic peaks. The 5 peak model which considers the 5 most intense aliphatic peaks, does not appear to give a clear representation of the data with fuel sample # 52 in particular appearing to show a higher peak area ratio (PAR) % of total aliphatic and aromatic content over 90% compared to the comprehensive analysis at around 87%, whereas the other two models appeared to be more accurate.

In fuel sample # 53 and 54, the 5 peak model is the only model that appears to under estimate the value this is due to the limited number of data points in this 5 peak model. The 5 peak data reduction model does not represent an accurate representation of the whole dataset due to limited data points and a larger spread of data is needed. The 10 peak and 20 peak model appear to give accurate results compared to comprehensive analysis. The 10 peak data reduction model was chosen due to its ease of use and effectiveness, this method gave a 10 fold reduction in analysis times compared to comprehensive analysis and a reduction in analysis time compared to the 20 peak data reduction model.

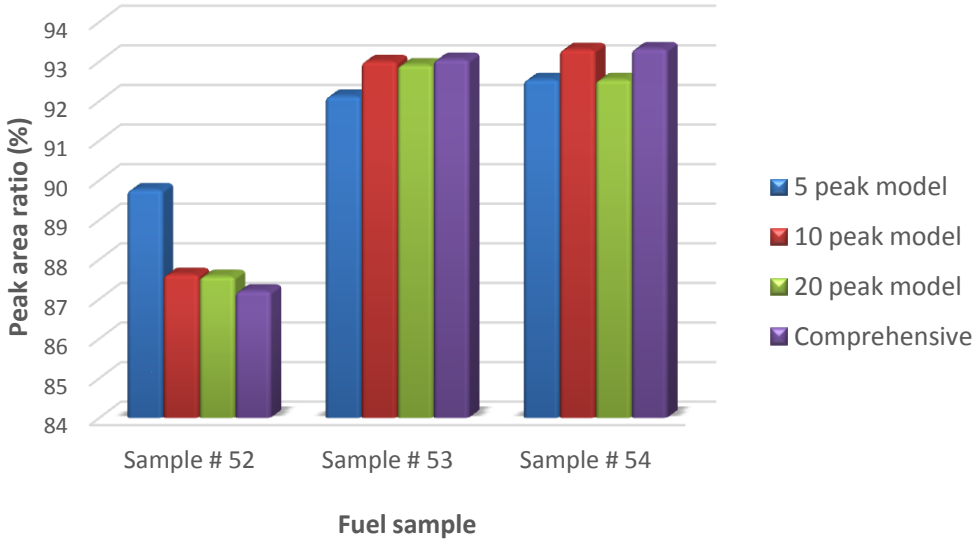

Figure 3-2. Bar chart to show a comparison of the 5 (blue), 10 (red) and 20 (green) peak data reduction model compared to comprehensive analysis (purple) of fuel samples.

3.3.2 G-Diesel fuel

A range of G-diesel fuel samples were investigated by GC-MS and the following chromatograms in Figure 3-3 show G-Diesel fuel samples # 52-59. The data reduction model (10 peak model) was then chosen to explore the aliphatic and aromatic content of the samples with comparisons to comprehensive analysis of the full data set.

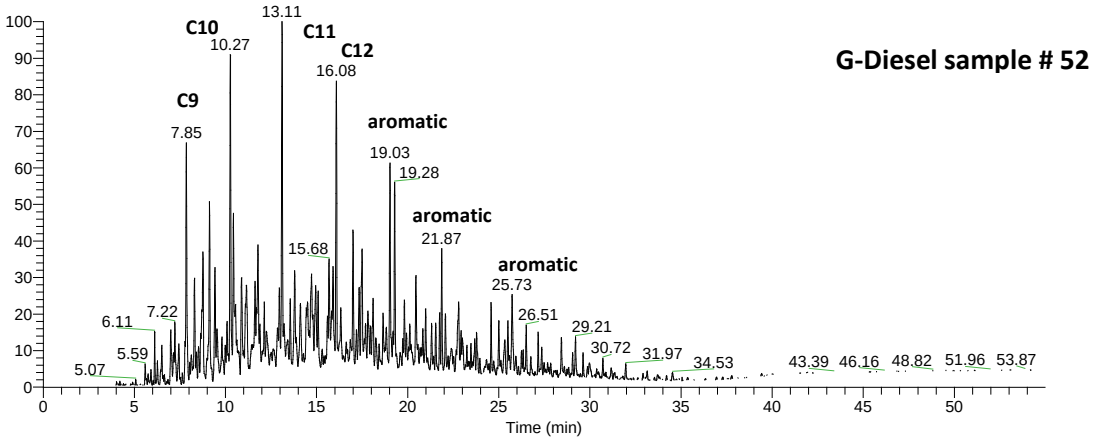
G-Diesel sample # 52
C9
C10
C11
C12
aromatic
aromatic
aromatic
7.85
10.27
13.11
16.08
19.03
19.28
21.87
25.73
26.51
29.21
30.72
31.97
34.53
43.39
46.16
48.82
51.96
53.87
15.68
6.11
7.22
5.59
5.07
Time (min)

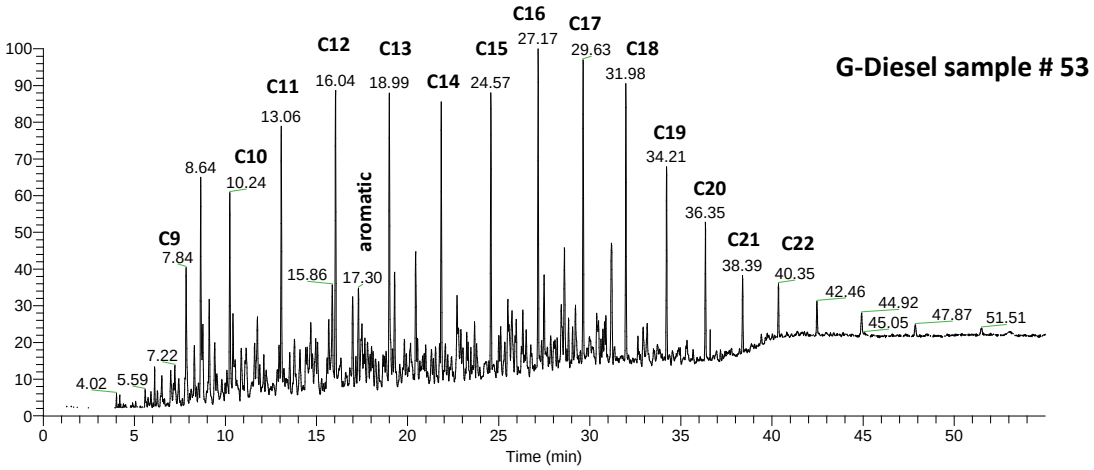
G-Diesel sample # 53
C9
C10
C11
C12
C13
C14
C15
C16
C17
C18
C19
C20
C21
C22
aromatic
7.84
8.64
10.24
13.06
16.04
18.99
24.57
27.17
29.63
31.98
34.21
36.35
38.39
40.35
42.46
44.92
45.05
47.87
51.51
15.86
17.30
7.22
4.02
5.59
Time (min)

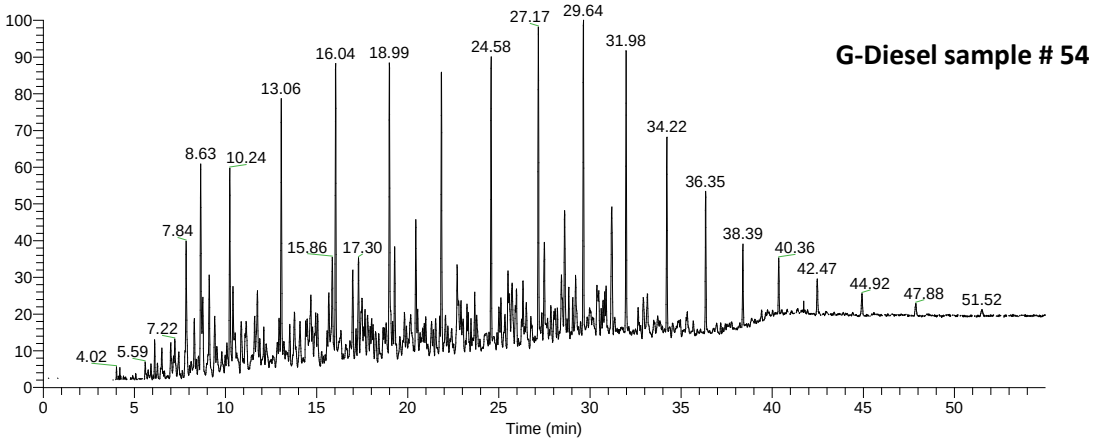
G-Diesel sample # 54
7.84
8.63
10.24
13.06
16.04
18.99
24.58
27.17
29.64
31.98
34.22
36.35
38.39
40.36
42.47
44.92
47.88
51.52
15.86
17.30
7.22
4.02
5.59
Time (min)

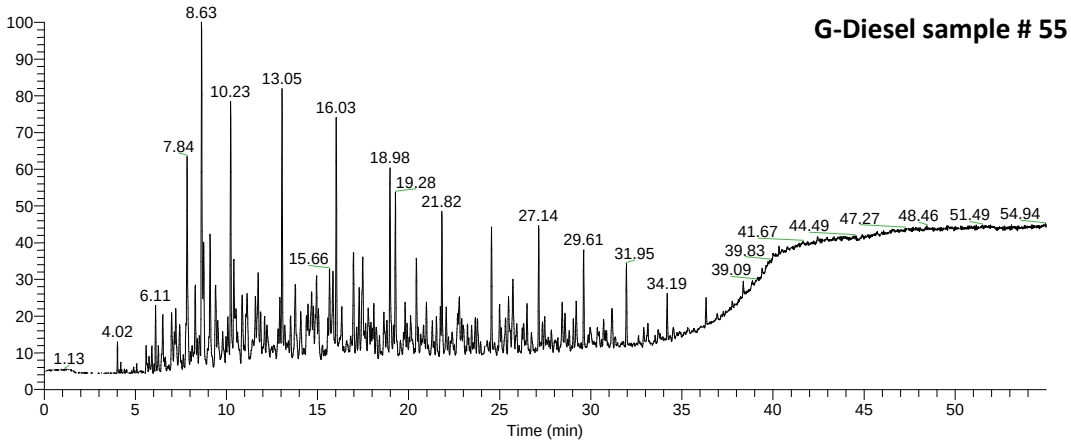
G-Diesel sample # 55
8.63
10.23
13.05
16.03
7.84
18.98
19.28
21.82
27.14
29.61
31.95
34.19
15.66
6.11
4.02
1.13
41.67
44.49
47.27
48.46
51.49
54.94
39.83
39.09
Time (min)

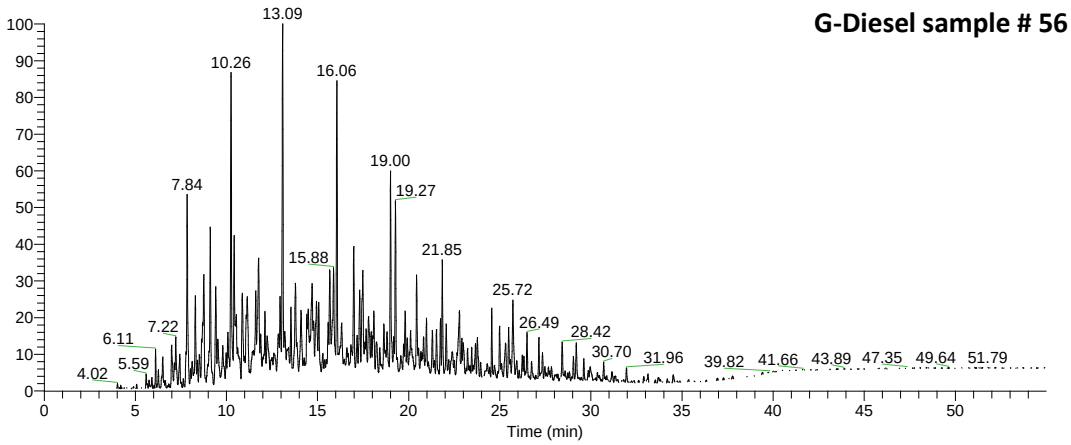
G-Diesel sample # 56
13.09
10.26
16.06
19.00
19.27
7.84
15.88
21.85
25.72
26.49
28.42
6.11
7.22
5.59
4.02
30.70
31.96
39.82
41.66
43.89
47.35
49.64
51.79
Time (min)

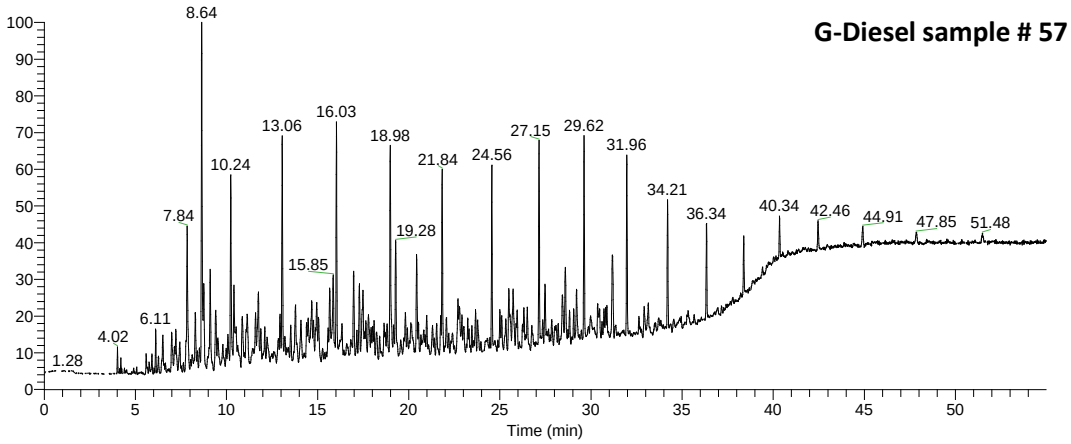
G-Diesel sample # 57
8.64
13.06
16.03
18.98
27.15
29.62
31.96
10.24
21.84
24.56
34.21
36.34
40.34
42.46
44.91
47.85
51.48
7.84
19.28
15.85
6.11
4.02
1.28
Time (min)

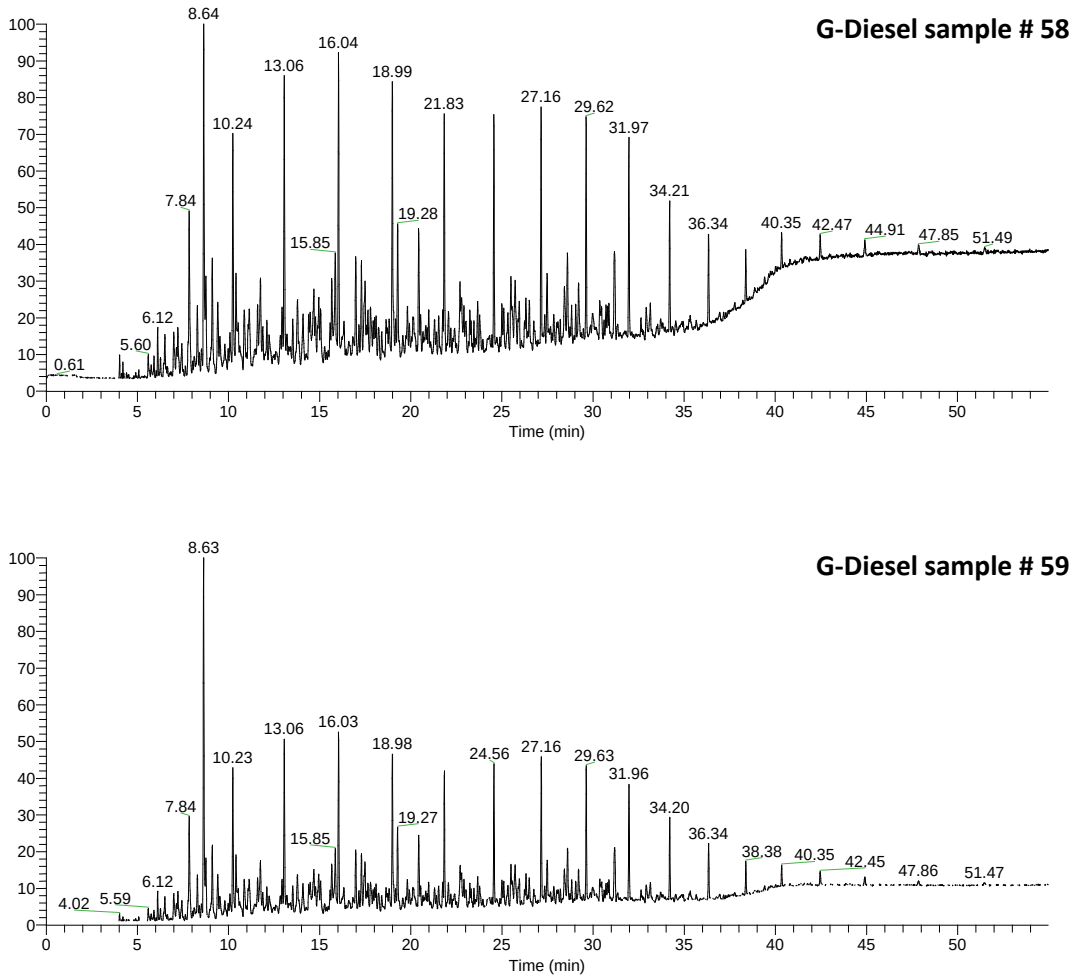

Figure 3-3. Chromatograms of G-Diesel samples # 52- 59 obtained by GC-MS analysis.

From the chromatograms shown in Figure 3-3, it is apparent that each G-diesel sample seems to have a differing range of components present. The higher intensity peaks are aliphatic compounds, a homologous series, and the smaller peaks are mainly the aromatic compounds present in the samples.

Most samples appear to have a greater amount of aliphatic content with varying quantities. For example it is evident in the chromatograms, that G-Diesel sample # 53, 54, 57, 58 and 59 contain greater amount of aliphatic compounds due to the homologous series of higher intensity peaks that is observed. G-Diesel sample # 52, 55 and 56 contain smaller peaks which are not a homologous series and are aromatic compounds. However, both samples contain a greater amount of aliphatic content.

For G-Diesel sample # 52 there are two peaks of interest at retention times of 19.03 and 19.28 minutes, the mass spectra of these peaks are shown in Figure 3-4 A and B respectively, these two peaks are also observed in the other G-Diesel samples also.

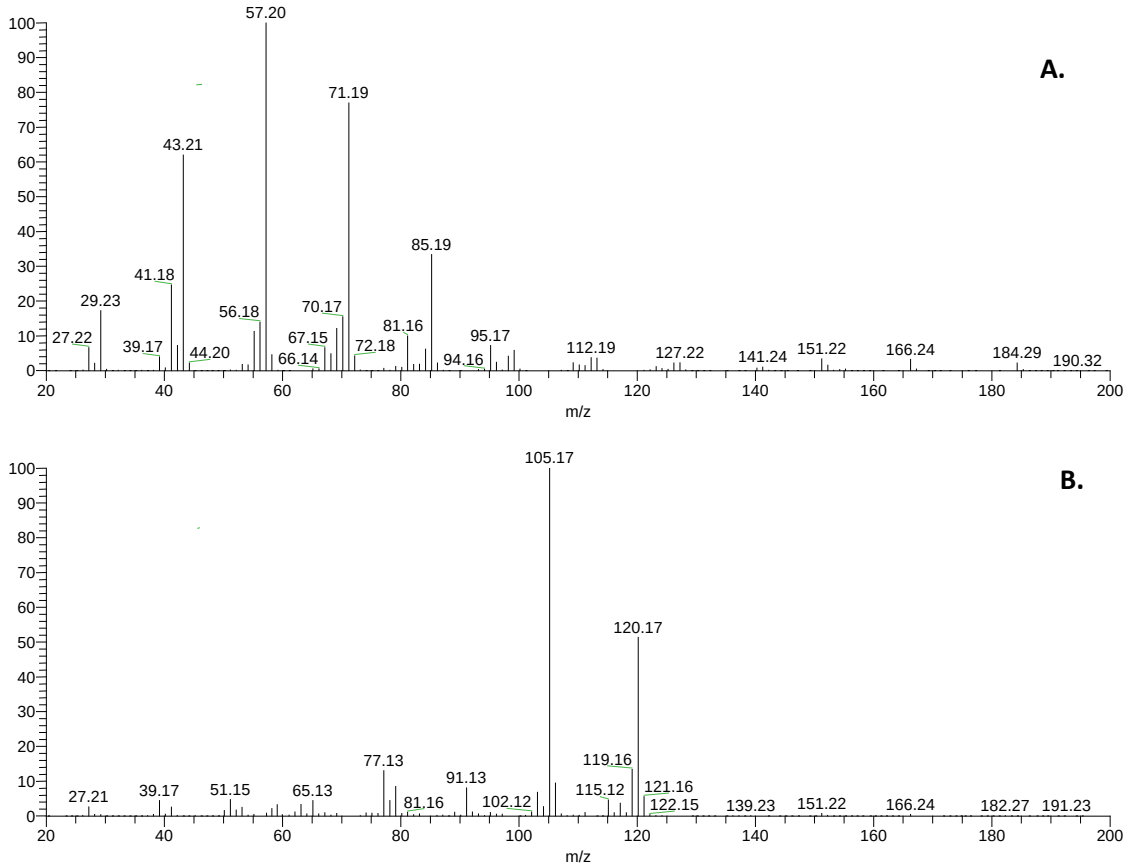

Figure 3-4. A. Mass spectra of G-Diesel sample # 52 of peak at retention time 19.03 minutes and B. peak at retention time 19.28 minutes.

The mass spectra shown in Figure 3-4A, show the peak which is confirmed through the NIST library database as tetradecane ($C_{14}H_{30}$) with a similarity index (SI) as 950 and Figure 3-4B the peak at 19.28 minutes is benzene,1,3,5-trimethyl (C_9H_{12}) with a SI of 932.

Figure 3-5A shows comprehensive analysis of G-Diesel samples # 52- 59 and B shows the 10 peak data reduction model analysis of the samples.

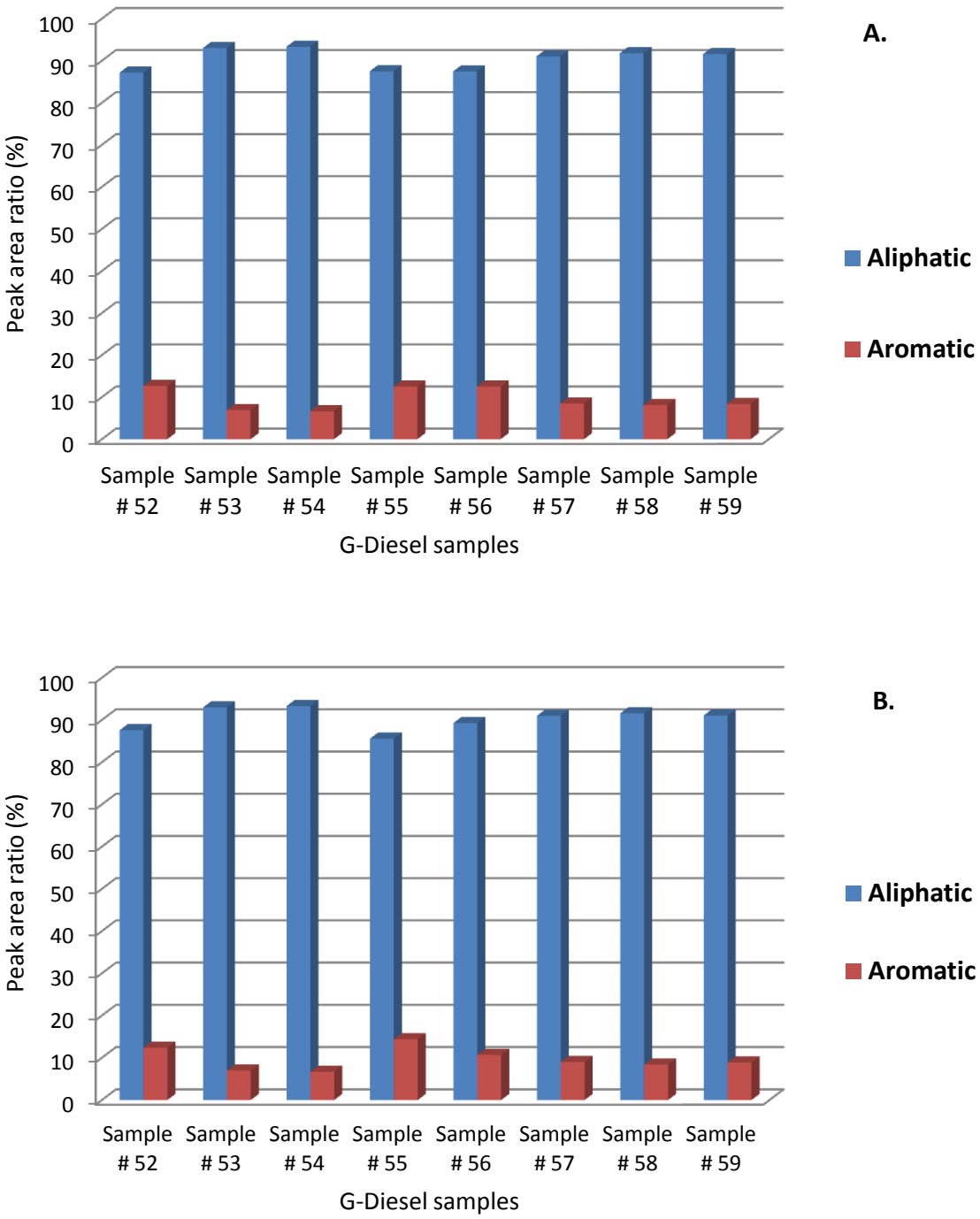

Figure 3-5. A. Comprehensive analysis of G-Diesel samples # 52- 59 showing the aliphatic (blue) and aromatic (red) content, and B, using the 10 peak data reduction model.

Table 3-3. Table to show comprehensive analysis vs. 10 peak data reduction model of aliphatic and aromatic content shown as peak area ratios (PAR).

	Comprehensive analysis		10 Peak data reduction model	
G-Diesel fuel	Aliphatic content (PAR)	Aromatic content (PAR)	Aliphatic content (PAR)	Aromatic content (PAR)
Sample # 52	87.2	12.7	87.6	12.4
Sample # 53	93.1	7.0	93.0	7.0
Sample # 54	93.3	6.7	93.3	6.7
Sample # 55	87.5	12.5	85.6	14.4
Sample # 56	87.5	12.5	89.3	10.7
Sample # 57	91.1	8.5	91.0	9.0
Sample # 58	91.8	8.2	91.6	8.4
Sample # 59	91.6	8.4	91.1	8.9

Figure 3-5 and Table 3-3, show a bar chart and Table to compare the different G-Diesel samples (# 52-59) showing the aliphatic content (shown in blue) and aromatic content (shown in red) as expressed as peak area ratio (PAR) compared to comprehensive analysis.

The graph shown in Figure 3-5, using the 10 peaks hypothesis data reduction model seems to correlate with the data obtained from GC-MS experiments as shown in Figure 3-3 in terms of aliphatic and aromatic content. The data from the 10 peak model shows comparable results to comprehensive analysis of the full data set, with a low relative standard deviation of 0.5%. This supports the effectiveness of the 10 peak data reduction model.

The inventors of G-diesel claim that the fuel contains a greater proportion of hydrocarbons with lower molecular weight and fewer components with higher molecular weight, compared to conventional diesel fuel. The increased amount of low mass aliphatic components in G-diesel has been linked to increased efficiency and reduction in higher mass components which are more likely to form deposits and produce soot.

This statement was investigated using the 10 peaks hypothesis. Peak area ratios of aliphatic compounds from C8-C21 were identified using total ion current chromatograms (TICC) and divided into two sub-groups of low mass aliphatic components (C8-C14) and high mass aliphatic components (C15-C21). The resulting peak area ratios are shown in Figure 3-6.

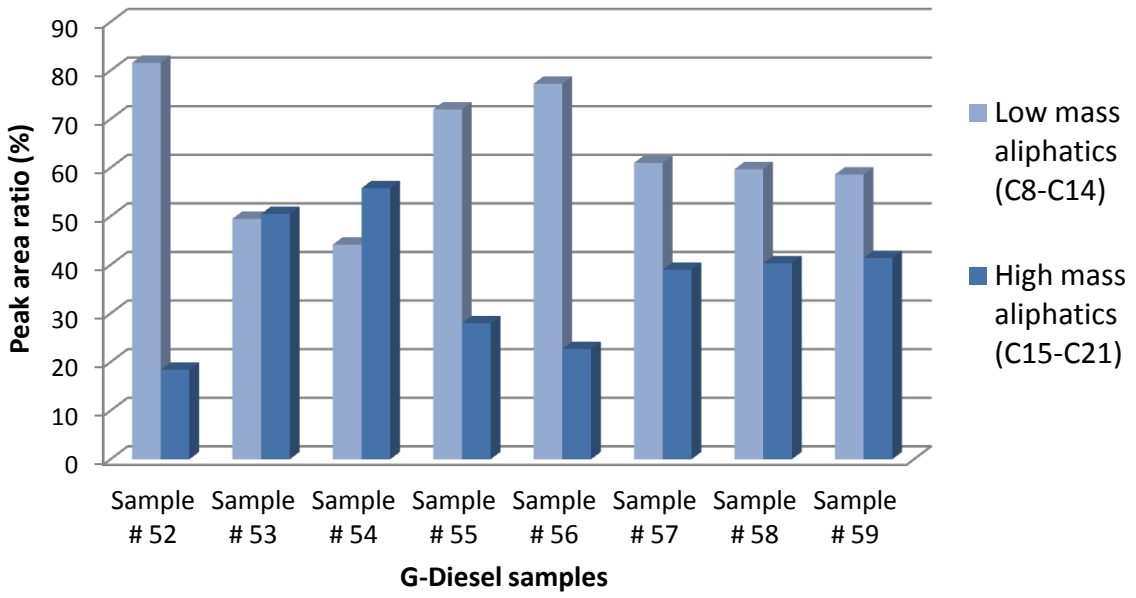

Figure 3-6. A graph to show low mass (C8-C14 light blue) and high mass aliphatic content (C15-C21 dark blue) of the G-diesel samples.

Figure 3-6 shows that the percentage of low mass (as shown in light blue) and high mass aliphatic content (as shown in dark blue) of G-Diesel samples is quite varied, G-Diesel samples # 53 and # 54 appear to have a similar composition of aliphatic, with more high mass aliphatic compared to low mass aliphatics, whereas samples # 52, 55-59 have a greater amount of low mass aliphatics which relates to what the inventors of G-Diesel claim to have.

G-Diesel samples # 52, 55 and 56 have the highest content of low mass aliphatics (over 70%), whereas # 57, 58 and 59 have less than 60% low mass aliphatic content. The results are varied and do not necessarily show that all G-Diesel samples have high content of low mass aliphatics. Therefore, the data does not support the claim of G-Diesel having reduced amounts of high mass aliphatic content.

3.3.3 Ultra-low sulfur diesel (ULSD) fuel

The 10 peaks data reduction model was also used to analyse all of the ULSD samples # 1-6, 10, 20-37. The results are shown in Figure 3-7, where the aliphatic and aromatic content were compared.

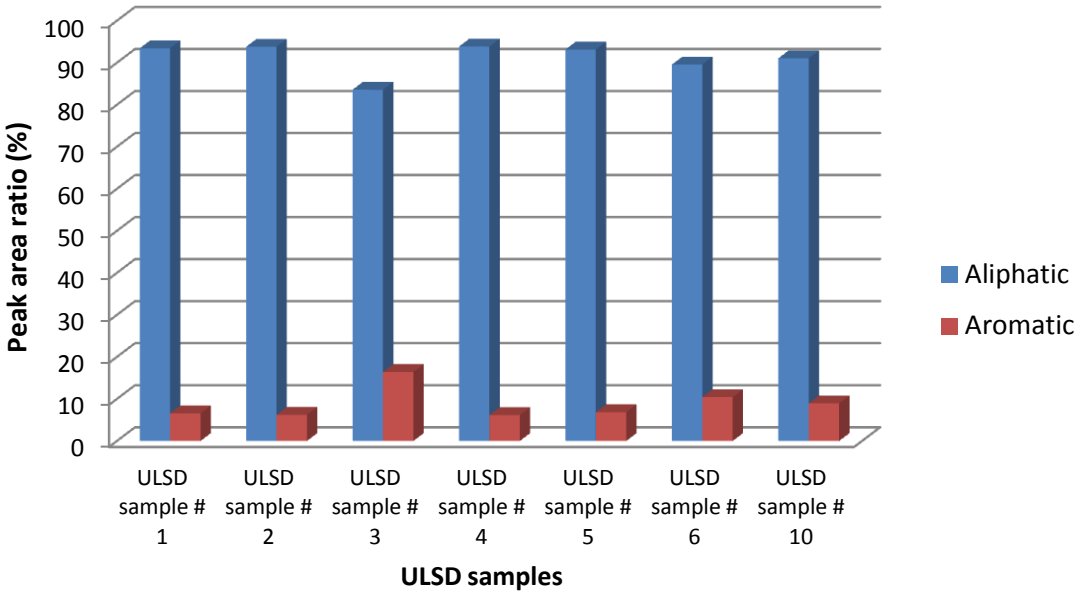

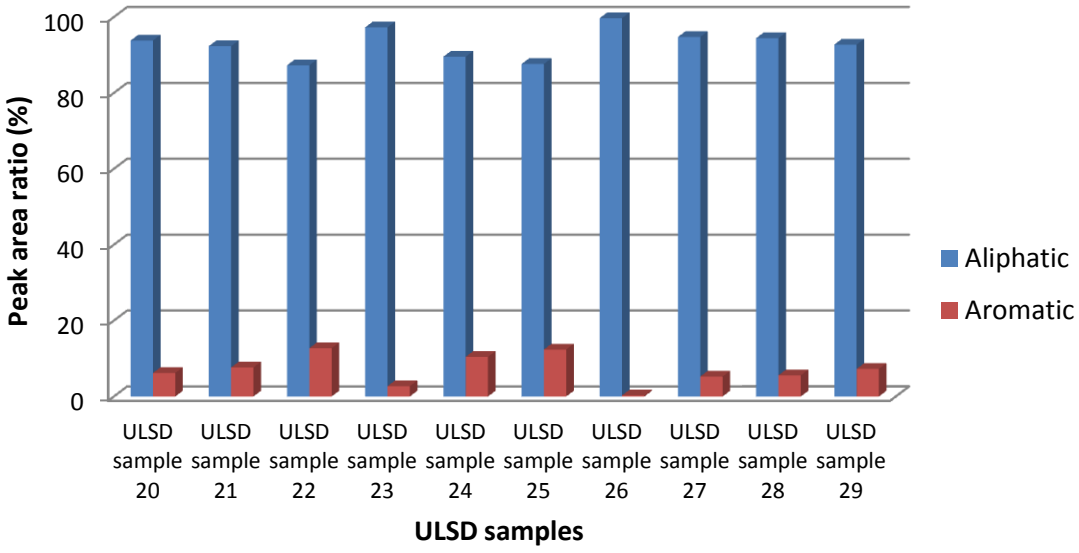

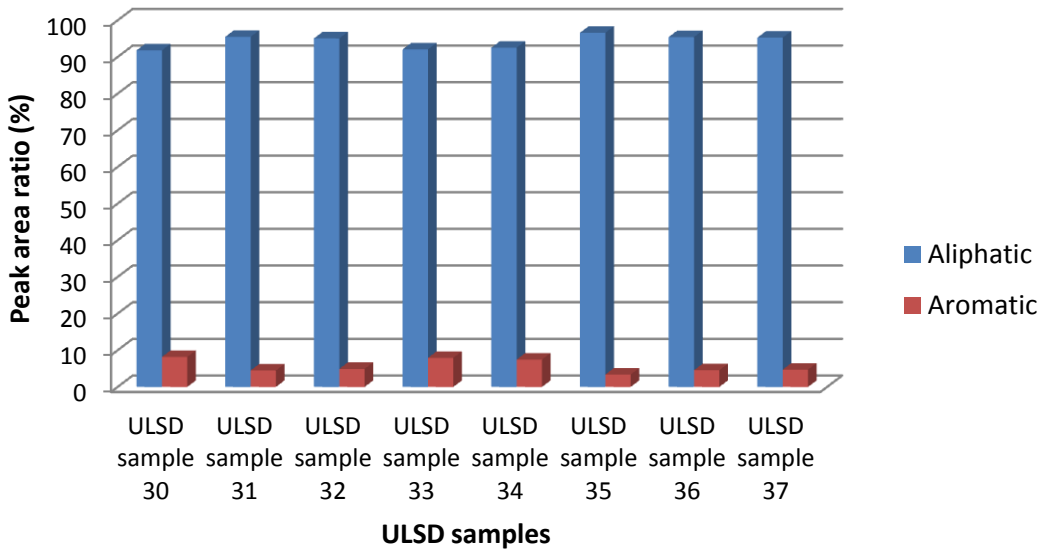

Figure 3-7. Graphs to show the aliphatic (blue) and aromatic (red) content of ULSD samples # 1-37.

Figure 3-7 shows that the ULSD sample set # 1-37 all have a low content of aromatic compounds. From the results it seems that the biodiesel samples # 3, # 24 and # 25have higher aromatic content compared to the ULSD samples, with ULSD # 3 (filter deposit tendencies) having over 20% aromatic content.

Table 3-4. Table to show injector and filter deposit samples with the peak area ratio % of aliphatic content.

Injector deposit samples	Aliphatic content (%)	Filter deposit samples	Aliphatic content (%)
ULSD # 10	91.1	**ULSD # 2**	93.7
ULSD # 20	93.8	**ULSD # 3**	83.6
ULSD # 21	92.3	**ULSD # 4**	93.9
ULSD # 25	87.6	**ULSD # 25**	87.6
ULSD # 26	99.7	**ULSD # 27**	94.7
ULSD # 28	94.4	**ULSD # 32**	95.1
ULSD # 29	92.7	**ULSD # 34**	92.5
ULSD # 31	95.5	**ULSD # 35**	96.6
ULSD # 35	96.6		

Table 3-4 shows a comparison of samples which have exhibited injector and filter deposits with the aliphatic content. This data however cannot account for any differences of the fuels that lead to filter and injector deposits, seeing as the aromatic content is not significantly higher in injector or filter deposit samples. The aliphatic content will be investigated further using the 10 peaks hypothesis for injector and filter deposit samples and low/high mass aliphatic content.

A comparison of samples that showed deposit formation (injector and filters) and ones that experienced no deposit formation are shown in Figure 3-8. An average was taken from 15 ULSD fuel samples, and the results show the deposit formation samples have slightly higher aliphatic content. This shows that the samples with no deposit formation have greater amounts of aromatic content, but both are below 10 %. This then can be an indicator for a possible problem, if a sample has greater aliphatic content. Both values however are statistically very close with 0.7 % difference, the scale of the graph goes from 92- 93.4% PAR aliphatic content, and therefore this could suggest that the deposit formation issue is more than just fuel solvency but a combination of different factors.

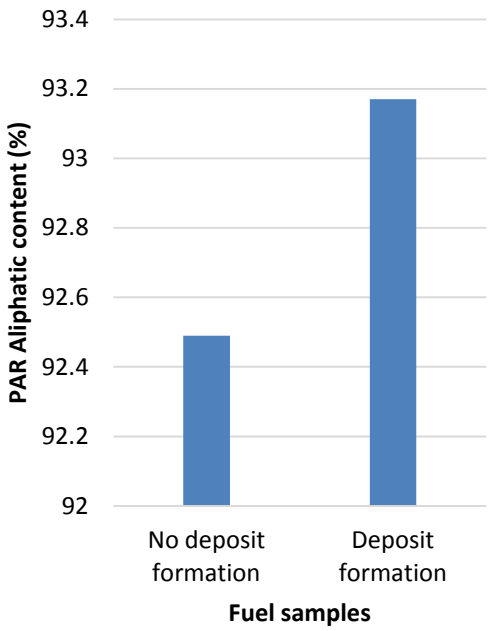

Figure 3-8. Graph to show peak area ratio (PAR %) of aliphatic content for samples with no deposit formation and deposit formation.

ULSD samples were also investigated by the 10 peaks hypothesis to examine the low mass and high mass aliphatic components present in the sample as shown below in Figure 3-9. The samples were then grouped into two separate graphs of samples with known tendencies for injector (B) and filter (C) deposits.

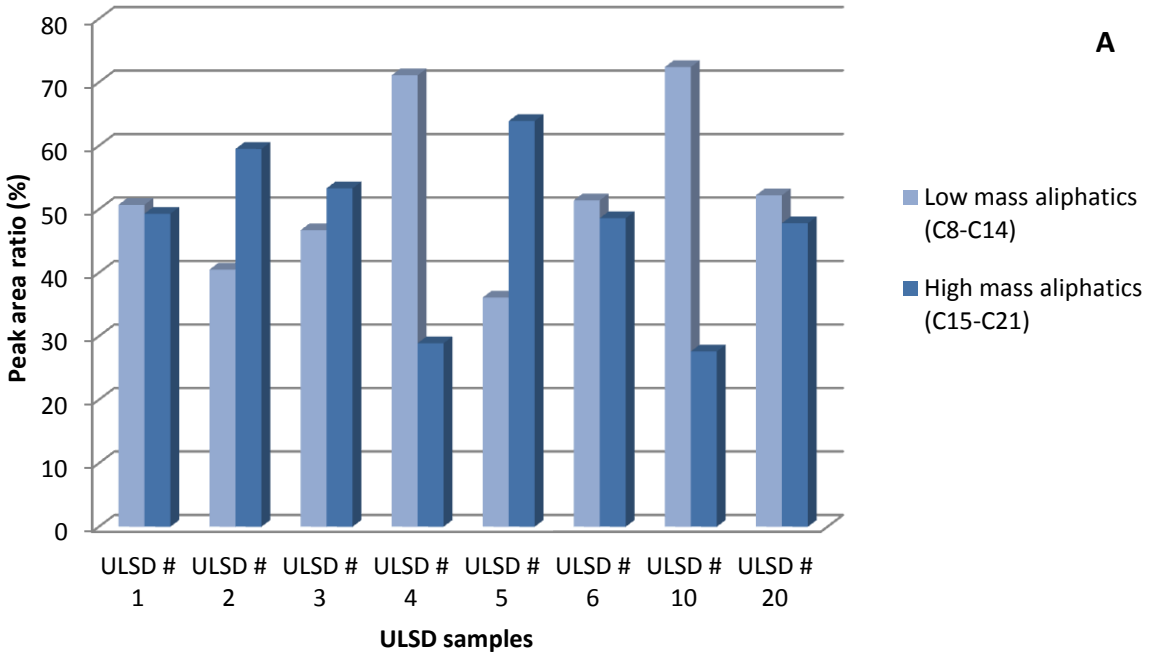

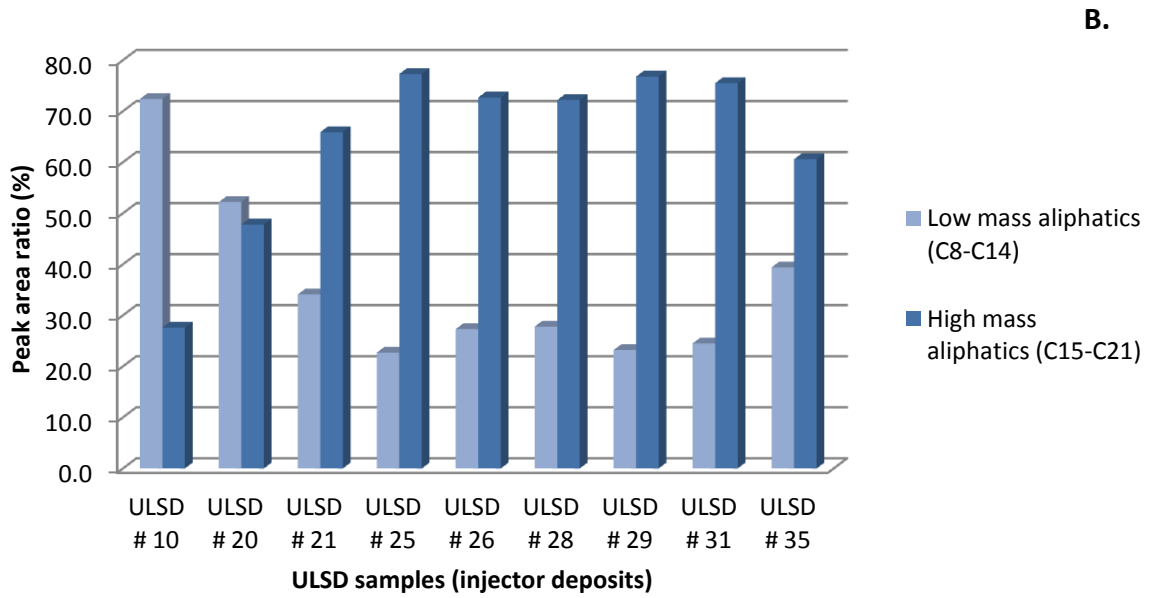

C.

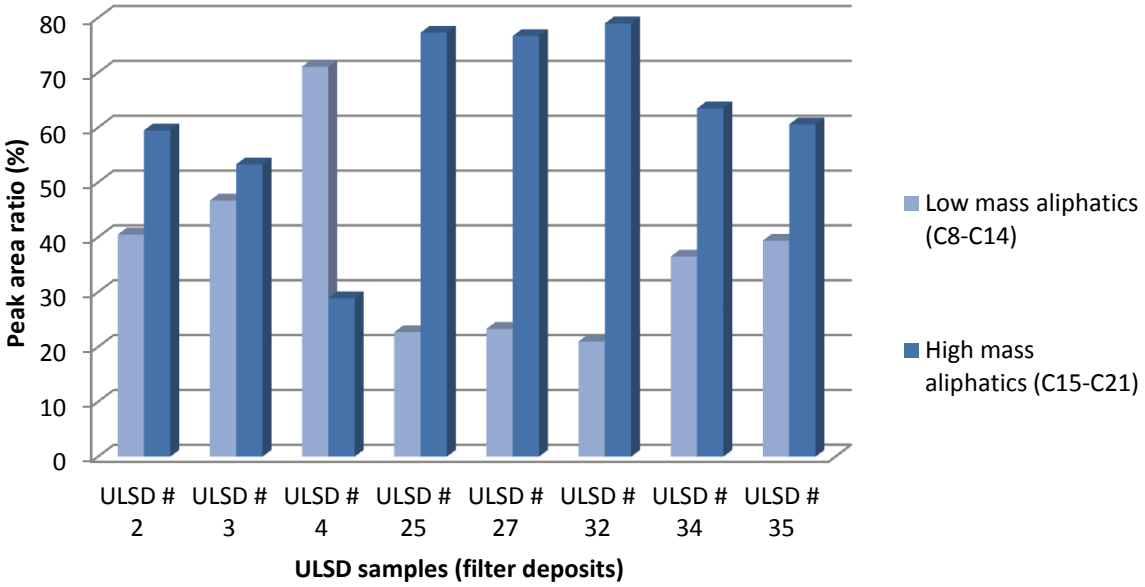

Figure 3-9. A. Graph to show low and high mass aliphatic content of the ULSD samples # 1-6, 10 and 20 using the 10 peak data reduction model, B. Graph shows samples with known injector deposits, C. Graph shows samples with known filter deposits.

Figure 3-9 shows the low and high mass aliphatic content of the ULSD samples. For injector deposits, ULSD samples # 21, 25, 26, 28, 29, 31 and 35 appear to have a much greater content of high mass aliphatics, with an average of around 62%. For filter deposit samples, they also appear to have a greater amount of higher mass aliphatics (C15-C21) of around 60%.

For filter and injector deposit samples, the general trend shows increased high mass aliphatics, these higher mass aliphatics (C15-C21) can react to form larger compounds. Studies have shown that diesel fuels instability is instigated by oxidation reactions with the presence of highly reactive long-chain paraffins and dissolved oxygen in the fuel. [68, 157]

Oxidation reactions are of particular concern at high temperatures typical of the diesel engine, oxidation can lead to undesirable thickening of the base oil, formation of insoluble deposits and the creation of corrosive acidic compounds. [158]

Auto-oxidation refers to the oxidation that occurs in open air in the presence of oxygen. Auto-oxidation is a free radical chain process, which is divided into three stages including chain initiation, propagation and termination as shown in Figure 3-10. [47, 159]

Initiation

$$RH + O_2 \rightarrow R\cdot + H_2O$$ **Equation 3-2**

Propagation

$$R\cdot + O_2 \rightarrow ROO\cdot$$ **Equation 3-3**

$$ROO\cdot + RH \rightarrow ROOH + R\cdot$$ **Equation 3-4**

$$ROOH \rightarrow RO\cdot + \mathrm{H0}$$ **Equation 3-5**

Termination

$$R\cdot + R\cdot \rightarrow R - R$$ **Equation 3-6**

Figure 3-10. Auto-oxidation pathway to show initiation, propagation and termination reactions.

The initiation step as shown in Figure 3-10 involves a hydrogen atom which removed from a carbon atom to produce a carbon-based free radical (R·). During the propagation stage, hydrogen peroxide decomposes through the presence of metal ions to alkoxy (RO·) and peroxy radicals. These radicals can then react with the hydrocarbon base in fuel and can form a variety of compounds including radicals, oxygen containing compounds including alcohols, aldehydes, ketones and carboxylic acids. Aldehydes and ketones are particularly reactive and can form polymers in the presence of acids such as nitric acid and sulfuric acid. Carboxylic acids can attack metals including iron, copper and lead which could be present in the engine system to form metal carboxylates which can then further increase the rate of oxidation and lead to deposit formation. [160] During the termination stage, the radicals can either self-terminate or react with oxidation inhibitors which promote decomposition of hydroperoxides. [160]

Jenson *et al*. proposed the oxidation of n-hexadecane and the intermediates formed including hydroxyl and alkylperoxy radicals which can aid in hydrogen abstraction from

the alkane chains, as shown in Figure 3-11. The role of oxygen can then be of a catalyst in facilitating low temperature aromatization of aliphatic hydrocarbons. [161-165]

Initiation

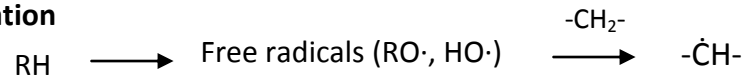

Peroxy Radical Formation

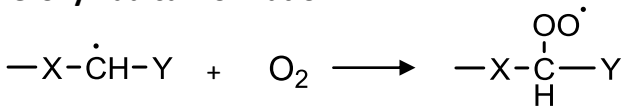

Intermolecular Hydrogen Abstraction

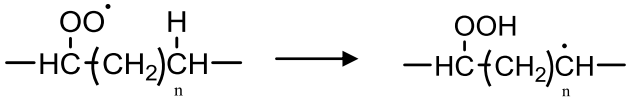

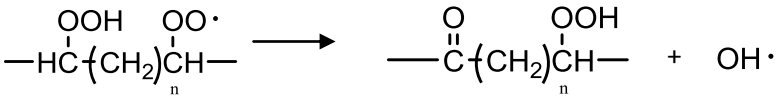

Termination and Alkoxy Radical Formation

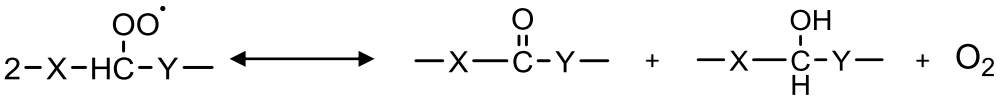

β- Scission of Alkoxy Radicals

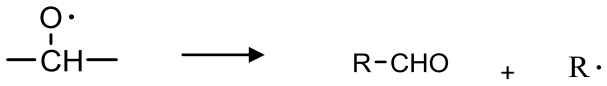

Intramolecular Alkoxy Abstraction

Figure 3-11. Schematic diagram as proposed by Jenson *et al*, adapted. [165]

3.3.4 Comparison of G-Diesel fuel and ULSD fuel

A comparison of the aliphatic and aromatic content of G-Diesel samples and ULSD samples was also investigated in order to account for any differences in the fuels, and for any claims in the benefits of G-Diesel fuel.

Figure 3-12 shows a comparison of G-Diesel and ULSD fuel samples, the results show no significant difference both sample sets. Roughly both sample sets show around 89-90 % aliphatic content, therefore the stated advantages of G-Diesel compared to ULSD appear to be inaccurate and no differences can be observed. G-Diesel samples have an average of 82% aliphatic whereas the ULSD samples have an average of 92% aliphatic content.

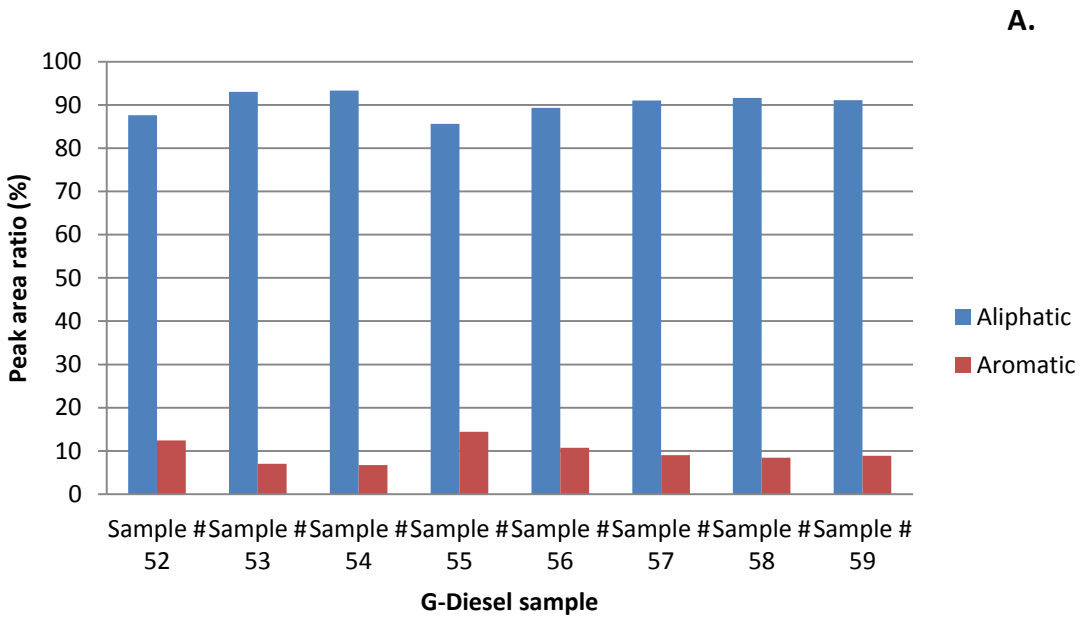

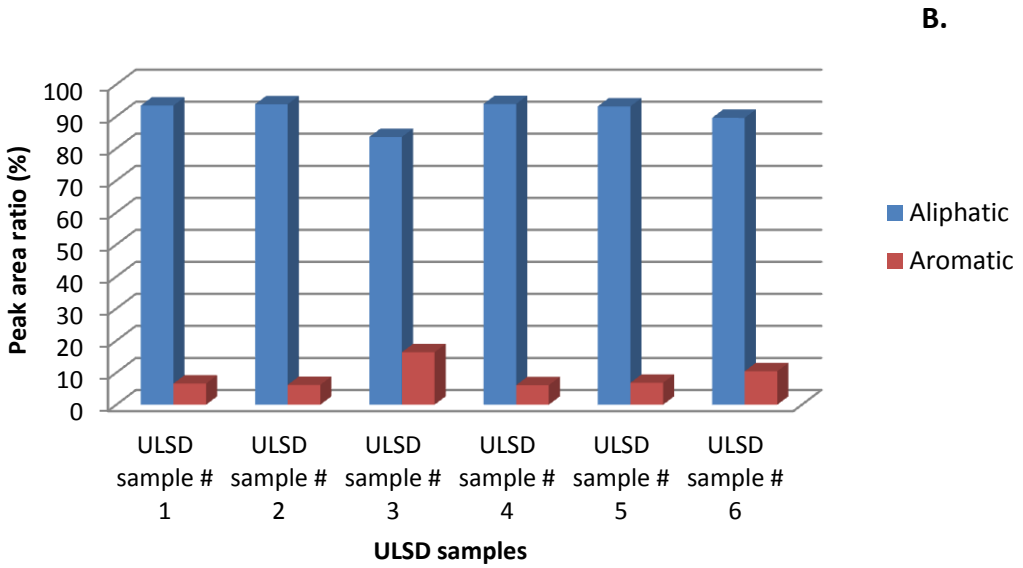

Figure 3-12. A. 10 peaks data reduction model of G-Diesel samples showing aliphatic and aromatic content, B. 10 peaks data reduction model of ULSD fuel samples.

3.3.5 Additional components present in ULSD fuel

The 10 peak data reduction model can also be used for additional components of interest other than solely aliphatic and aromatic content, by changing the base ions of interest to other components, the 10 most intense peaks were chosen for the data reduction model.

This method can probe a range of compound classes within the generic aliphatic and aromatic compounds. The compound classes that were assessed include alkanes, substituted alkanes, substituted benzenes, substituted naphthalenes, substituted alkenes and other components such as FAME (Figure 3-13).

This method can investigate components present in fuel samples and link them to deposit formation.

ULSD samples # 2, 3 and 4 exhibit filter deposit samples and an expanded graph is shown in Figure 3-14A and ULSD samples # 10 and 20 exhibit solely injector deposits as shown in Figure 3-14B.

Table 3-5. A table to represent the peak area ratio (%) of components present in ULSD samples # 1-6, 10 and 20 as seen in GC-MS data analysis by 10 peaks data reduction model. The rows highlighted in blue indicate ULSD samples which exhibit filter deposit tendencies, rows highlighted in red injector deposits and rows highlighted in green indicate ULSD samples which exhibit both injector and filter deposits.

	Peak area ratio (%) from GC-MS data analysis					
ULSD sample	**Alkane**	**Substituted alkane**	**Substituted benzene**	**Substituted naphthalene**	**Cycloalkanes**	**Other components (incl. FAME)**
ULSD # 1	64.1	29.0	0.0	6.8	0.0	0.0
ULSD # 2	91.9	0.3	0.0	7.8	0.0	0.0
ULSD # 3	30.6	3.9	0.0	0.0	0.0	65.4
ULSD # 4	62.5	29.7	1.4	4.7	0.0	1.8
ULSD # 5	92.0	8.0	0.0	0.0	0.0	0.0
ULSD # 6	60.5	35.6	0.0	3.8	0.0	0.0
ULSD # 10	52.0	13.7	2.6	5.0	4.8	21.9
ULSD # 20	65.0	15.5	3.7	4.2	0.0	11.7
ULSD # 24	39.7	8.5	0.0	0.0	0.0	51.9
ULSD # 25	33.8	19.8	0.0	0.0	0.0	46.4

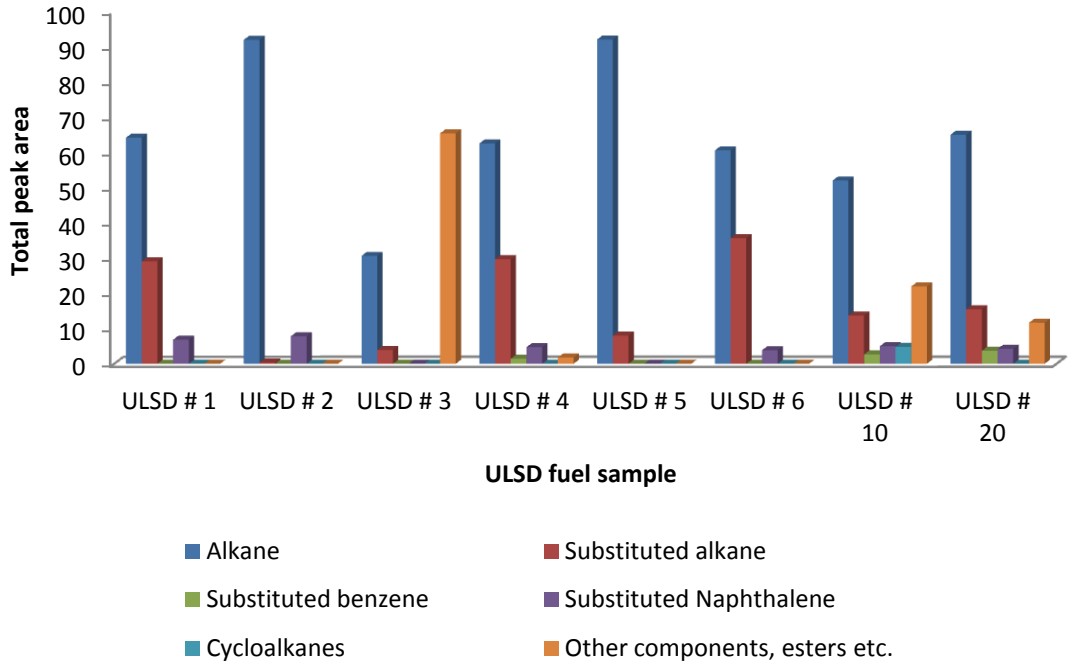

Figure 3-13. Additional components present in ULSD fuel samples # 1-6, 10 and 20.

ULSD samples # 2, # 3 and # 4 exhibit filter deposit tendencies and ULSD samples # 10 and # 20 exhibit injector deposits. From the graph of ULSD samples # 2, # 3 and # 4 shown in Figure 3-14A which exhibit filter deposit tendencies, it is apparent that alkane and naphthalene content is similar to other ULSD samples. Substituted-alkane, sub-benzene and sub-alkene content are relatively low compared to other samples.

ULSD # 3 a biodiesel sample, contains a large amount of other components that accounts for fatty acid methyl esters (FAME) compared to other compounds. However, there are no trends between filter deposit samples, as all samples have different amounts of components present in them. The FAME could also be considered as aliphatic, and would therefore make the aliphatic content from 30 % to 95 %. The aromatic content is low in these samples, showing that fuel solvency effect of the fuel is reduced.

ULSD samples # 10 and # 20 (Figure 3-14B) exhibited injector deposit tendencies; the alkane content is similar to other ULSD samples. Sub-alkane content is lower than other samples, however sub-benzene and sub-naphthalene is slightly higher in content compared to filter deposit samples but still low in relation to the components present in the fuel.

Other components are in very high concentrations for ULSD fuel sample # 10 and # 20 compared to other samples, these other components include alcohols, ethers, epoxide and ester containing groups formed from thermal oxidation reactions of components present in the sample. These groups are not normally present in diesel samples and potentially are deposit precursors. The trend between the samples is relatively similar with high levels of other compounds and substituted alkanes.

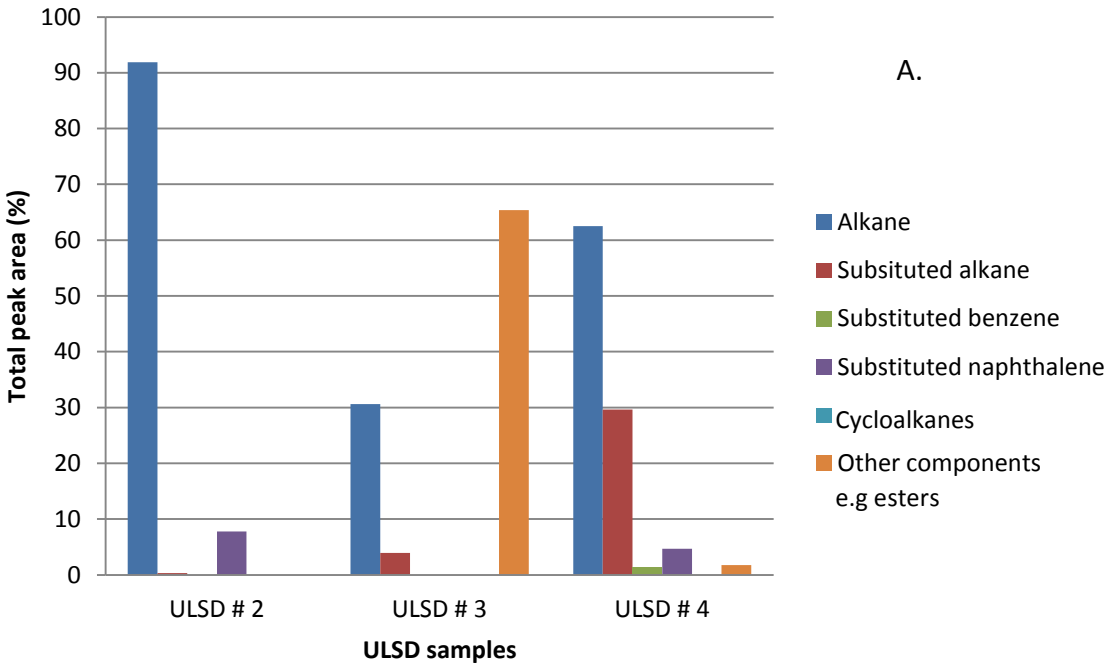

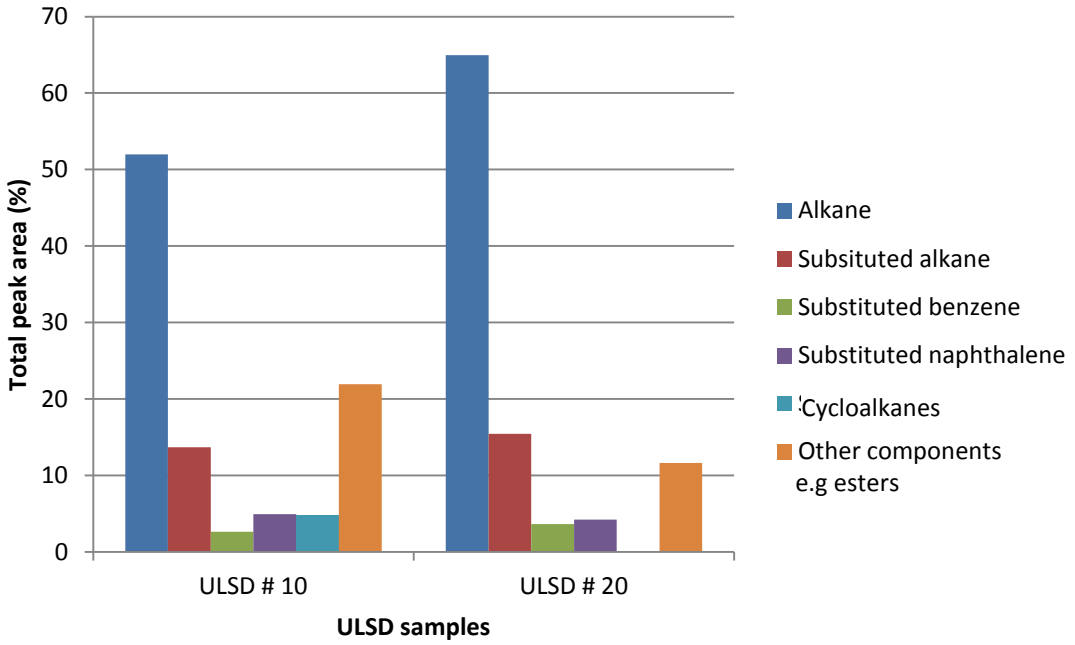

Figure 3-14. Graphs to show the peak area ratio (%) of components present in A. filter deposit samples and B. injector deposit formation samples as seen in GC-MS data analysis.

3.3.5.1 The role of FAME

Fuel solvency effects were also investigated for two biodiesel fuel samples # 24 and # 25, both of them are B20 (20% biodiesel, 80% diesel fuel) and fuel sample # 25 is the same fuel as # 24 however blackened whilst running through the engine of a vehicle. The result of this is the fuel exhibited both injector and filter deposits in contrast to sample # 24 which had no deposit formation tendencies.

Compounds were grouped together into sub-groups of alkanes, substituted alkanes and other compounds which accounts for FAME (see Figure 3-15).

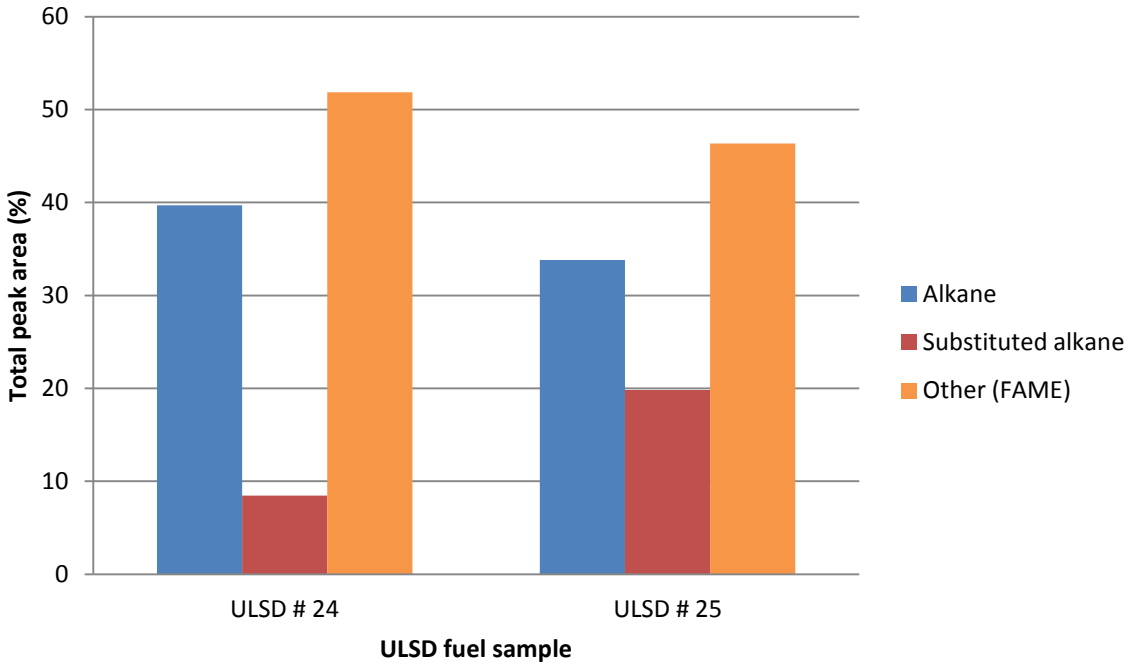

Figure 3-15. A graph to show the peak area ratio (%) of components present in ULSD samples # 24 and # 25 as seen in GC-MS data analysis.

ULSD # 24 has a higher content of alkanes present, however a lower amount of substituted alkanes. Aromatic compounds were not seen in either of these samples. The most significant difference between the samples is the content of fatty acid methyl ester (FAME) compounds. It can be seen that ULSD # 24 has a higher percentage of FAME compared to ULSD # 25 which exhibits both injector and filter deposits.

Previous literature has stated the role of FAME in deposit formation, and it could be a potential deposit precursor. [69, 166-170] However, these results do not support this and show that this initial increase in FAME content has resulted in no deposit formation.

FAME has been seen to have excellent solvency properties and may have acted by cleaning up the particulates present in the fuel and preventing deposit formation. The results suggest that the presence of FAME is not the issue; it however could be the absence or reduction in FAME content or the increased presence of FAME oxidation products that could be the issue, possibly present due to the high temperatures and pressures encountered in the engine. [47, 171]

3.4 Conclusions

From the results, the 10 peak data reduction model appears to be the most effective approach for processing large amounts of complex GC-MS data sets and can give an estimation of the components present in the samples. This method can be used to provide quick identification of aliphatic, aromatic and other components by changing the common fragment ions.

The 5, 10 and 20 peak models were tested for effectiveness as a data reduction model. The 5 peak model did not appear to be an accurate representation of the comprehensive dataset and generally would over- or under-estimate the data. The 10 peak data reduction model was chosen to be the most effective model, with a 10 fold reduction in analysis time and general ease of use.

G-Diesel samples and ULSD fuel samples were investigated and compared to account for any differences in the fuels, as G-Diesel fuel samples had high claims of being more effective than ULSD fuel with increased fuel efficiencies and a reduction in emissions. A range of G-Diesel fuel samples were investigated, and comprehensive analysis gave comparable results to the 10 peak data reduction model. The aliphatic and aromatic content of the samples were very varied throughout the G-Diesel samples, and the investigations into low and high mass aliphatic content showed that the G-Diesel samples had around 65% low mass aliphatic content. Which was comparable to ULSD fuel, therefore no vast differences were seen with the fuels.

ULSD fuel samples were also investigated, samples # 1-37 also showed low content of aromatic compounds. Injector and filter deposit samples were examined to account for any difference between them, however no difference between aliphatic and aromatic content was observed. The low and high mass aliphatic content was also investigated and the results showed both injector and filter deposit samples had greater amounts of high mass aliphatic content. This could explain why deposit formation occurs due to increased high mass aliphatic content which can then form larger compounds through oxidation reactions.

G-Diesel fuel samples were then compared to ULSD fuel samples, and both sample sets gave comparable results. Suggesting that G-Diesel fuel and ULSD fuel are similar in componentry and performance characteristics.

The data reduction model was also explored beyond aliphatic and aromatic content, other components tested included alkanes, alkenes, substituted benzenes, naphthalenes and fatty acid methyl esters (FAME). Results showed that the data reduction model could be tailored to the components of interest and was successful at identifying a range of other components such as alkenes, napthalenes and FAME.

The role of FAME was also considered. Two biodiesel samples # 24 and # 25 were compared as both are the same sample, however # 25 was truck blackened and exhibited both injector and filter deposits. FAME content was analysed for both, and the results showed that biodiesel sample # 24 (no deposit formation) had an increased amount of FAME content. Therefore this disproves the theory that FAME content is linked to deposit formation, however it could be from FAME oxidation which could have taken place at high temperatures and pressures inside the truck's engine.

Chapter 4: Analysis of steryl glucosides in biodiesel

4.1 Introduction

Internal diesel injector deposits (IDID) in high pressure common rail fuel injection systems are a relatively new problem facing many original equipment manufacturers across the world for both light duty and heavy duty diesel applications. These deposits can have serious implications for engine performance. They can form on the nozzle needle which can restrict the fuel flow and modify the fuel spray pattern leading to insufficient mixing of fuel and air, distortion of the optimum spray pattern and inefficient combustion. They can also cause sticking of the moving internal injector parts resulting in a loss of control of injection event timings and the amount of fuel delivered. [59, 172]

Many researchers have found a correlation between the introduction of biodiesel fuel and the increased occurrence of IDID. The instability of fatty acid methyl ester (FAME) has been seen to play a role in deposit formation. [173-175]

4.1.1 Biodiesel

Requirements for the incorporation of bio-derived components in the fuel have also been listed in the regulations and a requirement to meet the Renewable Fuels Transport Fuel Obligations Order (2007) [34] which requires renewable fuels to make up 5% of road fuel, has caused the fuel industry to replace conventional hydrocarbon fuel with equivalents from renewable resources.

At present, the most common renewable fuel used is biodiesel, which is formed from the inclusion ofesterified seed oils, collectively known as fatty acid methyl esters (FAME in Europe) or fatty acid ethyl esters (FAEE in South America). The chemistry and composition of FAME is different from that of regularly hydrocarbon based fuels. Biodiesel is produced from vegetable oils and animal fats by a process known as transesterification. The process involves reacting triglycerides with methanol in the presence of a catalyst to yield biodiesel and glycerol.

Biodiesel contains a range of fatty acid chains, ranging from carbon atoms 8 to 22 with some chains being fully saturated, whilst others may be mono-unsaturated or polyunsaturated containing one or more carbon-carbon double bonds.

Polyunsaturated fatty acid chains are those containing more than one double bond, and are particular chemically reactive and susceptible to oxidative degradation, in particular fatty acid chains with adjacent double bonds. This fatty acid composition has effects on the physical and chemical properties of the FAME/FAEE product. The increasing proportion of FAME/FAEE as blending components to diesel fuels has a significant impact on the filterability of the final product. Therefore it is recommended that biodiesel be used at no more than 5 %, also known as B5 (5 % biodiesel and 95 % petrodiesel). [176-177]

Steryl glucosides, which are naturally occurring in vegetable and plant oil and therefore present in biodiesel, have been found to be a major component in biodiesel precipitates and have been linked to deposit formation in diesel injectors.[70]

4.1.2 Steryl glucosides

Plant sterols also known as phytosterols, are naturally occurring steroids in all plants. They exist to stabilise the phospholipid bilayer in plant cell membranes. Sterols are the most common minor components present in plant tissues and vegetable oils, and can exist naturally in the form of free sterols, acylated (sterol esters), alkylated (steryl alkyl ether), sulfated (sterol sulfate) or linked to a glycoside moiety (steryl glycosides). [178-179]

Among the sterols, steryl glucoside (SG) has been found to be a major component in biodiesel precipitates.[180] SG consists of a sugar unit (typically glucose) glycosidically bound to a sterol. They are initially present in vegetable oils in an acylated form with a long chain fatty acid attached, however during the transesterification process to produce biodiesel; the fatty acid chain is removed leaving the steryl glucoside reducing the solubility of the compound.[72-73]

Steryl glucosides (SG) occur naturally in the acylated form in vegetable oils and are very soluble. During the biodiesel transesterification process, these acylated SGs are converted to non-acylated SGs. Common steryl glucosides include campesteryl glucoside, sitosteryl glucoside and stigmasterol glucoside. Figure 4-1 shows the structure of campesteryl glucoside in the free form or acylated steryl glucoside form depending on the functional groups (R).

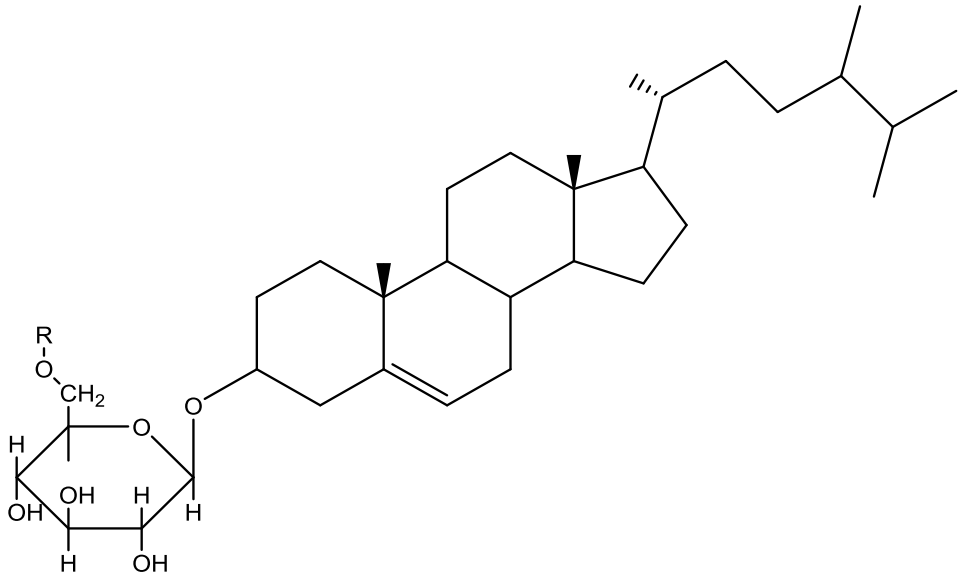

Figure 4-1. Campesteryl glucoside, where R=H; free steryl glucoside or R= $CH_3(CH_2)_nCO$; acylated steryl glucoside.

Table 4-1 shows the different sterol compositions that occur in different sources of oil, with sitosteryl, campesteryl and stigmasterol in the highest concentrations in the different sources. Sitosteryl glucoside has been seen to be the most abundant SG found in many of the oil sources. [53, 181-182]

Table 4-1. Sterol composition in different sources of oil. [182-183]

	Concentration (mg/kg)						
Composition	**Palm oil**	**Soy bean oil**	**Rapeseed oil**	**Cottonseed oil**	**Corn oil**	**Safflower oil**	**Sunflower oil**
β-Sitosteryl	1894	1908	3549	3961	7722	1809	2352
Campesteryl	358	720	1530	170	2691	452	313
Stigmasterol	204	720	-	42	702	313	313
Δ5-Avenasterol	51	108	122	85	468	35	156
Δ7-Avenasterol	25	108	306	-	117	696	588
Other	26	36	612	-	-	173	195

Currently there are few procedures for the analysis of SG in biodiesel; analytical methods generally involve GC-FID [183-185] or GC-MS [116] which both involve a sample preparation step which consists of sample derivatisation required due to the nature of the chromatography technique. Literature has also seen HPLC methods [72, 179] with longer analysis time and also requiring sample derivisation steps.

4.1.3 Analytical methods for SG analysis

A study carried out by Gutiérrez and Rio developed a method using GC-MS, the samples were analysed as the trimethylsilyl derivatives and the steryl glucosides were identified successfully in Kraft pulp and Eucalyptus wood. [186]

Sterol lipids were also identified by quadrupole time-of-flight mass spectrometry in a study by Wewer *et al.*, who were also able to resolve and identify molecular species from four sterol lipid classes including free sterols, sterol esters, sterol glucosides and acylated sterol glycosides. The sterol lipid classes were derivatized with trimethylsilyl ethers, purified by SPE and quantified by GC-MS. [187]

Hoed *et al.* also developed a method for SG analysis by GC-MS [70] with qualitative and quantitative identification of the free steryl glucosides, at a detection limit of below 15 mg/kg.

Free and esterified steryl glucosides (ESG) were also analysed in vegetable oils and biodiesel by Lacoste *et al.* [72] Purification of SGs and ESGs were achieved through the use of a silica gel column, and the analysis of trimethylsilyl derivatives were achieved by GC-FID. The quantification limit they achieved was 10 mg/kg of SG and ESG, with recoveries of around 75-90 % depending on the species and content. A common problem they encountered was the vast amount of solvents necessary to isolate the compounds.

A study carried out by Dulf *et al.* used GC coupled to a flame ionisation detector (FID) with deritivatization by trimethyl silyl ether. Results showed β-sitosteryl was the most prevalent of phytosterol in grape seed oil and corn oil. [188]

Wang *et al.* have also evaluated HPLC coupled to an Evaporative Light Scattering Detector (ELSD) for the analysis of sterol glucosides; however, the technique was only able to quantify the SG concentrations in biodiesel higher or equal to 30 ppm. An additional centrifugation step can be used to purify the sample and meet the analysis requirements for lower concentrations of SG. [179]

A study by Bondioli *et al.* investigated Fourier transform-infrared spectroscopy (FT-IR) and GC-MS methods for SGs in biodiesel, the results showed the palm oil biodiesel had significant proportions of campesteryl, stigmasterol and β-sitosteryl glucosides. [75]

There are no requirements for determining SGs by either the ASTM or the European biodiesel specifications. In the ASTM D7501 this contaminant issue is controlled by the cold soak filterability test. However, plant sterols or SGs are not initially identified as a problem at

ambient temperatures due to their small concentrations in biodiesel. However, these compounds have a very high melting point and limited solubility in biodiesel and, as the temperature is decreased or after long-term storage, these compounds start to crystallise and precipitate out, causing issues such as filter plugging deposits and they can seed crystallisation of other materials.

In this chapter, a UHPSFC-MS method was developed for screening SGs in a range of fuel samples. The limits of detection and limits of quantitation were analysed and also tandem mass spectrometry was investigated. Product ion scans and multiple reaction monitoring (MRM) assays were developed for the SG standards, to detect SGs at low levels in fuel samples.

4.2 Experimental

4.2.1 Steryl glucoside standards

Table 4-2. Steryl glucoside standards used, with structures and ions observed in MS.

Structure	Name	Ions observed
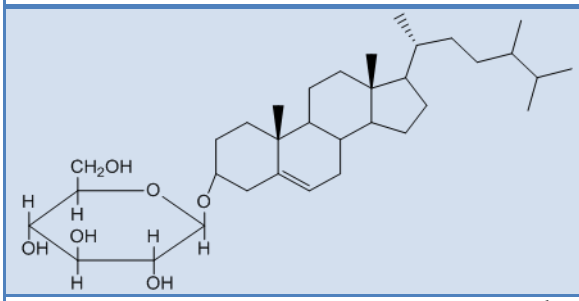	Campesteryl glucoside	$[M + Na]^+ = 585$ *m/z* $[M + H - sugar]^+ = 383$ *m/z*
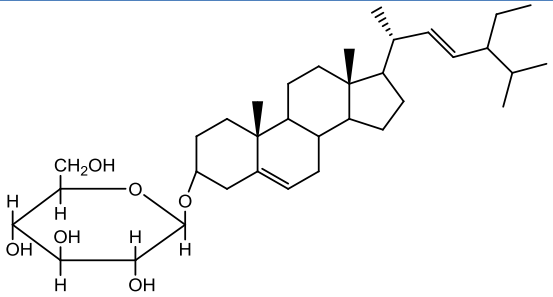	Stigmasterol glucoside	$[M + Na]^+ = 597$ *m/z* $[M + H - sugar]^+ = 395$ *m/*
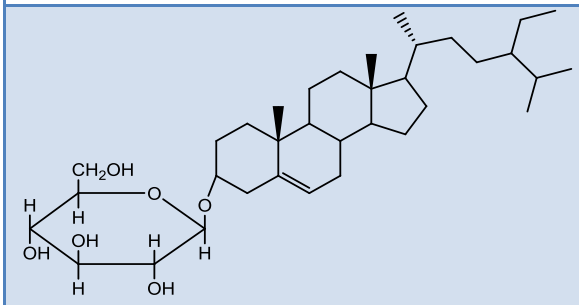	Sitosteryl glucoside	$[M + Na]^+ = 599$ *m/z* $[M + H - sugar]^+ = 397$ *m/z*

4.2.1.1 Calibration solution preparation

Calibration standards were prepared containing nominally 0, 2, 4, 6, 8, 10, 20, 40, 60, 80 and 100 mg/kg of each SG standard using volumetric dilution of the working solution (100 mg/kg) in a methanol/dichloromethane (85:15 *v/v*) mixture.

4.2.1.2 Sample Preparation

A range of fuel samples were obtained from Innospec Ltd. for screening of SGs containing a range of UltraLow Sulfur Diesel (ULSD) and biodiesel fuel samples, the samples were prepared by volumetric dilution in a methanol/dichloromethane (85:15 *v/v*) mixture.

4.2.2 Ultrahigh Performance Supercritical Fluid Chromatography- Mass Spectrometry (UHPSFC-MS) conditions

The chromatography was performed using a Waters Acquity ultra-performance convergence chromatograph (UPC^2) (Manchester, UK) instrument with $scCO_2$ as the supercritical fluid and methanol as the organic modifier. Gradient conditions of 2-40 % methanol at a flow rate of 1.5 mL/min was used and an injection volume of 2 µL. The make-up solvent of methanol with 1 % formic acid was used at a flow of 0.45 mL/min. A HSS C18 SB column was used (100 mm x 3.0 mm, with 1.8 µm particle size) at an optimized column temperature of 45 °C.

4.2.3 Electrospray Ionisation – Mass Spectrometry (ESI-MS) conditions

Positive ion ESI mass spectra were recorded using a triple quadrupole mass spectrometer, TQD, (Waters, Manchester, UK) with the following conditions: capillary voltage 3.5 kV; cone voltage 20 V; extractor 3.0 V; source temperature 150 °C; desolvation temperature 500 °C and desolvation gas flow 650 L/h. The mass spectra were acquired over an *m/z* range of 150-800 and the data was acquired and processed using MassLynx™.

4.3 Steryl glucoside analysis

4.3.1 UHPSFC-MS Optimisation

Initial column and modifier screening on the SG standards, showed that the HSS C18 SB column (100 mm x 3.0 mm, with 1.8µm particle size) was best suited for the analysis with a 2-40 % modifier at 3 minutes. Methanol was chosen as the modifier of choice after optimisation studies.

4.3.2 Effect of cone voltage on ESI mass spectra of SG

Electrospray ionisation (ESI)-MS is a soft ionisation technique used for the production of gas phase ions, where little residual energy is retained by the analyte and generally little fragmentation occurs upon ionisation.

Fragmentation can however occur within the source of the mass spectrometer, known as 'in-source' fragmentation. This occurs when the ions are accelerated in the source, in a high-pressure region. The acceleration is produced by applying a voltage between the sampling cone and the extraction lens known as the cone voltage (CV). The ions collide with residual gas molecules if the cone voltage is increased sufficiently and collision induced fragmentation (CID) can occur producing product ions. [105]

To study the effect of cone voltage on ESI mass spectra, steryl glucoside internal standard at 100 mg/kg was chosen and varying cone voltages were investigated including 20 and 80 V. Figure 4-2 and Figure 4-3 show cone voltage of 20 V and 80 V respectively for SGs.

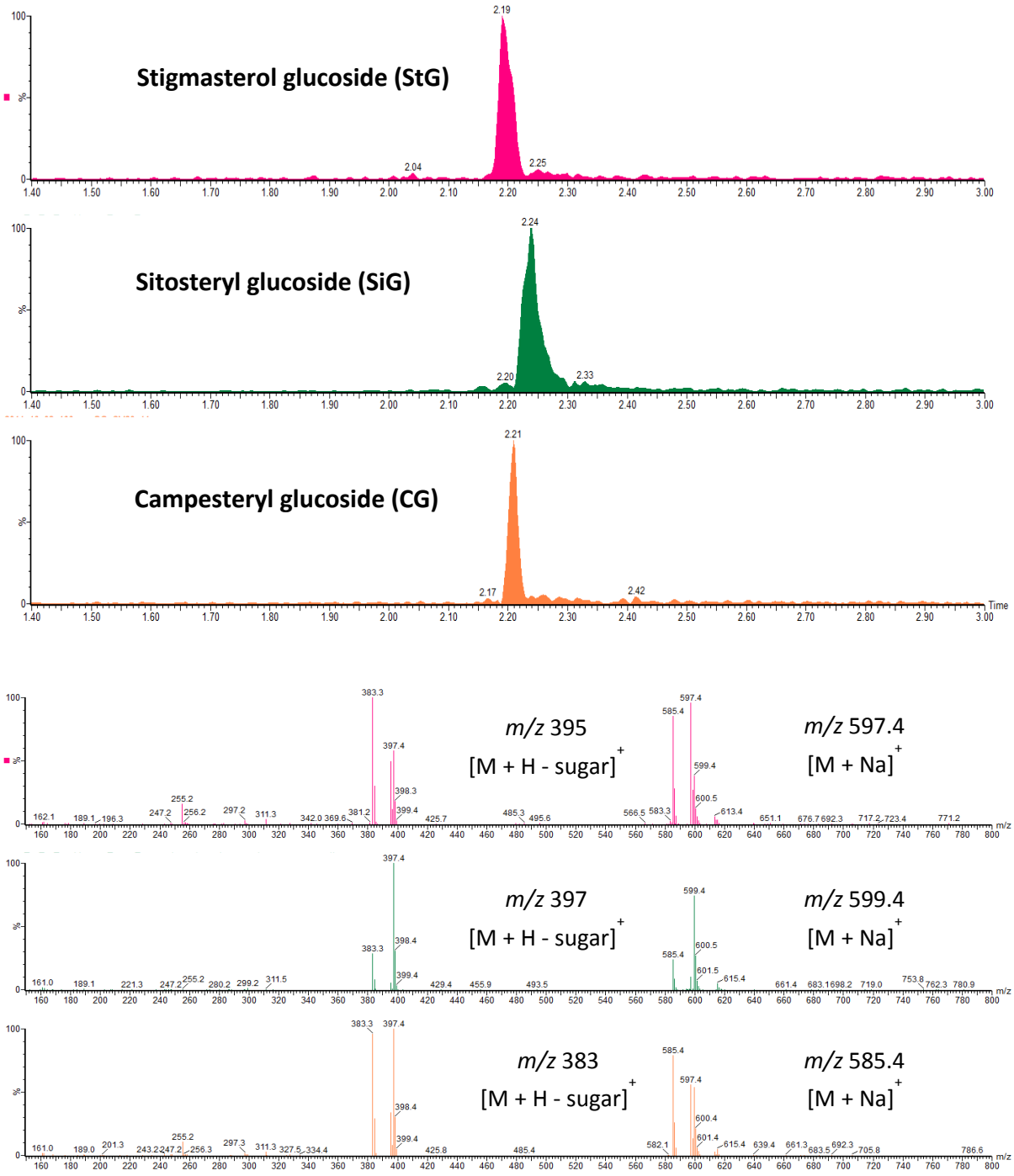

Figure 4-2. RICC of *m/z* 585.4 [Campesteryl glucoside + Na]$^+$, *m/z* 599.4 [Sitosteryl glucoside + Na]$^+$, and *m/z* 597.7 [Stigmasterol glucoside + Na]$^+$ at cone voltage 20 V.

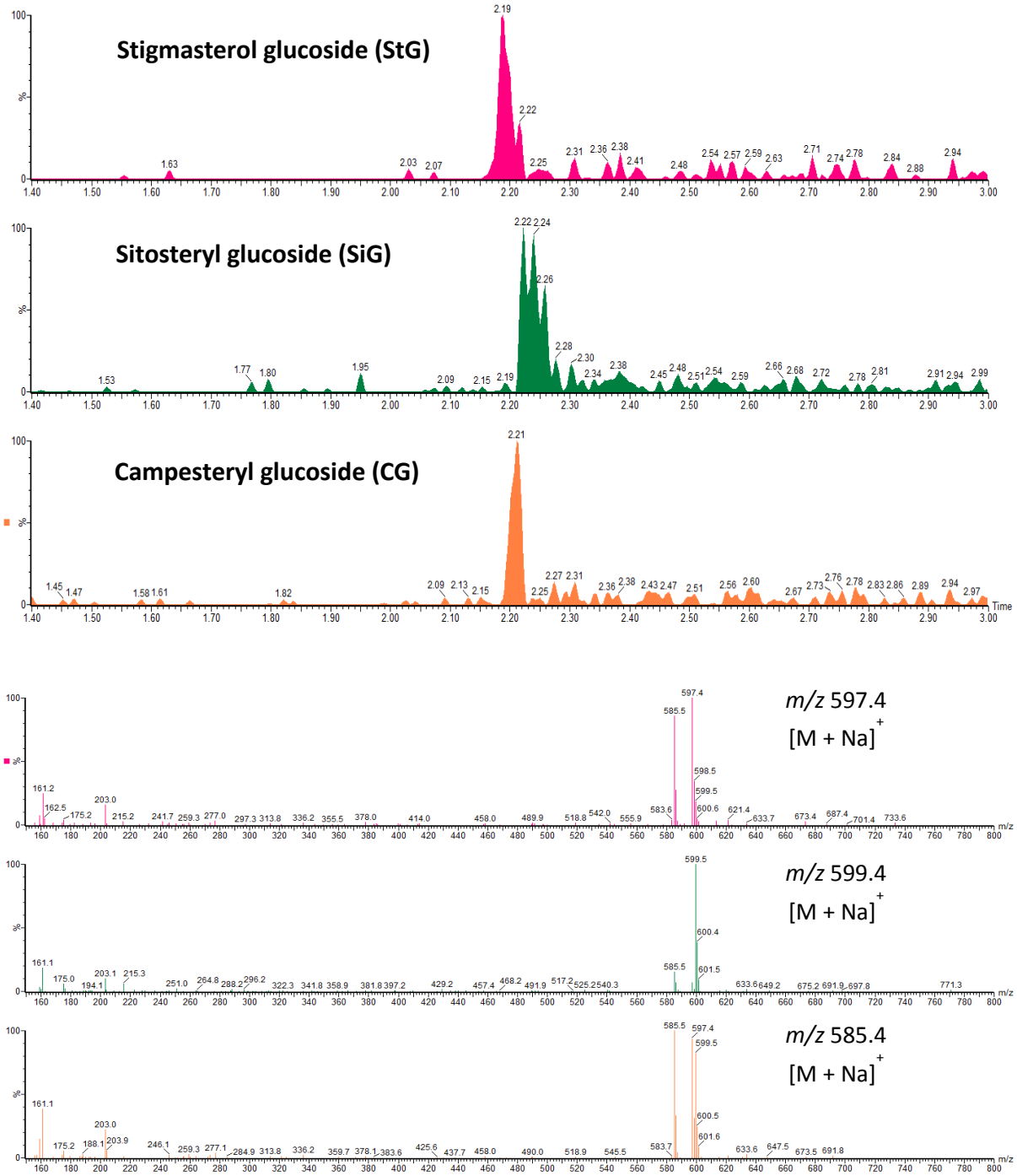

Figure 4-3. RICC of *m/z* 585.4 [Campesteryl glucoside + Na]$^+$, *m/z* 599.4 [Sitosteryl glucoside + Na]$^+$, and *m/z* 597.7 [Stigmasterol glucoside + Na]$^+$ at cone voltage 80 V.

Comparing Figure 4-2 (cone voltage 20 V) and Figure 4-3 (cone voltage 80 V), cone voltage of 20V shows the loss of sugar moiety at *m/z* 395, 397 and 383 (free sterol). These fragments are thought to be derived from the protonated molecule and therefore are less stable than the sodiated species, therefore as cone voltage is increased these ions seem to disappear. There are also a number of secondary higher mass products being formed. More experiments are needed to identify these, however would appear to result from combination reactions.

The sodiated species still appears however as cone voltage is increased to 80 V this intensity reduces, as shown in the following graphs.

The intensity of the sodium containing ions (sodiated ions) $[M + Na]^+$ and loss of sugar ions are shown in Figure 4-4 below, both graphs show a general trend of as cone voltage increases the intensity of the steryl glucosides reduce. In Figure 4-4A, the slight increase at cone voltage of 60 V seems to be an anomaly, which does not follow the same trends as others.

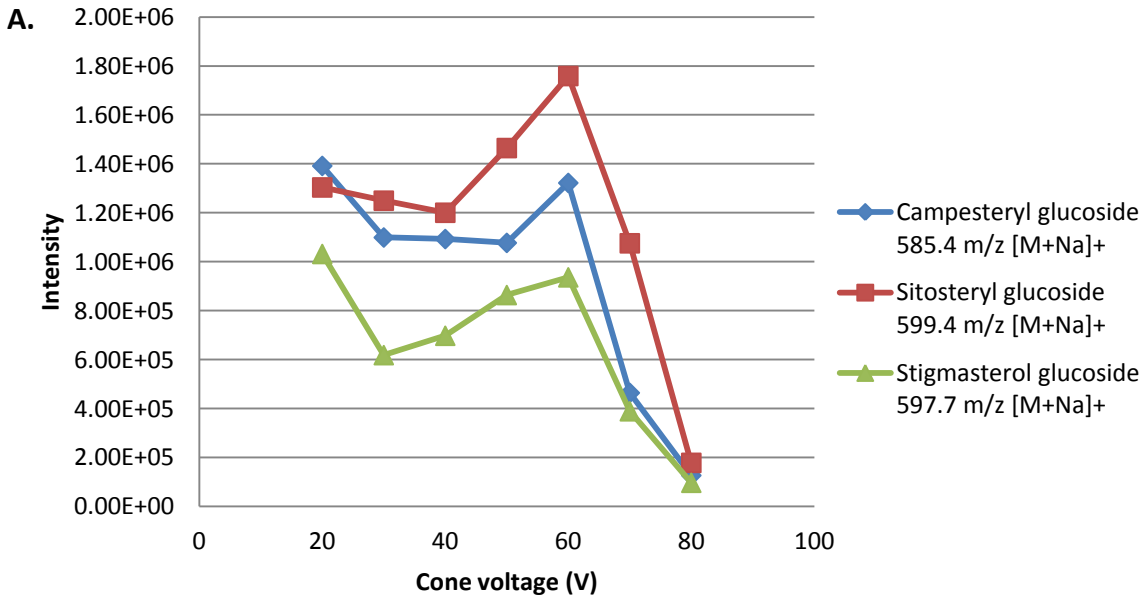

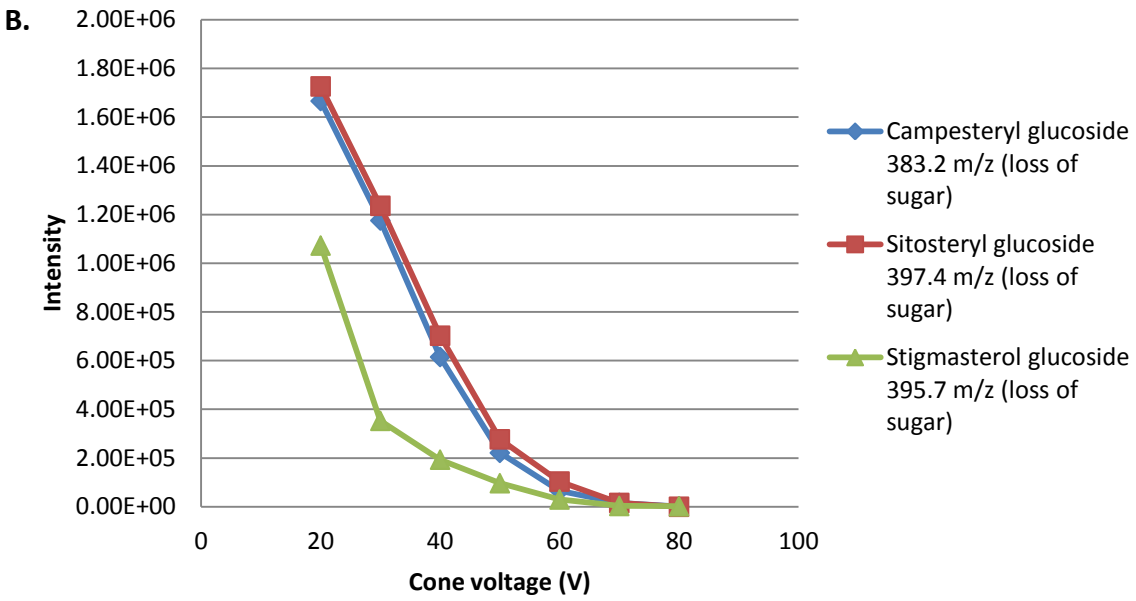

Figure 4-4. Graphs to show the effects of cone voltage on the intensity of the intact steryl glucoside $[M + Na]^+$ (A.) and (B.) the steryl glucoside with loss of sugar.

4.3.3 Screening of fuel samples

Whilst screening ULSD fuel samples for the presence of SGs, isobars were detected. Isobars in mass spectrometry refer to atomic or molecular species with the same nominal mass but different exact masses, this is problematic in screening analysis as in mass spectrometry the ion is shown with the same nominal mass and can often be confused. Using chromatography gave an important extra dimension of confirmation in regards to matching the retention times to standards. Direct infusion which is a method of sample introduction in which the sample is continuously flowed into a mass spectrometry ion source and bypassing the chromatographic separation step or shotgun analysis could therefore lead to mis-assignment of the SGs.

Figure 4-5 and Figure 4-6 both refer to ULSD fuel samples which show peaks when RICCs of ions at *m/z* 597 and 599 for stigmasterol and sitosteryl glucoside, however the retention time and resulting mass spectra do not match to the SGs. The retention times for campesteryl glucoside, stigmasterol glucoside and sitosteryl glucoside are 2.21, 2.19 and 2.24 minutes respectively.

When the resulting mass spectra is investigated, the main ions of interest are not observed at the correct retention time but appear at around 1.2 minutes for both fuel samples and therefore confirming the absence of SGs in these fuel samples.

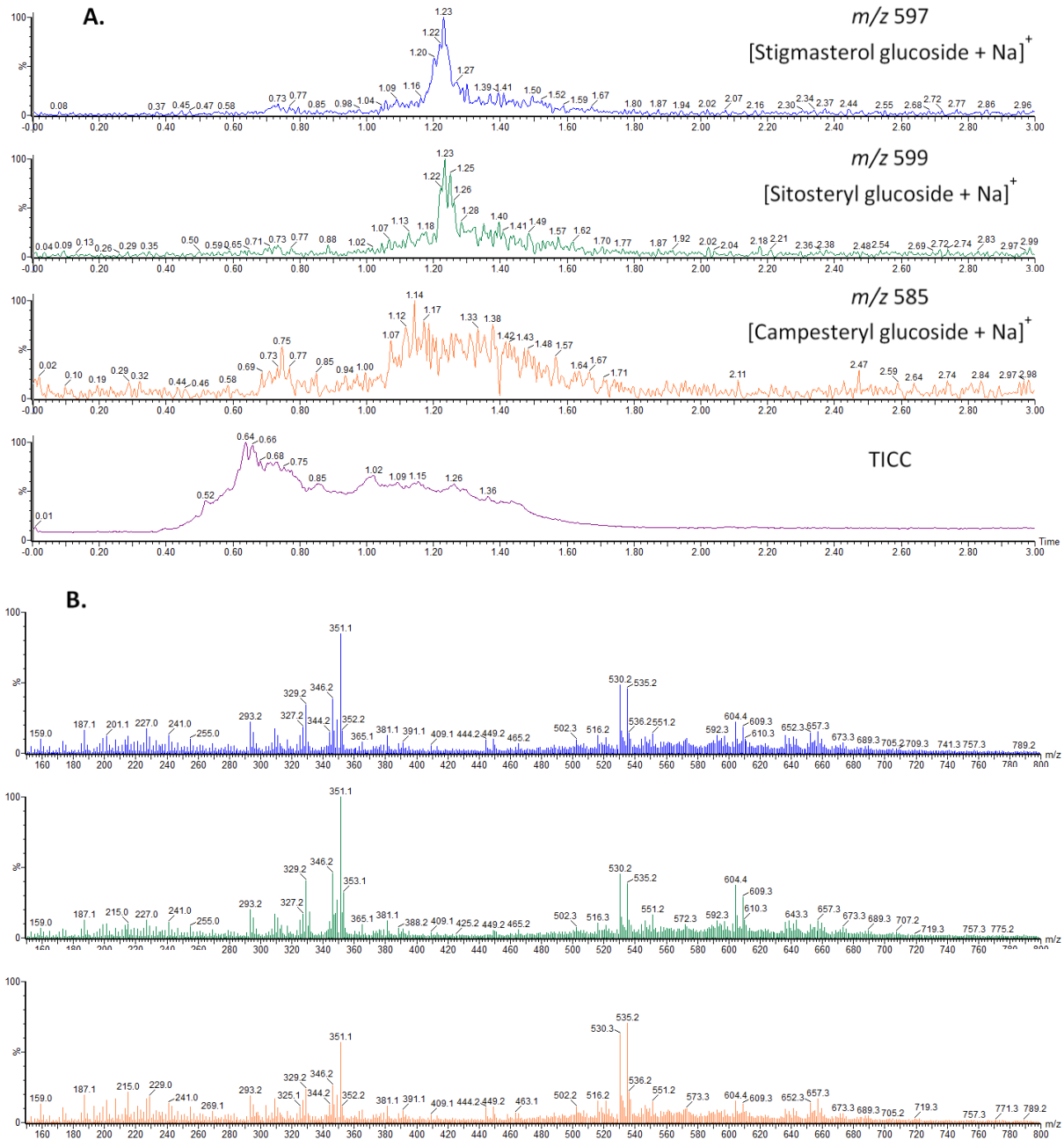

Figure 4-5. ULSD fuel sample # 24, A. RICCs and TICC of ion at *m/z* 597, 599 and 585 and B. resulting mass spectra.

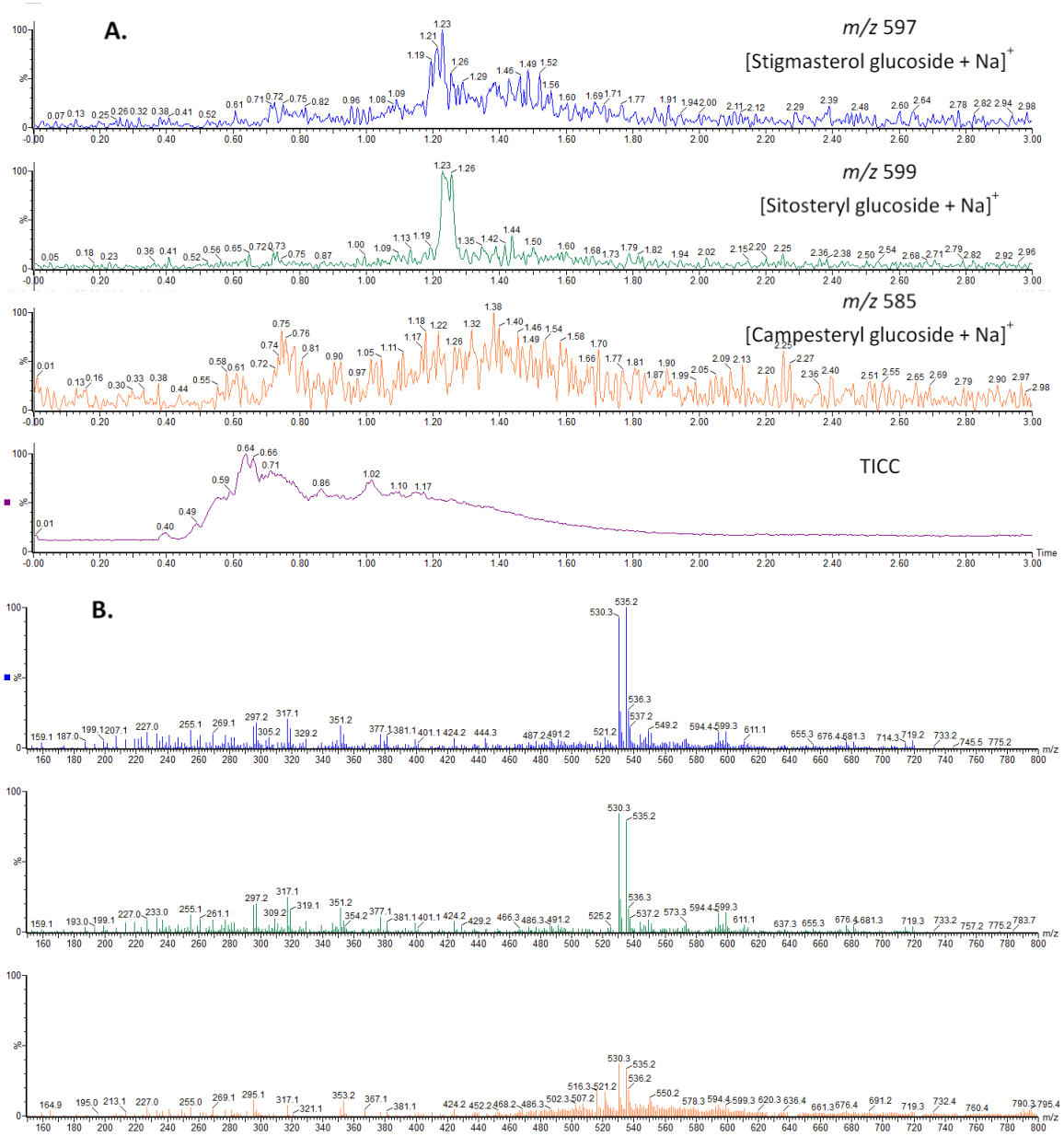

Figure 4-6. Fuel sample ULSD # 29, A. RICCs and TICC of ion at *m/z* 597, 599 and 585 and B. resulting mass spectra.

Figure 4-7 shows the RICCs of campesteryl, sitosteryl and stigmasterol glucoside + ammonium ion and the free sterols. Interestingly the sodiated species which was previously seen when analysing the steryl glucoside standards was not observed in ULSD fuel sample A, instead the ammoniated species $[M + NH_4]^+$ is observed.

The source of the ammonium ion however is still unknown. Sources potentially could be from the instrument itself, such as contamination from other samples, presence of ammonium salt, a mislabelled bottled or from the fuel itself. Replicates were analysed for this sample with similar results, therefore ruling out introduction of the ammonium ion from the instrument or sample preparation.

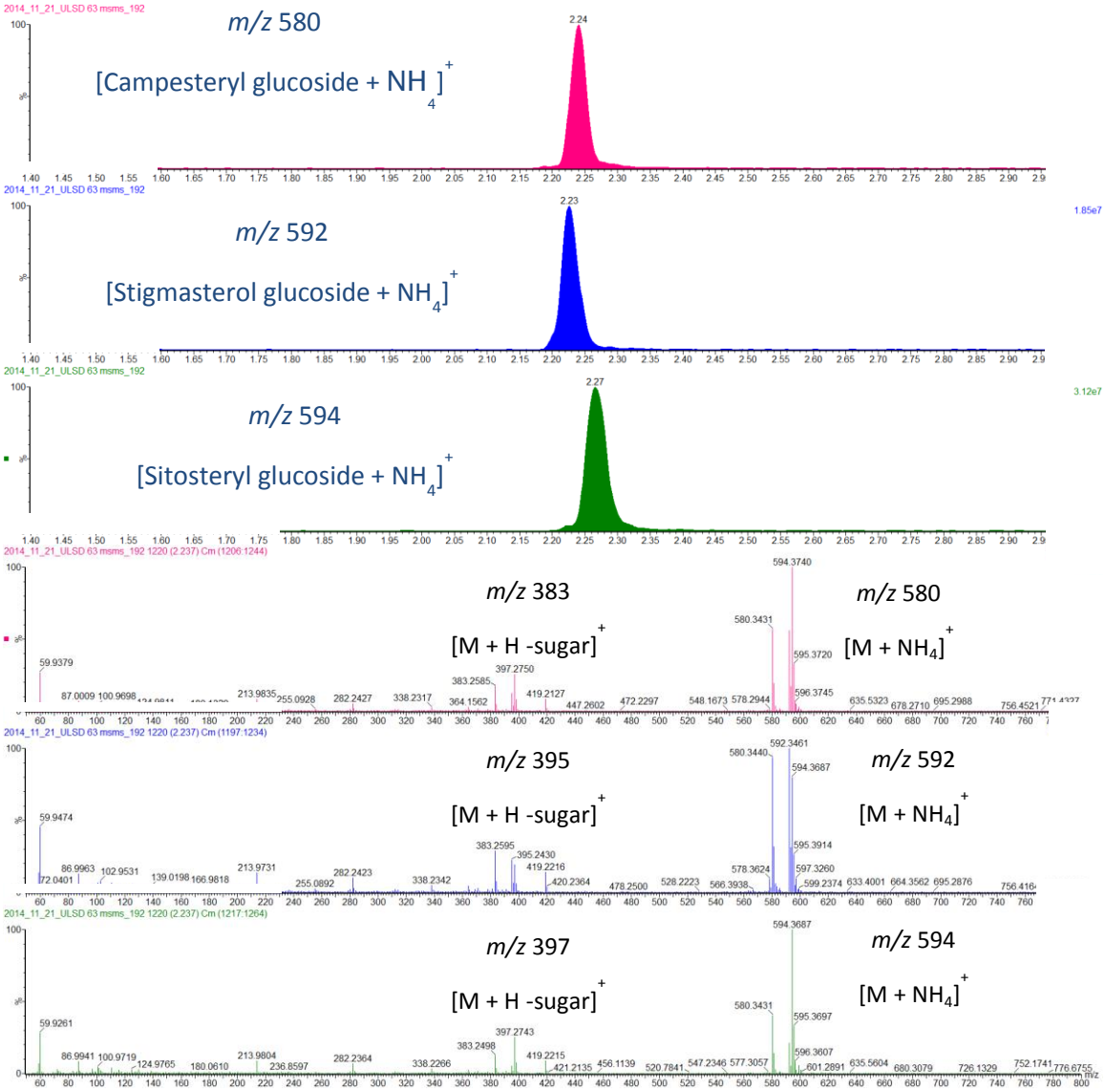

Figure 4-7. RICCs of *m/z* 580, 594 and 592 showing [Campesteryl, Sitosteryl and Stigmasterol glucoside + NH_4]$^+$ and representative mass spectra.

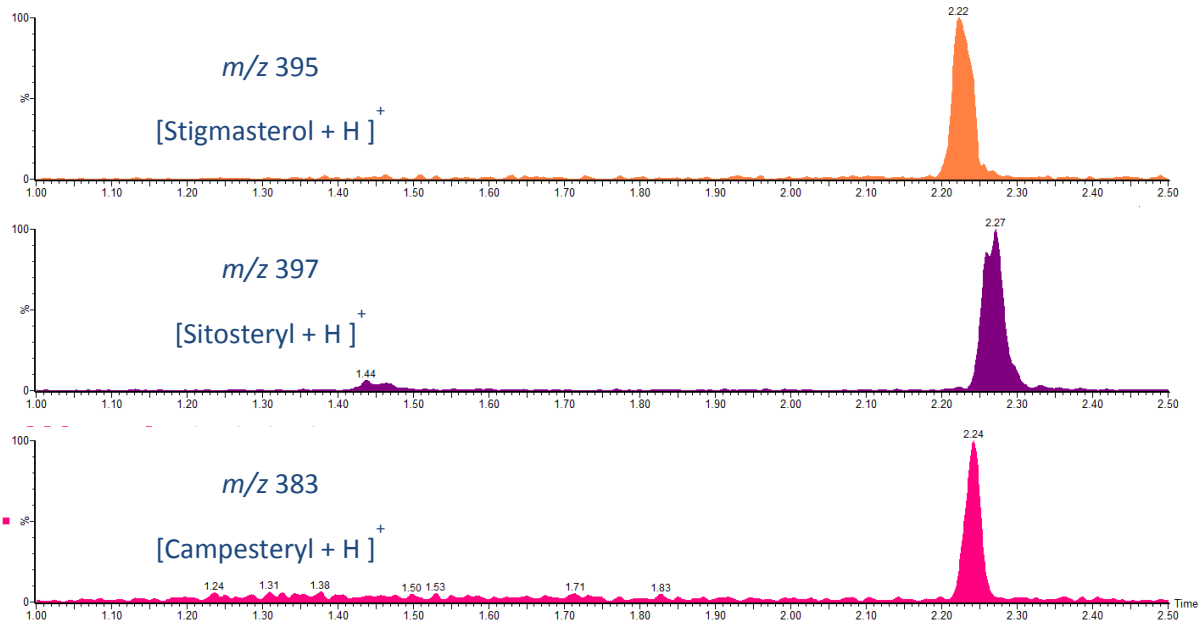

Figure 4-8. RICCs of *m/z* 383, 397 and 395 showing [Campesteryl, Sitosteryl and Stigmasterol + H]$^+$ in fuel sample A.

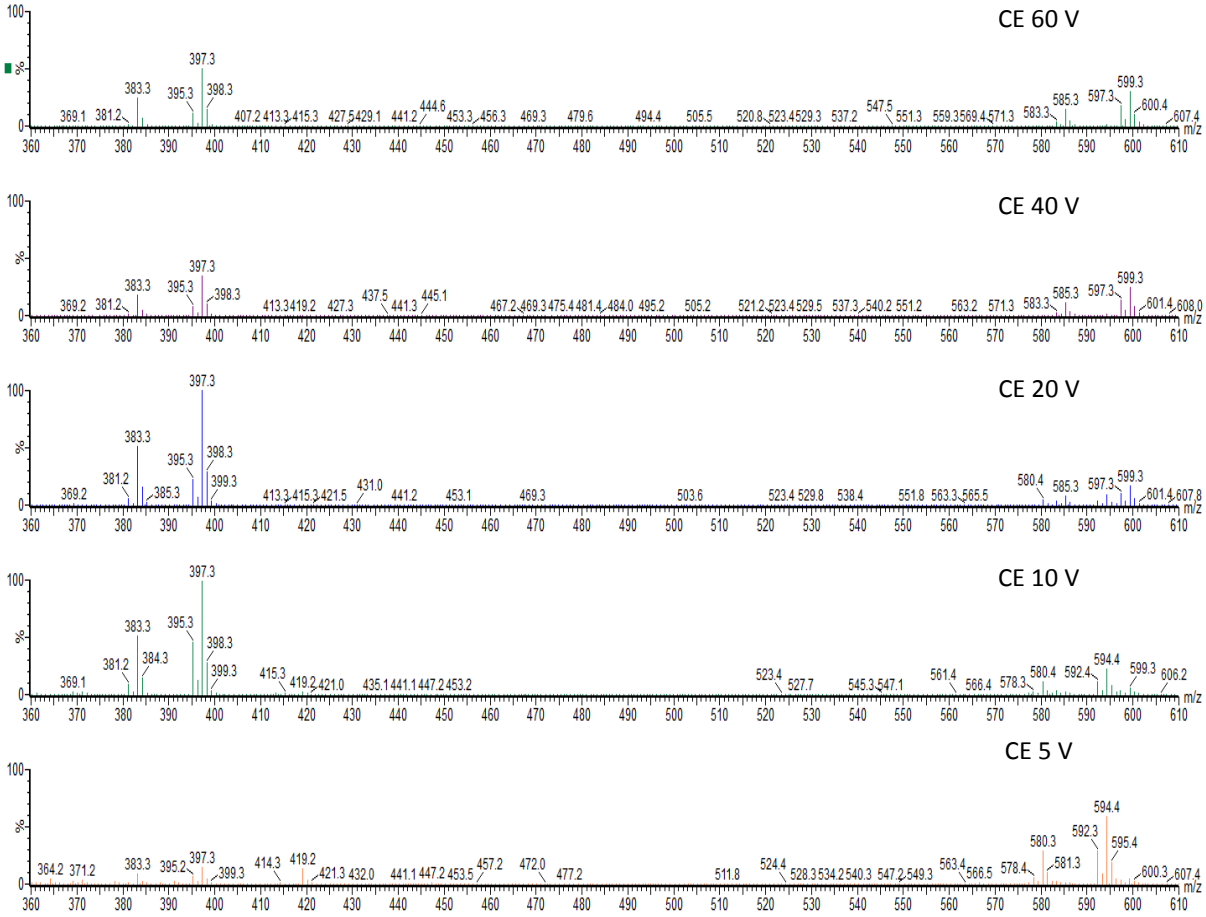

Figure 4-9. Mass spectra of collision energy from 5 to 60 V of fuel sample A.

Figure 4-9 shows the optimisation of collision energies (CE) from 5 to 60 V, at 5 V the intensity of the ammoniated species is the highest given that the collision energy is too low to allow for fragmentation; by increasing the collision energy to 10 V a vast difference can be seen. The base peak is the [free steroid + H]$^+$ ion at *m/z* 383, 397 and 395, the optimal collision energy for this ion seems to be at CE 20 V, above this the intensity of both the adduct ion and protonated steroid molecule are low.

Figure 4-10 shows a comparison of CE 5 and 10 V, in which a vast difference can be seen as a 5 V increase can lead to extensive fragmentation from steryl glucoside to the free steroid showing loss of the sugar portion.

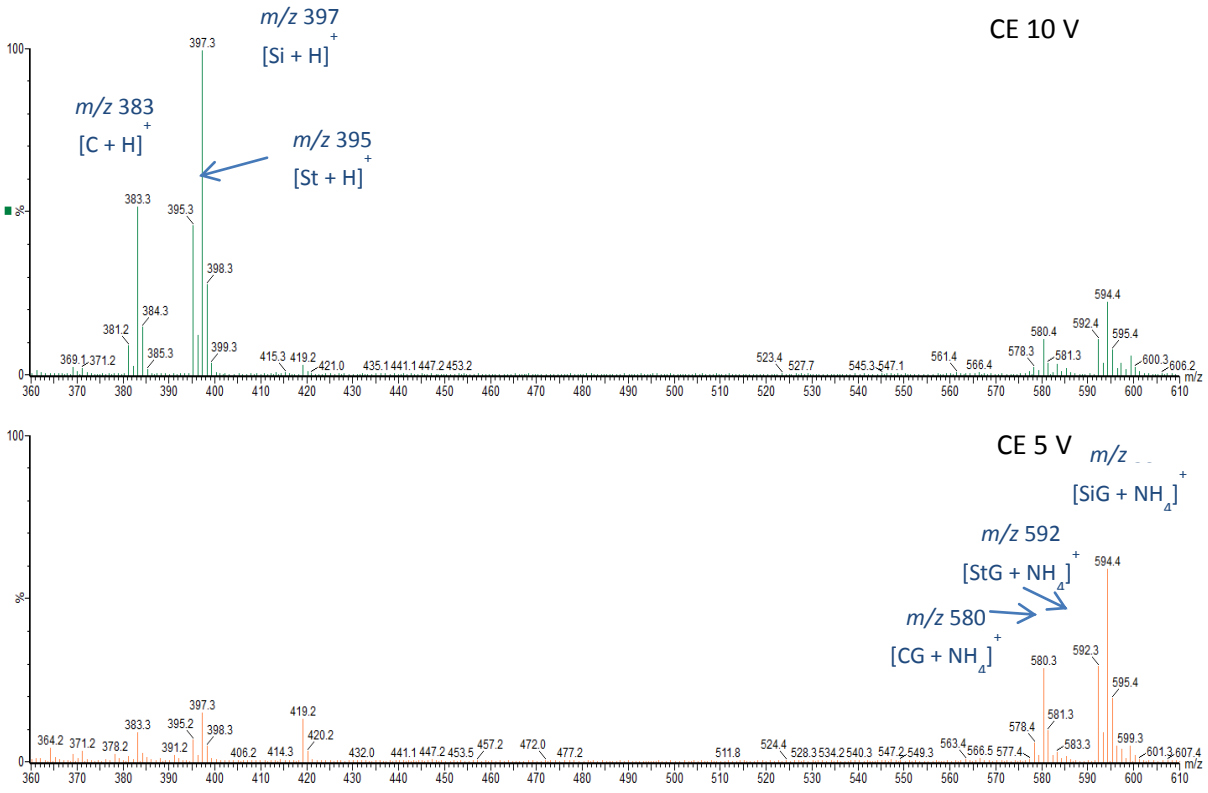

Figure 4-10. Mass spectra showing collision energies of 5 and 10 V; where CG, SiG and StG refer to Campesteryl (C) glucosideSitosteryl (Si) glucoside and Stigmasterol (St) glucoside.

4.3.4 Limits of detection

The LOD is defined as the lowest amount of analyte necessary to obtain a signal that is distinguishable from the background noise. It can be calculated from a range of analytical methods such as standard deviation of the blank, calibration plots and signal-to-noise ratio (S/N).

In this study, LOD was calculated using the S/N method of 3:1, and detection limits of the reconstructed current chromatograms (RICCs) for the sodiated molecules $[M + Na]^+$ were calculated, campesteryl glucoside (1.64 mg/kg), stigmasterol glucoside (1.76 mg/kg) and sitosteryl glucoside (0.91 mg/kg).

4.3.5 Linear dynamic range

The linear dynamic range of the UHPSFC-ESI-MS method was determined using the standard solutions of SG in DCM/MeOH (85:15 *v/v*) from 0-100 mg/kg, as described in the Experimental Section. Figure 4-11 shows the calibration graph for total SGs ($R^2 = 0.99$), peaks areas of RICCs of sodiated molecules $[M + Na]^+$ of campesteryl glucoside (*m/z* 585), stigmasterol glucoside (*m/z* 597) and sitosteryl glucoside (*m/z* 599) against concentration of SGs.

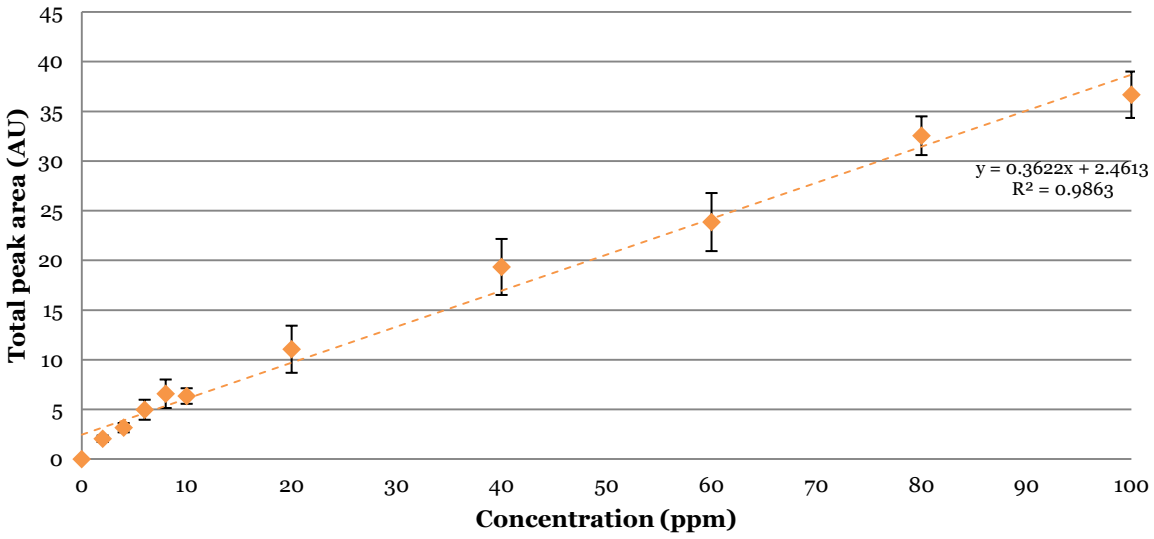

Figure 4-11. Calibration graph of total SGs from the summed RICC peak areas of the sodiated molecules from 0-100 mg/kg. Number of replicate measurements =3.

Figure 4-12 shows the two calibration plots taken from Figure 4-11, showing 0-10 mg/kg and 10-100 mg/kg for total SGs, showing two different regions of linear response. A more linear response is observed at the lower concentration with R^2 value of 0.99 and 10-100 mg/kg at 0.9886, due to the saturation of the ESI detector at high concentrations.

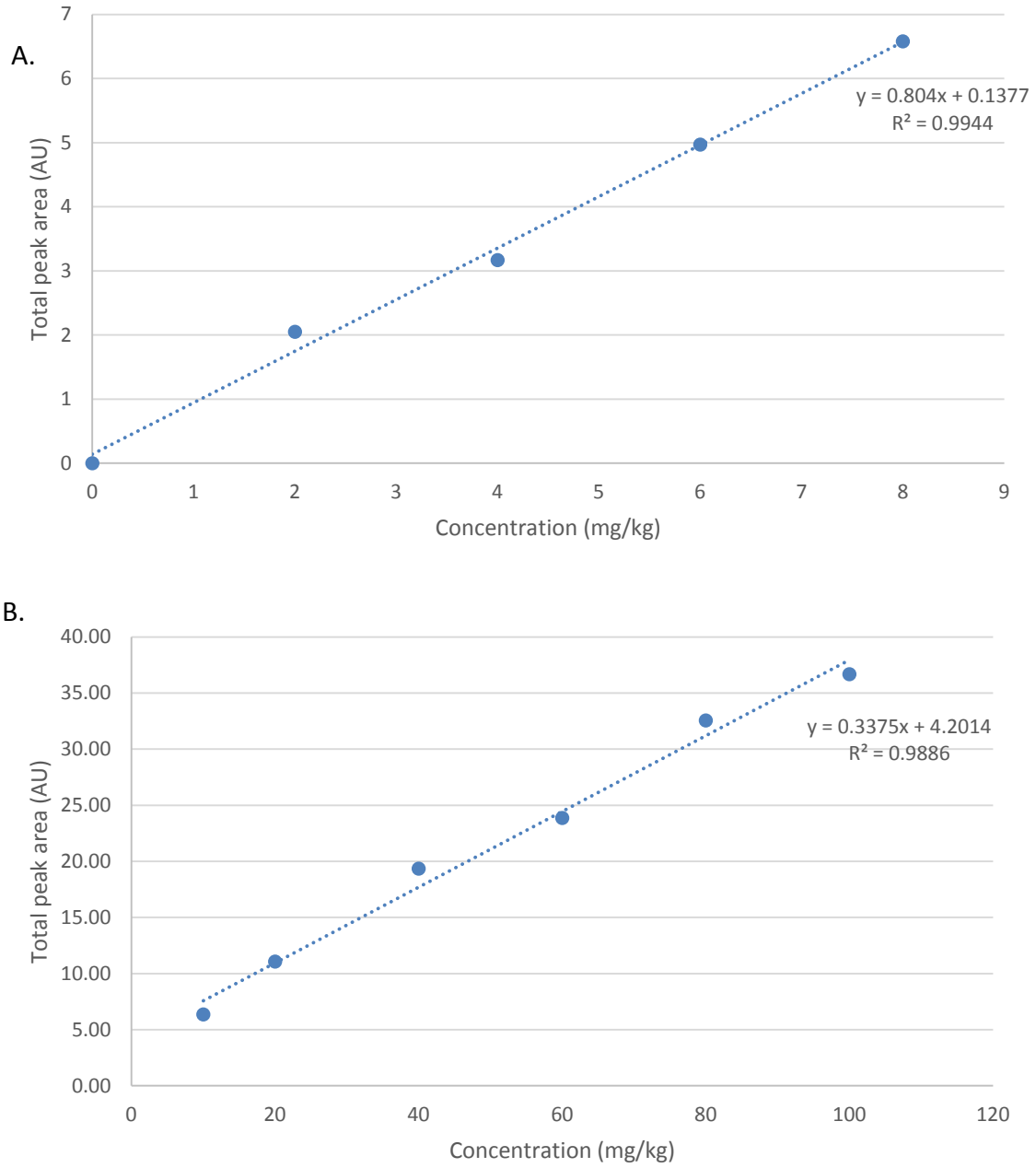

Figure 4-12. Calibration graph of 0-10 mg/kg (A) and 10-10 mg/kg (B) for total SGs from the summed RICC peak areas of the sodiated molecules.

Figure 4-13 shows a calibration graph for the individual SGs, all three SGs show good linearity with all R^2 values of 0.9857, 0.9861 and 0.9917 for campesteryl glucoside, sitosteryl glucoside and stigmasterol glucoside, respectively. Two linear regions are observed again in the graph from 0-10 ppm and 20-100 ppm.

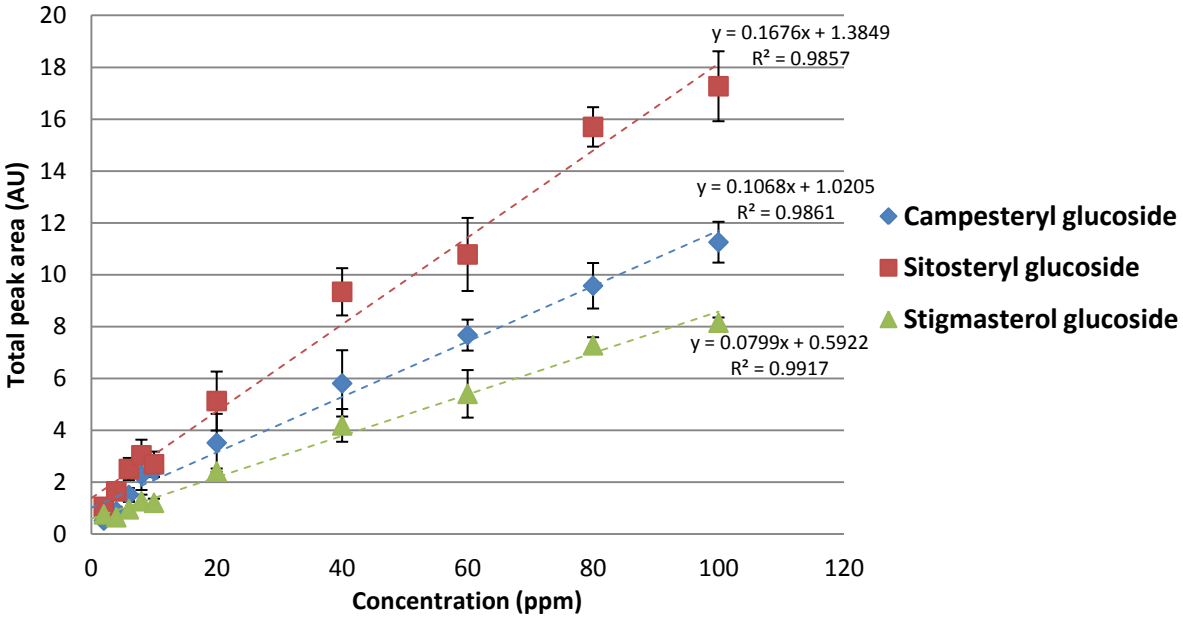

Figure 4-13. Calibration graph of individual SGs from the RICC peak areas of the campesteryl, sitosteryl and stigmasterol glucoside molecules from 0-100 mg/kg. Number of replicate measurements =3.

4.3.6 Tandem MS experiments

Steroid fragmentation has been extensively researched since the 1960s by Carl Djerassi and others who investigated structure elucidation of unknown steroids by electron ionisation. 5α-Cholestane (I) was first subjected to scrutiny by Djerassi, to see how the fundamental skeleton of the steroid behaves after electron ionisation. [189-198]

From the results, the two most intense fragment ions were seen at *m/z* 217 and 218. Three fragmentation mechanisms were proposed, shown below as II, III and IV in Figure 4-14.

Hydrogen transfers are observed however closer inspection of the three fragmentation proposals involve different parts of the molecule being retained. [189, 199]

The ion at *m/z* 217 produced by fragmentation structure II retains carbon atoms 15 and 16 whereas structure III retains C15 but not C16. Fragmentation structure IV retains neither of these carbon atoms, however does contain the methyl group attached to C13 which is lost in structures II and III. Isotopic labelling experiments confirmed that schematic IV was correct and the hydrogen atom attached to C14 was principally involved in the hydrogen transfer. [189]

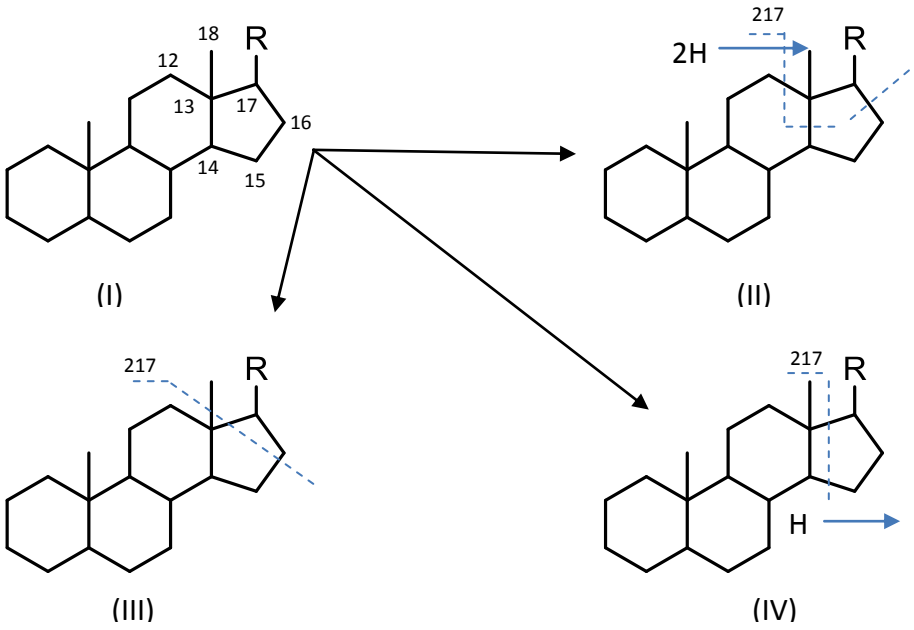

Figure 4-14. Three fragmentation proposals for 5α- cholestane (I) for *m/z* 217, showing fragmentation structures II, III and IV.

The fragmentation pathways shown below in Figure 4-15 show the fragment ion at *m/z* 218, Figure 4-15a shows an initial fragmentation pathway for 5α- cholestane going from structure a→b, however through deuterium labelling experiments they appear to be more complex as shown in Figure 4-15b and involves steps a→ c→d→b, which shows an exchange between the hydrogen atoms originally attached to C16 and C18, and instead of a cyclopropane being ejected a neutral olefin is instead ejected, resulting in the formation of structure b.

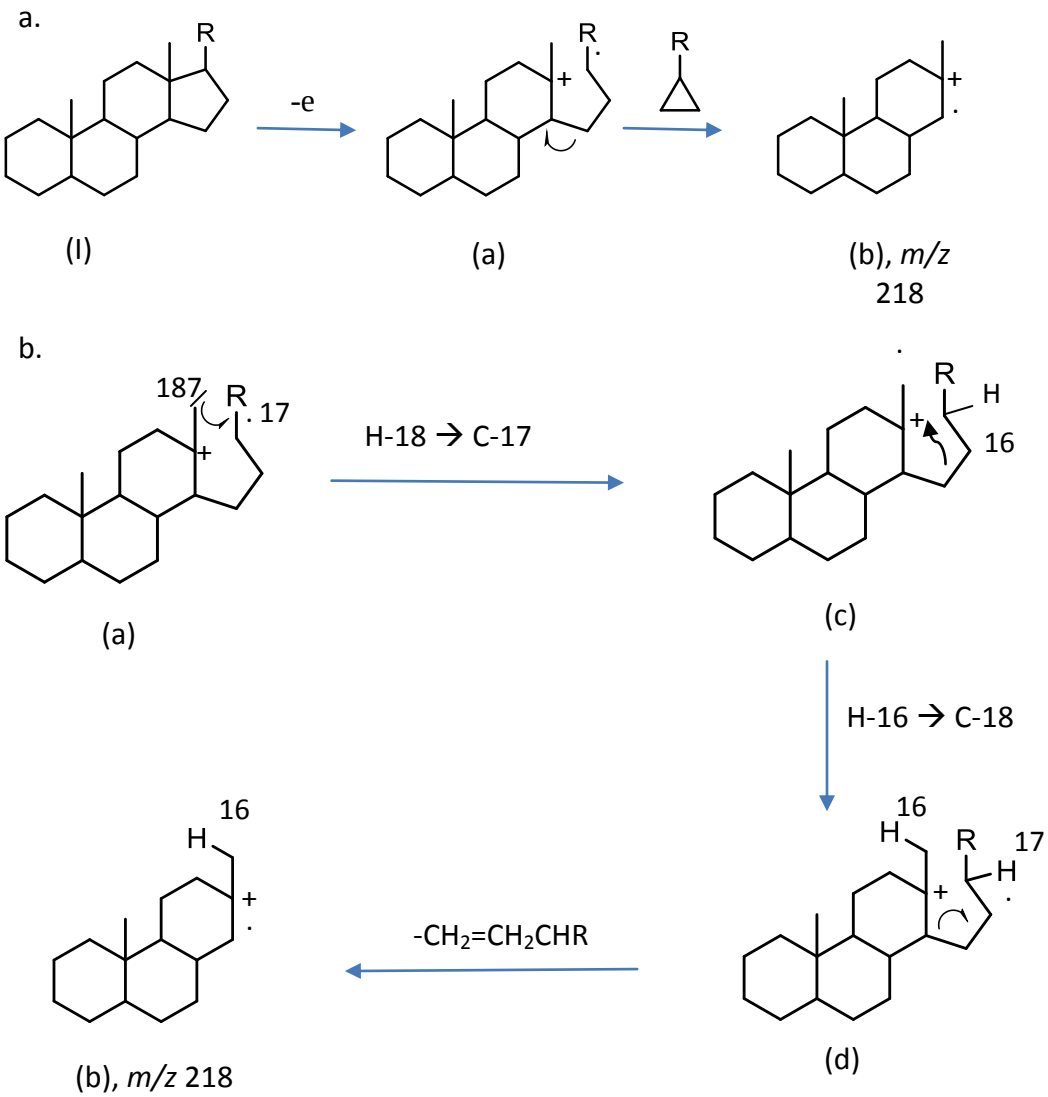

Figure 4-15a. Initial reaction pathway of 5α- cholestane structure (I) and production of the fragment ion at *m/z* 218. Structures I → a → b

b. Revised reaction pathway for 5α- cholestane, structures a → c → d → b.

It is important to note that the presence of double bonds can drastically change the course of the fragmentations pathways. In saturated hydrocarbons such as 5α- cholestane, ionisation will lead to a tertiary carbonium ion and secondary radical which are responsible for triggering the

subsequent fragmentations. However for unsaturated hydrocarbons alternative ionised species occur leading to different fragmentation ions.

An example of an unsaturated steroid was also explored by Djerassi, for this isomers of cholestene were chosen, Δ^5, Δ^7 and Δ^{14} cholestene. For Δ^5-cholestene (Figure 4-16A, structure VII) and Δ^7-cholestene (Figure 4-16B, structure VIII) both produce an ion at *m/z* 257 which shows loss of the C side chain triggered by allylic fission of the double bonds leading to species e and f respectively.

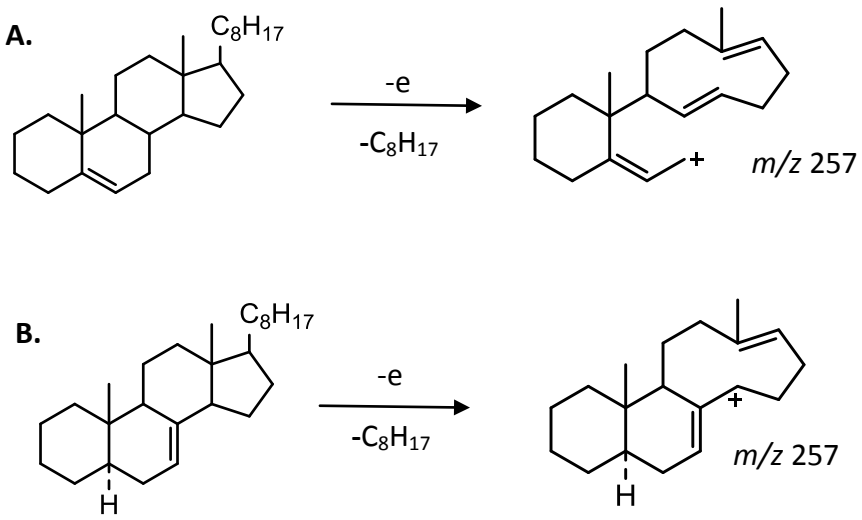

Figure 4-16. Reaction pathway of Δ^5-cholestene as shown as structure (A. VII) and of Δ^7-cholestene as shown as structure (B. VIII).

For Δ^{14}- cholestene as shown as structure IX below, a hydrogen transfer between positions 16 and 18 lead to a highly stabilised dienic tertiary carbonium ion as shown as structure g below at *m/z* 257. The double bond here effectively blocks the loss of ring D and competes with the C13-17 bond scission in the saturated C-17 substituted hydrocarbons, to produce structure g.

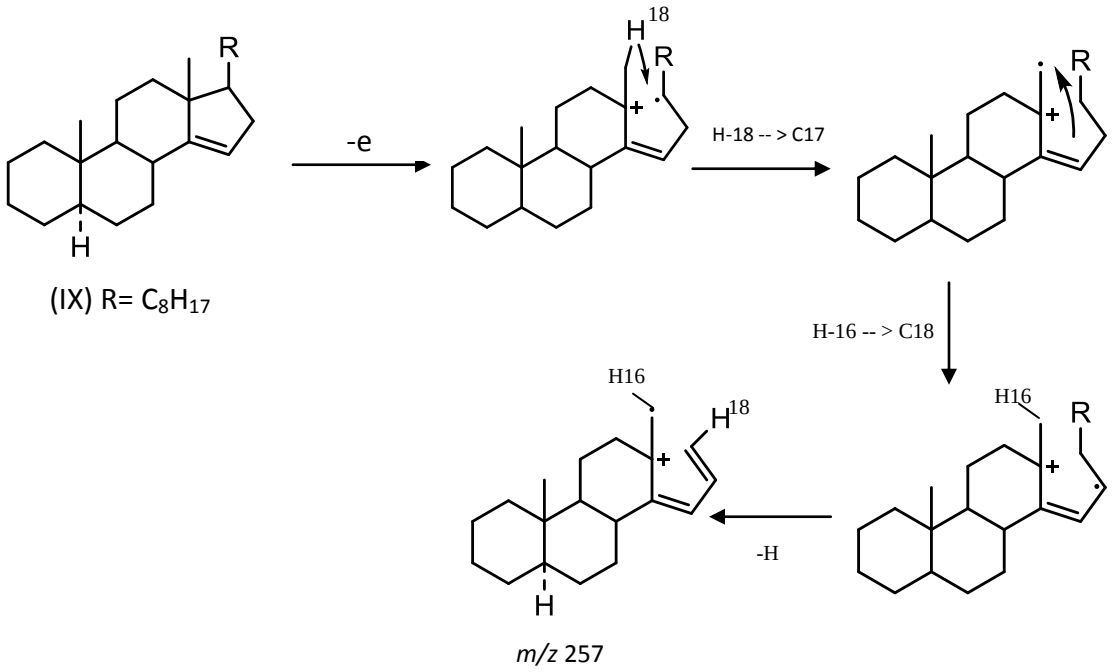

(IX) R= C_8H_{17}

Figure 4-17. Reaction pathway of Δ^{14}- cholestene as shown as structure (IX).

Tandem MS was used to investigate the steryl glucosides for structure elucidation studies and development of MRM assays for targeted analysis of SGs.

4.3.6.1 Effect of collision energy

Product ion scans were performed on the SG standards with differing collision energies (CE) from 10-60 V for optimization and investigation of the fragmentation patterns of free steroids.

For campesteryl shown in Figure 4-19, the collision energy (CE) of 10 V was not enough to aid in fragmentation and the presence of the molecular ion at *m/z* 383 showing the free steroid ion was seen. However, when collision energy was increased to 20 V a vast different in spectra can be seen. A hydrocarbon series is observed with a mass difference of 14 *m/z* units relating to a CH_2 difference, with ions at *m/z* 43, 57 and 71 with structures $[C_3H_7]^+$, $[C_4H_9]^+$ and $[C_5H_{11}]^+$ respectively. As CE increases to 40 V and 60 V, these same diagnostic fragment ions are not

seen and the hydrocarbon series separated by 14 *m/z* units is instead observed this is because of the high energy used and the relative instability of the fragment ions.

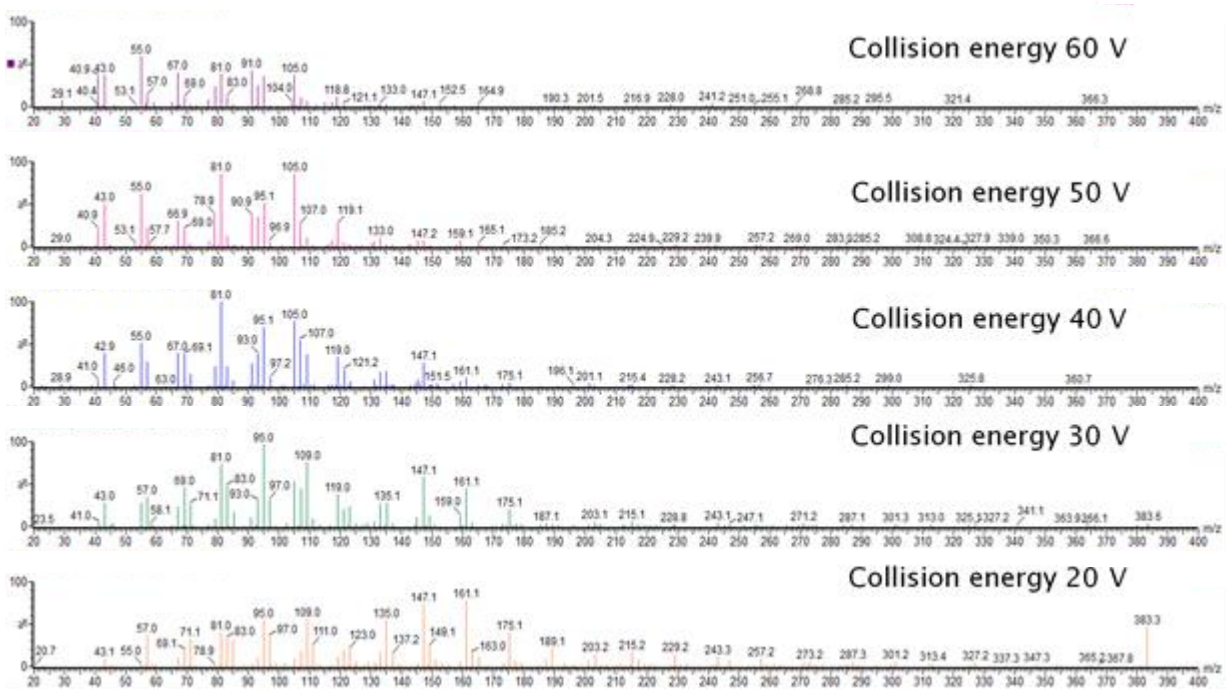

Figure 4-18. Product ion mass spectra of campesteryl at collision energies of 10-60 V.

CE 20 V was chosen as the optimal collision energy for fragmentation of the steryl glucosides as the spectra is rich with fragment ions. The most abundant ions in the product ion scan of campesteryl at CE 20V (Figure 4-19) being ions at *m/z* 95, 135, 147, 161, 203 and 257. Fragment ions at *m/z* 147 and 161 are diagnostic of sterols that have a double bind in the B ring and can be used to identify these steroids. The ions at *m/z* 257 and 203 arises from the complete loss of the side chain, with ion at m/z 203 losing the A ring as well as the side chain. The other fragment ions arise from multi carbon ring cleavage.

Figure 4-19. Product ion scan mass spectra of campesteryl at collision energy 20V.

4.3.6.2 Comparison of SGs

Figure 4-20 shows a fragmentation schematic of sitosteryl as a free steroid and shows the possible fragments which are common to both sitosteryl and campesteryl (blue) and fragments for sitosteryl (green).

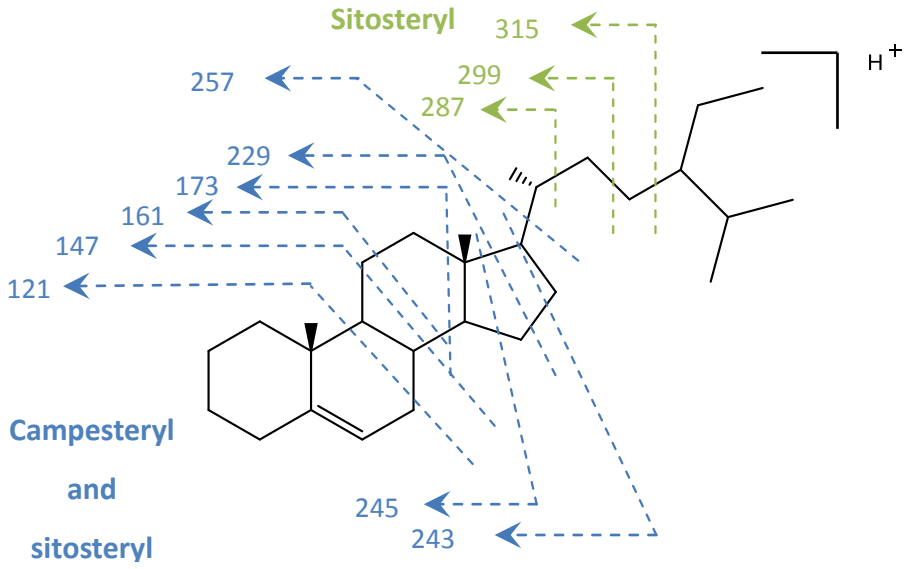

Figure 4-20. Fragmentation schematic of campesteryl and sitosteryl as free steroids, fragments in blue show ions common to campesteryl and sitosteryl and fragments in green are only relevant to stigmasterol.

Figure 4-21 and Figure 4-22 show fragmentation patterns of sitosteryl and stigmasterol from collision energy 20- 60 V, the profile for sitosteryl shows similar fragmentation profile to campesteryl.

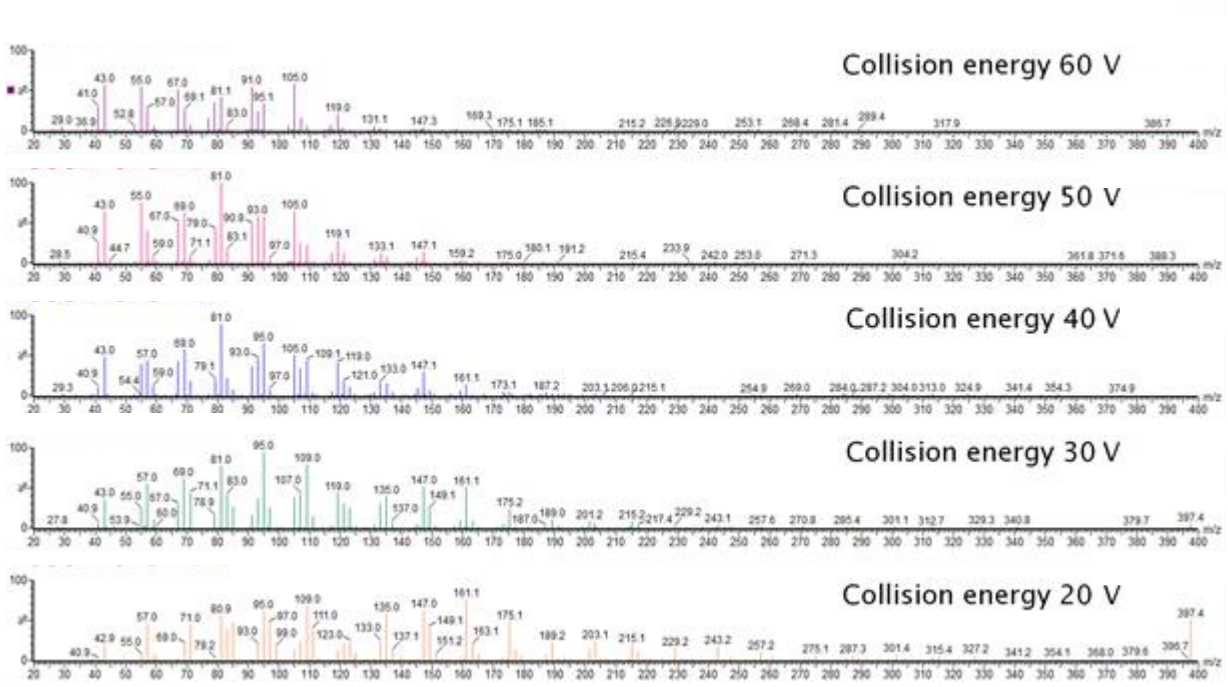

Figure 4-21. Product ion scan mass spectra of sitosteryl at collision energy of 20-60 V.

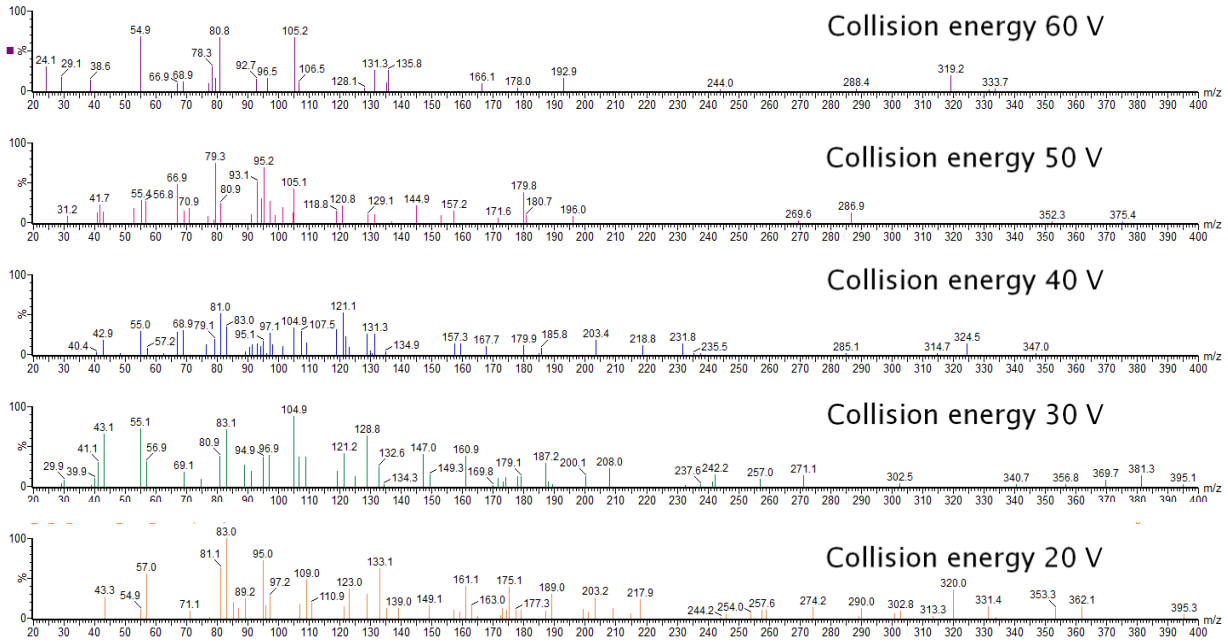

Figure 4-22. Product ion scan mass spectra of stigmasterol at collision energy of 20-60 V.

The product ion scan mass spectra of SG standards are shown in Figure 4-23 at collision energy of 20 V. A similar fragmentation pattern is seen for campesteryl and sitosteryl glucoside. Both contain hydrocarbon series at low *m/z* and abundant ions at *m/z* 147 and 161 from multi carbon ring cleavage. Ions are also present at *m/z* 257 and 203 from loss of side chain and loss of side chain and ring A respectively.

For sitosteryl glucoside, additional fragment ions are also observed at *m/z* 287, 299 and 315 which are diagnostic ions for side chain cleavage due to the addition of the methyl group on the side chain.

The similarities in the fragmentation pattern of campesteryl and sitosteryl are due to the similarities in their side chain with sitosteryl having an additional methyl group attached to the side chain. However the addition of a carbon double bond in the side chain for stigmasterol affects the fragmentation dramatically as can be seen in the figures.

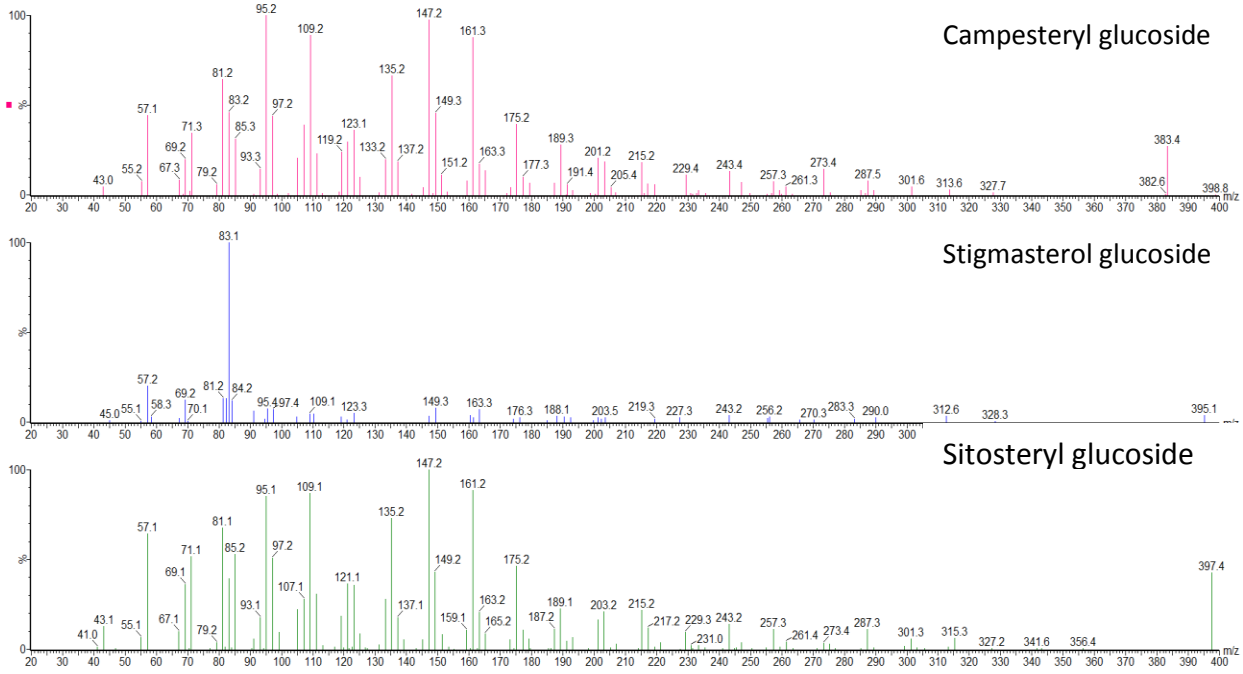

Figure 4-23. Comparison of steryl glucosides at collision energy of 20 V.

4.3.6.3 MRM development

MRM assays allow for targeted analysis of SGs with increased sensitivity and selectivity. MRM transitions of campesteryl glucoside (*m/z* 383.2) and sitosteryl glucoside (*m/z* 397.4) were *m/z* 95.2, 109.2, 147.2 and 161.3 due to the similarity in their structures. For stigmasterol glucoside the ions used for MRM assays were *m/z* 83.2 and 57.2 as shown in Table 4-3.

Table 4-3. MRM ion transitions for campesteryl, stigmasterol and sitosteryl glucoside.

Campesteryl glucoside ion transitions *(m/z)*	Stigmasterol glucoside ion transitions *(m/z)*	Sitosteryl glucoside ion transitions *(m/z)*
	57.2	
	83.2	
95.2		95.2
109.2		109.2
147.2		147.2
161.3		161.3

A linear response was observed at concentrations of 1-10 ppm SG (Figure 4-24). Above 10 ppm SG however the linearity of the ESI-MS response is lost and the response plateaus. This could be due to saturation of the ESI droplets at higher concentrations.

Kostiainen and Bruins [200] showed that the linear dynamic range is limited by an analyte's concentration, which effects the upper limit of the dynamic range. There have been several theories as to why the ESI response is limited at higher concentrations. One of these theories is from the limited amount of excess charge of the analyte. There is a point at which the analyte concentration exceeds the excess charge concentration, and this is where the ESI response levels off. [201] Another theory suggests that at high concentrations, the ESI droplets become saturated with analyte so that the droplet surfaces become filled, and ion ejection becomes inhibited. [200] Suppression and competition at higher concentrations can also occur. When a compound becomes more solvated it is expected to evaporate slower from the ESI droplet. [202]

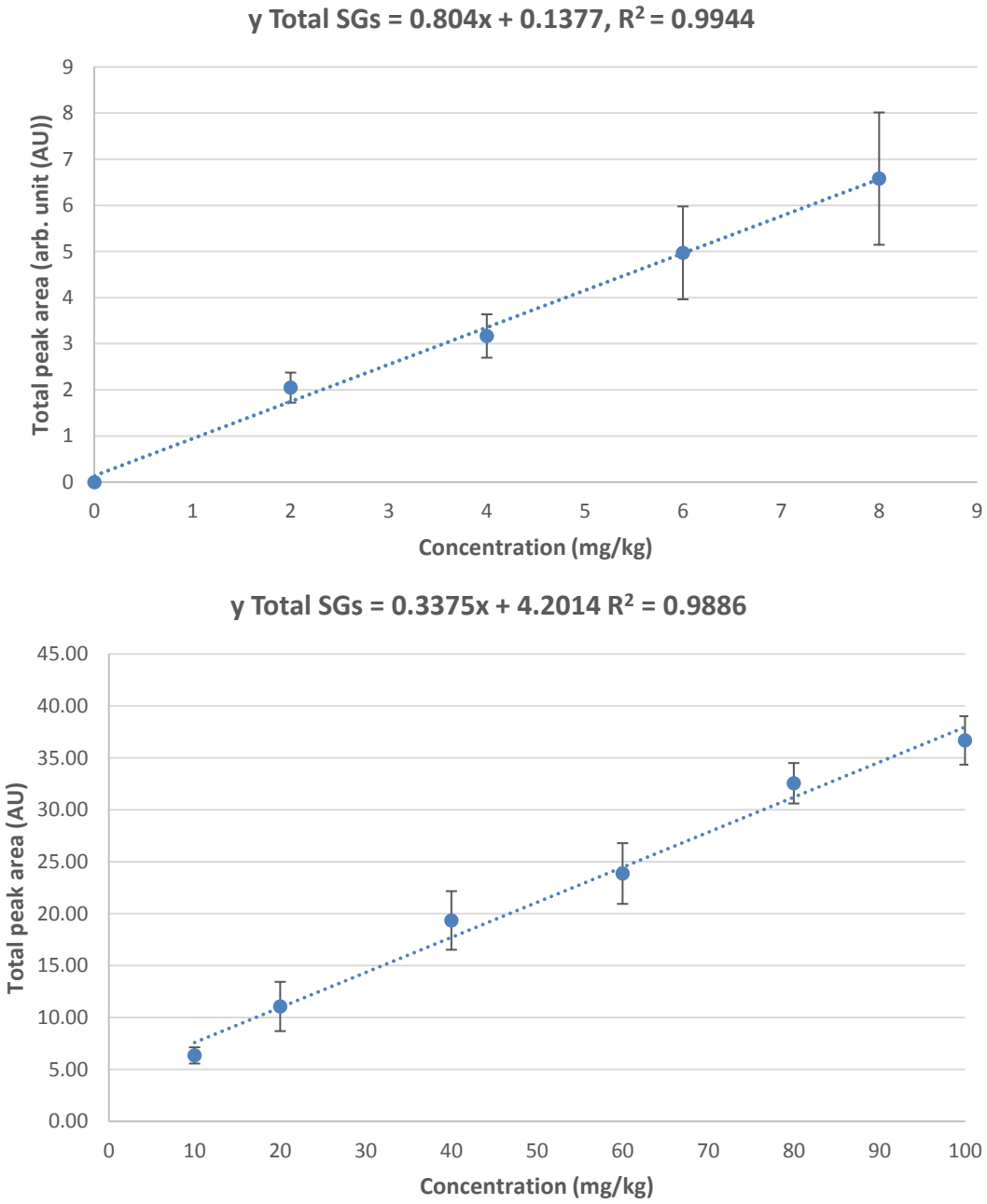

Figure 4-24. Calibration curves of total SGs at 0-10 mg/kg and 10-100 mg/kg from the transitions in Table 4-3 summed RICCs of the sodium containing molecules. Number of replicate measurements = 3.

4.4 Conclusions

UHPSFC-MS has proved to be a successful tool in the analysis of steryl glucoside samples. The method offers a robust and quantitative assay for the detection of SG, with excellent linear correlation ($R^2 > 0.99$). The UHPSFC-MS method requires minimal sample preparation including sample dilution compared to other techniques which require sample derivatisation such as GC-MS and offers rapid analysis times.

The importance of using both chromatography and mass spectrometry has also been shown for the analysis of steryl glucoside, due to fuel samples which were screened for the presence of SGs and isobars (ions of the same nominal mass, but differing exact masses) were detected. Using chromatography allowed for an extra confirmation aspect from matching retention times to standards. Direct infusion or shotgun analysis could therefore lead to mis-assignment of the SGs.

Tandem MS experiments have offered an understanding of fragmentation patterns of steryl glucosides. Similarities have been identified in campesteryl and sitosteryl fragmentation patterns, however for stigmasterol glucoside these vary due to the presence of the carbon double bond in the side chain altering the fragmentation pathways. A collision energy of 20 V has been identified as the optimal CE for the fragmentation of steryl glucosides due to the large number of fragment ions that have been identified.

MRM assays have been developed for targeted analysis of SGs with a number of MRM transitions being developed for the standard SGs. The limit of detection to ppm level, MRM is more sensitive than

Chapter 5: Surface analysis techniques for the JFTOT tube

5.1 Introduction

This chapter will focus on surface analysis techniques including DART-MS and SEM-EDX for the analysis of diesel injectors and jet fuel- thermal oxidation tester (JF-TOT) tubes.

5.1.1 Ambient ionisation mass spectrometry

Ambient ionisation refers to a range of mass spectrometric ionisation techniques performed under ambient conditions that allows the direct analysis of sample surfaces with little or no prior sample pre-treatment steps. Over the last few years, the field of ambient MS has progressed rapidly with a range of techniques being constantly developed. Desorption electrospray ionisation (DESI) [203] was first introduced in 2004 and direct analysis in real time (DART) [204] was introduced shortly afterwards in 2005. These were the first techniques to bring widespread attention to the concept of open-air surface analysis under ambient-MS conditions.

Ambient ionisation can be grouped into several subdivisions:

- One-step where desorption occurs by solid-liquid extraction followed by ESI, APPI, sonic spray or CI ion production mechanisms
- One-step plasma-based techniques followed by gas-phase chemical ionisation
- Two-step techniques involving thermal desorption or mechanical ablation and a separate step where secondary ionisation occurs
- Two-step techniques involving laser desorption/ablation [134]

The first group where desorption occurs by solid-liquid extraction includes DESI and easy ambient sonic-spray ionisation (EASI). [205] DESI uses charged solvent droplets for the sampling and ionisation of analytes on sample surfaces. Solid-phase analytes are extracted into a thin liquid film that is formed on the sample surface. Small, charged droplets impact this film, producing secondary droplets containing dissolved analytes, which are both driven upwards. These are electrically charged and lead to Coulombic

explosions forming smaller droplets assisting in the formation of ions by ion evaporation or by the charge-residue model. [134]

EASI uses sonic-spray ionisation [206] to form a stream of bipolar charged droplets to bombard the sample surface. This aids in desorption and ionisation of analyte molecules at ambient conditions. [134]

Another subdivision of ambient ionisation are plasma-based techniques involving metastable and reactive ions. These species react with the analyte directly or indirectly through proton and charge-transfer reactions. Examples of these techniques include DART and atmospheric solids analysis probe (ASAP). [207] ASAP is a direct analysis ionisation technique that is capable of analysing both solids and liquids. The method, uses a heated stream of nitrogen gas to thermally desorb components which are introduced to the ion source by a melting point tube inserted into the ASAP probe. This stream of hot gas causes the sample to evaporate from the tube's surface and then become ionised at atmospheric pressure by the corona discharge of an APCI source.

These techniques offer rapid, non-contact or limited sampling with the samples usually maintaining their original chemical and physical states, with applications in forensic science, biological and environmental areas. Surfaces such as paper, metallic surfaces *etc*. can also be characterised by ambient mass spectrometry techniques such as DESI-MS and DART-MS. Ion production relies heavily on the molecular interaction and charge-transfer processes which occur on the sample surface. The primary ions, for example protonated reagent species, are generated using electrospray ionisation for DESI, or a corona discharge for DART. [208-210]

5.1.2 Direct analysis in real time (DART)

DART-MS is a form of atmospheric pressure chemical ionisation (APCI), in which the sample can be analysed in the open air under ambient conditions. DART grew out of discussions between Laramèe and Cody at JEOL USA, Inc., regarding the development of an atmospheric pressure thermal electron source which could replace the radioactive sources commonly used in detectors for chemical weapons agents and explosives. [133, 204]

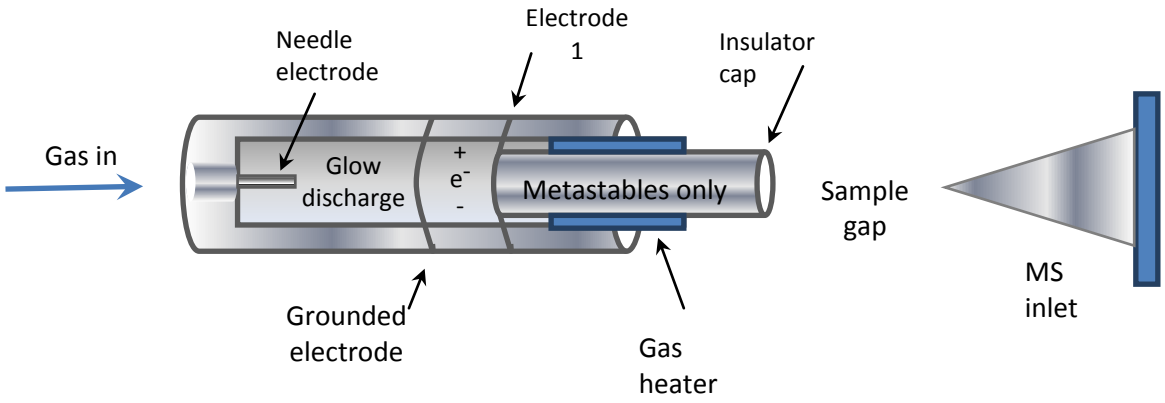

Figure 5-1. Schematic diagram to show the DART ion source and MS inlet. Reference adapted from www.nap.edu.

The source typically consists of two chambers through which the DART gas flows, as shown in Figure 5-1. In the first chamber, a corona discharge between a needle electrode and perforated disk electrode produces ions, electrons and excited state atoms known as metastable atoms or molecules. The cold plasma then passes through the second chamber where an electrode is used to remove cations from the gas stream. This plasma is then passed over a gas heater and onto a final grid electrode which removes oppositely charged species, leaving only neutral gas molecules and metastable species. [134]

The sample is introduced in the sample gap through simply placing the sample in front for solids or liquids are dripped into a glass capillary tube. The ability to heat the gas allows for control of both the thermal desorption and pyrolysis of samples in the gap in-between the DART source and mass spectrometer. Finally, as the gas exits the insulator cap, it is directed towards the sampling orifice of an API interface or may impinge on the sample surface at an angle suitable for its reflection into the entrance of the mass spectrometer. The insulator cap ensures that no exposure to high voltages occurs outside the plasma chamber. [204, 208, 211]

5.1.2.1 Ion formation

Ion formation in DART typically involves gas-phase ionisation processes, and DART-ionisation may generate positive or negative ions which are predominately even-electron species. Several ionisation mechanisms are possible in DART depending on the polarity and the reagent gas used, the proton affinity and ionisation potential of the analyte as well as the presence of dopants or additives. [204]

The simplest process in DART is Penning ionisation, [212] which involves transfer of energy from an excited gas molecule (M^*) to an analyte (S) having an ionisation potential lower than the energy of the (M^*) this produces a radical molecular cation ($S^{+\bullet}$) and an electron (e^-), as shown in Equation 5-1. [204]

$$M^* + S \rightarrow S^{+\bullet} + M + e^- \qquad \textbf{Equation 5-1}$$

Penning ionisation is the dominant reaction mechanism when nitrogen or neon is used in the DART source, however when helium is used another mechanism is seen, as shown below.

For helium, the dominant positive-ion formation mechanism involves the formation of ionised water clusters followed by proton transfer reactions as seen in the equations below. [204]

$$He(2^3S) + H_2O \rightarrow H_2O^{+\bullet} + He(1^1S) + e^- \qquad \textbf{Equation 5-2}$$

$$H_2O^{+\bullet} + H_2O \rightarrow H_3O^+ + OH^- \qquad \textbf{Equation 5-3}$$

$$H_3O^{+\bullet} + nH_2O \rightarrow [(H_2O)nH]^+ \qquad \textbf{Equation 5-4}$$

$$[(H_2O)nH]^+ + M \rightarrow MH^+ + nH_2O \qquad \textbf{Equation 5-5}$$

Negative-ion formation is achieved by surface Penning ionisation, where electrons produced by surface ionisation [213] (Equation 5-6) are rapidly thermalised by collisions with atmospheric pressure gas, producing thermal electrons which undergo electron capture

by atmospheric oxygen to produce O_2^- which reacts with the analyte to produce anions.[204]

$$M^* + \text{surface} \rightarrow M + \text{surface} + e^- \qquad \textbf{Equation 5-6}$$

The benefits of DART-MS include the speed and simplicity of the technique, with spectra being obtained in a few seconds and also requiring no or limited sample preparation which is useful for trace analysis. DART-MS does not produce multiply charged species or adduct ions, instead it only produces $[M + H]^+$.

5.1.3 Scanning electron microscope

The scanning electron microscope (SEM) allows the observation and characterisation of heterogeneous organic and inorganic material on a nanometre (nm) to micrometre (μm) scale. In SEM, the surface to be examined is irradiated with a focused electron beam, which can either be swept across the surface of the specimen to form images or be stationary to obtain an analysis at one position. There are a number of signals produced from the interaction of the electron beam with the sample; these include secondary electrons, backscattered electrons, characteristic X-rays and other photons (Figure 5-2).[145]

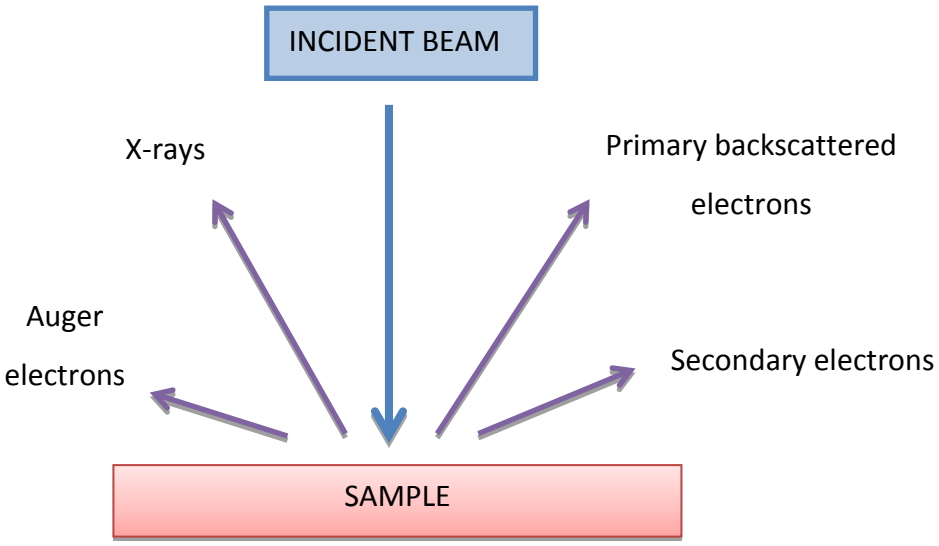

Figure 5-2. Illustration of several signals created by the electron beam and sample interaction in the scanning electron microscope. Figure adapted from www.jeol.co.jp.

The most commonly used signals include secondary and backscattered electrons. This is because they vary primarily as a result of differences in surface topology. Secondary electrons are produced by ejection of loosely bound outer orbital shell electrons from the sample through inelastic scattering. When the incident electron beam interacts with the sample, secondary electrons are produced from the emission of valence electrons from the sample. The energy of secondary electrons is very small, and the electrons are quickly absorbed by the sample. Only electrons generated at the top of the surface are emitted and analysed. Secondary electron signals are used to observe the topography of the sample surface.

Backscattered electrons are produced when primary beam electrons are elastically scattered backward and emitted out of the sample. Backscattered electrons possess higher energy than secondary electrons, and therefore can penetrate deeper into the sample surface. They are particularly sensitive to the composition of the sample. Therefore, this image is suitable for observing a compositional difference in the sample surface. [145]

As a result of electron bombardment X-rays are also emitted, this can yield qualitative identification of the sample. When a specimen is irradiated with an electron beam, inner

shell electrons of specimen atoms are ejected and vacancies are formed. Outer shell electrons transfer to the free vacancies and their excessive energy is emitted in the form of an electromagnetic wave or X-ray. Since the energies of individual shell electrons are determined by the type of elements, the X-rays generated by electron transfer are characteristic of the elements.

There are two methods of analysing X-rays, one by the wave-length dispersive X-ray spectrometer (WDX) and the other by an energy dispersive X-ray spectrometer (EDX). In WDX, the X-rays emitted from the specimen impact on the analysing crystal. This crystal, diffracts the X-rays and they then enter the detector and their wavelengths are measured. EDX analysis is more widely used due to its ease of operation and relative fast analysis compared to WDX and increased resolution. In addition multi-element simultaneous measurement can be detected by EDX analysis. This will be explained further in chapter 5.1.3.1. [214]

There are two major components of an SEM, these include the electron column and the control console. The electron column consists of an electron gun and electron lenses which influence the electron path. The control console consists of a cathode ray tube (CRT) viewing screen and controls for the electron beam. Figure 5-3 shows a schematic diagram of a scanning electron microscope (SEM).

The electron gun generates electrons and accelerates them to an energy in the range of 0.1-30 keV. Electrons are emitted from a white-hot tungsten filament.The beam emerges from a set of lenses that focus the electron beam to a small spot around 5-50 nm in diameter. The beam is then focused into the specimen chamber, where it interacts with the specimen sample. The beam current absorbed by the specimen can be detected and used to create images of the distribution of the current in the specimen. Electronic amplifiers are used to amplify the signal, such as a cathode ray tube. [214]

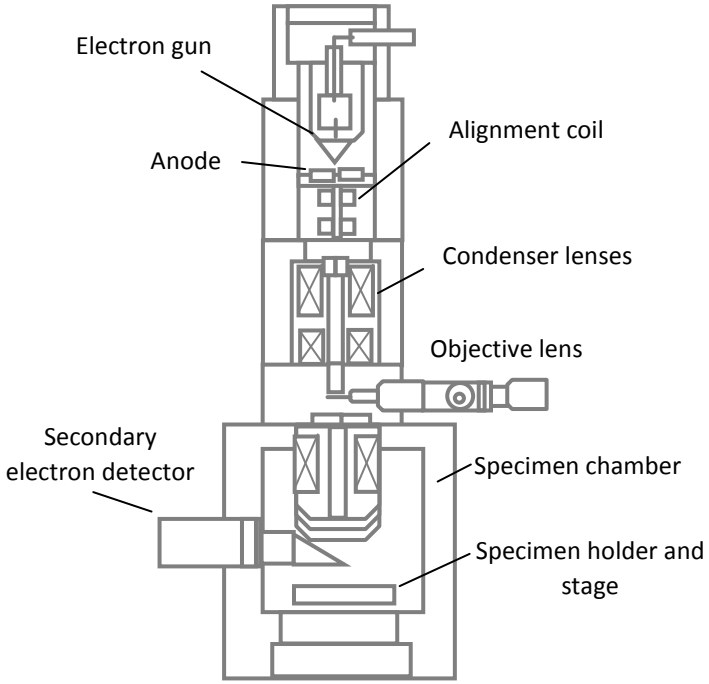

Figure 5-3. Schematic diagram of a scanning electron microscope (SEM). Reference adapted from Zhou *et al.* [144]

5.1.3.1 Energy dispersive X-ray spectrometer (EDX)

Characteristic X-rays emitted from samples have energies that are characteristic of individual elements. With energy dispersive X-ray spectroscopy (EDX), X-rays are detected by a Si(Li) semiconductor detector. The height of a current pulse generated by X-ray illumination is proportional to the energy of incident X-rays, therefore allowing characteristic X-rays from an unknown sample to be measured for elemental identification.

EDX is typically utilised in conjunction with SEM (known as SEM-EDX) and allows for semi-quantitative characterisation of the sample's chemical composition. The technique is non-destructive and relies on the interaction between X-ray excitation and the sample, see Figure 5-4. The impact of the electron beam on the sample may excite an electron in the inner shell, ejecting it from the shell (shown as ejected electron). An electron from an outer, higher energy shell then fills in the vacancy and the difference in energy between the higher-energy shell and lower-energy shell may be released in the form of X-ray emission, as shown as Lα, Kα and Kβ. The number and energy of the X-rays emitted from the specimen can be measured by the EDX spectrometer. X-rays emitted from the sample atom are characteristic in energy and wavelength of a specific element. Characteristic X-

rays emitted by the excitation of the electrons in the K shell are called K lines, whereas those emitted by the L and M shell excitations are known as L or M lines.

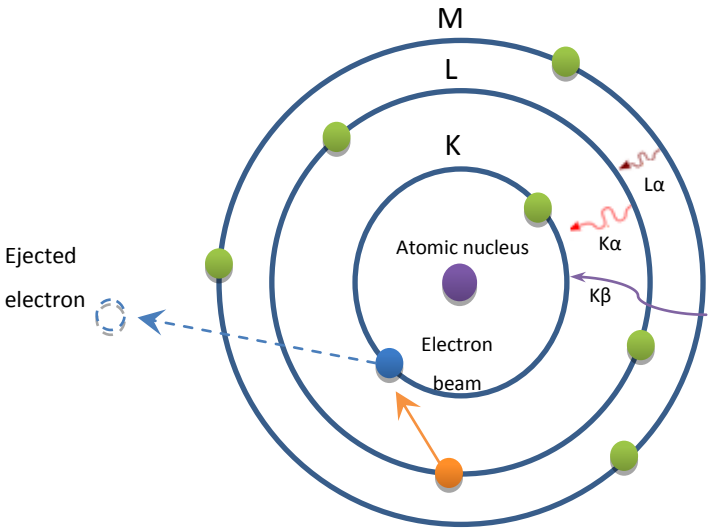

Figure 5-4. EDX schematic showing energy shells (M, L and K) and the impact of the electron beam with subsequent ejection of electrons. Reference adapted from www.ammrf.org.au.

5.1.3.2 Thermal oxidative stability of fuel

For fuels, stability to oxidation and polymerisation at the operating temperatures encountered in engines is an important performance characteristic. The thermal stresses experienced in engines may lead to the formation of undesirable components such as lacquers and deposits which are insoluble materials forming deposit layers on engine parts. Thermal stability measurements are related to the amount of deposits which are formed in the fuel system upon heating of the fuel. Initially, there was a test method for the thermal stability of fuel known as “test method D 1660- ASTM coker”, however this method was replaced by the ASTM D 3241/IP 323 test method for thermal oxidation stability of aviation turbine fuels (JFTOT procedure).The ASTM coker method required large volumes of fuel to be tested for a long period of time, and was a low throughput method with low precision and was therefore replaced with the JFTOT method. This method allows for the testing of the tendency of fuel to form deposits within the fuel injection system. [215]

5.1.3.2.1 Jet fuel thermal oxidation tester (JFTOT)

The thermal stability of the fuel can be measured by the quantity of deposits formed on metal surfaces, mimicking the diesel injector with conditions similar to those experienced in the diesel engine. It is known that thermally initiated fuel degradation is accelerated by the presence of oxygen through autoxidative processes involving free-radical chain reactions. [68]

The Jet Fuel Thermal Oxidation Tester (JFTOT) is used to test the thermal oxidative stability of fuel, the quantity of insoluble products formed under the conditions used in JFTOT provides a measure of the deposit-forming characteristics of the fuel tested. For these experiments, an Alcor JFTOT III was adapted to assess the deposit formation tendencies of different diesel fuels.

Figure 5-5 shows a schematic diagram of a JFTOT. Fuel is placed in a stainless steel sample reservoir, a motor-driven pump forces fuel through the system over an aluminium (or stainless steel) test piece (also known as JFTOT tubes).

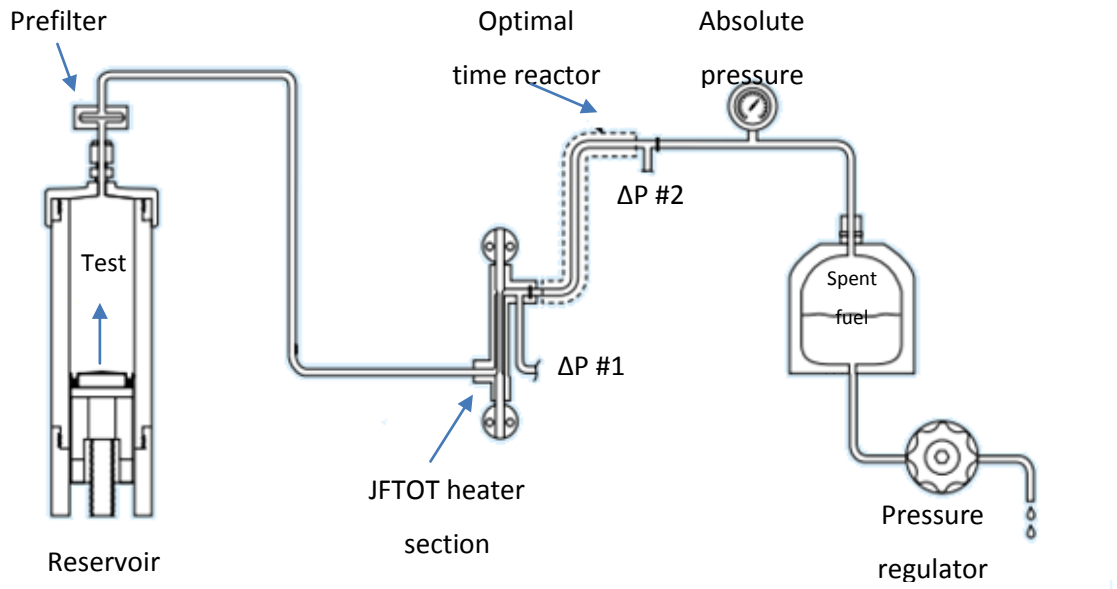

Figure 5-5. JFTOT schematic diagram including system reservoir, JFTOT heater section, and pressure regulator. Image adapted from www.paclp.com.

5.2 Experimental

Innospec undertook experiments using an adapted Alcor JFTOT III to assess the deposit formation tendencies of different diesel fuels (see Table 5-1). Fuel was placed in a stainless steel sample reservoir, aerated and purged. A motor-driven syringe pump forces the fuel out of the reservoir, through a prefilter, past the heater tube and through a precision stainless steel differential pressure filter at a flow rate of 3.0 mL/min.

The fuel was then passed over an aluminium test piece heated to 260 °C (which is seated in the JFTOT heater section), with a total test time of 2.5 hours and at the end of the test the metal test piece was cleaned with analytical grade toluene and acetone, dried and tested for deposit formation. The amount of deposits which adhere to the tube and the degree of plugging of the pressure differential filter are indicative of the thermal stability of the fuel at the test temperature.

Four jet fuel thermal oxidation tester (JFTOT) fuel tubes were tested by DART-MS; the fuels that were run through the JFTOT system were sampled before and after analysis through the system to account for any differences.

Table 5-1. JFTOT fuel tube and samples taken before and after analysis through the JFTOT system.

Sample	Before analysis	After analysis
JFTOT tube 1	Diesel # 81	Diesel # 82
JFTOT tube 2	Diesel # 83	Diesel # 84
JFTOT tube 3	Diesel # 85	Diesel # 86
JFTOT tube 4	Diesel # 87	Diesel # 88

5.3 Results and discussion: DART-MS analysis

DART-MS was initially investigated to analyse JFTOT fuels and JFTOT tubes, a range of optimisation experiments were undertaken to investigate ionisation gas temperatures and positioning of samples. In addition, accurate mass measurements were investigated to identify unknown components present in the samples.

5.3.1 JFTOT fuels analysis

Caffeine was used as calibration to align the axis of travel of the tube with the MS data of the deposited region on the tube. Figure 5-6 shows a spot of the caffeine sample was placed at either end of the deposited region of the JFTOT tube. Two peaks are identified in Figure 5-6 at either side of the deposited area, which appear at 0.46 and 2.45 minutes with an ion at *m/z* 195 identified as $[C_8H_{11}N_4O_2]^+$ protonated caffeine, and the sample peak at 1.47 minutes.

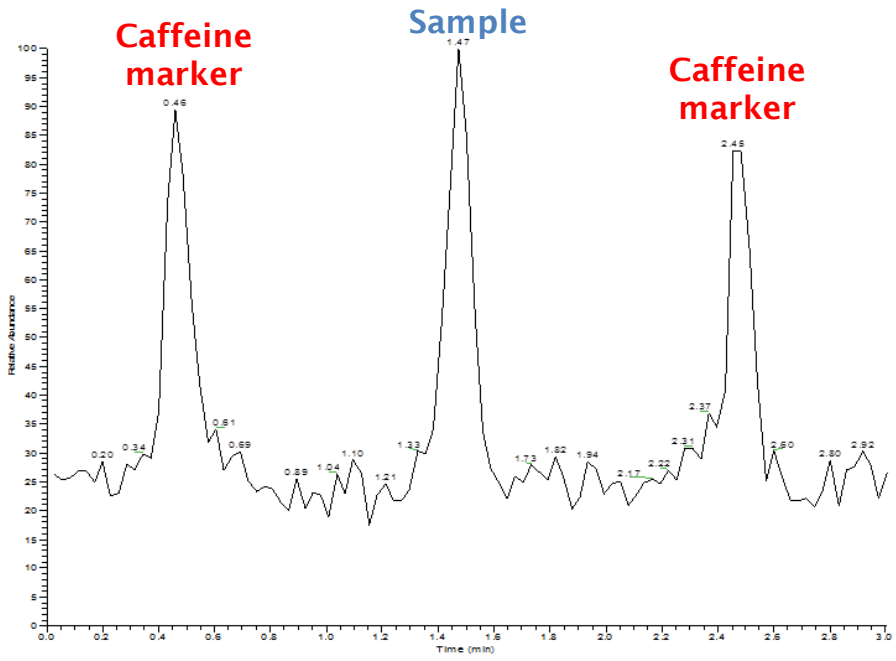

Figure 5-6. Chromatogram of caffeine marker placed at either end of the JFTOT tube on the DART-MS instrument.

The temperature of the ionisation gas was also optimised as it is seen as a key factor affecting ionisation. Ionisation is only possible when the compounds thermally desorb from the sampling surface and transfer into the gaseous phase.

Figure 5-7 shows the mass spectra of diesel fuel # 81 (rod 1, before analysis) at ionisation gas temperatures 150, 250, 350 and 450 °C.

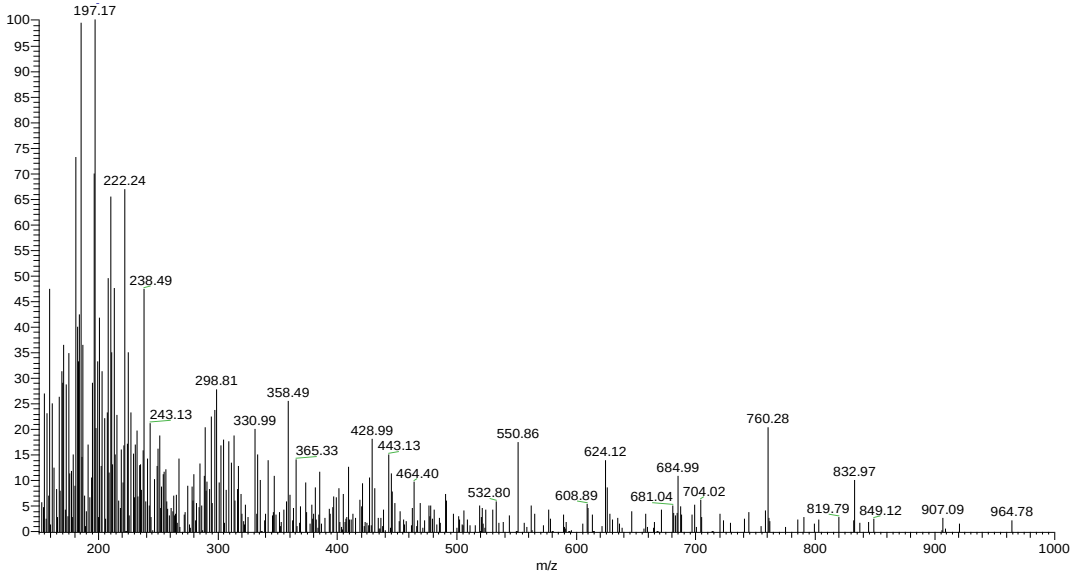

A. Ionisation gas temperature 150 °C

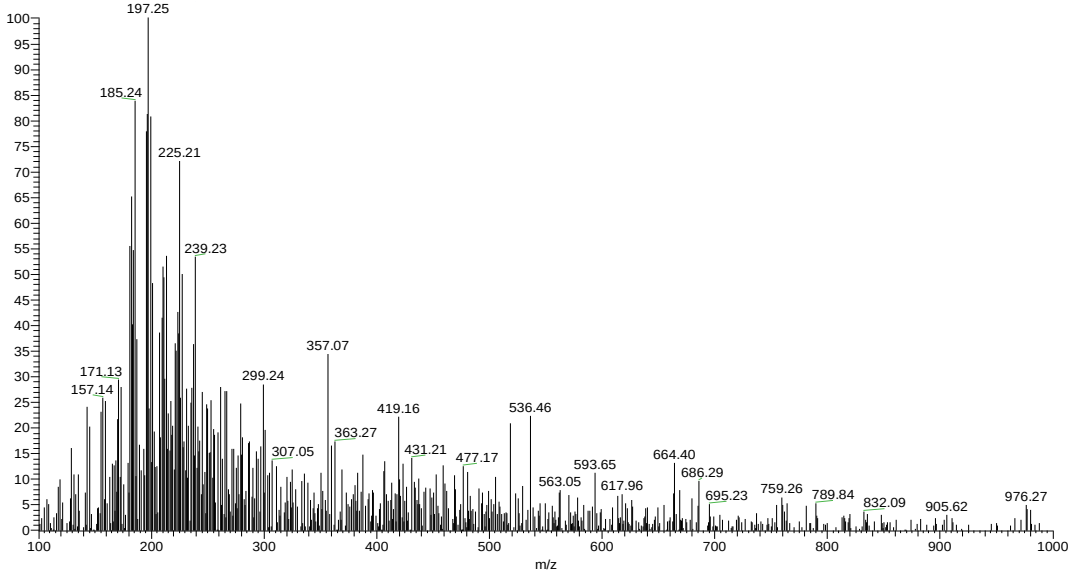

B. Ionisation gas temperature 250 °C

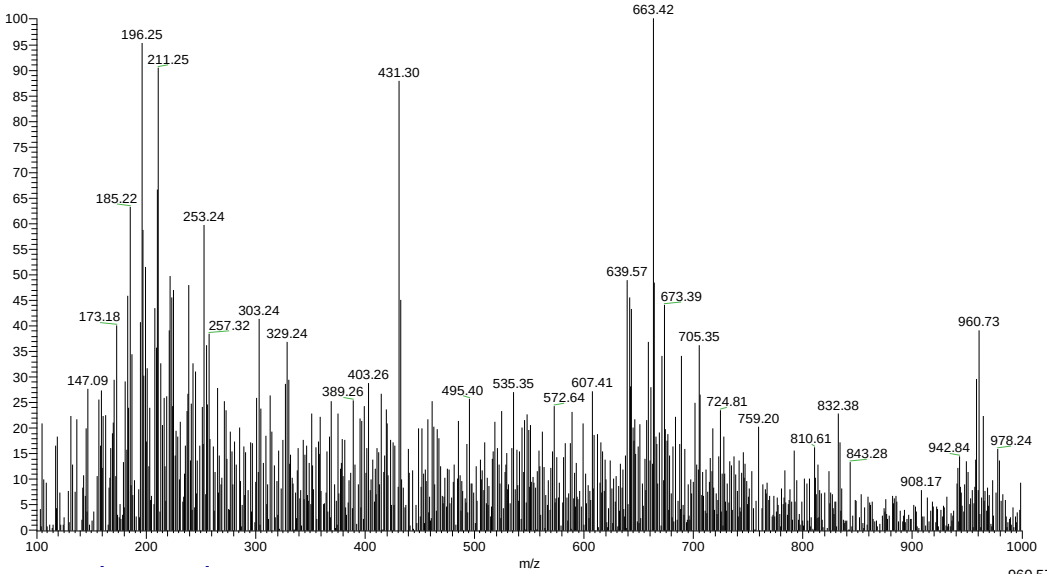

C. Ionisation gas temperature 350 °C

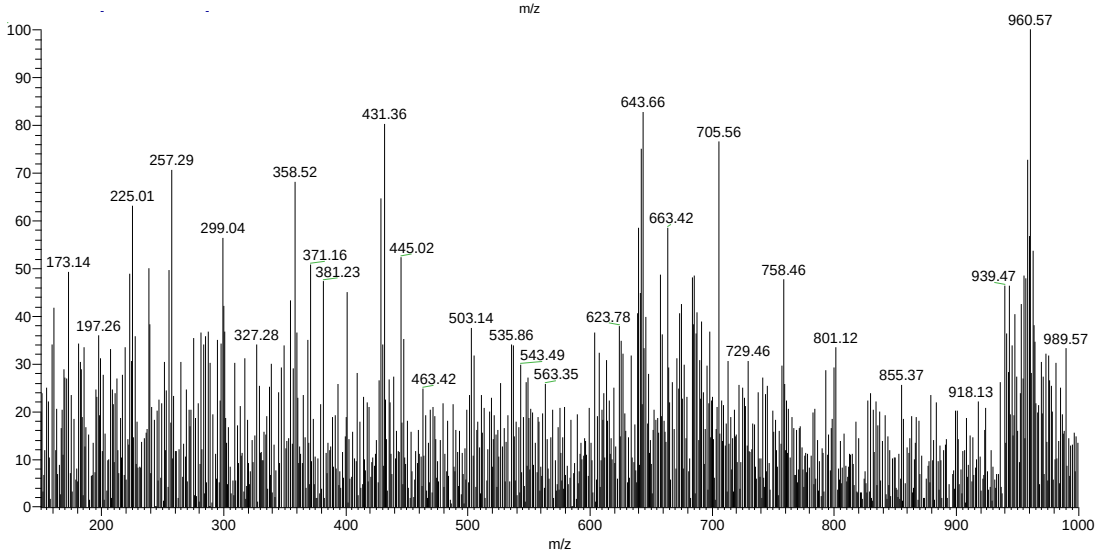

D. Ionisation gas temperature 450 °C

Figure 5-7. Mass spectra of diesel fuel # 81 (rod 1, before analysis) at a range of ionisation gas temperatures ranging from 150, 250, 350 and 450 °C (A-D respectively).

Figure 5-7 shows that as the ionisation temperature increases, as does the amount of higher molecular weight compounds due to the higher temperatures being able to desorb the less volatile compounds. These could be formed by combination reactions with other compounds present in the fuel. At 150 °C, the mass spectrum shows an increased amount of lower mass ions such as ions at *m/z* 185, 197 and 239. At 250 °C *m/z* 431, 610 and 663 are present, and as temperature increases to 350 °C and 450 °C these ions become increasingly more abundant with additional ions at *m/z* 956 and 960 observed.

The ion at *m/z* 610 was identified as dimethylsiloxane with an accurate mass measurement of $[C_{16}H_{52}NSi_8O_8]^+$ this ion is observed in the background signal obtained by DART-MS analysis. This ion is commonly seen in the background signal for DART-MS and other ambient ionisation techniques.

Figure 5-8 shows the mass spectra of diesel fuel # 82, which is of rod 1 where the fuel sample was taken after the analysis through the JFTOT system. The same trend at lower temperatures around 150/250 °C lower mass ions are observed in the range of 100-400 *m/z* units and as temperatures increase to 350 and 450 °C an increase in ions is seen at higher masses around *m/z* 900.

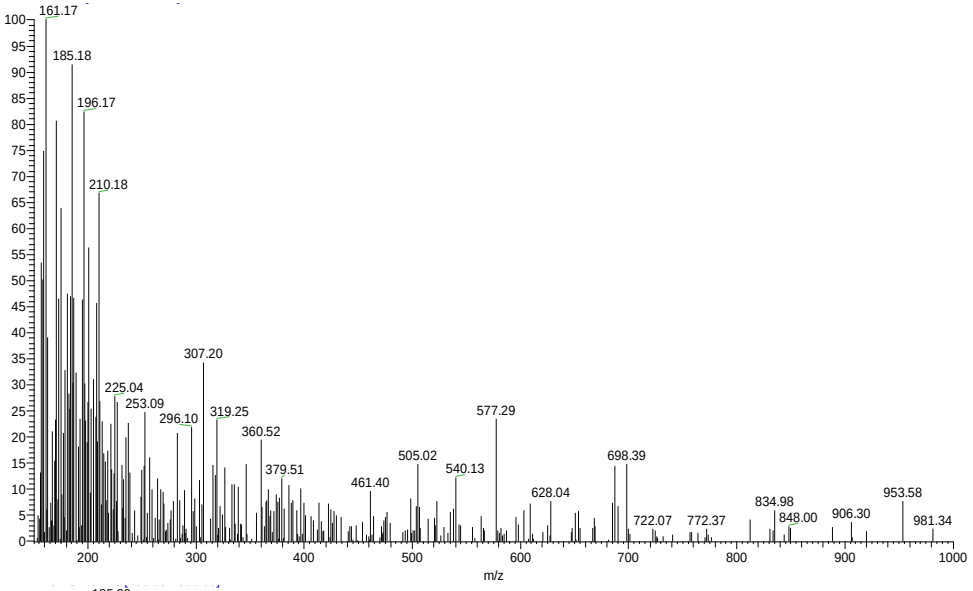

A. Ionisation gas temperature 150 °C

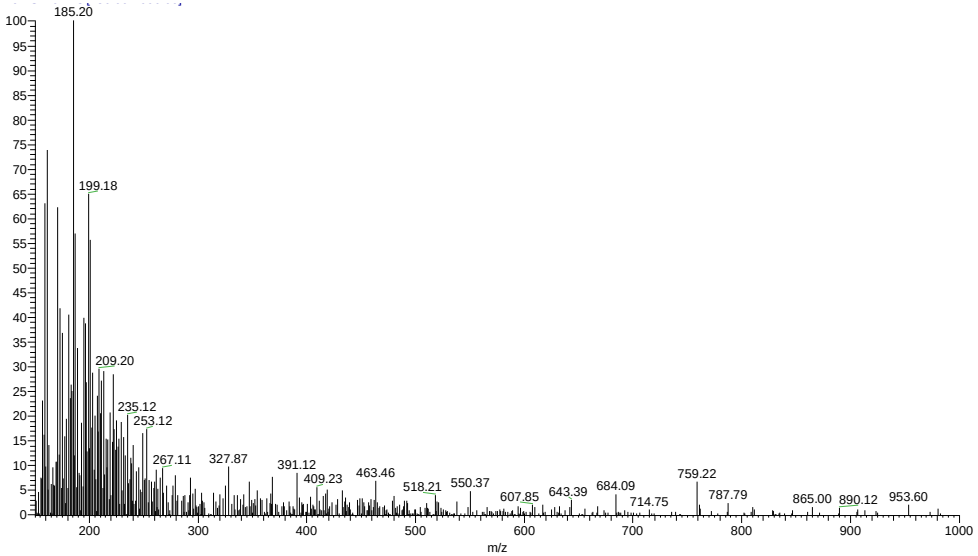

B. Ionisation gas temperature 250 °C

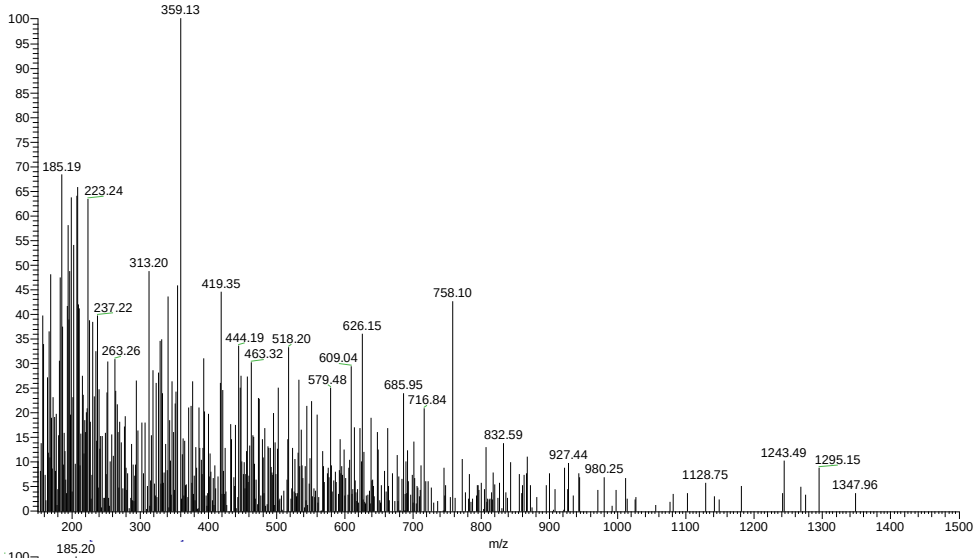

C. Ionisation gas temperature 350 °C

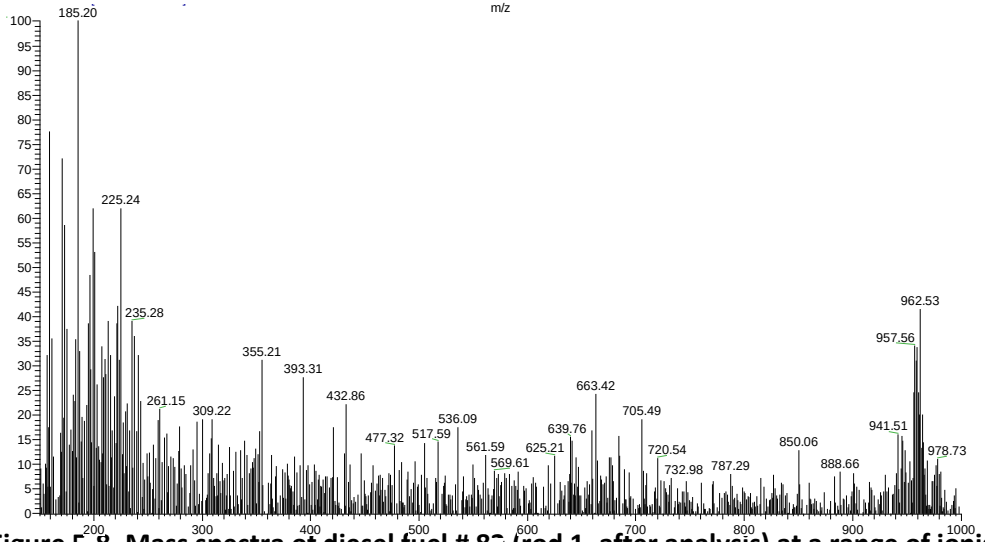

D. Ionisation gas temperature 450 °C

Figure 5-8. Mass spectra of diesel fuel # 8 (rod 1, after analysis) at a range of ionisation gas temperatures ranging from 150, 250, 350 and 450 °C (A-D respectively).

Table 5-2 shows ions observed for fuel samples # 81 and # 82 at a range of temperatures from 150-450 °C. By comparing fuel samples # 81 and # 82, significant differences can be seen between the samples. The ion at *m/z* 197 is not observed in fuel sample # 82 (after analysis) however it is seen abundantly in fuel sample # 81 (before analysis).

At higher temperatures (350 and 450 °C), higher molecular weight compounds are present especially in fuel sample # 81 and are subsequently lost in sample # 82. This could be as a result of the high temperatures and pressures experienced in the JFTOT system and diesel engine, dissociating and degrading these higher molecular weight components.

Table 5-2. Ions observed for fuel samples # 81 (before JFTOT analysis) and # 82 (after JFTOT analysis) for a range of ionisation gas temperatures ranging from 150-450 °C.

Temperature	Fuel sample # 81 before analysis- ions observed (relative abundance)	Fuel sample # 82 after analysis- ions observed (relative abundance)
150 °C	197 (100%) 222 (65%)	161 (100%) 185 (93%)
250 °C	185 (85%) 197 (100%) 225 (75%) 357 (35%) 536 (20%)	185 (100%) 199 (65%)
350 °C	196 (95) 211 (90%) 431 (85) 663 (100%) 960 (35%)	185 (70%) 359 (100%)
450 °C	257 (62%) 431 (55%) 641 (85%) 705 (80%) 960 (100%)	185 (100%) 663 (25%) 957 (35%) 962 (40%)

Other JFTOT fuels analysed (# 83/84, 85/86 and 87/88) also showed the same characteristic ions present as ionisation gas temperatures increase as shown in Table 5-3. In particular, ions of interest observed at 450 °C include ions at m/z 297, 624, 663 and 960.

Table 5-3. Ions of interest observed in diesel fuel #81-88 at two differing ionisation gas temperatures- 150 and 450 °C.

Ions of interest	Diesel fuel #81	Diesel fuel #82	Diesel fuel #83	Diesel fuel #84	Diesel fuel #85	Diesel fuel #86	Diesel fuel #87	Diesel fuel #88
At 150 °C	197,222, 238,550	161,197, 307,577	263,293, 311	184,207, 293,444	196,294, 391	185,199, 359	184,295	161,185, 267
At 450 °C	641,705, 960	185,663, 962	297,397, 601,694, 958	295,369, 624,696, 772	297,641, 663,947, 960	199,354, 663,699	354,371, 624,698	285,313

Table 5-3 shows a general trend, again that the higher molecular weight components at 450 °C are seen before JFTOT analysis and appear to dissociate after analysis. These lower molecular weight components could be possible precursors to deposit formation.

5.3.2 JFTOT tube analysis by DART-MS

JFTOT tubes were optimised using the optimised DART gun position at an inclined angle, in this position it was possible to successfully desorb analytes from the metal sample surface.

Figure 5-9 shows mass spectra obtained from DART-MS of the deposited region on JFTOT tube 1 at the desorption temperatures of 250 °C, 350 °C and 400 °C (A, B and C respectively). As temperature increases to 350 and 400 °C the abundance of an ion at *m/z* 371 is observed. Accurate mass measurement analysis of this ion will be investigated further on and will explore possible elemental formulae for this ion.

In Figure 5-9C, in addition to the ion at *m/z* 371 there is also an ion at *m/z* 387 which could be $[M + O]^+$ a product containing the addition of an oxygen atom.

Other ions at 250 °C are also seen such as ions at *m/z* 536, 610, 684 and 758. These ions appear to be 74 *m/z* units difference, and consistent with the presence of siloxanes. This was later confirmed through accurate mass measurements as a series of siloxanes that are also observed in background mass spectra, therefore the presence of siloxanes does not appear to be related to the JFTOT tube or deposit formation. Polydimethylsiloxanes are frequently employed in silicone oil, greases and

lubricants.

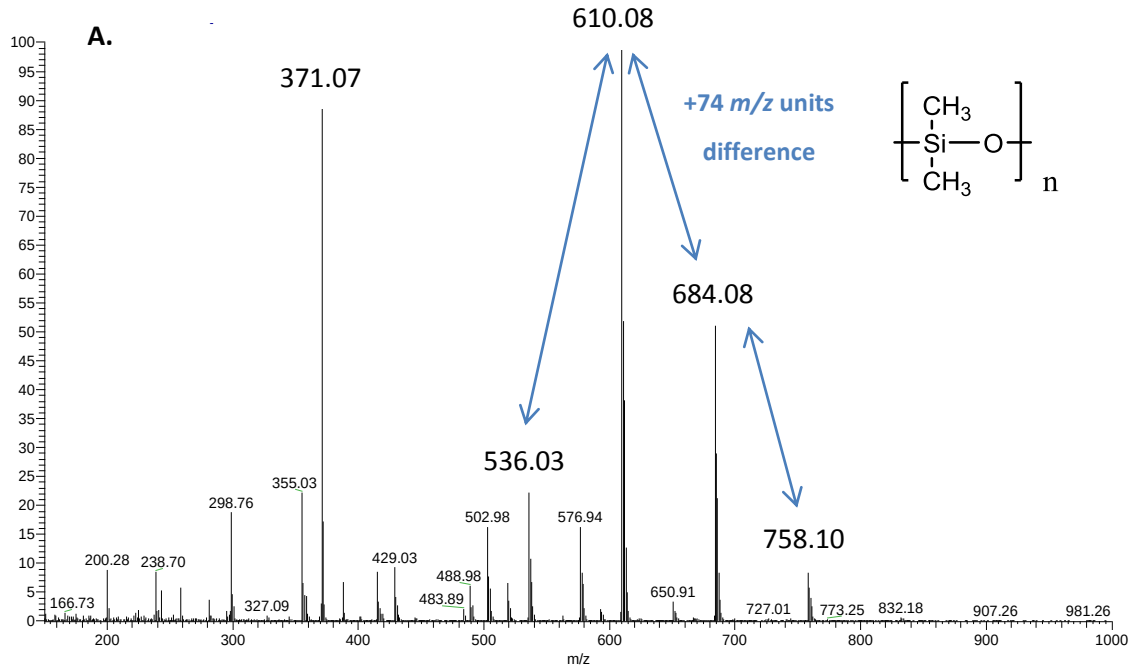
A.
610.08
371.07
+74 m/z units
difference
CH3
Si
O
CH3
n
684.08
536.03
758.10
355.03
298.76
502.98
576.94
200.28
238.70
429.03
488.98
483.89
650.91
166.73
327.09
727.01
773.25
832.18
907.26
981.26
m/z

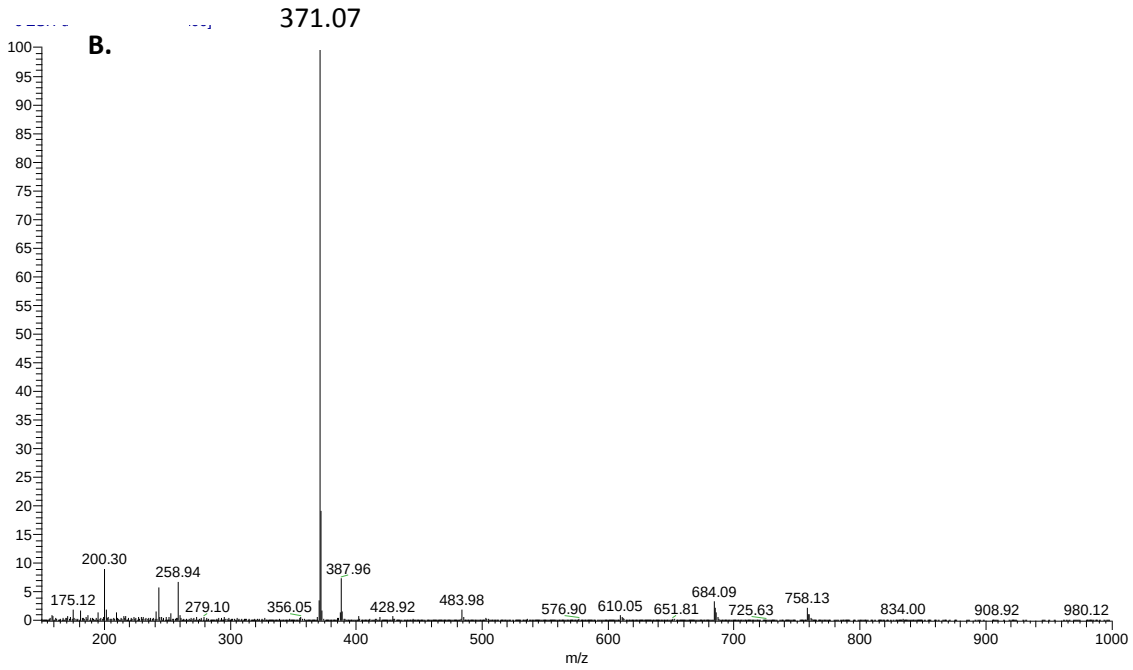
371.07
B.
200.30
258.94
387.96
175.12
279.10
356.05
428.92
483.98
576.90
610.05
651.81
684.09
725.63
758.13
834.00
908.92
980.12
m/z

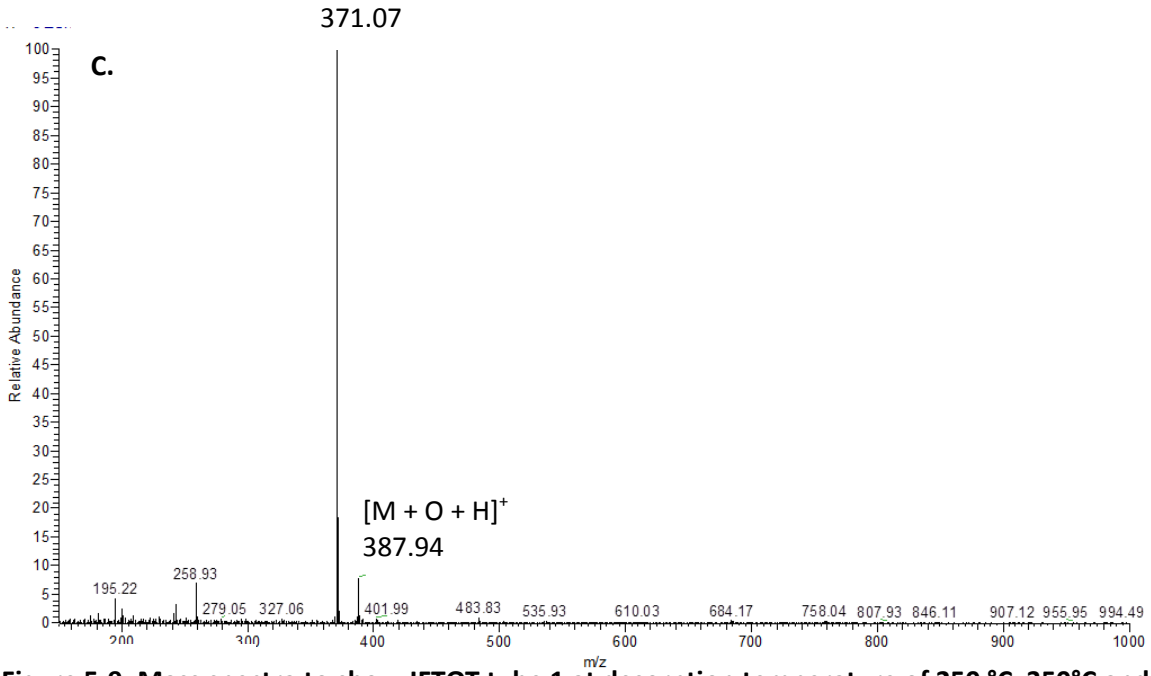

Figure 5-9. Mass spectra to show JFTOT tube 1 at desorption temperature of 250 °C, 350°C and 400°C (A, B and C, respectively).

The mass spectra of other JFTOT tubes 2, 3 and 4 are shown in Figure 5-10 also appear to show the presence of this ion at *m/z* 371 at high relative abundance. This ion of interest will be examined further using accurate mass spectrometry and tandem MS, this will allow the assignment of elemental formula and structure elucidation of this ion.

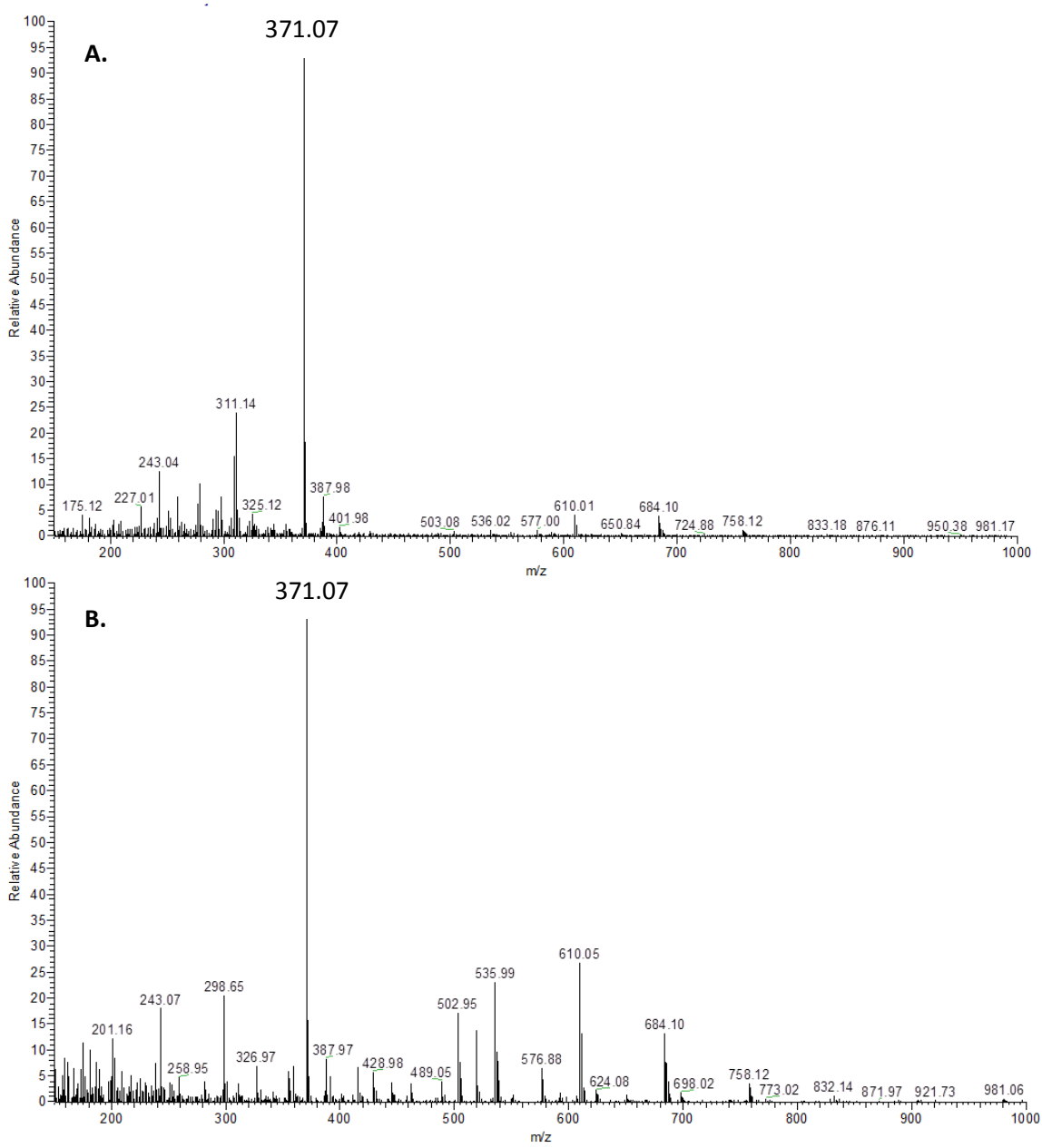
A.
371.07
Relative Abundance
m/z
311.14
243.04
387.98
175.12
227.01
325.12
401.98
503.08
536.02
577.00
610.01
650.84
684.10
724.88
758.12
833.18
876.11
950.38
981.17
B.
371.07
Relative Abundance
m/z
610.05
535.99
298.65
243.07
502.95
684.10
201.16
387.97
326.97
428.98
258.95
489.05
576.88
624.08
698.02
758.12
773.02
832.14
871.97
921.73
981.06

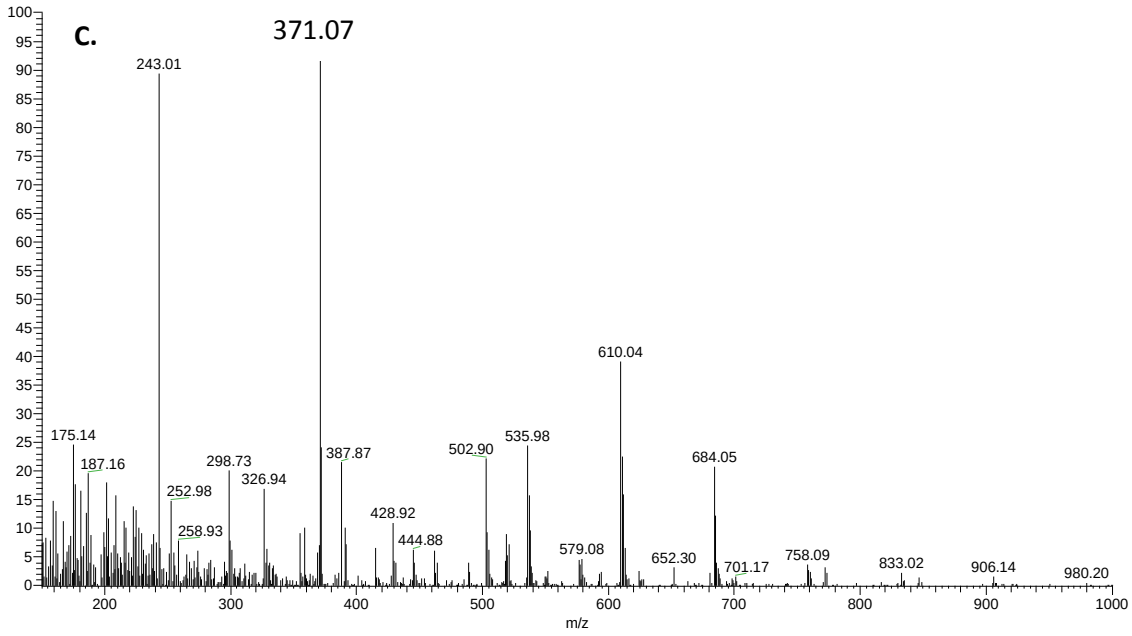

Figure 5-10. Mass spectra to show JFTOT tube 2, 3 and 4 at desorption temperature of 350 °C, as shown as A, B and C respectively.

5.3.3 Accurate mass measurements by DART-MS interfaced to Q-TOF MS (Synapt)

Initially, a background spectrum was obtained as shown in Figure 5-11, this mass spectrum is heavily dominated by ions at *m/z* 536, 610 and 684 again 74 *m/z* units apart, confirmed as siloxanes.

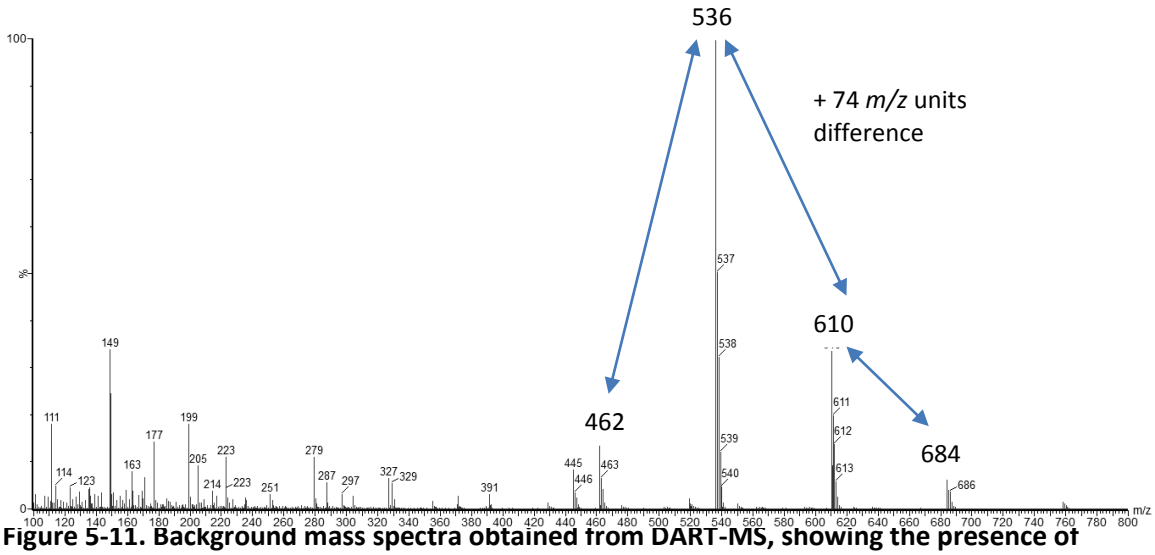

Figure 5-11. Background mass spectra obtained from DART-MS, showing the presence of dimethylsiloxanes.

During experimentation, a range of calibration standards were tested due to the absence of a lock mass typically used in ESI sources for accurate mass measurements. Lock mass allows for real-time recalibration of correction of *m/z* shifts typically arising from instrumental drift and other environmental and experimental conditions and is sprayed directly into the ESI source alongside the analyte. When the ESI source was replaced with the DART ion source this capability of lock mass introduction was removed due to the different instrumental configurations, therefore another calibration standard was investigated.

Reserpine was tested as a calibration standard, by placing a capillary tip dipped into the standard, and subsequently analysed. Again, this method supressed the ions of interest in the deposit and was not seen as an effective method of calibration.

Dimethyl siloxanes were then assessed as potential calibration standards, seeing as they appear as background ions in abundance. Siloxanes are a subgroup of silicones containing Si-O bonds with organic subgroups such as methyl, phenyl etc. attached to silicon, with a generic formula of $(RO)_3Si$. They are widely used for a variety of industrial processes such as detergents, cosmetics and textiles. [216]

Table 5-4 shows the calculated *m/z* and polydimethylsiloxane formula and the ion series. There are a range of silicone ion series observed in DART-MS literature, however the ion series that was observed in our DART-MS results was ion series C, which is attributed to ammonium ion adduct formation rather than protonation and incorporates the general formula of $[OSi(CH_3)_2)_n + NH_4]^+$

Table 5-4. Mass reference list for mass calibration in positive-ion DART-MS using polydimethysliloxanes.

Calculated *m/z*	Polydimethylsiloxane formula	Ionic series
462.1480	$[C_{12}H_{40}NSi_6O_6]^+$	C
536.1647	$[C_{14}H_{46}NSi_7O_7]^+$	C
610.1841	$[C_{16}H_{52}NSi_8O_8]^+$	C
684.1941	$[C_{18}H_{58}NSi_9O_9]^+$	C
758.6552	$[C_{20}H_{64}NSi_{10}O_{10}]^+$	C

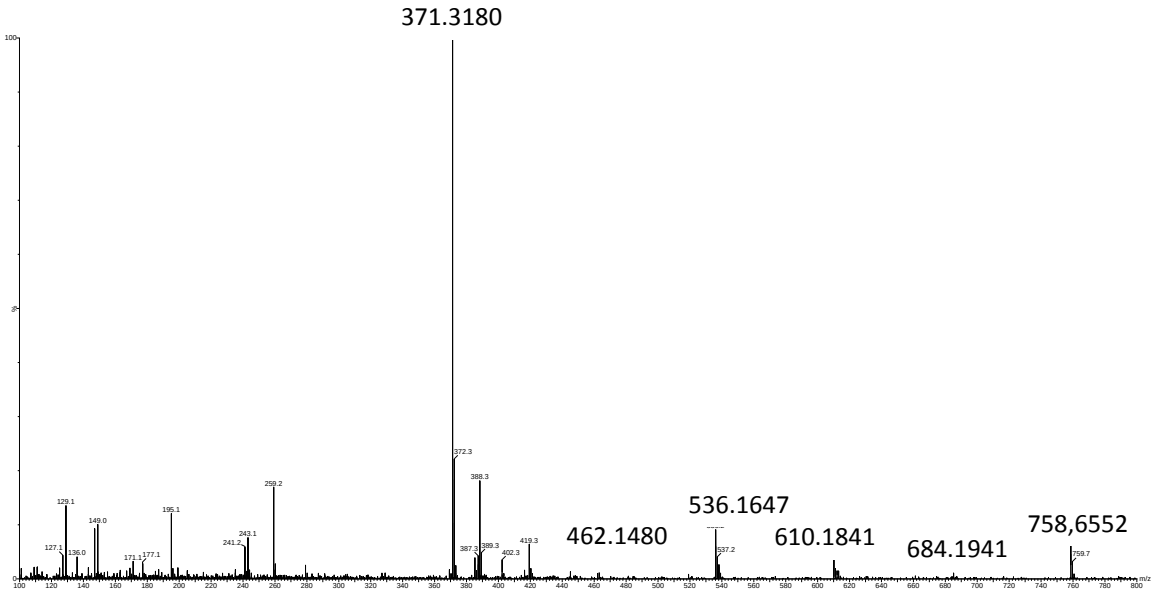

Figure 5-12. Mass spectra for JFTOT tube 1, showing deposited region with base peak ion at *m/z* 371.3 and calibration ions at *m/z* 462.2, 536.2, 610.2, 684.2 and 758.2.

Figure 5-12 shows the mass spectra obtained for JFTOT tube 1 in the deposited region, showing the base peak ion at m/z 371.3180 and in addition dimethylsiloxane calibration ions at *m/z* 462, 536, 610, 684 and 758.

Table 5-5 shows accurate mass measurement information for ion at *m/z* 371.3180 including calculated mass, error (in ppm and mDa) and elemental formula. The formulae containing nitrogen compounds are unlikely to be correct, due to the absence of nitrogen from the fuel. Therefore the only likely formula would be of $[C_{22}H_{43}O_4]^+$, which from literature could be an adipate.

Table 5-5. Accurate mass measurement data for ion at *m/z* 371 including calculated mass, error (in mDa (millidaltons) and ppm (parts per million) and elemental formula.

Mass	Calculated mass	mDa	Ppm	Formula
371.3180	371.3180	0.5	1.3	$C_8H_{35}N_{16}O$
	371.3175	1.0	2.7	$C_{23}H_{39}N_4$
	371.3165	2.0	5.4	$C_{21}H_{47}NOSi_2$
	371.3206	-2.1	-5.7	$C_{19}H_{43}N_4OSi$
	371.3207	-2.2	-5.9	$C_{12}H_{39}N_{10}O_3$
	371.3161	2.4	6.5	$C_{22}H_{43}O_4$

The general structure of adipate ($C_6H_8O_4$) is shown in Figure 5-13A and the structure of dioctyl adipate ($C_{22}H_{42}O_4$).

A.

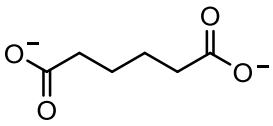

B.

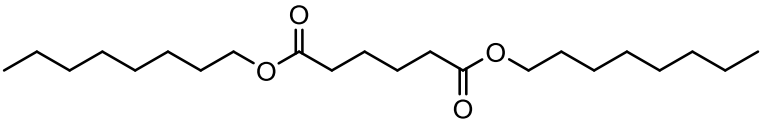

Figure 5-13. A. General structure of adipate, B. Structure of dioctyl adipate.

Literature has also confirmed the use of oxygenated fuel as alternative fuels, and only till recently the use of diethyl adipate (DEA) $C_{10}H_{18}O_4$ has been investigated. DEA has been mixed with diesel fuel at normal pressure at temperature, due to its high oxygen content and low tendency to form soot deposits, the use of DEA has increased. DEA can be synthesised relatively easily through the esterification of adipic acid and ethanol in the presence of concentrated sulfuric acid. It also has excellent physico-chemical properties such as low toxicity, corrosivity and reactivity for application to diesel engine. [217-221]

Dioctyl adipate (DOA), is also typically used in the aerospace and automative industries, due to its good thermal conductivity and large specific heat capacity. They can be used as a plasticiser for PVC and can be blended with other plasticisers. Di(2-ethylhexyl) adipate

and diisooctyl adipate has also been seen to be used in fuel lubricants and as plasticiser. [217, 222]

Plasticisers are additives that serve to increase the polymer's flexibility, elongation and ease of processing. Adipate esters have also been frequently used in hydraulic fluids, in particular for maritime, offshore drilling and construction applications where the need for an environmentally safe fluid is needed. [148]

5.3.3.1 Tandem MS experiments by DART-MS

Tandem MS investigations were carried out for structure elucidation of the ion of interest and an understanding of the fragmentation patterns.

Collision induced dissociation (CID) product ion mass spectrum were acquired for *m/z* 371, Figure 5-14A, B and C refer to mass spectra obtained at a range of collision energies (CE) at 3 V, 5 V and 10 V, respectively. At CE of 10 V, the collision energy is too high and the $[M + H]^+$ ion does not remain intact and also fragment ions at *m/z* 241 and 259 are lost. At CE 5 V, both fragment ions at *m/z* 241 and 259 are low in abundance and the optimal collision energy is observed at CE 3 V where both the protonated molecule and fragment ions remain.

Figure 5-15 shows tandem mass spectrum at CE 3 V, showing the fragment ions at *m/z* 129, 147, 241 and 259 and $[M + H]^+$ at *m/z* 371. Ions at *m/z* 147, 259 and 371 are separated by 112 *m/z* units, and could relate to the loss of an octyl group in the structure. The fragmentation pattern of this sample will be examined against NIST library in section 5.3.5.

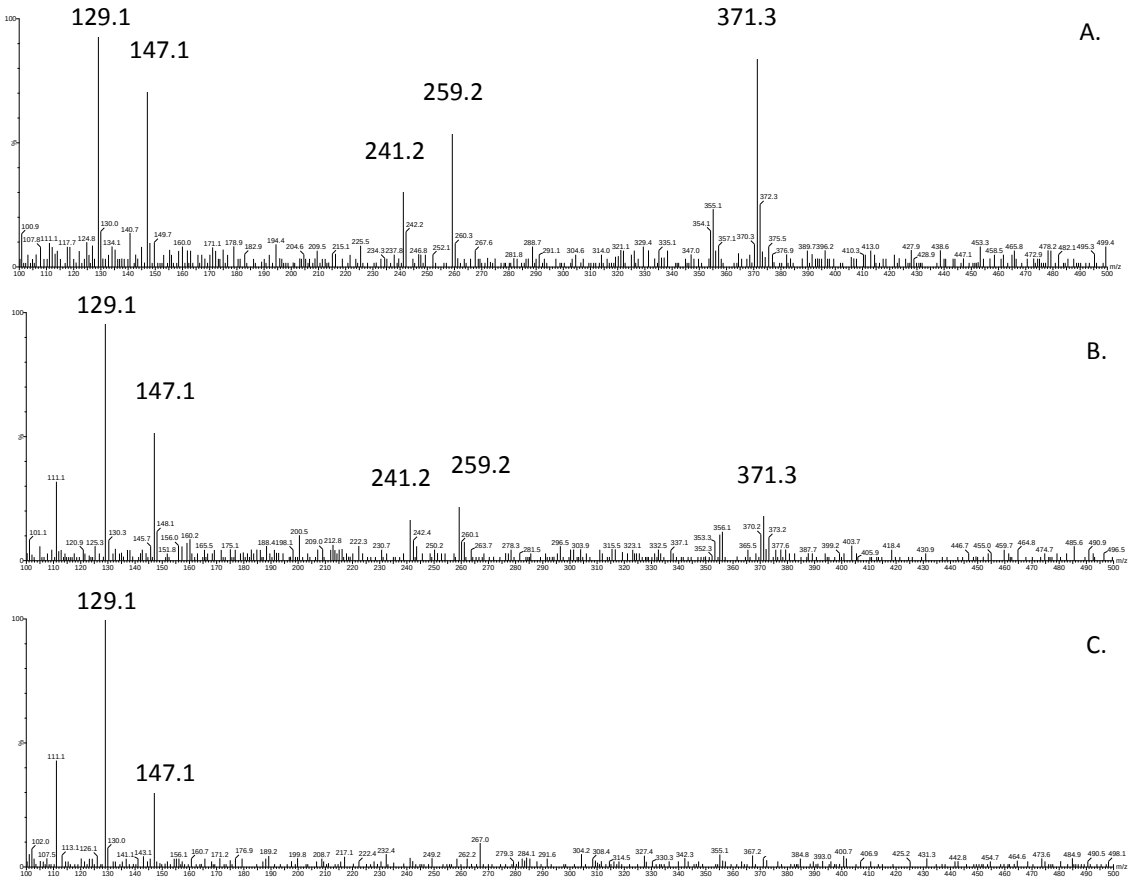

Figure 5-14. Tandem mass spectra for ion at *m/z* 371, A. acquired at collision energy (CE) 3 V, B. acquired at CE 5 V and C. acquired at 10 V.

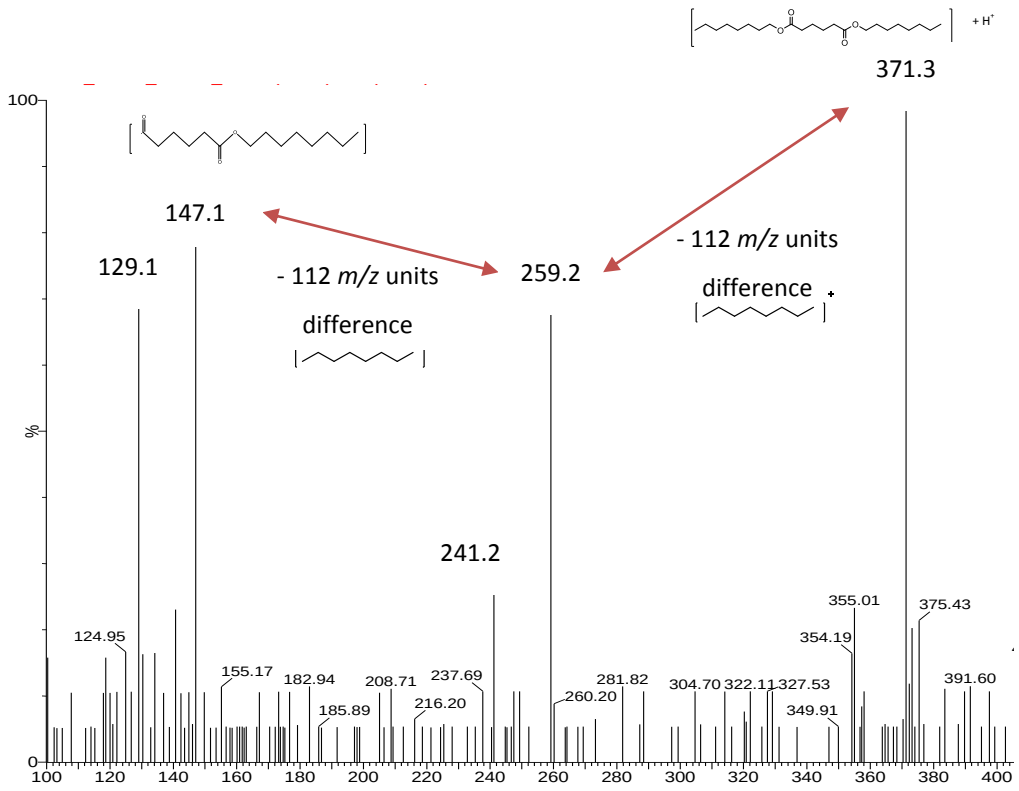

Figure 5-15. Tandem mass spectra of ion at *m/z* 371 at CE 3V, structures are shown for possible fragments.

5.3.4 FT-ICR MS analysis of JFTOT tube solvent extract

JFTOT tube 3 was also analysed using Fourier transform-ion cyclotron resonance mass spectrometry (FT-ICR MS). The deposited region of the JFTOT tube was extracted into methanol and analysed by positive-ion electrospray ionisation (ESI) FT-ICR MS. The resulting mass spectrum is shown in Figure 5-16. A base peak ion is observed at *m/z* 393 $[M + Na]^+$, which could relate to the ion at *m/z* 371 $[M + H]^+$ previously seen in the DART-MS data. The accurate mass measurement results of this ion give an elemental formula of $C_{22}H_{42}O_4Na$, which again suggests the presence of adipate.

Also present in the mass spectrum are FAME oxidation products with ions at *m/z* 331 $[C18:3 + O + Na]^+$, 349 $[C18:2 + 2O + Na]^+$, 363 $[C18:3 + 3O + Na]^+$ and ions at *m/z* 379 referring to $[C18:3 + 4O + Na]^+$.

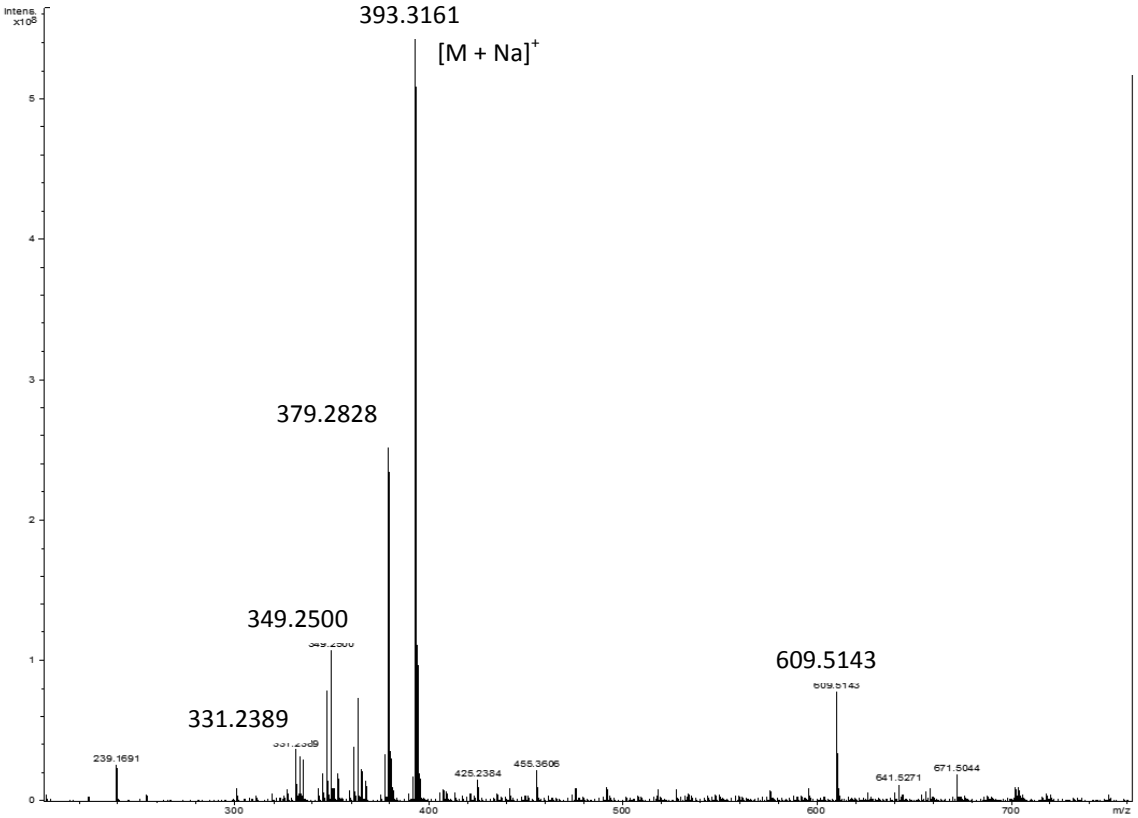

Figure 5-16. Positive ion electrospray ionisation FT-ICR mass spectrum obtained for solvent extract sample of JFTOT tube 1.

The positive ion electrospray ionisation mass spectrum above shows the ion at *m/z* 393 $[M + Na]^+$. To force the formation of protonated species formic acid was added to the sample as shown in Figure 5-17. Here, the base peak ion is shown as *m/z* 371.3164 $[M + H]^+$ the accurate mass measurement of this ion gave an elemental formula of $C_{22}H_{43}O_4$ which again confirms the DART-MS data and could possibly show the presence of adipate in the deposited region of the JFTOT tube.

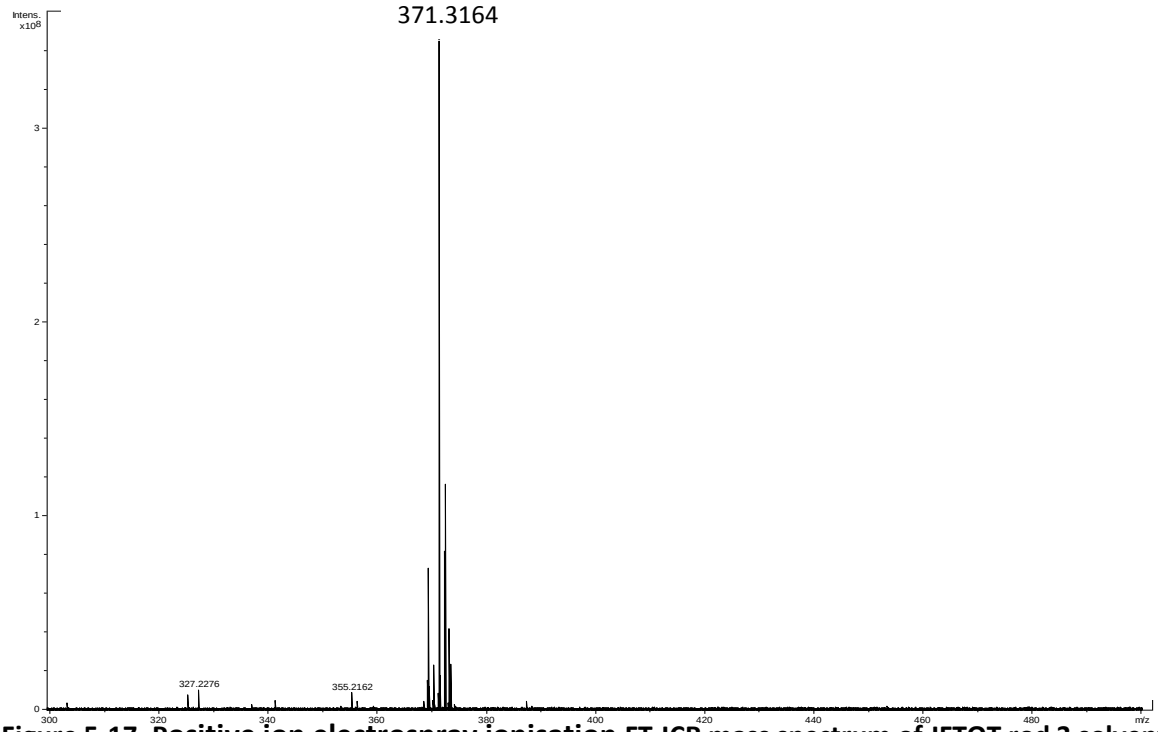

Figure 5-17. Positive ion electrospray ionisation FT-ICR mass spectrum of JFTOT rod 3 solvent extract sample, with addition of formic acid to force protonation.

5.3.4.1 FT-ICR MS analysis; tandem MS experiments

Tandem MS experiments were also performed on the ion at *m/z* 371 as shown in Figure 5-18, where A, B and C refer to the use of collision energies of 0, 3 and 6 V.

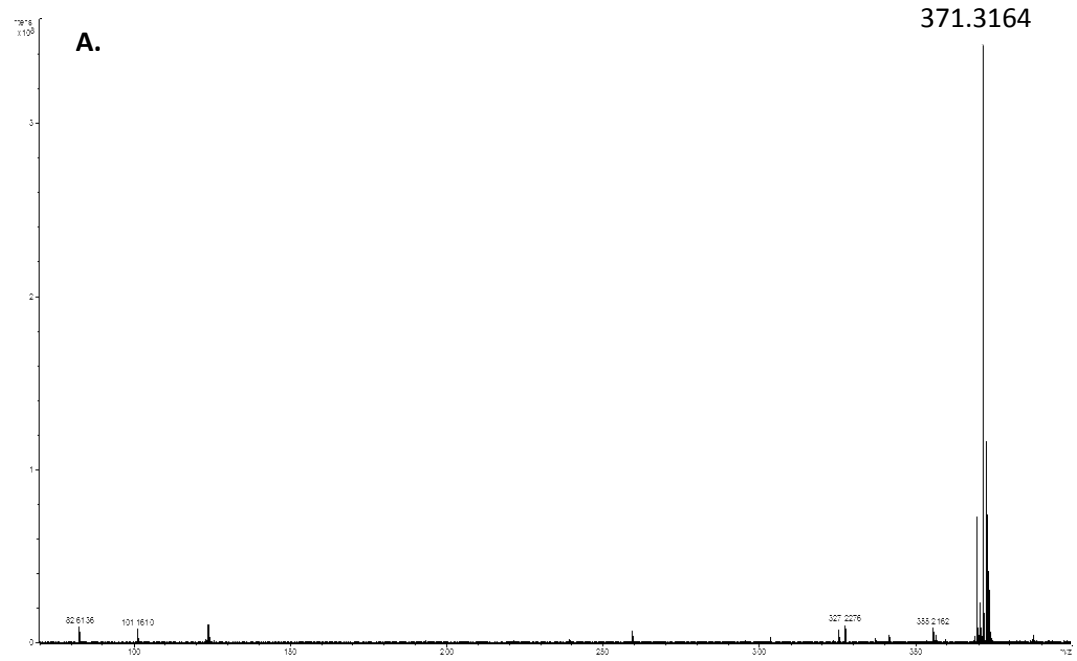

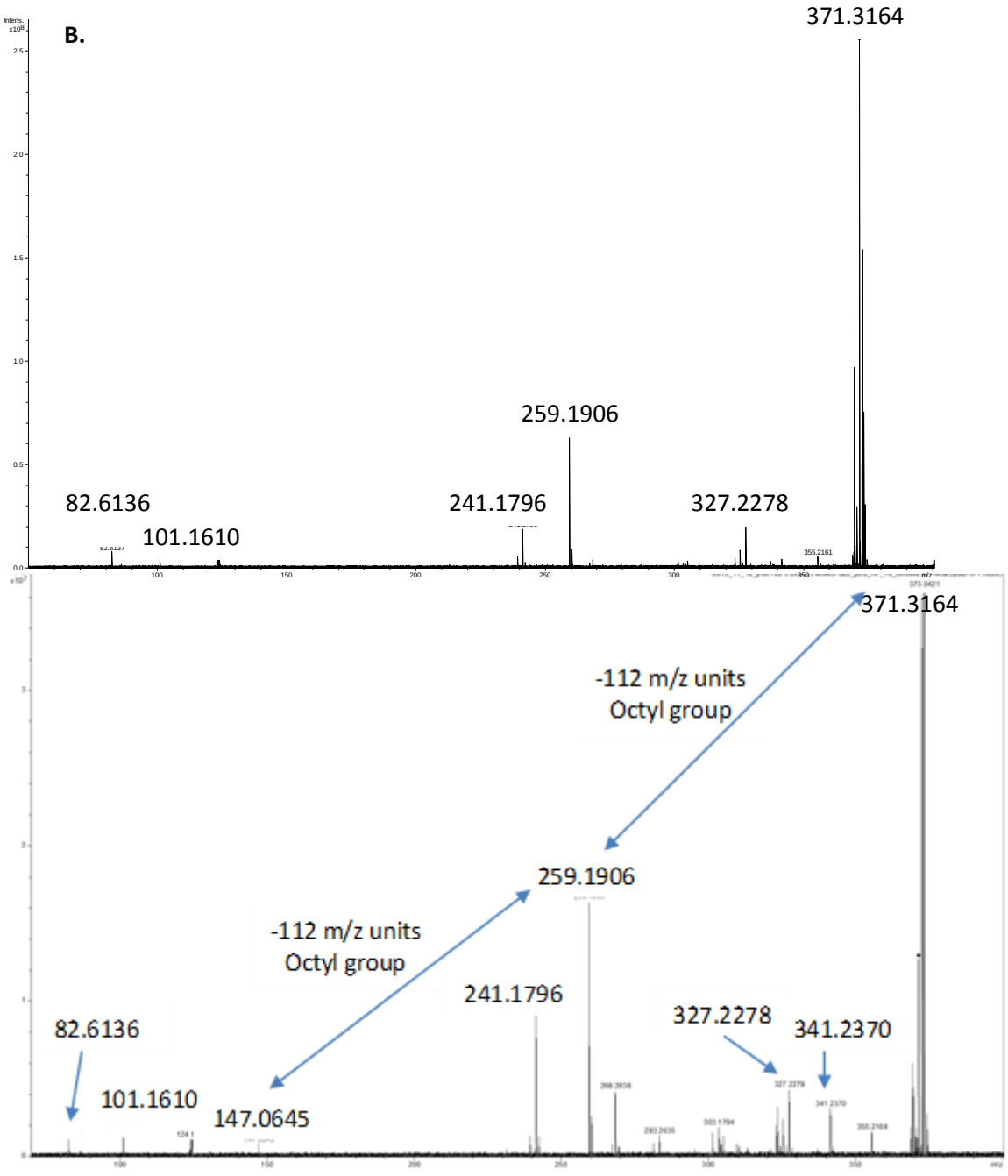

Figure 5-18. Positive ion electrospray ionisation product ion mass spectra obtained from the FT-ICR MS for ion at *m/z* 371, A, B and C refer to collision energy of 0, 3 and 6 V, respectively.

Figure 5-18A shows that at CE of 0 V, no fragmentation is observed, only the intact protonated molecule. At CE 3 V, fragment ions at *m/z* 327, 259, 241, 101 and 82 are

observed. However at CE 6 V the following fragment ions can be observed at *m/z* 341, 327, 259, 241, 147, 101 and 82. The ion at *m/z* 341 shows a loss of 30 *m/z* units which could refer to the loss of a C_2H_6 group, which could occur from the proposed structure of a dioctyl or diisooctyl adipate compound or the loss could also refer to a $[CH_2O]^+$ group which would not occur from adipate group. An ion with the loss of 112 *m/z* units is also observed which could refer to the loss of an octyl group which would readily occur in the adipate compound.

The mass spectra obtained from tandem MS experiments using DART-MS and FT-ICR MS will be compared to the GC-MS NIST library database for mass spectra with similar fragmentation patterns.

5.3.5 GC-MS data from the NIST library

Electron ionisation mass spectra were obtained from a database search for the elemental formula $C_{22}H_{42}O_4$ as shown in Figure 5-19 and Figure 5-20, these spectra show the best matches for adipate. Figure 5-19 (A-D) show the four mass spectra with the best match in comparison to positive-ion ESI CID product ion mass spectra obtained by DART-MS and FT-ICR MS data.

In particular, A (dioctyl adipate) and D (diisoctyl adipate) are two good candidates with a series of fragment ions being identified at *m/z* 29, 43, 57, 71 and 85 all with a 14 *m/z* difference (CH_2) Together with a base peak ion identified at *m/z* 129, other fragment ions at *m/z* 147, 241, 259 and molecular ion at *m/z* 370. Both of these mass spectra from the NIST library search gave comparable data obtained from DART-MS and FT-ICR MS.

The proposed fragmentation scheme is shown in Figure 5-21. Here the molecular ion at *m/z* 370 undergoes fragmentation to produce fragment ions at *m/z* 129 and 241. The DART-MS and FT-ICR MS data also shows ions at *m/z* 147, 259 and 371 which all have a loss of 112 *m/z* units which could refer to the loss of an octyl group (C_8H_{16}). These are likely to be fragments from dioctyl adipate and diisoctyl adipate.

Figure 5-20 E-G shows three mass spectra with the same elemental formula ($C_{22}H_{42}O_4$). These mass spectra however do not show the characteristic fragment ions that have been

obtained from DART-MS and FT-ICR MS experiments.

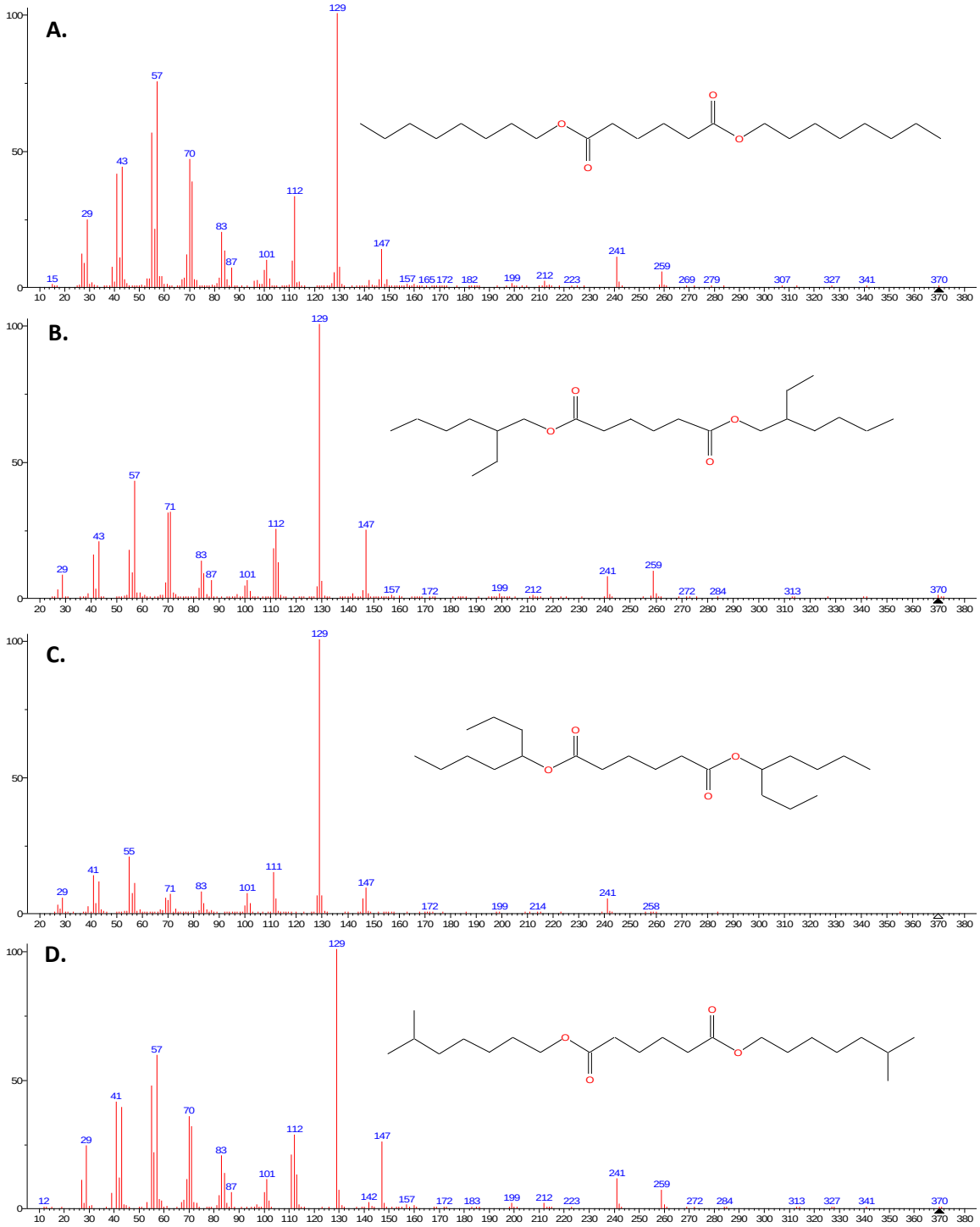

Figure 5-19. EI mass spectra obtained from the NIST library database:
A. Dioctyl adipate (DOA),
B. Hexanedioic acid (bis-2-ethylhexyl) ester,
C. Adipic acid (di(oct-4-yl ester),
D. Diisoctyl adipate (DEHA).

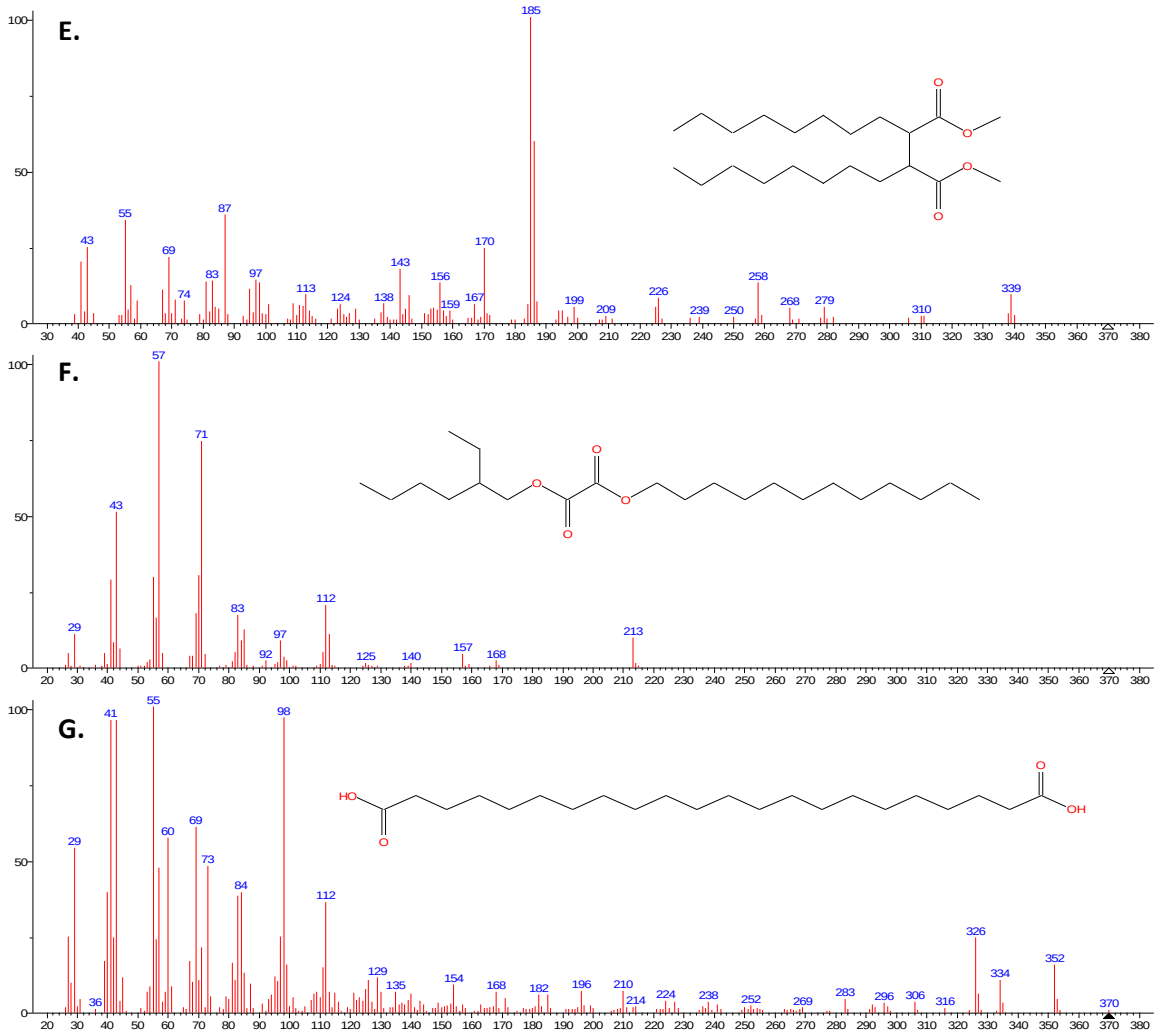

Figure 5-20. EI mass spectra obtained from the NIST library database:
E. Butanedioic acid (2,3-dioctyl-dimethyl ester),
F. Oxalic acid (dodecyl 2-ethyl hexyl ester),
G. Docosanedioic acid.

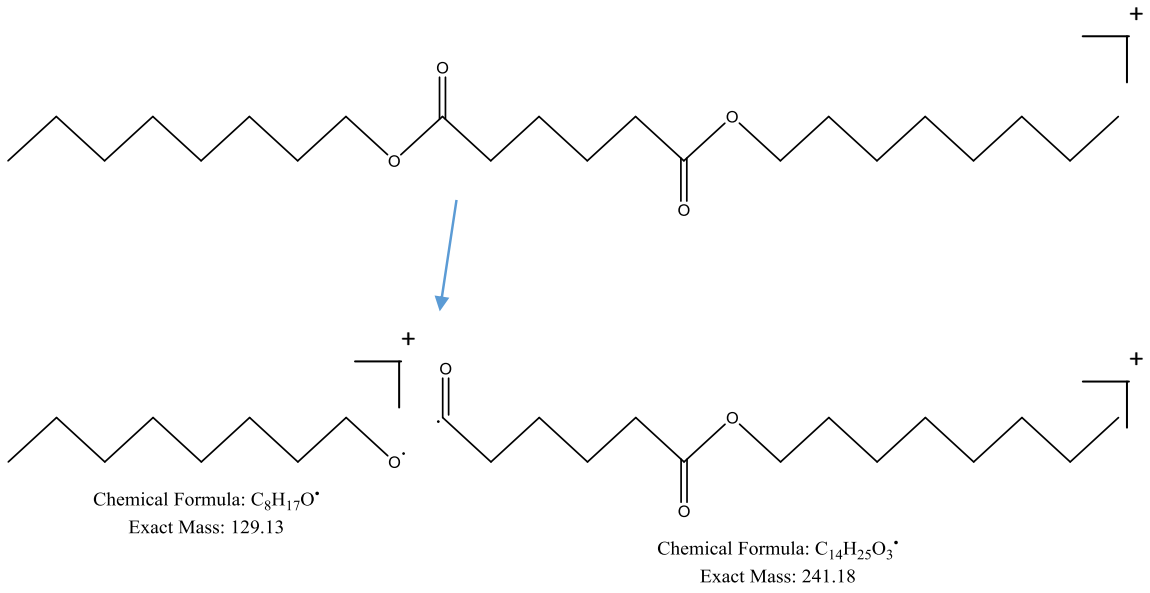

Figure 5-21. Proposed fragmentation scheme for ion at *m/z* 371, showing the loss of two ions at *m/z* 129 and 241.

Table 5-6 shows a list of the possible candidates from A-G with the relative likelihood of being the proposed compound of interest. Dioctyl adipate (A) and diisoctyl adipate (D) appear to be the most likely candidates due to the loss of the octyl groups. Hexanedioic acid (B) and adipic acid (C) are also possibilities, but neither can show the loss of an octyl group. Butanedioic acid (E), oxalic acid (F) and oocosanedioic acid (G) are all unlikely candidates.

Table 5-7 shows the fragment ions observed from electron ionisation MS (EI-MS) for candidate A (dioctyl adipate) and D (diisoctyl adipate), and DART-MS/FT-ICR MS of the deposited region of the JFTOT rod. The alkyl series of the lower mass ions (*m/z* 15, 29, 43, 57 and 71) are only observed by EI-MS. This is because fragmention occurs easily with hard ionisation energy as seen by EI-MS and these are readily analysed. These ions are generally not seen in DART-MS and ESI-MS (FT-ICR MS) techniques due to both techniques being soft ionisation techniques.

Ions at *m/z* 147, 241 and 259 are observed using all three techniques, and the radical cation at *m/z* 370 is observed in EI-MS, whereas the protonated molecule $[M + H]^+$ is observed in DART-MS and FT-ICR MS with the ion at *m/z* 371.

Oxidation transforms these molecules into higher molecular weight compounds, which become insoluble and form deposits. Straight-run fuels have excellent storage stability, however, due to the process of hydrotreating and extensive processing these inhibitors have been removed. The consequence of this is an increase in oxidation of the fuel resulting in particulate formation which then could lead to the formation of deposits.

Table 5-6. Possible candidates A-G with the likelihood of being the proposed compound.

Candidates	Likelihood
Dioctyl adipate (A)	✓✓ (loss of 112, could be loss of octyl)
Hexanedioic acid (B)	✓
Adipic acid (C)	✓
Diisoctyl adipate (D)	✓✓ (loss of 112, could be loss of octyl)
Butanedioic acid (E)	✗
Oxalic acid (F)	✗
Docosanedioic acid (G)	✗

Table 5-7. Fragment ions observed in electron ionisation mass spectra (EI-MS) for candidate A (dioctyl adipate) and D (diisoctyl adipate), DART-MS and FT-ICR MS data. * Ions at *m/z* 370 and 371 $[M + H]^+$ relate to the same molecule.

EI-MS ions (A, D) *m/z*	DART-MS ions *m/z*	FT-ICR MS ions *m/z*
15, 29, 43, 57, 71		
101		101
112		
129	129	
147	147	147
241	241	241
259	259	259
327, 341		327, 341
370*		
	371*	371*

5.4 Results and discussion: SEM-EDX analysis of JFTOT tubes

SEM was used to analyse the surface of the JFTOT tube, the locations of SEM imaging are shown below in Figure 5-22 as shown on JFTOT tube 5.

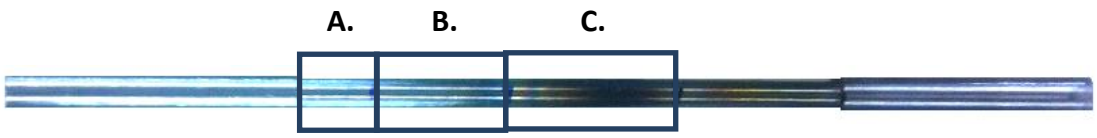

Figure 5-22. JFTOT tube 5 with locations of sampling referred to as regions A, B and C.

Figure 5-23 shows the SEM images acquisitioned for JFTOT tube 5 in locations A, B and C. From the images shown below, three distinct regions were identified. Figure 5-23A shows the non-deposited region and from the image no deposit formation can be seen. Figure 5-23B shows a transitional region between the non-deposited and deposited region here the formation of small white clusters of particles seem to be present. Figure 5-23C shows the deposited region, a vast difference in topology is seen here with a large amount of deposits appearing that seem to be in a cluster formation.

From these images, it is apparent that surface profiling of JFTOT tubes can be undertaken and from this energy dispersive X-ray spectroscopy (EDX) can provide elemental analysis of the distinct regions, which will be investigated further.

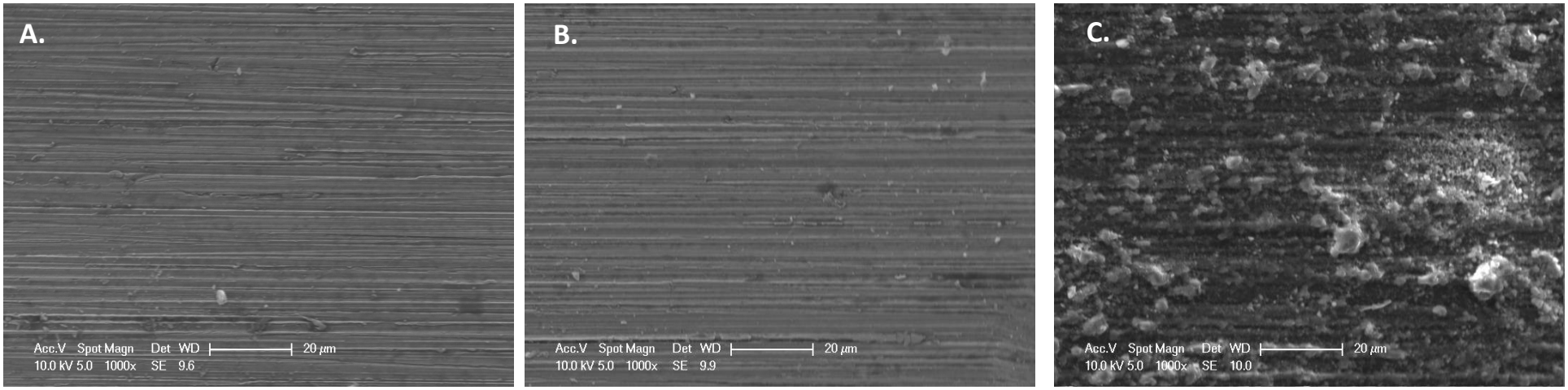

Figure 5-23. SEM images of JFTOT tube 5;

A. non-deposited region

B. transitional region

C. the deposited region of the JFTOT tube.

Energy dispersive X-ray spectroscopy (EDX) was used for elemental analysis of the sample and semi- quantitative compositional information was obtained.

Figure 5-24 shows the EDX results from JFTOT tube 5 of the non-deposited region (A) and deposited region (B). In Figure 5-24A, the EDX spectra shows the presence of a range of metals including nickel and aluminium these are not seen in high abundance in the deposited region (Figure 5-24B) this is due to the thickness of the deposit covering the metal surface therefore it is absent in the EDX spectra.

EDX is a semi-quantitative technique and some of the elements could be mislabelled as other elements with a similar wavelength so care needs to be taken with assignment.

Focusing on carbon and oxygen content, looking at the absolute values, carbon content seems to increase vastly from approximately 2000 AU (arbitrary units) in the non-deposited region to around 25,000 AU in the deposited region. The oxygen content seems to increase slightly from 3000 AU (non-deposited region) to 5000 AU (deposited region), however this oxygen is likely to be present as metal oxides.

The increase in carbon content could be from pyrolised carbon due to the high temperatures or the presence of polycyclic aromatic hydrocarbon (PAH) [68]

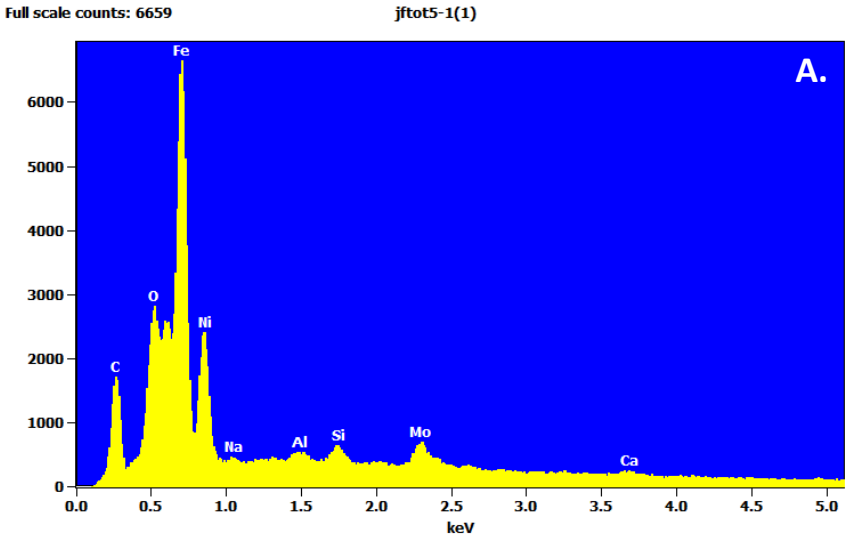

Element	Weight (%)	Atom (%)	Absolute value (AU)
Carbon (C)	32.5	40.6	2000
Oxygen (O)	60.4	56.6	3000

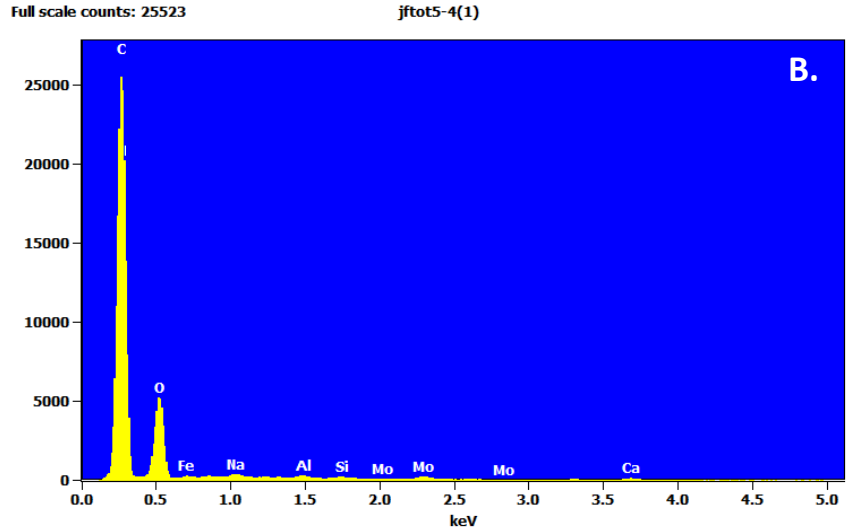

Element	Weight (%)	Atom (%)	Absolute value (AU)
Carbon (C)	71.9	77.9	25000
Oxygen (O)	26.3	21.4	5000

Figure 5-24. EDX spectra of JFTOT tube 5, A; shows the non-deposited region and B; shows the deposited region and the elements present Carbon and Oxygen.

Carbon deposits have been seen to be formed from hydrocarbon degradation including soot which contains carbonaceous solids formed by gas-phase pyrolysis of hydrocarbons, pyrolytic carbon deposits which nucleate in the gas phase, filamentous carbon produced from the catalytic dehydrogenation of hydrocarbons such as transition metals, and amorphous carbon formed from hydrocarbon degradation at lower temperatures. [223, 224]

Kossiakoff and Rice have described the mechanism of radical-chain decomposition in which thermolysis of the C-C bond in alkanes is initiated by the formation of alkyl radicals. This is then followed by a series of chain propagation reactions which involve hydrogen abstraction and β bond scission. Termination of the reaction is achieved by hydrogen donation to a free radical species. [225-226]

Song *et al.* proposed a reaction mechanism for the thermal cracking of on n-tetradecane which is commonly found in many fuels especially diesel fuel. At high pressures in the range of 400-450 psi and temperatures over 450 °C, free radical chain reactions can lead to the formation of alkenes, followed by cyclisation to form alkyl cycloalkenes or cycloalkanes. These then undergo dehydrogenation to form alkylbenzenes which with repeated dehydrogenation and condensation form polyaromatic hydrocarbons (PAH) which eventually form solid carbonaceous deposits. This deposit can grow by comination with smaller hydrocarbons or aromatisation reactions with aromatic rings. [223]

This has been reported to be a major component in injector deposits as seen by Venkataraman and Eser [223], who proposed a mechanism for oxygen-assisted aromatisation of cycloalkanes by hydrogen abstraction using alkylperoxy and alkoxy radicals as seen in Figure 5-25. The aromatic compounds undergo condensation and polymerisation to form large polycyclic aromatic hydrocarbon (PAH) groups. [165]

These results could also be consistent with the presence of adipate formation in the deposited region of the JFTOT tube, as shown in the DART-MS and FT-ICR MS data.

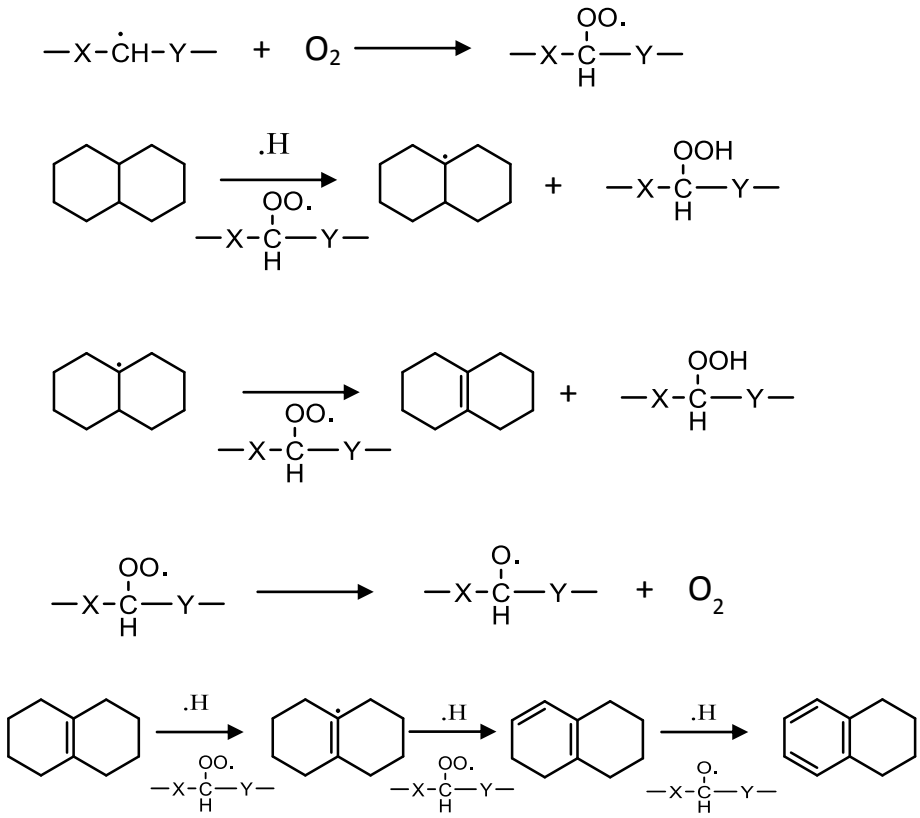

Figure 5-25. Proposed mechanism of the formation of alkylperoxy and alkoxy radicals which act as hydrogen scavengers. Mechanism 2 proposes the subsequent conversion of cycloalkane to hydroaromatic compound. Reference adapted from [165, 223]

5.4.1 SEM-EDX analysis of JFTOT tube 6

Figure 5-26 shows JFTOT tube 6 with the various locations of sampling as shown as A, B, C and D with distinct regions apparent. The images produced by SEM of the regions are shown in Figure 5-27, with distinct regions A (non-deposited region), B/C (transitional regions) and D (deposited region).

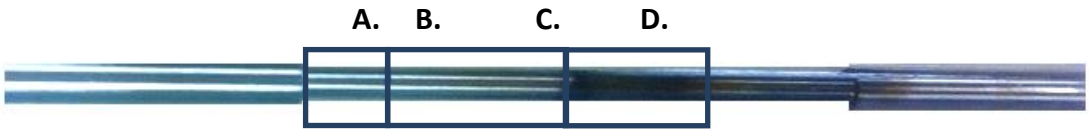

Figure 5-26. JFTOT tube 6 with locations of sampling referred to as regions A, B, C and D.

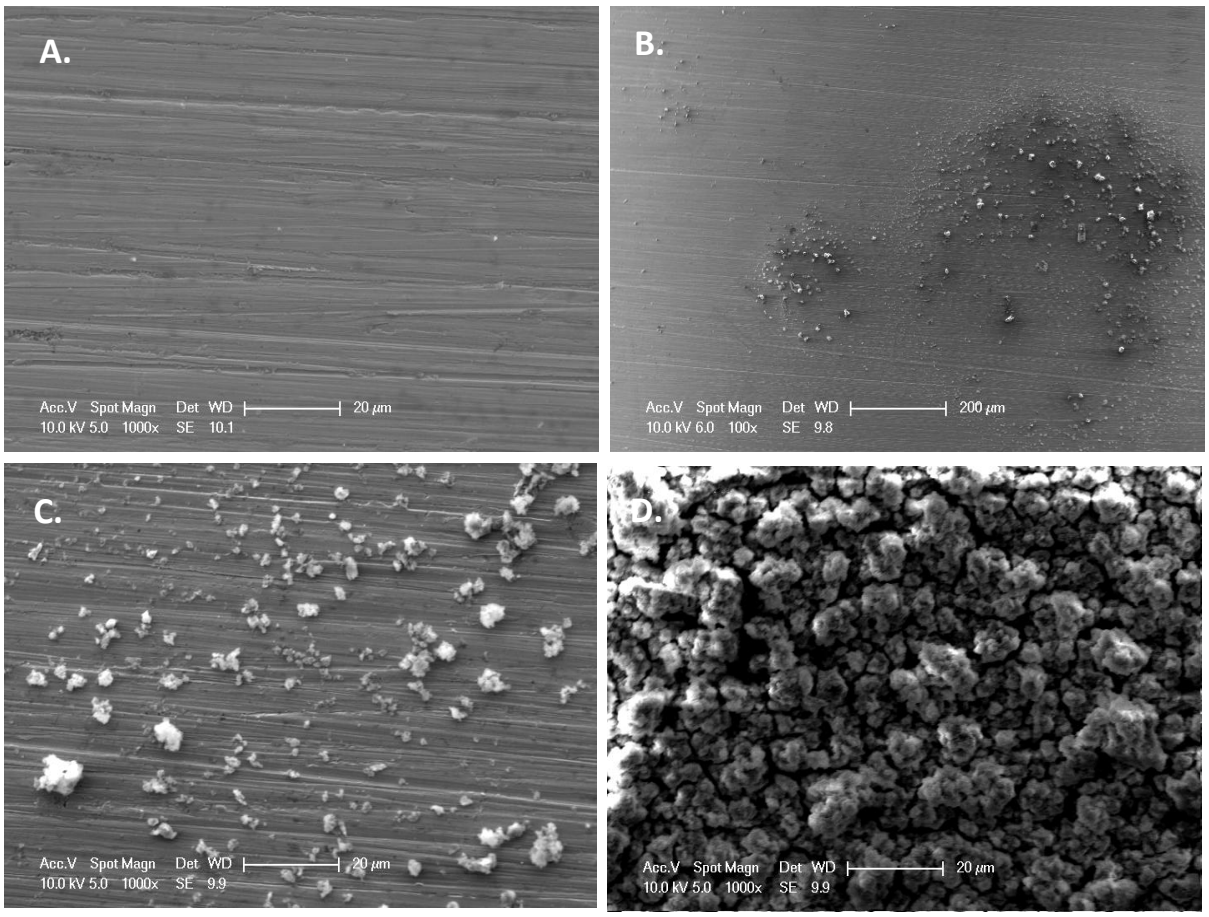

Figure 5-27. SEM images of JFTOT tube 6; A refers to the non-deposited region, B/C- transitional region and D which refers to the deposited region of the JFTOT tube.

In Figure 5-27A the non-deposited region shows no indication of deposit formation. However Figure 5-27B shows the transitional region (x 100 magnification) showing the appearance of two distinct regions of deposits starting to appear. Figure 5-27C shows the same magnification as previous images of the transitional region (x 1000 magnification) and clearly show the appearance of a crystal-like structure. Figure 5-27D shows the heavily deposited region showing large clusters covering the whole of the metal surface which appear to be dense in nature.

Figure 5-28 shows the EDX spectra of JFTOT tube 6, again focusing on carbon and oxygen content. The absolute value for carbon in the non-deposited region is approximately 1000 AU dramatically increasing to 25,000 AU, whereas oxygen remains constant at around 3000 AU. Nitrogen doesn't appear to be detected in either sample so these types of deposits do not appear to be linked with polyimide or polyamide formation which has been seen to be one cause of deposit formation.

The increase in carbon content could either be in the form of carbon bound to oxygen such as in carboxylic acids or esters or could be a result of pyrolised fuel in the form of polycyclic aromatic hydrocarbons (PAH) which have been previously been identified in deposit formation in the literature. This could also show the presence of adipate formation. [14]

Figure 5-28 also shows the presence of zinc, however this has also been attributed to sodium as they have the same wavelength, and would be more likely to be attributed to sodium. A slight increase is seen in the deposited region for sodium from around 400 AU to 1000 AU, the presence of sodium in the fuel has also been contributed to fouling problems.

Sodium can enter the fuel during the refinery process such as sodium compounds are used as the catalyst for the esterification process for producing FAME and sodium hydroxide is commonly used in the refining process to produce ULSD from crude oil. Sodium nitrite is often used as a corrosion inhibitor at low levels, but poor housekeeping can allow for sodium to contaminate the final product. The presence of sodium could lead to the formation of metal carboxylate salts depending on the presence of carboxylic acid in the system causing the formation of deposits. [15]

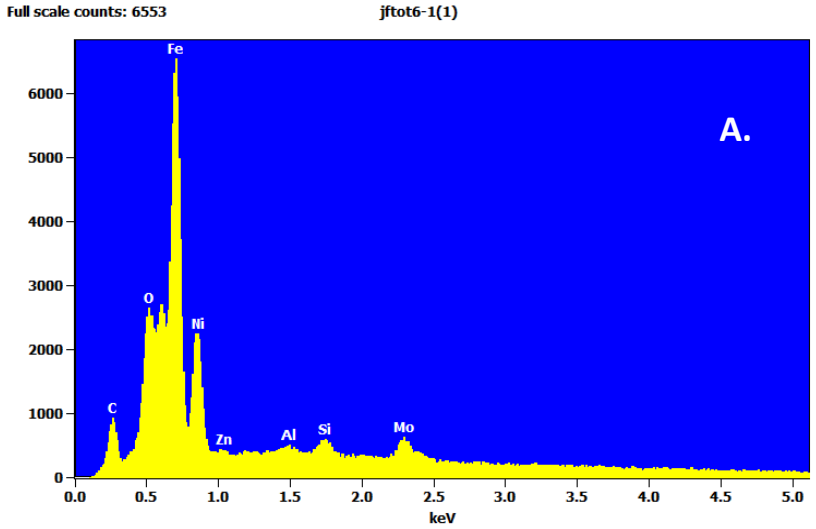

Element	Weight (%)	Atom (%)	Absolute value (AU)
Carbon	27.2	33.3	1000
Oxygen	72.8	66.7	2800

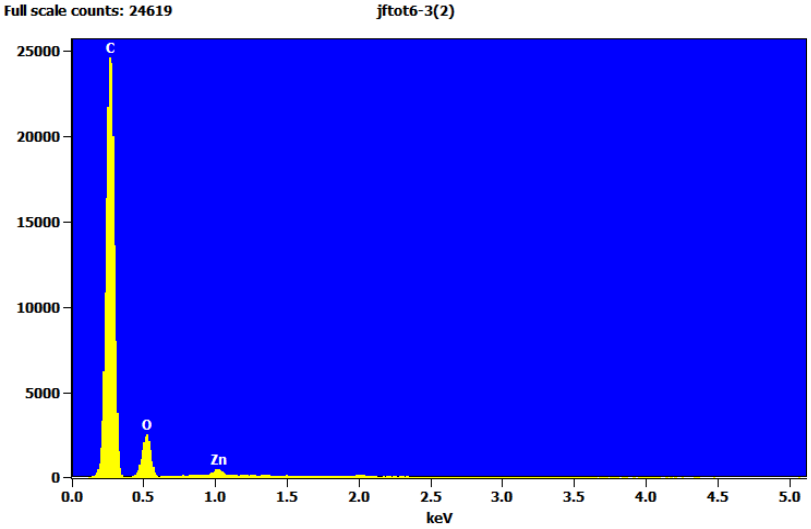

Element	Weight (%)	Atom (%)	Absolute value (AU)
Carbon	83.0	86.7	25000
Oxygen	17.0	13.3	3000

Figure 5-28. EDX spectra of JFTOT tube 6, A; shows the non-deposited region and B; shows the deposited region.

5.4.2 SEM-EDX analysis of injector needle

SEM-EDX analysis was also undertaken to analyse the surface of a diesel injector needle which showed the presence of deposits, Figure 5-29A shows an image of the injector with deposits appearing at the tip of the injector. The point-and-shoot feature of EDX was used for this analysis, as shown in Figure 5-29B were two points where chosen for the non-deposited region (point 1) and the deposited region (point 2).

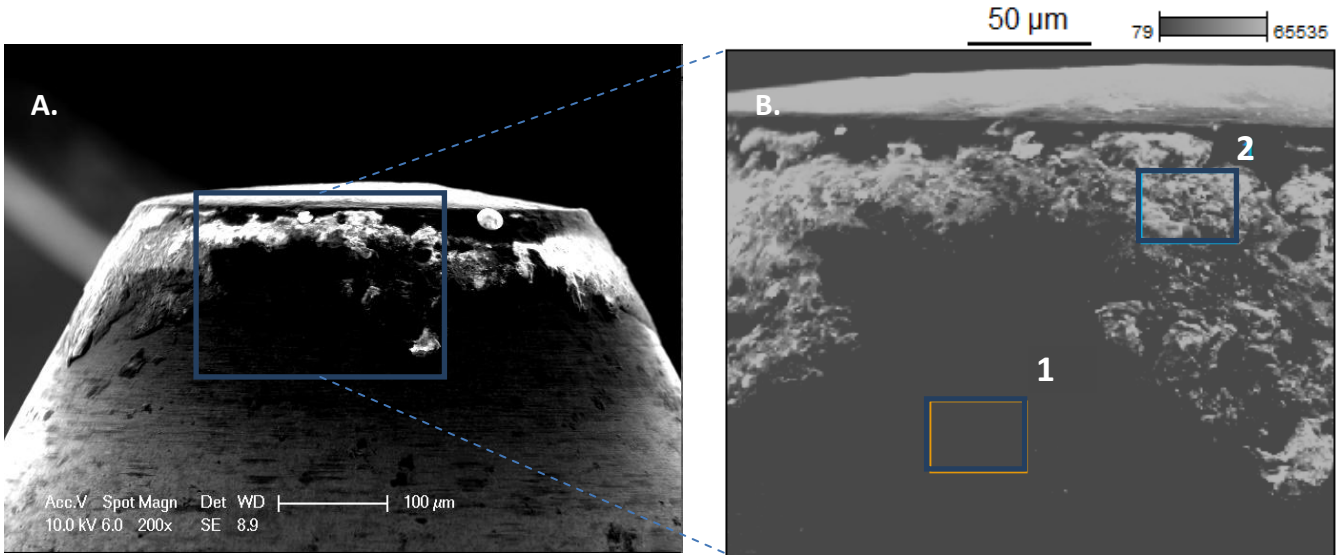

Figure 5-29. SEM images of injector needle, A shows the tip of the injector needle, and B shows a magnification of the region highlighted in A, with point 1 and 2 referring to the points chosen for non-deposited region (point 1) and deposited region (point 2).

Looking at the EDX spectra, Figure 5-30 (point 1, non-deposited region and point 2, deposited region) the deposited region shows an increase in carbon content from 5,200 to 14,000 AU and oxygen content seems to remain constant at around 9,500- 10,000 AU. This trend is the same in the JFTOT tubes seen previously which sees an increase in carbon content in the deposited region. This could be attributed to the formation of PAH and, shows that aromatisation of straight chain alkanes and polycondensation of aromatic rings is possible or the presence of adipate formation. [14]

Figure 5-30 (non-deposited region) shows again an increase in metal content compared to point 2 (deposited region) attributed to the thickness of the deposit on the JFTOT tube.

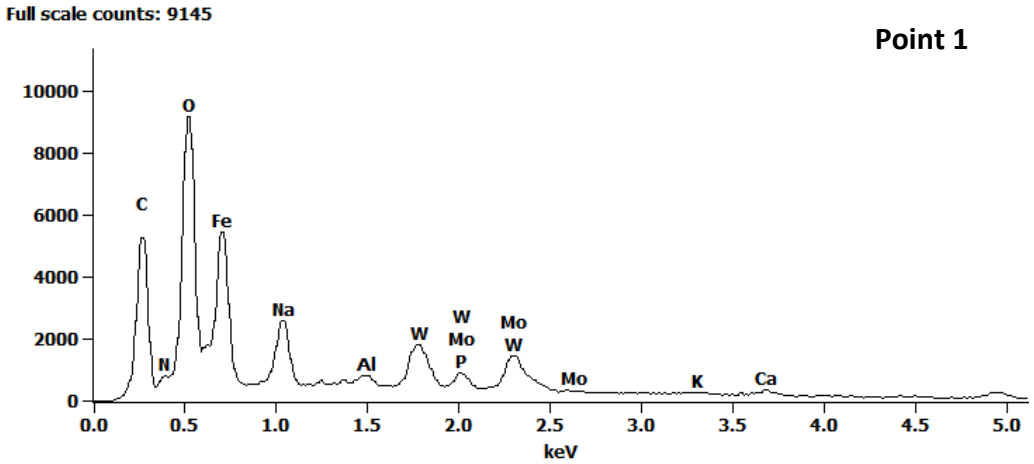

Element	Weight (%)	Atom (%)	Absolute value (AU)
Carbon	17.9	38.3	5200
Oxygen	16.2	26.1	9500

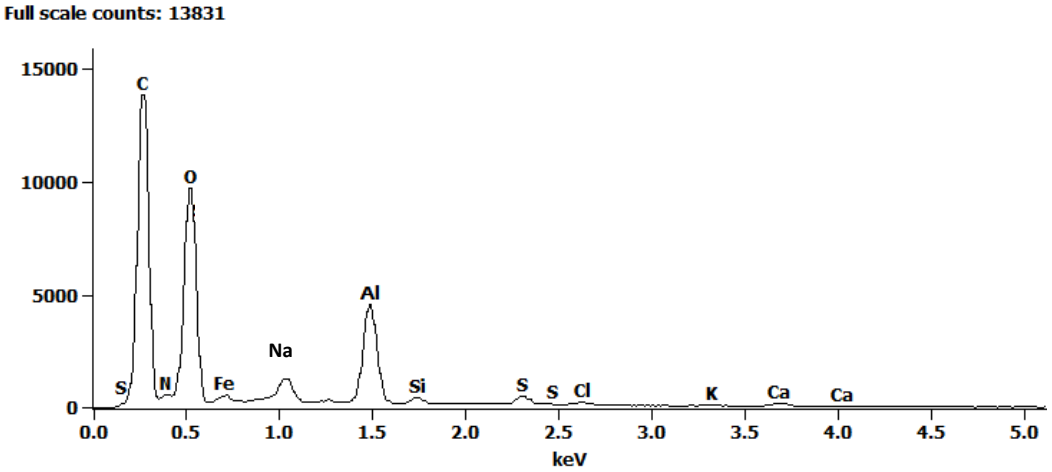

Element	Weight (%)	Atom (%)	Absolute value (AU)
Carbon	46.7	58.8	14000
Oxygen	29.2	27.6	10000

Figure 5-30. EDX spectra of injector needle, point 1 identified as the non-deposited region and point 2 identified as the deposited region.

5.5 Conclusions

DART-MS and SEM-EDX have both proven to be powerful tools for the surface analysis of JFTOT tubes and injector surfaces.

From the DART-MS data, the use of differing ionisation gas temperatures has allowed for the effective desorption of the deposited region of the JF-TOT tube. A method was developed for the use of dimethylsiloxanes present in the background to be used as a calibration method. An ion of interest was identified at *m/z* 371 by DART-MS and positive ion ESI FT-ICR MS, and was investigated by accurate mass measurement and tandem MS.

Tandem MS experiments by DART-MS and FT-ICR MS gave fragment ions of the ion at *m/z* 371. These fragmentation patterns were compared to GC-MS NIST library database and gave a list of possible candidates, two of which were identified as dioctyl adipate and diisooctyl adipate.

In the SEM-EDX data, the images showed three distinct regions on the JFTOT tube; the non-deposited region, the transitional region and deposited region. A vast difference in topology was seen through the different regions, and the deposited region showed a vast number of large clusters of deposits.

EDX was used for semi-quantitative characterisation of the sample's chemical composition. A general trend was seen in the JFTOT tube and injector needles that carbon content increased greatly in the deposited region compared to the non-deposited and transitional regions. This could be attributed to either carbon bound to oxygen such as carboxylic acids, or the formation of polycyclic aromatic hydrocarbons (PAH) by a pyrolysis reaction. However, this could also be from the presence of adipate compounds present in the fuel sample and this data would support the data produced from DART-MS and FT-ICR MS.

Chapter 6: Final conclusions

- This research has demonstrated the complexity of deposit formation in diesel engines. The issue is not a simple one solution problem, however takes into account many different aspects of the fuel and diesel engine. This work demonstrates the different approaches that can be used when investigating deposit formation
- Initially, fuel solvency was investigated. A data reduction model was developed to allow for easy qualitative analysis of data with a 10 fold reduction in analysis time. The method can provide quick identification of components which are present in samples such as aliphatic and aromatic content
- G-Diesel fuel and ULSD fuel, injector and filter deposit samples were examined to account for any difference between them, however no difference between aliphatic and aromatic content was observed
- High and low mass aliphatic content was investigated and diesel fuels with injector and filter deposits showed to contain greater amounts of high mass aliphatic content, this can result in the formation of larger compounds through oxidation reactions
- The role of FAME was also considered, two samples both biodiesel samples but one that exhibited injector and filter samples. The sample with no deposit formation showed increased amount of FAME. Disproving the theory that FAME content is linked to deposit formation, however it could be from FAME oxidation which could have taken place at high temperatures and pressures inside the trucks engine
- A UHPSFC-MS method was developed for the analysis of steryl glucoside samples. The method offered a robust and quantitative assay for the detection of SG with rapid analysis times (<5 minutes) and can analyse to sub ppm level. The UHPSFC-MS method requires minimal sample preparation compared to analysis with other techniques such as GC-MS and HPLC-MS which both involve sample derivitisation steps
- Using chromatography allowed for an extra confirmation aspect from matching retention times to standards. Direct infusion or shotgun analysis could therefore lead to mis-assignment of the SGs.
- Tandem MS experiments and MRM assays have been developed for understanding of fragmentation patterns of SGS and targeted analysis of SGs.
- Another important aspect of deposit formation was also explored, and involves surface analysis of the metal injector surfaces to characterise the components that may be

present in the deposits. For this, DART-MS and SEM-EDX were investigated and both proved to be powerful tools for analysis of JF-TOT tubes and injector surfaces.

- For DART-MS, a method was developed for the use of dimethylsiloxanes present in the background to be used as a calibration method. An ion of interest was identified at *m/z* 371 by DART-MS and was confirmed by positive ion ESI FT-ICR MS and investigated by accurate mass measurement and tandem MS. These fragmentation patterns were compared to GC-MS NIST library database and was identified as dioctyl adipate and diisooctyl adipate.
- In the SEM-EDX data, the images showed three distinct regions on the JFTOT tube; the non-deposited region, the transitional region and deposited region. A vast difference in topology was seen through the different regions, and the deposited region showed a vast number of large clusters of deposits.
- A general trend was seen in the JFTOT tube and injector needles that carbon content increased greatly in the deposited region compared to the non-deposited and transitional regions. This could be attributed to either carbon bound to oxygen such as carboxylic acids, the formation of polycyclic aromatic hydrocarbons (PAH) by a pyrolysis reaction. However, this could also be from the presence of minor constituents adipate compounds present in the fuel sample and this data would support the data produced from DART-MS and FT-ICR MS.

Future work

- These different approaches to investigate deposit formation work well to give an understanding into the complexity of the problem, and different ways to investigate this. These methods will be further explored in more depth as well as investigating a range of other potential deposit precursors including succinic acid, metal carboxylates and PIBSI.
- From the results, a database will be developed for all of the fuel samples with the best approaches to take, so fast confirmation experiments can be carried out and identify the components of interest.
- Other surface analysis approaches will be explored including time-of-flight SIMS (TOF-SIMS) which is a surface- sensitive analytical technique that uses a pulsed ion beam to

remove molecules from the outermost surface of the sample. This allows for depth profiling so that layers of compounds can be observed.

- The origin of the adipate found in the diesel fuel sample will be confirmed, standard compounds of adipate will be analysed and analytical methods will be developed and optimised.

Appendices

Appendix A- Conferences and Seminars attended

Conferences and seminars attended

British Mass Spectrometry Society (BMSS), Warwick 80/60 Mass spectrometry Conference, Warwick, UK, 10th-11th December 2012.

34th BMSS Annual Meeting, Eastbourne, UK, 9th-11th September, 2013.

Meeting the Petrochemical Challenge with Separation Science and Mass Spectrometry, Burlington House, London, UK 14th November, 2014.

36th BMSS annual meeting, Eastbourne, UK, 15th September 2015. Poster presentation: The analysis of steryl glucosides using ultrahigh performance supercritical fluid chromatography mass spectrometry.

List of References

1. European commission. EU energy in figures: statistical pocketbook 2014. European Union. Luxembourg, Belgium, 2014.

2. Babich, I. V.; Moulijn, J. A., Science and technology of novel processes for deep desulfurization of oil refinery streams. *Fuel* **2003,** *82* (6), 607-631.

3. Meyers, R., *Handbook of petroleum refining processes*. Third ed.; McGraw-Hill company: USA, 2003.

4. Berger, B.; Anderson, K., *Modern petroleum, a basic primer of the industry* Third ed.; PennWell Books: USA, 1992.

5. Gary, J.; Handwerk, G.; Kaiser, M., *Petroleum refining technology and economics*. Taylor and Francis Group: USA, 2007.

6. Little, D., *Catalytic reforming*. PennWell Books: USA, 1985.

7. Maples, R., *Petroleum Refinery Process Economics*. Second ed.; PenWell Corporation: USA, 2000.

8. ASTM International. D975 Standard specification of diesel fuel oils. In *Subcommitee D02.EO on burner, diesel, non-aviation gas turbine and marine fuels. ASTM volume 05.01 Petroleum products, liquid fuels and lubricants*, USA.

9. European committee for standardization. EN 590:2009, Gaseous and liquid fuels, lubricants and related products of petroleum, synthetic and biological origin. In *ICS 75.160.20*, 2009.

10. Knothe, G.; Matheaus, A. C.; Ryan, T., Cetane numbers of branched and straight-chain fatty esters determined in an ignition quality tester. *Fuel* **2003,** *82* (8), 971-975.

11. Santana, R.; Do, P.; Santikunaporn, M.; Alvarez, W.; Taylor, J.; Sughrue, E.; Resasco, D., Evaluation of different reaction strategies for the improvement of cetane number in diesel fuels. *Fuel* **2006,** *85* (5–6), 643-656.

12. Alptekin, E.; Canakci, M., Characterization of the key fuel properties of methyl ester–diesel fuel blends. *Fuel* **2009,** *88* (1), 75-80.

13. Batts, B. D.; Fathoni, A. Z., A literature review on fuel stability studies with particular emphasis on diesel oil. *Energ. Fuel* **1991,** *5* (1), 2-21.

14. Knothe, G., Some aspects of biodiesel oxidative stability. *Fuel Process. Technol.* **2007,** *88* (7), 669-677.

15. Dinkov, R.; Hristov, G.; Stratiev, D.; Boynova Aldayri, V., Effect of commercially available antioxidants over biodiesel/diesel blends stability. *Fuel* **2009,** *88* (4), 732-737.

16. Diesel, R., The diesel oil engine. *Nav. Eng. J.* **1912,** *24* (1), 653-692.

17. Diesel, R., Internal-combustion engine. Google Patents: 1898.

18. *Diesel-engine management: systems and components*. Third ed.; Robert Bosch GmbH: Germany, 2004.

19. Hillier, V.; Pittuck, E., *Fundamentals of motor vehicle technology*. Third ed.; Hutchinson publishing group: UK, 1981.

20. Wellington, B.; Asmus, A., *Diesel engines and fuel systems*. Fourth ed.; Longman Australia: Australia, 1995.

21. Bauer, H.; Dietsche, K.; Jager, T.; Kimberley, W., *Diesel-engine management: Systems and components*. Third ed.; Robert Bosch GmbH: Germany, 2004.

22. Groysman, A., *Corrosion in systems for storage and transportation of petroleum products and biofuels: identification, monitoring and solutions*. Springer: New York, USA, 2014.

23. Ban-Weiss, G. A.; McLaughlin, J. P.; Harley, R. A.; Lunden, M. M.; Kirchstetter, T. W.; Kean, A. J.; Strawa, A. W.; Stevenson, E. D.; Kendall, G. R., Long-term changes in emissions of nitrogen oxides and particulate matter from on-road gasoline and diesel vehicles. *Atmos. Environ.* **2008,** *42* (2), 220-232.

24. König, G.; Brunda, M.; Puxbaum, H.; Hewitt, C. N.; Duckham, S. C.; Rudolph, J., Relative contribution of oxygenated hydrocarbons to the total biogenic VOC emissions of selected mid-European agricultural and natural plant species. *Atmos. Environ.* **1995,** *29* (8), 861-874.

25. Guenther, A.; Hewitt, C. N.; Erickson, D.; Fall, R.; Geron, C.; Graedel, T.; Harley, P.; Klinger, L.; Lerdau, M.; McKay, W. A.; Pierce, T.; Scholes, B.; Steinbrecher, R.; Tallamraju, R.; Taylor, J.; Zimmerman, P., A global model of natural volatile organic compound emissions. *J. Geophys. Res.* **1995,** *100* (D5), 8873-8892.

26. Guenther, A.; Geron, C.; Pierce, T.; Lamb, B.; Harley, P.; Fall, R., Natural emissions of non-methane volatile organic compounds, carbon monoxide, and oxides of nitrogen from North America. *Atmos. Environ.* **2000,** *34* (12–14), 2205-2230.

27. Di, Y.; Cheung, C. S.; Huang, Z., Experimental investigation on regulated and unregulated emissions of a diesel engine fueled with ultra-low sulfur diesel fuel blended with biodiesel from waste cooking oil. *Sci. Total Environ.* **2009,** *407* (2), 835-846.

28. von Storch, H.; Costa-Cabral, M.; Hagner, C.; Feser, F.; Pacyna, J.; Pacyna, E.; Kolb, S., Four decades of gasoline lead emissions and control policies in Europe: a retrospective assessment. *Sci. Total Environ.* **2003,** *311* (1–3), 151-176.

29. Charron, A.; Harrison, R. M., Primary particle formation from vehicle emissions during exhaust dilution in the roadside atmosphere. *Atmos. Environ.* **2003,** *37* (29), 4109-4119.

30. Perry, R.; Gee, I. L., Vehicle emissions in relation to fuel composition. *Sci. Total Environ.* **1995,** *169* (1–3), 149-156.

31. Brocco, D.; Fratarcangeli, R.; Lepore, L.; Petricca, M.; Ventrone, I., Determination of aromatic hydrocarbons in urban air of Rome. *Atmos. Environ.* **1997,** *31* (4), 557-566.

32. Lowenthal, D. H.; Zielinska, B.; Chow, J. C.; Watson, J. G.; Gautam, M.; Ferguson, D. H.; Neuroth, G. R.; Stevens, K. D., Characterization of heavy-duty diesel vehicle emissions. *Atmos. Environ.* **1994,** *28* (4), 731-743.

33. Knothe, G., Monitoring a progressing transesterification reaction by fiber-optic near infrared spectroscopy with correlation to (1)H nuclear magnetic resonance spectroscopy. *J. Am. Oil Chem. Soc.* **2000,** *77* (5), 489-493.

34. The Renewable Transport Fuel Obligations Order. *Renew. Sust. Energ. Rev.* **2007,** *3072*.

35. Barker, J.; Snape, C.; Scurr, D., A Novel Technique for Investigating the Characteristics and History of Deposits Formed Within High Pressure Fuel Injection Equipment. *SAE International* **2012,** *5* (3), 1155-1164.

36. Knecht, W., Diesel engine development in view of reduced emission standards. *Energy* **2008,** *33* (2), 264-271.

37. Flaig, U.; Polach, W.; Ziegler, G., Common Rail System (CR-System) for passenger car DI diesel engines; Experiences with applications for series production projects. *SAE international* **1999,** *01* (191), 1.

38. Knudsen, K.; Cooper, B.; Topsoe, H., Catalyst and process technologies for ultra low sulfur diesel. *Appl. Catal. A-Gen.* **1999,** *189* (2), 205-215.

39. Stanislaus, A.; Marafi, A.; Rana, M. S., Recent advances in the science and technology of ultra low sulfur diesel (ULSD) production. *Catal. Today* **2010,** *153* (1–2), 1-68.

40. Knudsen, K. G.; Cooper, B. H.; Topsoe, H., Catalyst and process technologies for ultra low sulfur diesel. *Appl. Catal., A* **1999,** *189* (2), 205-215.

41. Barker, J.; Langley, G. J.; Richards, P., Insights into Deposit Formation in High Pressure Diesel Fuel Injection Equipment. *SAE International* **2010,** *2243*, 1-21.

42. Ma, X.; Sun, L.; Song, C., A new approach to deep desulfurization of gasoline, diesel fuel and jet fuel by selective adsorption for ultra-clean fuels and for fuel cell applications. *Catal. Today* **2002,** *77* (1–2), 107-116.

43. Richards, P.; Reid, J.; Tok, L.; MacMillan, I., The Emerging Market for Biodiesel and the Role of Fuel Additives. *SAE International* **2007**, 1886-1893.

44. Ma, F.; Hanna, M. A., Biodiesel production: a review. *Bioresour. Technol.* **1999,** *70* (1), 1-15.

45. Meher, L. C.; Vidya Sagar, D.; Naik, S. N., Technical aspects of biodiesel production by transesterification. *Renew. Sust. Energ. Rev.* **2006,** *10* (3), 248-268.

46. Kralova, I.; Sjoblom, J., Biofuels-Renewable Energy Sources: A Review. *J. Dispersion Sci. Technol.* **2010,** *31* (3), 409-425.

47. Hoekman, S.; Broch, A.; Robbins, C.; Ceniceros, E.; Natarajan, M., Review of biodiesel composition, properties, and specifications. *Renew. Sust. Energ. Rev.* **2012,** *16* (1), 143-169.

48. Agarwal, A.; Bijwe, J.; Das, L., Effect of biodiesel utilization of wear of vital parts in compression ignition engine. *J. Eng. Gas Turb. Power* **2003,** *125* (2), 604-611.

49. Holman, R.; Elmer, O., The Rates of Oxidation of Unsaturated Fatty Acids and Esters. *AOCS* **1947,** *24* (4), 127.

50. Canakci, M.; Van Gerpen, J., Biodiesel Production via. Acid Catalysis. *Am. Soc. Agric. Eng.* **1999,** *44* (6), 1429.

51. Pullen, J.; Saeed, K., Experimental Study of the Factors Affecting the Oxidation Stability of Biodiesel FAME Fuels. *Fuel Process. Technol.* **2014,** *125*.

52. Gunstone, F., *Fatty Acid and Lipid Chemistry*. Springer: USA, 1996.

53. Gunstone, F.; Harwood, J.; Padley, F., *The lipid handbook*. Second ed.; Chapman & Hall: London, UK, 1994.

54. Caprotti, R.; Breakspear, A.; Graupner, O.; Klaua, T.; Kohnen, O., Diesel injector deposits potential in future fueling systems. *SAE international* **2006,** *01* (3359).

55. Lacey, P.; Gail, S.; Kientz, J.; Benoist, G.; Downes, P.; Daveau, C., Fuel Quality and Diesel Injector Deposits. *J. Fuels Lubri.* **2012,** *1693* (3), 61.

56. Schwab, S.; Bennett, J.; Dell, S.; Galante-Fox, J.; Kulinowski, A.; Miller, K., Internal Injector Deposits in High-Pressure Common Rail Diesel Engines. *SAE International* **2010,** *3* (2), 865-878.

57. Quigley, R.; Barbour, R.; Fahey, E.; Arters, D.; Wetzel, W.; Ray, J. In *A study of the internal diesel injector deposit phenomenon*, TAE International Colloquium Fuels, Esslingen, 2011.

58. Ulmann, J.; Geduldig, M.; Stutzenberger, H.; Caprotti, R., Investigation into the formation and prevention of internal diesel injector deposits. *SAE International* **2008,** *01* (0926).

59. Arondel, M.; Rodeschini, H.; Lopes, M.; Dequenne, B., Fuel additives for reduction of internal diesel injectors deposits (IDID): A critical and priority route. *SAE international* **2012,** *01* (1687).

60. Matzke, M.; Litzow, U.; Caprotti, R.; Balfour, G., Diesel lubricity requirements of future fuel injection equipment. *SAE international* **2009,** *0848* (1).

61. Mikkonen, S.; Tenhunen, E., Deposits in diesel-injection pumps caused by the incompatibility of fuel and oil additives. *SAE international* **1987,** *872119* (1).

62. Barker, J.; Snape, C.; Scurr, D., Diesel deposits. In *9th International Colloqium: fuels and future energy for automobiles*, International, T., Ed. TAE, Stuttgart, 2013.

63. Quigley, R.; Barbour, R.; Fahey, E.; Arters, D.; Wetzl, J., A study of the internal diesel injector deposit phenomenon. *TAE international* **2010,** *15* (01), 152.

64. Ullmann, J.; Geduldig, M.; Stutzenberger, H.; Caprotti, R.; Balfour, G., Investigation into the formation and prevention of internal diesel injector deposits. *SAE International* **2008,** *01* (1), 926.

65. Barker, J.; Reid, J.; Snape, C.; Scurr, D.; Meredith, W., Spectroscopic studies of internal injector deposits (IDID) resulting from the use of non-commercial low molecular weight polyisobutylenesuccinimide (PIBSI). *SAE International* **2014,** *2720* (1), 01.

66. Venkataraman, R.; Eser, S., Characterization of solid deposits formed from short durations of jet fuel degradation: carbonaceous solids. *Ind. Eng. Chem. Res.* **2008,** *47* (1).

67. Kouame, S.; Liu, E., Characterization of fully and partially additized lubricant deposits by temperature programmed oxidation. *Tribol. Int.* **2014,** *72* (1), 58.

68. Venkataraman, R.; Eser, S., Characterization of deposits formed on diesel injectors in field test and from thermal oxidative degradation of n-hexadecane in a laboratory reactor. *Chem. Cent. J.* **2008,** *2* (1), 25.

69. Sem, T., Effect of various lubricating oils on piston deposits in biodiesel fueled engines. *SAE international* **2004,** *0098* (01).

70. Hoed, V.; Zyaykina, N.; Greyt, W.; Maes, J.; Verhe, R.; Demeestere, K., Identification and occurence of steryl glucosides in palm and soy biodiesel. *J. Am. Oil Chem. Soc.* **2008,** *85* (1), 481.

71. Dunn, R., Effects of minor constituents on cold flow properties and performance of biodiesel. *Prog. Energy Combust. Sci.* **2009,** *35* (1).

72. Lacoste, F.; Dejean, F.; Griffon, H.; Rouquette, C., Quantification of free and esterified steryl glucosides in vegetable oils and biodiesel. *Eur. J. Lipid Sci. Technol.* **2009,** *111* (1), 822.

73. Pauls, R., A review of chromatographic characterization techniques for biodiesel and biodiesel blends. *J. Chromatogr. Sci.* **2011,** *49* (1), 384.

74. Oppliger, S.; Munger, L.; Nystroem, L., Rapid and highly accurate detection of steryl glucosides by ultraperformance liquid chromatography/quadrupole time of flight mass spectrometry. *J. Agric. Food. Chem.* **2014,** *62* (4), 9410.

75. Bondioli, P.; Cortesi, N.; Mariani, C., Identification and quantification of steryl glucosides in biodiesel. *Eur. J. Lipid Sci. Tech.* **2008,** *110* (2), 120-126.

76. Feng, F.; Wu, Q.; Zeng, L., Rapid analysis of diesel fuel properties by near infrared reflectance spectra. *Spectrochim. Acta Mol. Biomol. Spectrosc.* **2015,** *149*, 271-278.

77. Alves, J. C. L.; Poppi, R. J., Quantification of conventional and advanced biofuels contents in diesel fuel blends using near-infrared spectroscopy and multivariate calibration. *Fuel* **2016,** *165*, 379-388.

78. Tarkanic, S.; Crnko, J., Rapid Development of Sulfur in liquid hydrocarbons for At-line process applications using combustion/oxidation and UV-fluorescence detection. *J. ASTM Int.* **2005,** *2* (9), 137-140.

79. Harvey, S. D.; Jarman, K. H.; Moran, J. J.; Sorensen, C. M.; Wright, B. W., Characterization of diesel fuel by chemical separation combined with capillary gas chromatography (GC) isotope ratio mass spectrometry (IRMS). *Talanta* **2012,** *99*, 262.

80. Zhao, B.; Zhang, S.; Zhou, Y.; He, D.; Li, Y.; Ren, M.; Xu, Z.; Fang, J., Characterization and quantification of PAH atmospheric pollution from a large petrochemical complex in Guangzhou: GC–MS/MS analysis. *Microchem. J.* **2015,** *119*, 140-144.

81. Zhang, J.; Yang, Q., GC/MS Analysis on Combustion Smoke of Different Flammable Liquids. *Procedia Eng.* **2014,** *71*, 139-144.

82. Elghawi, U.; Theinnoi, K.; Sitshebo, S.; Tsolakis, A.; Wyszynski, M. L.; Xu, H. M.; Cracknell, R. F.; Clark, R. H.; Mayouf, A., GC-MS determination of low hydrocarbon species (C1–C6) from a diesel partial oxidation reformer. *Int. J Hydrogen Energ.* **2008,** *33* (23), 7074-7083.

83. Knothe, G., Analyzing biodiesel: standards and other methods. *J. Am Oil Chem. Soc.* **2006,** *83* (10), 823-833.

84. Ali, O. M.; Mamat, R.; Abdullah, N. R.; Abdullah, A. A., Analysis of blended fuel properties and engine performance with palm biodiesel–diesel blended fuel. *Renew. Energ.* **2016,** *86*, 59-67.

85. Pindado Jiménez, O.; Pérez Pastor, R. M.; Escolano Segovia, O.; del Reino Querencia, S., Exploring petroleum hydrocarbons in groundwater by double solid phase extraction coupled to gas chromatography–flame ionization detector. *Talanta* **2015,** *131*, 315-324.

86. Kamiński, M.; Gilgenast, E.; Przyjazny, A.; Romanik, G., Procedure for and results of simultaneous determination of aromatic hydrocarbons and fatty acid methyl esters in diesel fuels by high performance liquid chromatography. *J. Chromatogr. A* **2006,** *1122* (1–2), 153-160.

87. Brandão, L.; Braga, J.; Suarez, P., Determination of vegetable oils and fats adulterants in diesel oil by high performance liquid chromatography and multivariate methods. *J. Chromatogr. A* **2012,** *1225*, 150-157.

88. Shang, N.; Liu, R.; Chen, Y.; Chang, C.; Lin, R., Characterization of fatty acid methyl esters in biodiesel using high-performance liquid chromatography. *J. Taiwan Inst. Chem. Eng.* **2012,** *43* (3), 354-359.

89. Paproski, R. E.; Cooley, J.; Lucy, C. A., Comparison of titania, zirconia, and silica stationary phases for separating diesel fuels according to hydrocarbon group-type by supercritical fluid chromatography. *J. Chromatogr. A* **2005,** *1095* (1–2), 156-163.

90. Thiébaut, D., Separations of petroleum products involving supercritical fluid chromatography. *J. Chromatogr. A* **2012,** *1252*, 177-188.

91. Ashraf-Khorassani, M.; Yang, J.; Rainville, P.; Jones, M. D.; Fountain, K. J.; Isaac, G.; Taylor, L. T., Ultrahigh performance supercritical fluid chromatography of lipophilic compounds with application to synthetic and commercial biodiesel. *J. Chromatogr. B* **2015,** *983–984*, 94-100.

92. Cunha, D.; Montes, L.; Castro, E.; Barbosa, L., NMR in the time domain: A new methodology to detect adulteration of diesel oil with kerosene. *Fuel* **2016,** *166*, 79-85.

93. Nomngongo, P. N.; Ngila, J. C., Determination of trace Cd, Cu, Fe, Pb and Zn in diesel and gasoline by inductively coupled plasma mass spectrometry after sample clean up with hollow fiber solid phase microextraction system. *Spectrochim. Acta B* **2014,** *98*, 54-59.

94. Cook, S.; Richards, P., Possible influence of high injection pressure on diesel fuel stability: a review and preliminary study. *SAE international* **2009,** *01* (1878).

95. Barker, J.; Richards, P.; Snape, C.; Meredith, W., Diesel injector deposits- an issue that has evolved with engine technology. *SAE International* **2011,** *1923* (01).

96. Frysinger, G. S.; Gaines, R. B., Comprehensive Two-Dimensional Gas Chromatography with Mass Spectrometric Detection (GC × GC/MS) Applied to the Analysis of Petroleum. *J. High Res. Chrom.* **1999,** *22* (5), 251-255.

97. Barker, J.; Richards, P.; Pinch, D.; Cheeseman, B., Temperature programmed oxidation as a technique for understanding diesel fuel system deposits. *SAE international* **2010,** *3* (2), 85.

98. Schwab, S.; Bennett, J.; Dell, D.; Galante-Fox, J.; Kulinoowski, A.; Miller, K., Internal injector deposits in high pressure common rail diesel engines. *SAE international* **2010,** *01* (2242).

99. Quigley, R.; Barbour, R.; Fahey, E.; Arters, D.; Wetzl, J., A study of the internal diesel injector deposit phenomenon. *TAE international* **2010,** *01*.

100. Zechmeister, L., Mikhail Tswett- The Inventor of Chromatography. *Isis* **1946,** *36*, 108-109.

101. Crouch, S.; Skoog, D.; West, D.; Holler, J., *Fundamentals of Analytical Chemistry*. Eighth ed.; Brooks/Cole: USA, 2003.

102. Miller, J., Chromatography concepts and contrasts. Second ed.; Wiley-Interscience: USA, 2005.

103. Martin, A. J. P.; Synge, R. L. M., A new form of chromatogram employing two liquid phases: A theory of chromatography. 2. Application to the micro-determination of the higher monoamino-acids in proteins. *Biochem. J.* **1941,** *35* (12), 1358-1368.

104. James, A. T.; Martin, A. J. P., Gas-liquid partition chromatography: the separation and micro-estimation of volatile fatty acids from formic acid to dodecanoic acid. *Biochem. J,* **1952,** *50* (5), 679-690.

105. Hoffmann, E.; Stroobant, V., *Mass Spectrometry: Principles and Applications*. Third ed.; Wiley: Wiltshire, UK, 2007.

106. Wang, F.; Qian, K.; Green, L., GC×MS of Diesel: A Two-Dimensional Separation Approach. *Anal. Chem.* **2005,** *77* (9), 2777-2785.

107. Snyder, L.; Kirkland, J.; Glajch, J., *Practical HPLC method development*. Third ed.; Wiley-Interscience: USA, 2012.

108. Lough, W.; Wainer, I., *High performance liquid chromatography.* Chapman & Hall: UK, 1996.

109. Adam, F.; Thiebaut, D.; Bertoncini, F.; Courtiade, M.; Hennion, M. C., Supercritical fluid chromatography hyphenated with twin comprehensive two-dimensional gas chromatography for ultimate analysis of middle distillates. *J. Chromatogr. A* **2010,** *1217* (8), 1386-94.

110. Taylor, L., Supercritical fluid chromatography. *Anal. Chem.* **2010,** *82*, 4825-4935.

111. Berger, T. A., Supercritical fluid chromatography: overview. In *Reference module in chemistry, molecular sciences and chemical engineering*, Elsevier: 2013.

112. Nováková, L.; Grand-Guillaume Perrenoud, A.; Francois, I.; West, C.; Lesellier, E.; Guillarme, D., Modern analytical supercritical fluid chromatography using columns packed with sub-2μm particles: A tutorial. *Anal. Chim. Acta* **2014,** *824* (1), 18-35.

113. Grand-Guillaume Perrenoud, A.; Veuthey, J.; Guillarme, D., Comparison of ultra-high performance supercritical fluid chromatography and ultra-high performance liquid chromatography for the analysis of pharmaceutical compounds. *J. Chromatogr. A* **2012,** *1266* (0), 158-167.

114. Chester, T. L.; Pinkston, J. D., Supercritical-fluid chromatography. *Anal. Chem.* **1990,** *62* (12), 394-402.

115. Johnston, K.; Penninger, J., Supercritical fluid science and technology. *ACS* **1989,** *406* (1), 52.

116. Phillips, K.; Ruggio, D.; Ashraf-Khorassni, M., Analysis of steryl glucosides in foods and dietary supplements by solid-phase extraction and gas chromatography. *J. Food Lipids* **2005,** *12* (1).

117. Zhou, Q.; Gao, B.; Zhang, X.; Xu, Y.; Shi, H.; Yu, L., Chemical profiling of triacylglycerols and diacylglycerols in cow milk fat by ultra-performance convergence chromatography combined with a quadrupole time-of-flight mass spectrometry. *Food Chem.* **2014,** *143*, 199-204.

118. Watson, T.; Sparkman, D., *Introduction to Mass Spectrometry: Instrumentation, Applications and Strategies for Data Interpretations*. Fourth ed.; John Wiley & Sons, Ltd: Chichester, UK, 2007.

119. Mark, T., Fundamental aspects of electron impact ionization. *Int. J. Mass Spectrom. Ion Processes* **1982,** *45* (1), 125-145.

120. Dole, M.; Mack, L.; Hines, R.; Mobley, R.; Ferguson, L.; Alice, M., Molecular Beams of Macroions. *J. Chem. Phys.* **1968,** *49* (5), 2240-2249.

121. Yamashita, M.; Fenn, J., Electrospray ion source. Another variation on the free-jet theme. *J. Phys. Chem. A* **1984,** *88* (20), 4451.

122. Fenn, J. B.; Mann, M.; Meng, C. K.; Wong, S. F.; Whitehouse, C. M., Electrospray ionization–principles and practice. *Mass Spectrom. Rev.* **1990,** *9* (1), 37-70.

123. Mora, J.; Van Berkel, G.; Enke, C.; Cole, R.; Martinez-Sanchez, M.; Fenn, J., Electrochemical processes in electrospray ionization mass spectrometry. *J. Mass Spectrom.* **2000,** *35* (8), 939-952.

124. Ho, C.; Lam, C.; Chan, M.; Cheung, R.; Law, L.; Lit, L.; Suen, M.; Tai, H., Electrospray ionisation mass spectrometry: principles and clinical applications. *Clin. Biochem.* **2003,** *24* (1), 3-12.

125. Banerjee, S.; Mazumdar, S., Electrospray ionization mass spectrometry: a technique to access the information beyond the molecular weight of the analyte. *Int. J. Anal. Chem.* **2012,** *2012*.

126. Wilm, M. S.; Mann, M., Electrospray and Taylor-Cone theory, Dole's beam of macromolecules at last? *Int. J. Mass Spectrom. Ion Processes* **1994,** *136* (2–3), 167-180.

127. Fernandez de la Mora, J., Electrospray ionization of large multiply charged species proceeds via Dole's charged residue mechanism. *Anal. Chim. Acta* **2000,** *406* (1), 93-104.

128. Iribarne, J.; Thomson, B., On the evaporation of small ions from charged droplets. *J. Chem. Phys.* **1976,** *64* (6), 2287-2294.

129. Mack, L.; Kralik, P.; Rheude, A.; Dole, M., Molecular beams of macroions. *J. Chem. Phys.* **1970,** *49* (10), 4977-4986.

130. Fenn, J.; Mann, M.; Meng, C.; Wong, S.; Whitehouse, C., Electrospray ionization for mass spectrometry of large biomolecules. *Science* **1989,** *246* (4926), 64-71.

131. Gaskell, S., Electrospray: principles and practice. *J. Mass Spectrom.* **1997,** *32* (7), 677.

132. Moreau, R.; Scott, K.; Haas, M., The identification and quantification of steryl glucosides in precipitates from commercial biodiesel. *J. Am Oil Chem. Soc.* **2008,** *85*, 761-770.

133. Cody, R., Observation of molecular ions and analysis of nonpolar compounds with the direct analysis in real time ion source. *Anal. Chem.* **2008,** *81* (3), 1101-1107.

134. Domin, M.; Cody, R., *Ambient ionization mass spectrometry (new developments in mass spectrometry)*. Royal Society of Chemistry: Cambridge, UK, 2014.

135. Smith, R. M., Supercritical fluids in separation science--the dreams, the reality and the future. *J. Chromatogr. A* **1999,** *856* (1-2), 83-115.

136. Ibañez, E.; Señoráns, F. J., Tuning of mobile and stationary phase polarity for the separation of polar compounds by SFC. *J. Biochem. Bioph. Methods* **2000,** *43* (1–3), 25-43.

137. Miller, P. E.; Denton, M. B., The quadrupole mass filter: basic operating concepts. *J. Chem. Educ.* **1986,** *63* (7), 617.

138. March, R. E., An Introduction to quadrupole ion trap mass spectrometry. *J. Mass Spectrom.* **1997,** *32* (4), 351-369.

139. Mathieu, E.; Math, J., The vibratory motion of an elliptical membrane. *J. Math Pure Appl.* **1868,** *137*.

140. Guilhaus, M., Principles and instrumentation in time-of-flight mass spectrometry. Physical and instrumental concepts. *J. Mass Spectrom.* **1995,** *30* (11), 1519-1532.

141. Niessen, W., *Liquid Chromatography- Mass Spectrometry*. Third ed.; CRC Press: Florida, USA, 2006.

142. Chernushevich, I. V.; Loboda, A. V.; Thomson, B. A., An introduction to quadrupole–time-of-flight mass spectrometry. *J. Mass Spectrom.* **2001,** *36* (8), 849-865.

143. Wells, O., Scanning Electron Microscopy. McGraw-Hill: New York, USA, 1974.

144. Zhou, W.; Wang, Z., *Scanning Microscopy for Nanotechnology*. Springer Science: New York, USA.

145. Goldstein, J.; Newbury, D.; Joy, D.; Lyman, C.; Echlin, P.; Lifshin, E.; Sawyer, L.; Michael, J., *Scanning electron microscopy and x-ray microanalysis*. Kluwer Academic/ Plenum Publishers: New York, USA, 2003.

146. Simazhenkov, V.; Idem, R., *Crude Oil Chemistry*. Marcel Dekker, Inc: New York, USA, 2003.

147. Goderdhan, D.; Hunt, R., Exploiting the understanding of diesel fuel solvency to improve low temperature properties as exemplified for the korean market. *SAE International* **2015,** *01* (01), 1921.

148. Totten, G., *Fuels and Lubricants Handbook: Technology, Properties, Performance and Testing*. ASTM International: USA, 2003.

149. D1133-13 Standard test method for Kauri-Butanol value of hydrocarbon solvents. ASTM International: USA, 2013.

150. Hall, F.; Berger, P.; Collins, H., *Pesticide Formulations and Application Systems*. ASTM International: Philadelphia, USA, 1995.

151. Erwin, J., Assay of Diesel Fuel Components Properties and Performance. *J. Phys. A* **1992,** *37* (4), 54.

152. Goderdhan, D.; Hunt, R., The impact of fuel solvency on middle distillate cold flow performance. *SAE International* **2015,** *512* (1), 522.

153. Barker, J.; Richards, P.; Goodwin, M.; Wooler, J., Influence of high injection pressure on diesel fuel stability: a study of resultant deposits. *SAE international* **2009,** *1877* (1).

154. Rand, S., *Significance of tests for petroleum products*. 2003.

155. Gibbons, J.; Drozdoff, L.; Cripps, C., Nevada Division of Environmental Protection: Notice of Proposed Action. State of Nevada, 2010. http://ndep.nv.gov/

156. Concepts, A. R. http://www.advancedrefiningconcepts.com/.

157. Venkataraman, R.; Eser, S., Characterisation of solid deposits from the thermal-oxidative degradation of jet fuel. *Int. J. Oil Gas Coal T.* **2007,** *1* (1/2), 126 - 137.

158. Igarshi, J., Oxidative Degradation of Engine Oils. *J. Jpn. Soc. Tribologis.* **1990,** *35* (10).

159. Jain, S.; Sharma, M., Stability of biodiesel and its blends: A review. *Renew. Sust. Energ. Rev.* **2009,** *14* (2), 667.

160. Ofunne, G.; Maduako, A.; Ojinnaka, C., High Temperature Oxidation Stability of Automative Crankcase Oils and their Base Oils. *Tribol. Int.* **1990,** *23* (6), 407.

161. Jensen, R.; Korcek, S.; Zinbo, M., Liquid-phase autoxidation of organic compounds at elevated temperatures. Absolute rate constant for intermolecular hydrogen abstraction in hexdecane autoxidation at 120-190 °C. *Int. J. Chem. Kinet.* **1994,** *26* (6), 673.

162. Korcek, S.; Jensen, R., Relationship Between Base Oil Composition and Oxidation Stability at Increased Temperatures. *ASLE Trans.* **1975,** *19* (2).

163. Korcek, S.; Johnson, M.; Jenson, R.; Zinbo, M., Determination of High-Temperature Antioxidant Capability of Lubricants and Lubricant Components. *Ind. Eng. Chem. Res.* **1986,** *25* (1), 621.

164. Blaine, S.; Savage, P., Reaction Pathways in Lubricant Degradation- n-Hexadecane Autooxidation. *Ind. Eng. Chem. Res.* **1991,** *30* (9), 2185.

165. Jenson, R.; Korcek, S.; Mahoney, L.; M, S., Liquid-phase autoxidation of organic compounds at elevated temperatures. *J. Am. Chem. Soc.* **1981,** *103* (7), 1742-1749.

166. Demirbas, A., Biodiesel. In *Biodiesel: A Realistic Fuel Alternative for Diesel Engines*, Springer: London, 2008; pp 111-119.

167. McCormick, R.; Ratcliff, M.; Moens, L.; Lawrence, R., Several factors affecting the stability of biodiesel in standard accelerated tests. *Fuel Process. Technol.* **2007,** *88* (7), 651-657.

168. Shahid, E.; Jamal, Y., A review of biodiesel as vehicular fuel. *Renew. Sust. Energ. Rev.* **2008,** *12* (9), 2484-2494.

169. Theis, M.; Skrifvars, B.; Zevenhoven, M.; Hupa, M.; Tran, H., Fouling tendency of ash resulting from burning mixtures of biofuels. Part 2: Deposit chemistry. *Fuel* **2006,** *85* (14–15), 1992-2001.

170. Fang, H.; McCormick, R., Spectroscopic study of biodiesel degradation pathways. *SAE international* **2006,** *01* (1), 3300.

171. Kalnes, T.; Marker, T.; Shonnard, D., Green Diesel: A Second Generation Biofuel. *Int. J. Chem. React. Eng.* **2007,** *05* (1), 14.

172. Trobaugh, C.; Burbink, C.; Zha, Y.; Whitacre, S., Internal diesel injector deposits: theory and investigations into organic and inorganic based deposits. *SAE International* **2013,** *10* (01), 2670.

173. Schmidt, B., Off-road diesel fuel system deposits- field experience. *SAE Powertrain, Fuels and Lubricants Meeting* **2010,** *01* (1), 162.

174. Wilson, S., Injector deposits in high load off-road applications. *SAE Powertrain, Fuels and Lubricants Meeting* **2010,** *2* (1).

175. Blizard, N., Continuing studies of injector deposit formation and field operational problems. *JSAE Powertains, Fuels and Lubricants Meeting* **2011**.

176. Demirbas, A., Biofuels, sources, biofuel policy, biofuel economy and global biofuel projections. *Energ. Convers. Manage.* **2008,** *49* (1), 88.

177. Singh, S. P.; Singh, D., Biodiesel production through the use of different sources and characterization of oils and their esters as the substitute of diesel: A review. *Renew. Sust. Energ. Rev.* **2010,** *14* (1), 200-216.

178. Perevozchikov, A., Sterols and their transport in animal development. *Russ. J. Dev. Biol.* **2008,** *39* (3), 131-150.

179. Wang, H., Analysis of sterol glycosides in biodiesel and biodiesel precipitates. *J. Am Oil Chem. Soc.* **2010,** *87* (1), 215.

180. Bondioli, P.; Cortesi, N.; Mariani, C., Identification and quantification of steryl glucosides in biodiesel. *Eur. J. Lipid Sci. Technol.* **2008,** *110* (2), 120-126.

181. Yang, S.; El-Ensashy, H.; Thongchul, N., *Bioprocessing technologies in biorefinery for sustainable production of fuels, chemicals and polymers*. John Wiley & Sons, Inc: New Jersey, USA, 2013.

182. Lee, M., *Mass spectrometry handbook*. John Wiley & Sons, Inc: New Jersey, USA, 2012.

183. Clement, L.; Hansen, S.; Costin, C.; Perri, G., Quantitation of sterols and steryl esters in fortified foods and beverages by GC/FID. *J. Am. Oil Chem. Soc.* **2010,** *87* (9), 973.

184. Gomez-Coca, R.; Camino-Perez, M.; Moreda, W., On the glucoside analysis: Simultaneous determination of free and esterified steryl glucoside in olive oil. Detailed analysis of standards as compulsory first step. *Food Chem.* **2013,** *141* (1), 1273.

185. Tang, H.; Guzman, R.; Salley, S.; Simon, K., Comparing process efficiency in reducing steryl glucosides in biodiesel. *J. Am. Oil Chem. Soc.* **2010,** *87* (1).

186. Gutierrez, A.; del Rio, J. C., Gas chromatography/mass spectrometry demonstration of steryl glycosides in eucalypt wood, Kraft pulp and process liquids. *Rapid Commun. Mass Spectrom.* **2001,** *15* (24), 2515-20.

187. Wewer, V.; Dombrink, I.; vom Dorp, K.; Dormann, P., Quantification of sterol lipids in plants by quadrupole time-of-flight mass spectrometry. *J. Lipid Res.* **2011,** *52* (5), 1039-54.

188. Dulf, F.; Unguresan, M.; Vodnar, D.; Socaciu, C., *Free and Esterified Sterol Distribution in Four Romanian Vegetable Oil*. Not. Bot. Horti Agrobot. Cluj-Napoca, 2010; Vol. 38.

189. Djerassi, C., Applications of mass spectrometry in the steroid field. In *Chemistry of natural products*, ISCNP, Ed. Buttersworth Scientific Publications: Norwich, UK, 1970; Vol. 21, pp 205-227.

190. Rinehart, K. L., Structure Elucidation of Natural Products by Mass Spectrometry. Volume II. Steroids, Terpenoids, Sugars, and Miscellaneous Classes. *J. Am. Chem. Soc.* **1965,** *87* (19), 4407-4407.

191. Budzikiewicz, H.; Djerassi, C.; Williams, D., *Structure elucidation of natural products by mass spectrometry*. Holden-Day, Inc.: San Francisco, USA, 1968; Vol. 2.

192. Gorgog, S., *Quantitative analysis of steroids*. Elsevier Science Publishing Company, Inc.: New York, USA, 1983; p 435.

193. Diekman, J.; Thomson, J.; Djerassi, C., Mass spectrometry in structural and stereochemical problems. Electron impact induced fragmentations and rearrangements of some trimethylsilyl ethers of aliphatic glycols and related compounds. *J. Org. Chem.* **1968,** *33*, 2271-2284.

194. Brown, F.; Djerassi, C., Elucidation of the course of the electron impact induced fragmentation of α,β-unsaturated 3-keto steroids. *JACS* **1980,** *102*, 802-817.

195. Karliner, J.; Budzikiewicz, H.; Djerassi, C., Mass spectrometry in structural and stereochemical problems. The electron impact induced elimination of water from 3-hydroxy steroids. *J. Org. Chem.* **1966,** *31* (1), 710.

196. Djerassi, C.; Kielczewski, M., The introduction of deuterium into the C-19 angular methyl group. *Steroids* **1963,** *2* (1), 125.

197. Djerassi, C., Isotope labelling and mass spectrometry of natural products. *Pure Appl. Chem.* **1964,** *9* (159-178).

198. Budzikiewicz, H.; Djerassi, C., Mass spectrometry in structural and sterochemical problems. Steroid ketones. *JACS* **1962,** *84* (1), 1430.

199. Thevis, M., Mass spectrometry in sports drug testing. In *Characterization of prohibited substances and doping control analytical assays* [Online] John Wiley & Sons, Inc: Canada, 2010.

200. Kostiainen, R.; Bruins, A. P., Effect of multiple sprayers on dynamic range and flow rate limitations in electrospray and ionspray mass spectrometry. *Rapid Commun. in Mass Spectrom.* **1994,** *8* (7), 549-558.

201. Enke, C. G., A predictive model for matrix and analyte effects in electrospray ionization of singly-charged ionic analytes. *Anal. Chem.* **1997,** *69* (23), 4885-93.

202. Tang, L.; Kebarle, P., Dependence of ion intensity in electrospray mass spectrometry on the concentration of the analytes in the electrosprayed solution. *Anal. Chem.* **1993,** *65* (24), 3654-3668.

203. Takats, Z.; Wiseman, J.; Gologan, B.; Cooks, G., Mass Spectrometry Sampling Under Ambient Conditions with Desorption Electrospray Ionization. *Science* **2004,** *306* (5695), 471-473.

204. Cody, R.; Laramee, J.; Nilles, M.; Durst, D., Direct Analysis in Real Time (DART) Mass Spectrometry. *JEOL News* **2005,** *40* (1), 8.

205. Haddad, R.; Sparrapan, R.; Kotiaho, T.; Eberlin, M., Easy ambient sonic-spray ionization-membrane interface mass spectrometry for direct analysis of solution constituents. *ACS* **2008,** *80* (3), 898.

206. Hirabayashi, A.; Sakairi, M.; Koizumi, H., Sonic Spray Ionization Method for Atmospheric Pressure Ionization Mass Spectrometry. *Anal. Chem.* **1994,** *66* (24), 4557-4559.

207. McEwen, C.; Gutteridge, S., Analysis of the Inhibition of the Ergosterol Pathway in Fungi Using the Atmospheric Solids Analysis Probe (ASAP) Method. *JACS* **2007,** *18* (7), 1274-1278.

208. Gross, J., *Mass Spectrometry: A Textbook*. Springer-Verlag: Heidelberg, Germany, 2011.

209. Cooks, G.; Ouyang, Z.; Takats, Z.; Wiseman, J., Ambient Mass Spectrometry. *Science* **2006,** *311*.

210. Venter, A.; Neufliu, M.; Cooks, G., Ambient desorption ionization mass spectrometry. *Trend Anal. Chem* **2008,** *27* (4).

211. Hajslova, J.; Cajka, T.; Vaclavik, L., Challenging applications offered by direct analysis in real time (DART) in food-quality and safety analysis. *Trend Anal. Chem* **2011,** *30* (2), 204.

212. Kruithof, A.; Penning, F., Determination of the Townsend ionization coefficient α for pure argon. *Physica* **1936,** *3* (6), 515-533.

213. Craig, R., Surface ionization source for mass spectrometry. *Rev. Sci. Instrum.* **1959,** *36* (1), 38.

214. Lyman, C.; Newbury, D.; Goldstein, J.; Williams, D.; Romig, A.; Armstrong, J.; Echlin, P.; Fiori, C.; Joy, D.; Lifshin, E.; Peters, K., *Scanning electron microscopy, x-ray microanalysis, and analytical electron microscopy*. Plenum Press: New York, USA, 1990.

215. Morris, R. E.; Hazlett, R. N., Methods for quantifying JFTOT heater tube deposits produced from jet fuels. *Energ Fuel* **1989,** *3* (2), 262-267.

216. Gross, J., Polydimethylsiloxane-based wide-range mass calibration for direct analysis in real-time mass spectrometry. *Anal. Bioanal. Chem.* **2013,** *405* (26), 8663.

217. Zhu, R.; Cheung, C. S.; Huang, Z.; Wang, X., Regulated and unregulated emissions from a diesel engine fueled with diesel fuel blended with diethyl adipate. *Atmos. Environ.* **2011,** *45*.

218. Ren, Y.; Huang, Z.; Miao, H.; Di, Y.; Jiang, D.; Zeng, K.; Liu, B.; Wang, X., Combustion and emissions of a DI diesel engine fuelled with diesel-oxygenate blends. *Fuel* **2008,** *87* (12), 2691-2697.

219. Rudnick, L., *Synthetics, Mineral Oils and Bio-based Lubricants*. CRC Press: USA, 2013.

220. Maleville, X.; Faure, D.; Legros, A.; Hipeaux, J., Oxidation of Mineral Base Oils of Petroleum Origin: The Relationship between Chemical Composition, Thickening, and Composition of Degradation Products. *Lubr. Sci.* **1996,** *9* (1), 1.

221. Kolwzan, B.; Gryglewicz, S., Synthesis and biodegradability of some adipic and sebacic esters. *J. Synthetic Lubric.* **2006,** *20* (2), 99.

222. Qian, X.; Xiang, Y.; Shang, H.; Cheng, B.; Zhan, S.; Li, J., Thermal-oxidation mechanism of dioctyl adipate base oil. *Friction* **2015,** *4* (1), 29.

223. Venkataraman, R.; Eser, S., Characterization of deposits formed on diesel injectors in field test and from thermal oxidative degradation of n-hexadecane in a laboratory reactor. *Chem. Cent. J.* **2009,** *2* (25), 1.

224. Altin, O.; Eser, S., Analysis of solid deposits from thermal stressing of a JP-8 fuel on different tube surfaces in a flow reactor. *Ind. Eng. Chem. Res.* **2001,** *40* (2), 596.

225. Zaikin, Y.; Zaikina, R., *Petroleum Radiation Processing*. CRC Press: Florida, USA, 2014.

226. Gray, M., *Upgrading petroleum residues and heavy oils*. Marcel Dekker: New York, USA, 1994.